Tunable dipolar interactions and collisional shielding in a quantum gas of polar molecules

by

Kyle Matsuda

A.B., Harvard University, 2016

A thesis submitted to the

Faculty of the Graduate School of the

University of Colorado in partial fulfillment

of the requirements for the degree of

Doctor of Philosophy

Department of Physics

2022

Committee Members:

Jun Ye, Chair

Ana Maria Rey

John L. Bohn

Eric A. Cornell

J. Mathias Weber

Matsuda, Kyle (Ph.D., Physics)

Tunable dipolar interactions and collisional shielding in a quantum gas of polar molecules

Thesis directed by Prof. Jun Ye

Ultracold polar molecules open new directions in quantum science owing to their complex internal structure and long-range dipolar interactions. Creation of a quantum-degenerate molecular gas, described in the first part of this thesis, is an important step toward unlocking the rich potential of molecular systems. However, simultaneously controlling both elastic and inelastic molecular interactions has remained an outstanding experimental challenge. Strong dipolar interactions have generally led to even stronger molecular losses, preventing the creation of deeply-degenerate and strongly dipolar molecular gases.

In this thesis, we demonstrate several methods for tuning molecular interactions with external electric fields. First, by tightly confining the molecules into a two-dimensional (2D) geometry and applying a strong electric field, we induced repulsive dipolar interactions that suppressed molecular losses while enhancing the elastic collision rate, allowing for direct evaporation of the molecules to below the Fermi temperature in 2D. Second, at particular electric field strengths, we observed resonant collisional shielding of rotationally excited molecules. At these resonances, the molecular loss rate could be tuned over nearly three orders of magnitude, and could be suppressed by up to a factor of 10. Third, we leveraged our highly controllable electric field to address and select single 2D layers of molecules, which allowed the observation of chemical reactions induced by interlayer dipolar interactions. Finally, we studied the intralayer interactions between molecules placed in a coherent superposition of rotational states, a first step toward engineering the collective spin dynamics in this system with long-range interactions.

Dedication

To Rich and Leslie, George and Irene, and Fujio and Amy.

Acknowledgements

Jun, thank you for everything — your support and guidance over the years has meant so much to me. While you have shared an immense amount of physics insight and engineering knowledge, more important than any technical lesson was seeing your infectious enthusiasm and optimism for science. I hope to emulate your passion and fearlessness in solving problems wherever I go.

Thank you to my wonderful colleagues on the KRb experiment. Jake Covey built the new experiment and got us all up to speed on running the machine. For the first several years, the KRb team was postdocs Luigi De Marco and Giacomo Valtolina along with grad students Will Tobias and me, and later joined by postdoc Jun-ru Li. We had a lot of fun working together in those first few years, even throughout all of the challenges we faced in getting the new machine working. It's hard to express here just how much it meant to work with this team, so I'll keep it brief. Luigi, Giacomo, and Jun-ru, you were such great mentors and I feel extremely lucky to have learned from you. All of you took me under your wing in different ways, and I am so grateful. Will and I started on KRb at the same time and spent six years working together. Will, I learned a ton from working with you, both from your electronics and laser knowledge as well as your careful and methodical approach to thinking through scientific problems. We went through a lot of ups and downs together on the experiment, but we made it! The project is in great hands with the new team of Cal Miller, Annie Carroll, and Jake Higgins, and I'm excited to see what they will go on to do next.

Thank you also to the other members of the Ye group, for your scientific help and for your friendship, especially Will M., Ross, Lingfeng, Lindsay, Aki, Sara, Ed, Toby, Alex, Colin, Kyungtae, John, Dhruv, Tanya, Kia, Will C., Lee, Qizhong, Chuankun, Jutta, Yewei, Justin, Kameron, Dave,

Hao, Roman, Xin, and Vandy. Special thanks to Lee Liu, who was kind enough to read an early version of Chapter 2 of this thesis and provide helpful suggestions.

We had the opportunity to discuss and collaborate with some of JILA's amazing theorists, including Ana Maria Rey, Thomas Bilitewski, Peiru He, John Bohn, Reuben Wang, and Jose D'Incao. It was a privilege to collaborate with external theory groups as well — Goulven Quéméner and Lucas Lassablière from Université Paris-Saclay, and Peter Zoller and Andreas Kruckenhauser from Innsbruck. Thank you also to Eric Cornell and his group for many helpful discussions while we were getting the machine up and running. JILA also has a fantastic support structure of both technical and administrative staff — thank you to Terry Brown, Carl Sauer, Felix Vietmeyer, James Fung-A-Fat, Hans Green, Kim Hagen, James Ulrich, J.R. Raith, Corey Keesling, Brian Lynch, Amy Allison, Agnieszka Lynch, Krista Beck, Beth Kroger, and so many others for your help.

Thank you to John Doyle at Harvard for introducing me to experimental AMO physics as an undergrad. Before I joined John's lab, I wasn't sure about majoring in physics, let alone going to grad school. I had a wonderful experience in John's lab learning from grad students Ivan Kozyryev and Louis Baum. They were great teachers and so generous with letting me get involved in the experiment. John's incredible passion for cold molecule research also inspired me to seek out molecule experiments for my graduate research.

Outside of physics, thank you to the members of the wonderful jazz scene at CU and in Boulder and Denver with whom I had the pleasure of playing music over the past several years. I feel lucky to have found such a welcoming musical community here. Thank you to the friends who helped make my time in Colorado fun (in addition to those mentioned above), especially AJ, Cecilia, Claudia, Isabel, Max, Kat, Clare, Pete, Scott, Adam, Franz, Gary, BK, and Jonathan.

Thank you to my parents Rich and Leslie and brother Dan for your unconditional love and support. I am fortunate to have a big, crazy, and wonderful extended family — thank you to my grandparents, aunties and uncles, and cousins who have been there throughout everything. Most importantly, thank you to my partner Angela. This thesis wouldn't have been possible without your endless patience, encouragement, and support.

Contents

Chapter

1 Introduction **1**

1.1 Making ultracold molecules . . . 3

1.2 Ultracold molecular losses . . . 5

1.3 Our work: Controlling interactions with electric fields . . . 6

2 Ultracold polar molecules and dipolar interactions **9**

2.1 Energy scales . . . 9

2.2 Molecular Hamiltonian in the ground electronic and vibrational state . . . 10

2.3 Dipole moment . . . 13

2.3.1 Calculating the matrix elements . . . 14

2.3.2 Induced dipole moment . . . 16

2.3.3 Transition dipole moments . . . 18

2.3.4 AC Polarizability . . . 20

2.4 Dipolar interactions – Introduction . . . 25

2.5 Dipolar interactions – In the bulk . . . 26

2.5.1 General considerations . . . 27

2.5.2 Reactive losses . . . 28

2.5.3 Elastic scattering . . . 34

2.5.4 Resonant shielding . . . 35

2.6 Dipolar interactions – In the lattice . . . 37
2.6.1 Two-particle calculation . . . 38
2.6.2 Calculating the couplings . . . 40
2.6.3 Beyond the $p = 0$ term . . . 41
2.7 Summary . . . 42

3 Apparatus and experimental sequence **43**
3.1 Overview . . . 43
3.2 Optical trap setup . . . 47
3.3 Electric field control . . . 50
3.3.1 Back-of-the-envelope requirements . . . 51
3.3.2 Computing the field distribution . . . 55
3.3.3 Useful electrode linear combinations . . . 57
3.3.4 Minor imperfections of the electrode geometry . . . 58
3.3.5 Controlling the electrode voltages . . . 58
3.3.6 FPGA control of AD5791 DACs . . . 59
3.3.7 Cabling and connections . . . 60
3.3.8 High voltage rack . . . 62
3.4 Radio-frequency fields . . . 65
3.4.1 Amplitude-shaped pulses . . . 68
3.4.2 Limitations of the rods: polarization purity and AC field homogeneity . . . 69
3.5 CCD calibration . . . 72

4 Degenerate Fermi gas of molecules in 3D **75**
4.1 Experimental procedure . . . 76
4.2 Properties of the molecular Fermi gas . . . 79
4.2.1 TOF thermometry . . . 79
4.2.2 Reduced loss rate . . . 82

4.2.3 Density fluctuations . . . 85
4.3 Feshbach ramp thermalization . . . 88
4.3.1 Collisional damping . . . 89
4.3.2 Dependence on the Feshbach ramp rate . . . 92
4.4 Conclusion . . . 93

5 Dipolar evaporation of molecules in 2D **94**
5.1 Producing a 2D sample . . . 95
5.1.1 Large spacing lattice . . . 99
5.1.2 Layer counting . . . 103
5.1.3 Loading procedure . . . 106
5.2 Loss suppression . . . 108
5.3 Elastic dipolar collisions . . . 110
5.4 Direct evaporation of molecules . . . 111
5.4.1 Combined optical + electric potential . . . 111
5.4.2 Evaporation trajectory . . . 112
5.4.3 2D Fermi gas of molecules . . . 116
5.5 Conclusion . . . 118

6 Resonant shielding of molecules in 2D and 3D **120**
6.1 Physical mechanism . . . 121
6.1.1 Two-channel picture . . . 123
6.2 Shielding in 2D . . . 127
6.3 Probing the collision anisotropy . . . 130
6.3.1 Contribution of m_L states vs θ . . . 130
6.3.2 Shielding in $m_L = 0$ . . . 133
6.4 Shielding in 3D . . . 134
6.4.1 Elastic collisions at the shielding field . . . 135

6.4.2 Direct evaporation of molecules in 3D . . . 138
6.5 Conclusion . . . 139

7 Single-layer control of molecules in a 1D optical lattice **141**
7.1 Addressing a single layer . . . 142
7.2 Magic angle electric field . . . 145
7.3 Interlayer dipolar spin-exchange interactions . . . 147
7.4 Conclusion . . . 151

8 Dipolar density shifts in 2D **152**
8.1 Spin Hamiltonian . . . 153
8.1.1 More discussion of χ . . . 157
8.1.2 Validity of the spin model . . . 158
8.2 Dynamical decoupling . . . 159
8.3 Density shift . . . 161
8.4 Tuning the interactions . . . 163
8.5 Dynamically reversing the evolution . . . 164
8.6 Conclusion . . . 167

9 Conclusion and Outlook **168**

Bibliography **171**

Appendix

A KRb energy levels in external fields **189**
A.1 Molecular Hamiltonian . . . 190
A.2 AC Stark shift . . . 193
A.3 Comparison to experiment . . . 195

Tables

Table

2.1 Coupling strengths for equation (2.2) 12

2.2 Some handy dipole matrix elements. 17

3.1 Polarizabilities for K, Rb, KRb*, and KRb at 1064 nm 48

4.1 Atom and molecule conditions for Figure 4.2 78

Figures

Figure

2.1 Cartoon of molecular energy scales 10

2.2 Energies of $N = 0$ and 1 states as a function of E, including hyperfine structure . . . 13

2.3 Energy and induced dipole moment as a function of the applied electric field 18

2.4 Composition of field-dressed eigenstates as a function of E 19

2.5 Transition dipole moments vs E 20

2.6 Effect of hyperfine structure on transition dipole moments 21

2.7 Cartoon of differential light shifts in a non-magic trap 22

2.8 Limiting cases of $\alpha(\theta)$ 24

2.9 p-wave barrier and dipolar anisotropy 29

2.10 Adiabatic energy curves vs d 30

2.11 Adiabatic energy curves from quasi-2D to 2D 32

2.12 a_D and E_D vs d 35

2.13 Energies of rotational state pairs vs ϵ 36

2.14 Ramsey fringes for two interacting molecules 40

2.15 Electric field dependence of $J_\perp$ and J_z 41

3.1 Schematic of the JILA KRb machine 44

3.2 Atomic level diagrams 46

3.3 Relevant atomic hyperfine states 46

3.4 Optical trap geometry 48
3.5 Plug, ODT2, LSL, and imaging optics layout 49
3.6 ODT1 and side imaging optics layout 49
3.7 Geometry of the electrodes 50
3.8 Some useful electrode linear combinations 57
3.9 Simplified block diagram of the electric field control 59
3.10 Corona sphere for HV connection 61
3.11 Transfer function of the HV cabling 62
3.12 Heating in the optical lattice from HV amp vibrations 63
3.13 High voltage rack 64
3.14 Block diagram of the K/KRb RF setup 65
3.15 Example Ramsey fringe 66
3.16 AC rod configurations 67
3.17 Probing $N = 0 \leftrightarrow 1$ while dressing $1 \leftrightarrow 2$ 68
3.18 Calibration of the amplitude shaping setup 70
3.19 Comparison of lineshapes using square and Blackman pulses 70
3.20 Inhomogeneous AC electric field 71
3.21 Calibration of Andor iXon Ultra 888 CCD 73

4.1 Cartoon of molecule production 77
4.2 Molecule production from a degenerate Bose-Fermi mixture 78
4.3 TOF thermometry of the molecular DFG 81
4.4 Molecular loss measurements at $T = 65$ and 300 nK 83
4.5 Reduction of the chemical reaction rate at low T/T_F. 84
4.6 Comparison of T/T_F from fluctuations and TOF expansion 87
4.7 STIRAP-induced slosh of KRb* 90
4.8 Collisional damping from K-KRb* elastic collisions 91

4.9 Summary of K-KRb* elastic collisions 91
4.10 KRb T/T_F versus Feshbach ramp rate 92

5.1 Cartoon of intra- vs inter-band collisions 96
5.2 Optical trap geometry for 2D work 97
5.3 Band mapping K and KRb 98
5.4 LSL optics setup 99
5.5 Parametric heating in the LSL 100
5.6 Rb density distribution in the ODT vs LSL 102
5.7 Rb layer distribution from matter-wave imaging 104
5.8 Matter-wave magnification to align the LSL 107
5.9 Dipolar suppression of loss in 2D 108
5.10 Crossover from 3D to quasi-2D 109
5.11 Elastic dipolar collisions in quasi-2D 110
5.12 Combined optical and electric potential 113
5.13 Evaporation sequence and trajectory 114
5.14 2D Fermi gas of molecules 116
5.15 Expansion energy of the 2D molecular Fermi gas 117

6.1 $V_{\text{shield}}(R_b)$ as a function of $|\mathbf{E}|$ 123
6.2 Two-channel picture of the shielding 125
6.3 Angular dependence of the shielding 126
6.4 Large variation of β near the shielding resonance 128
6.5 Measurement of the shielding resonances 129
6.6 Collisions in quasi-2D with tilted $\mathbf{E}$ 131
6.7 Collisions of $|0,0\rangle$ in tilted $\mathbf{E}$ 133
6.8 Summary of 2D shielding 134
6.9 Resonant shielding in 3D 135

6.10 Thermalization measurements at $|\mathbf{E}_s|$ . . . 137

6.11 Evaporation of molecules in 3D . . . 138

7.1 Layer-resolved spectroscopy . . . 143

7.2 Spectroscopy on many layers . . . 144

7.3 Rotational coherence of $|0\rangle$ and $|1\rangle$ . . . 146

7.4 Cartoon of dipolar exchange induced losses . . . 147

7.5 Losses induced by interlayer dipolar exchange . . . 149

7.6 Dependence of the interlayer dipolar exchange on Δ . . . 150

8.1 Cartoon of the spin Hamiltonian . . . 154

8.2 Dependence of χ on $|\mathbf{E}|$ . . . 154

8.3 Contrast decay with and without dynamical decoupling . . . 160

8.4 Dynamical decoupling sequence . . . 160

8.5 Measurement of the dipolar density shift . . . 162

8.6 Tuning χ with $|\mathbf{E}|$ and α . . . 165

8.7 Internal state dependence of χ . . . 165

8.8 Reversing the spin Hamiltonian . . . 166

A.1 Microwave spectrum at $|\mathbf{E}| = 0$ . . . 197

A.2 Microwave spectrum at $|\mathbf{E}| = 1$ kV/cm . . . 197

Chapter 1

Introduction

Controlling interactions is a central theme in quantum science. In quantum computation, controlled interactions between individual quantum bits (or "qubits") generate entanglement, the key resource needed to achieve a quantum advantage over classical computers [1, 2, 3]. In quantum sensing and metrology, interactions can be harnessed to create highly entangled states such as squeezed states, which can have tremendously increased sensitivity over classical states [4, 5, 6]. And in quantum simulation, interacting systems can be used to create synthetic materials in the lab that are more easily tuned and probed than their real life counterparts, including novel states of matter that have never been observed in the solid state [7, 8, 9].

Modern atomic physics has demonstrated the profound insights that can be gained by controlling the interactions between atoms, nature's building blocks, to the highest degree. Quantum-degenerate gases, where the average spacing between particles is on the order of their de Broglie wavelength, are the experimental platform for many of these explorations. In these gases, normally subtle effects like quantum statistics play a leading role — ultracold bosons condense into a Bose-Einstein condensate (BEC) [10], where all of the atoms in the gas act in unison, while ultracold fermions form a degenerate Fermi gas (DFG) [11], mimicking the behavior of electrons in metals. The exquisite control afforded by ultracold gases has enabled beautiful experiments, including the direct observation of a quantum phase transition between a superfluid and an insulating state [12, 13]; the engineering of a smooth crossover in a fermionic gas between a Bardeen-Cooper-Schrieffer (BCS) superfluid, where the atoms are paired in momentum space as in conventional

superconductors, and a BEC of loosely-bound Feshbach molecules, where the atoms are paired in real space [14, 15, 16, 17]; and the creation of incredibly precise atomic clocks [18] that can sense the gravitational redshift over a 1 mm scale [19].

These amazing advances depended on the ability to tame and control atomic interactions. Even creating a quantum-degenerate gas, often the starting point for current experiments, requires favorable atomic properties to prevent undesired losses and to maintain thermal equilibrium throughout the cooling process [20]. Fortunately, the dominant inelastic processes in alkali atoms could be brought under control, which opened a path to the creation of BEC in 1995 [21]. In addition, the elastic collisions of the atoms were found to be highly tunable via Feshbach resonances [22], which allowed the interactions to be changed from attractive to repulsive and from zero to extremely strong, giving a powerful method of controlling the many-body physics of the gas [7].

The scientific richness of ultracold atomic systems inspires the following question: What if we consider more complicated quantum objects?

Molecules, with their chemical diversity and increased complexity over atoms, have the potential to open an even wider scientific frontier. Even simple diatomic molecules possess complicated internal structure and strong electric dipolar interactions that are desirable for applications including precision measurement, quantum metrology, and quantum simulation [23, 24, 25, 26, 27]. Cold ($\lesssim 1$ K) and ultracold molecules ($\lesssim 10\,\mu$K) have already been used in the lab to shed light on questions from molecular scales (chemistry) all the way up to cosmic ones (particle physics). The production of cold molecules, which have only a few internal states populated, has enabled controlled chemistry [28, 29] and the study of fundamental quantum processes like scattering resonances [30, 31]. In the ultracold regime, where the relative motion of two colliding molecules is quantized, effects like quantum statistics can control the chemical reaction rate in the gas [32]. Starting from a well-defined initial quantum state, one can perform state-to-state chemistry and observe how the product quantum state depends on that of the reactants [33, 34, 35]. At the other end of the spectrum, cold molecules have been used to probe the violation of fundamental symmetries — in this case, the product of charge and parity reversal (CP) — by setting limits on

the electric dipole moment of the electron [36, 37]. These tabletop measurements are a probe of CP-violating physics at energy scales comparable to those probed by the LHC, and are enabled, in part, by using specific quantum states of carefully chosen molecular species [38, 39].

If we can cool molecules deep into the quantum-degenerate regime, where experiments with atoms have uncovered such a wealth of quantum many-body phenomena, we should be in for a treat. In contrast to the contact interactions of atoms, polar molecules exhibit long-range and anisotropic dipolar interactions [24, 26]. Fascinating new phases of matter have been predicted to emerge as a result, including spin liquids [40], Wigner crystals [41], p-wave superfluidity and unconventional pairing [42, 43], and more. When confined to individual optical lattice sites, molecules can be used to simulate spin Hamiltonians with highly tunable couplings [44, 45, 46]. With molecules in the quantum regime, it is possible to envision engineering tunable molecular quantum matter that is tailored for certain precision measurements, in the spirit of recent work on optical clocks [47, 48]. As one example, dipolar interactions of molecules in 2D are predicted to generate spin-squeezed states that could be used for precision metrology [49].

Realizing the full promise of ultracold molecules requires gaining full control of molecular interactions. Nature has given us a good challenge here: taming molecules is a much trickier task than taming atoms. The very complexity that makes molecules fascinating to study also makes them difficult to control, even for the simple diatomic molecules discussed in this thesis. In particular, controlling the interactions of molecules has proven difficult, preventing the creation of quantum-degenerate gases until recently [50, 51, 52, 53, 54]. In the next sections, we discuss how ultracold molecules are produced and the challenges in controlling their interactions.

1.1 Making ultracold molecules

Nearly every ultracold atom experiment starts with a laser cooling stage that brings atoms from room temperature (or higher) down to typically several hundreds of microkelvin. Unfortunately, laser cooling is impractical for a generic molecule. Laser cooling relies on repeated cycles of optical excitation and spontaneous emission to exert a force. Any population that decays into an-

other internal state, outside of the main cooling transition, must be repumped using an additional laser wavelength. For commonly used atoms, a single repump laser is enough to close the cycle and scatter hundreds of thousands of photons. Molecules have so many more internal states than atoms that the number of repump lasers needed can quickly become impractical. In recent years, there has been rapid progress in identifying molecules with convenient structure for laser cooling. These molecules have an excited electronic potential with a very similar shape to the ground electronic potential, which means that the chance of changing vibrational states during a spontaneous emission event is low (in molecule jargon, "the Franck-Condon factors are highly diagonal"), drastically reducing the number of repump lasers needed [55]. By a clever choice of the rotational states used for cooling, leakage of molecules into higher rotational states can also be prevented [56]. With these advances, magneto-optical traps (MOTs) of diatomic molecules such as SrF [57], CaF [58, 59], and YO [60] have been produced, and even more complex polyatomic molecules are starting to be laser cooled [61, 62, 63]. Despite these exciting advances, samples produced by direct laser cooling have so far been limited to phase space densities (PSDs) several orders of magnitude away from quantum degeneracy [64].

Before the advent of direct laser cooling of molecules, an alternative approach was pioneered at JILA: simultaneously cool two different species of atoms down to near quantum degeneracy, and then coherently associate pairs of atoms into molecules. This cooling method has the advantage that molecules inherit the ultralow temperature of the parent atoms, and thus are created at a PSD approaching quantum degeneracy. The association process typically consists of two steps: (1) the magnetic field is swept through a Feshbach resonance, adiabatically converting pairs of colliding atoms into loosely bound molecules [22], and (2) lasers are used to coherently convert the Feshbach molecules into rovibrational ground state molecules via a process called stimulated Raman adiabatic transfer (STIRAP) [65]. This approach led to the successful formation of a quantum gas of $^{40}K^{87}Rb$ molecules in 2008, at a temperature just above quantum degeneracy [66]. Since then, many other molecule species have been produced near quantum degeneracy, such as RbCs [67, 68],

NaK [69, 70, 71], NaRb [72], NaLi [73], and NaCs [74, 75].[1]

1.2 Ultracold molecular losses

With the creation of near-quantum-degenerate KRb came the surprising observation of ultracold chemical reactions, even at ultralow temperatures. The KRb + KRb system is chemically reactive, with $\mathrm{KRb} + \mathrm{KRb} \rightarrow \mathrm{K_2} + \mathrm{Rb_2}$ exothermic by about 14 K [32], and these bimolecular chemical reactions were found to be the dominant loss process of the gas. With the molecules colliding in a single partial wave, this system was an exciting platform for studying fundamental connections between basic quantum mechanics and chemistry. In particular, the quantum statistics of the particles was extremely influential on the loss rate — KRb molecules in the same internal state, being identical fermions, must collide with odd motional angular momentum to have an overall antisymmetric wavefunction. In the ultracold regime, they collide in the lowest p-wave ($L = 1$) channel and must tunnel through the centrifugal barrier to get close enough to undergo a chemical reaction. However, if the molecules are put into a statistical mixture of internal states, then they can undergo s-wave collisions, which have no barrier. Thus, by controlling a single nuclear spin state, the chemical reaction rate could be changed by two orders of magnitude [32].

Those experiments demonstrated how long-range potential barriers, despite being much lower than typical chemical energy scales, play a key role in ultracold chemical reactions. Later studies showed that dipolar interactions could also be used to change the height of the centrifugal barrier, hence changing the loss rate [79]. Owing to the anisotropic nature of the dipolar interaction, attractive head-to-tail collisions dominated the behavior and led to a sharply increasing loss with increasing interaction strength. In conjunction with these experiments, theorists developed models to explain the observed loss rates. They found that the loss of KRb was "universal", in the sense that the strong short-range reactive loss simplified understanding of the collisions, making the behavior depend only on the long-range potentials [80, 81, 82, 83].

[1] A drawback of this method is that it has so far been limited to molecules consisting of two alkali atoms ("bialkalis"), though alkali + alkaline-earth combinations are under investigation [76, 77, 78].

While the reactive loss provided an interesting and fruitful research direction, it also represented a roadblock for studying quantum many-body physics with the molecules. One approach to suppressing the loss was to load the molecules into a deep three-dimensional (3D) optical lattice [84]. Since each lattice site had at most one molecule due to fermionic statistics, the chemical reactions were shut off, enabling the observation of many-body spin dynamics due to resonant dipolar spin exchange between molecules [46, 85]. Molecules loaded into optical tweezers [86, 74] are similarly protected from reactive losses.

However, to create the most general and versatile molecular system, one would like the ability to control the losses even in a bulk system. Many proposals require a deeply-degenerate gas of molecules, where the thermal energy is low enough for the interactions to be dominant. Ideally, one could use evaporative cooling [20], one of the workhorse techniques of atomic physics, to further cool the gas into deep degeneracy. However, successful evaporation depends on a favorable ratio of elastic ("good") to lossy ("bad") collisions, which was hindered by the strong reactive losses.

This motivated other research groups to choose molecular species such as RbCs, NaK, and NaRb, in which this chemical pathway is endothermic [87]. In principle, these molecules should be non-reactive, but in practice they have mostly exhibited (near-)universal loss [67, 69, 88, 89]. Investigation of the microscopic mechanism for the loss is still ongoing. Some experiments see evidence for losses of collisional complexes [90, 34] due to the optical trapping light [91, 92, 93], while others see no effect [94, 95]. Despite these challenges, there has been exciting progress on control of short-range atom-molecule collisions, with the recent observation of atom-molecule Feshbach resonances by two groups [96, 97, 98].

1.3 Our work: Controlling interactions with electric fields

In 2018, we were able to create the first quantum-degenerate gas of polar molecules by starting from a deeply-degenerate atomic mixture (Chapter 4). Similar results were also achieved by the Munich group in NaK in 2021 [53]. However, in both cases the molecules were produced at zero electric field and hence had zero dipolar interaction, and the dominant interaction in the gas was

still short-range losses. Subsequently, we turned our focus to the long-range dipolar interactions as a means of controlling the molecular collisions. By engineering long-range barriers to prevent the molecules from reaching short range, one can suppress the molecular losses while also turning on elastic dipolar collisions.

We were able to demonstrate two complementary methods for controlling the molecular collisions. First, by tightly confining the molecules along the direction of the applied electric field, we realized a quasi-two-dimensional (quasi-2D) system where the attractive head-to-tail dipolar collisions were suppressed [99, 100, 101, 102]. In 2D, the repulsive side-to-side collisions stabilized and thermalized the gas, allowing for efficient evaporative cooling of the molecules to below the Fermi temperature (Chapter 5). Second, we observed resonant electric field shielding of the molecules [103, 104]. By tuning the strength of the applied electric field, dipole-coupled molecular states could be made resonant, leading to a suppression of the loss in both 2D and 3D (Chapter 6).[2]

Both of these methods rely heavily on a large and tunable external electric field to polarize the molecules and control their dipolar interactions. The in-vacuum electrodes in our second-generation JILA KRb machine [106], combined with precision analog control electronics [107], allow us to apply stable electric fields of up to 15 kV/cm on the molecules. Additionally, we can apply flexible electric field gradients to control the potential energy landscape experienced by the molecules, and manipulate the direction of the molecular dipoles by tilting the electric field vector. These new technical capabilities (Chapter 3) were an essential ingredient for the experiments described in this thesis.

Since the dipolar interaction is long ranged, spatial control over the molecular distribution also provides a means of controlling interactions in the gas. Leveraging our precise electric field control, we were able to spectroscopically select individual 2D layers of molecules using an electric field gradient. This layer-by-layer control of the molecular internal state allowed us to observe and control dipolar spin exchange interactions between separated layers (Chapter 7). Most recently,

[2] For another complementary approach, see the microwave shielding work by the Harvard [105] and Munich [54] groups, which also leverages the long-range dipolar interactions between molecules.

we have been spectroscopically studying the effects of dipolar interactions in the gas using Ramsey spectroscopy, where the interactions manifest at lowest order as a density-dependent frequency shift of the molecular transition (Chapter 8).

Chapter 2

Ultracold polar molecules and dipolar interactions

Here, we give a short primer on ultracold polar molecules and their dipolar interactions, focusing on the aspects that are most relevant for the experiments in this thesis. We will primarily describe the behavior of $^1\Sigma$ molecules like KRb, though some of the general features may be applicable to molecules with more complicated internal structure. First, we give a quick overview of the molecular structure focusing on the most relevant states for our purposes, the rotational states of the ground electronic and vibrational manifold. Next, we show how to calculate the induced and transition dipole moments for the rotational states, and discuss their behavior as a function of the external electric field. We also discuss how to control the AC polarizability of the molecules, an important ingredient for achieving long coherence times in an optical trap. Finally, we conclude by describing some features of the dipolar interaction between molecules.

2.1 Energy scales

A major motivation for studying polar molecules is their rich internal structure [23, 27]. Compared to atoms, molecules have additional internal degrees of freedom, namely vibrations and rotations, that can be harnessed for quantum applications.[1] The experiments presented in this thesis are primarily concerned with the molecular rotations, which are long-lived and interact via long-range and anisotropic dipolar interactions.

[1] An illustrative example is the $^3\Delta_1$ state used for the electron electric dipole moment searches [36, 37]. In those experiments, a careful choice of molecule and of its internal state provides numerous benefits: enormous ($\sim$ GV/cm) internal electric fields that can be controlled by small ($\sim$ V/cm) fields in the lab, very low magnetic field sensitivity, and hyperfine states that act as an internal co-magnetometer [38, 39].

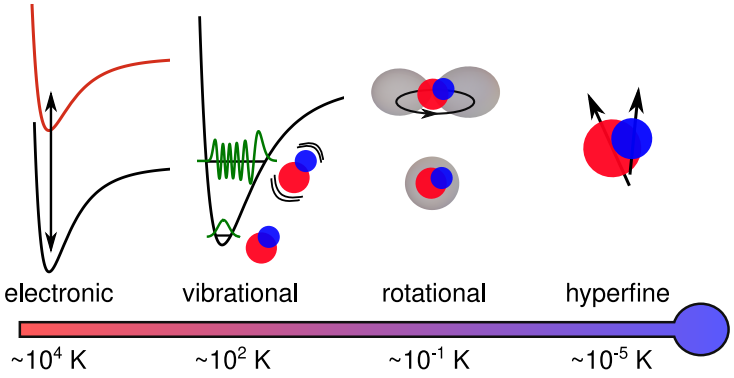

Figure 2.1: Cartoon of molecular energy scales.

To discuss the internal states of the molecule, it is helpful to invoke the Born-Oppenheimer approximation, which says that we can treat the electronic and nuclear degrees of freedom separately [108]. The approximation is based on the observation that electronic energy scales are typically far beyond vibrational or rotational energies, so the nuclear motion may be treated as adiabatic with respect to the electronic states. While the BO approximation can break down in some interesting cases, particularly where two electronic potentials intersect, it is appropriate for the states of KRb that we will work with in this thesis. Within the BO approximation, we can cleanly separate the electronic, vibrational, and rotational wavefunctions: the electronic potentials ($\sim$ 100s of THz) support a number of bound states, which are the vibrational states ($\sim$ 10s of THz); the vibrational wavefunctions determine the average separation of the nuclei, which determines the moment of inertia of the molecule and sets the rotational energy scale ($\sim$ 1s of GHz). This hierarchy of energies is depicted schematically in Figure 2.1.

2.2 Molecular Hamiltonian in the ground electronic and vibrational state

The experiments in this thesis are performed in the ground $X^1\Sigma^+(v = 0)$ electronic and vibrational state of KRb. In this relatively simple state, with no electronic spin or orbital angular momentum, and no vibrational quanta, the molecule can be imagined as two atoms connected by a rigid stick (the bond). Neglecting hyperfine states, the only degree of freedom left is the rotation

of the molecule, described quantum mechanically by the rotational angular momentum N and its projection m_N onto the $\hat{\mathbf{z}}$ axis. The energies are given by the rigid rotor Hamiltonian,

$$H_{\text{rot}} = B_v \mathbf{N}^2 = B_v N(N+1), \tag{2.1}$$

where $B_v = \hbar^2/2I$ is the rotational constant, and I is the moment of inertia of the molecule in the ground vibrational state.

Unfortunately, the picture given by equation (2.1) is a bit too simple. Generally, the atoms also have nuclear spin, which can complicate the spectrum due to couplings with the rotational states. In our case, ^{40}K has $I_{\text{K}} = 4$ and ^{87}Rb has $I_{\text{Rb}} = 3/2$, which give a total of $9 \times 4 = 36$ hyperfine states. We typically use the uncoupled basis $|N, m_N, m_{\text{K}}, m_{\text{Rb}}\rangle$ to describe the system, with m_{K} and m_{Rb} the nuclear spin projections for K and Rb, respectively.

Taking into account the rotational and hyperfine structure and external magnetic and electric fields $\mathbf{B}$ and $\mathbf{E}$, one obtains the following Hamiltonian [109],

$$H = H_{\text{rot}} + H_{\text{S}} + H_{\text{hf}} + H_{\text{Z}} \tag{2.2}$$

$$H_{\text{rot}} = B_v \mathbf{N}^2 \tag{2.3}$$

$$H_{\text{S}} = -\mathbf{d} \cdot \mathbf{E} \tag{2.4}$$

$$H_{\text{hf}} = \sum_{i=\text{K,Rb}} \mathbf{V}_i \cdot \mathbf{Q}_i + \sum_{i=\text{K,Rb}} c_i \mathbf{N} \cdot \mathbf{I}_i + c_3 \mathbf{I}_{\text{K}} \cdot \mathbf{T} \cdot \mathbf{I}_{\text{Rb}} + c_4 \mathbf{I}_{\text{K}} \cdot \mathbf{I}_{\text{Rb}} \tag{2.5}$$

$$H_{\text{Z}} = -g_r \mu_N \mathbf{N} \cdot \mathbf{B} - \sum_{i=\text{K,Rb}} g_i \mu_N \mathbf{I}_i \cdot \mathbf{B}(1 - \sigma_i). \tag{2.6}$$

The couplings are given in Table 2.1, and full matrix elements are given in Appendix A. For simplicity, we will assume throughout this chapter that $\mathbf{B} = B\hat{\mathbf{z}}$ and $\mathbf{E} = E\hat{\mathbf{z}}$.

The hyperfine Hamiltonian consists of several terms. The first term describes the interaction of the electrons with the electric quadrupole moment $\mathbf{Q}_i$ of the nucleus, which depends on the nuclear spin $\mathbf{I}_i$. The $\mathbf{V}_{\text{K}} \cdot \mathbf{Q}_{\text{K}}$ term couples $\Delta N \leq 2$, $|\Delta m_N| \leq 2$, and $\Delta m_N = -\Delta m_{\text{K}}$ (and similarly for $\mathbf{V}_{\text{Rb}} \cdot \mathbf{Q}_{\text{Rb}}$), although in practice states with different N are too far in energy to have an appreciable mixing by the interaction. The second term in the Hamiltonian describes the

Parameter	Value
B_v	1.1139514(5) GHz
$(eqQ)_{\mathrm{K}}$	0.452(9) MHz
$(eqQ)_{\mathrm{Rb}}$	−1.308(9) MHz
c_{K}	−24.1 Hz
c_{Rb}	420.1 Hz
c_3	−48.2 Hz
c_4	−2030.4 Hz
g_r	0.0140
g_{K}	−0.324
g_{Rb}	1.834
σ_{K}	1321×10^{-6}
σ_{Rb}	3469×10^{-6}

Table 2.1: Coupling strengths for equation (2.2). Values in the first section are experimental values from Ref. [110]. Values in the second section are theoretical values from Ref. [109].

interaction between the rotation of the molecule and the individual nuclear spins, and the final two terms describe the tensor and scalar spin-spin interactions. The Zeeman Hamiltonian contains the interaction of the rotation and screened nuclear spins with $\mathbf{B}$.

The hyperfine effects become very important at low electric field, leading to a maze of avoided crossings for the $N > 0$ states as the field strength E is increased. Figure 2.2 shows the energies of the $N = 0$ and 1 states in the low E region. While the $N = 0$ states (left panel) do not show any avoided crossings, the $N = 1$ states (right panel) show a number of avoided crossings due to the mixing from the electric quadrupole terms. Some of the avoided crossings are fairly narrow and difficult to ramp through adiabatically, so for some of the work in this thesis (particularly Chapter 6) it was helpful to produce the molecules at higher E above the crossings. At low E, the strong mixing from H_{hf} can also cause changes in properties like the transition dipole moments and differential polarizabilities between states.

Thankfully, we often do not need to consider the full hyperfine structure of the molecule. At large E, the energies are dominated by H_{S} and the nuclear spins are essentially decoupled from the rotations, so the hyperfine structure is largely irrelevant when working within a single $(m_{\mathrm{K}}, m_{\mathrm{Rb}})$ manifold. For most of the work described in this thesis, we will work in this regime. In the next

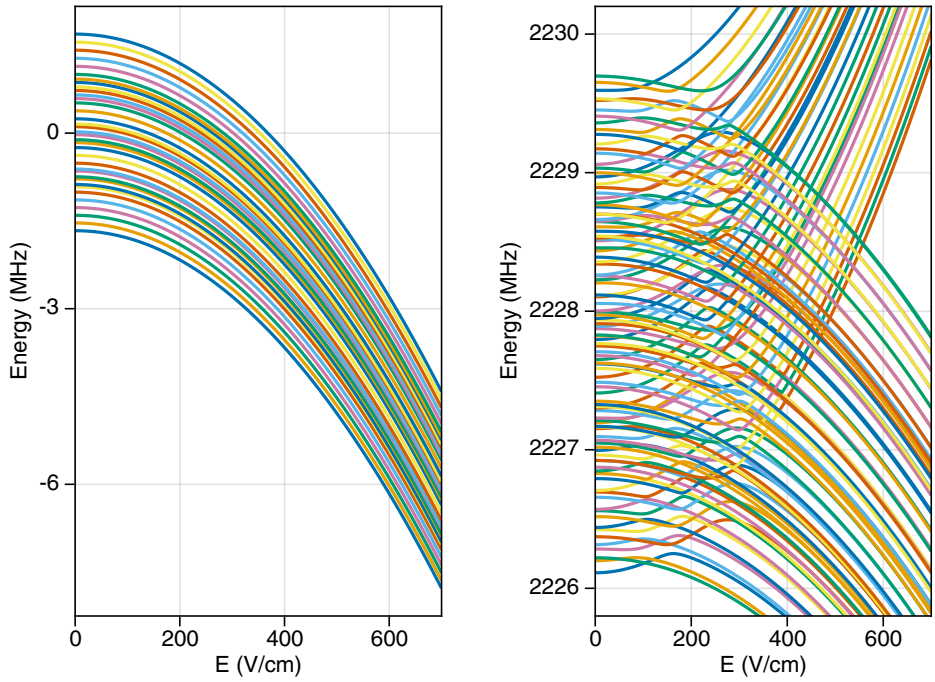

Figure 2.2: Energies of $N = 0$ (left) and $N = 1$ (right) states as a function of E, including hyperfine structure. A magnetic field of $B = 545.9$ G is also present. Both fields point along the $\hat{\mathbf{z}}$ direction.

section, we focus on the rotational states and their dipolar characteristics, ignoring the hyperfine structure unless otherwise noted.

2.3 Dipole moment

Polar molecules provide a very convenient experimental "handle": their electric dipole moment $\mathbf{d}$. Classically, $\mathbf{d}$ describes how the molecule responds to $\mathbf{E}$, according to $U = -\mathbf{d} \cdot \mathbf{E}$. Physically, $\mathbf{d}$ comes from the polarization of the electron distribution, which points along the internuclear axis in the frame of the molecule. At $E = 0$, the dipole moment averages to zero in the lab frame, but as we turn on E, the molecules start to align along the field, leading to an induced dipole moment in the lab frame.

To see this quantum mechanically, we need to study the behavior of

$$H = H_{\text{rot}} + H_{\text{S}} = B_v \mathbf{N}^2 - d_z E, \tag{2.7}$$

where $\mathbf{E} = E\hat{\mathbf{z}}$ and d_z is the dipole operator along $\hat{\mathbf{z}}$. At $E = 0$, H is rotationally symmetric and hence the eigenstates $|N, m_N\rangle$ have zero induced dipole moment, $\langle N, m_N|d_z|N, m_N\rangle = 0$. By turning on E, we mix adjacent rotational levels N and $N\pm1$, leading to new field-dressed eigenstates $|\tilde{N}, m_N\rangle$ that have a non-zero induced dipole moment, $\langle \tilde{N}, m_N|d_z|\tilde{N}, m_N\rangle \neq 0$. We define $|\tilde{N}, m_N\rangle$ as the field-dressed eigenstate that adiabatically connects to the bare rotational state $|N, m_N\rangle$ as $E \to 0$. Note that m_N is still a good quantum number when $\mathbf{E} \parallel \hat{\mathbf{z}}$.

Since the neighboring rotational states are mixed by $\mathbf{E}$, there must be a dipolar coupling between the bare states, $\langle N+1, m_N|d_z|N, m_N\rangle \neq 0$, which we call the transition dipole moment between the two states. In addition to coupling to a static electric field, the transition dipole moment allows us to drive Rabi oscillations between the states using near-resonant AC (microwave) electric fields. A resonant AC field $\mathbf{E}(t) = \hat{\mathbf{z}}\, E e^{i\omega t}$ causes strong mixing of the two states even for small field amplitude E, since the energy gap between the states (on the order of B_v) is bridged by the photon energy $\hbar\omega$. In contrast, mixing the states with a static field requires that the coupling $\langle N+1, m_N|d_z|N, m_N\rangle \times E$ is large enough to overcome the energy difference between the states. As we later discuss, the transition dipole moment also leads to dipolar spin-exchange interactions, whereby a molecule in $|N, m_N\rangle$ and another in $|N', m'_N\rangle$ may exchange rotational states.

2.3.1 Calculating the matrix elements

Here we give a short derivation of the matrix elements of the dipole operator, following the explanation given in section 8.4.2 of Brown and Carrington and using the angular momentum machinery from section 5.5 of that text [108]. The physical picture is that the molecule always has a dipole moment that points along the internuclear axis in the molecule (body-fixed) frame, with a strength given by the permanent dipole moment d_{perm}. We just need a way to rotate into the frame of the molecule.

How we transform a physical quantity between the lab and molecule frame depends on its associated angular momentum (the rank k of its spherical tensor representation). More formally, we need the Wigner rotation matrix, which tells us how states of different angular momentum

transform under rotations. Let $\mathcal{D}^{(k)}_{pq}(\omega)^*$ be the rank k rotation matrix, with ω representing the Euler angles for rotating from the molecule frame to the lab frame. With these definitions, the index p is associated with the lab frame while the index q is associated with the molecule frame. To rotate a rank k tensor $T^{(k)}_q(\mathbf{A})$ from the molecule frame to the lab frame, we contract it with $\mathcal{D}^{(k)}_{pq}(\omega)^*$ [108],

$$T^{(k)}_p(\mathbf{A}) = \sum_q \mathcal{D}^{(k)}_{pq}(\omega)^* T^{(k)}_q(\mathbf{A}). \tag{2.8}$$

Now we can see how to calculate the dipole matrix elements: we use $\mathcal{D}^{(k)}_{pq}(\omega)^*$ to rotate into the molecular frame, where the dipole operator is just a number d_{perm}. In other words, the dipole matrix elements are just those of the rotation matrix times d_{perm}.

The matrix elements of $\mathcal{D}^{(k)}_{pq}(\omega)^*$ are given on page 167 of Brown and Carrington [108],

$$\begin{aligned}\langle J, m_J, \Omega | \mathcal{D}^{(k)}_{pq}(\omega)^* | J', m'_J, \Omega' \rangle = (-1)^{m_J - \Omega} \sqrt{(2J+1)(2J'+1)} \\ \times \begin{pmatrix} J & k & J' \\ -\Omega & q & \Omega' \end{pmatrix} \begin{pmatrix} J & k & J' \\ -m_J & p & m'_J \end{pmatrix},\end{aligned} \tag{2.9}$$

where J is the total angular momentum, m_J is its projection onto $\hat{\mathbf{z}}$ in the lab frame, and Ω is the projection of J onto the internuclear axis. The terms in parentheses are Wigner $3j$ symbols.

We restrict our attention to the rotational states in the ground electronic state of KRb, so $J = N$ and $\Omega = \Omega' = 0$, which gives[2]

$$\begin{aligned}\langle N, m_N | \mathcal{D}^{(k)}_{pq}(\omega)^* | N', m'_N \rangle = (-1)^{m_N} \sqrt{(2N+1)(2N'+1)} \\ \times \begin{pmatrix} N & k & N' \\ 0 & q & 0 \end{pmatrix} \begin{pmatrix} N & k & N' \\ -m_N & p & m'_N \end{pmatrix}.\end{aligned} \tag{2.10}$$

Recall that the bottom row of a $3j$ symbol must sum to zero. This means that for the states we care about, the only nonzero matrix element of $\mathcal{D}^{(k)}_{pq}(\omega)^*$ is the one with $q = 0$.

[2] A brief explanation of why $J = N$ and $\Omega = \Omega' = 0$: The ground state of KRb is $^1\Sigma^+$. The ^{1} refers to the electronic spin multiplicity, $2S+1$, indicating that $S = 0$, and Σ refers to the projection Λ of electronic orbital angular momentum L onto the internuclear axis. Analogous to how we write S, P, D, ... for atomic orbitals, spectroscopists write Σ, Π, Δ, ... for $\Lambda = 0, 1, 2, ...$ Since $S = 0$ and $\Lambda = 0$, this implies that $\Omega = 0$. Finally, $J = N$ because S and L are zero.

Using this, we can calculate the dipole matrix elements in the lab frame,

$$\begin{aligned}\langle N, m_N|T_p^{(1)}(\mathbf{d})|N', m'_N\rangle &= \sum_{q=-1}^{1}\langle N, m_N|\mathcal{D}_{pq}^{(1)}(\omega)^* T_q^{(1)}(\mathbf{d})|N', m'_N\rangle \\ &= \langle N, m_N|\mathcal{D}_{p0}^{(1)}(\omega)^* T_{q=0}^{(1)}(\mathbf{d})|N', m'_N\rangle \\ &= d_{\text{perm}}\langle N, m_N|\mathcal{D}_{p0}^{(1)}(\omega)^*|N', m'_N\rangle \\ &= d_{\text{perm}}(-1)^{m_N}\sqrt{(2N+1)(2N'+1)} \\ &\times \begin{pmatrix} N & 1 & N' \\ 0 & 0 & 0 \end{pmatrix}\begin{pmatrix} N & 1 & N' \\ -m_N & p & m'_N \end{pmatrix}. \end{aligned} \tag{2.11}$$

In the second line, we used the fact that only the $q = 0$ term contributes for the rotational states in the same electronic state. Finally, in the third line, we used $T_{q=0}^{(1)}(\mathbf{d}) = d_{\text{perm}}$ (the dipole moment points along the internuclear axis in the frame of the molecule). Table 2.2 lists the dipole matrix elements between a few of the lowest rotational levels.

From equation (2.11), we can directly read off the dipole selection rules. The top rows of the $3j$ symbols must satisfy the triangle inequality, so $|N - N'| \leq 1$. In addition, the first $3j$ symbol is zero if $N = N'$, so we see that the dipolar coupling changes N by ± 1. The bottom rows must sum to zero, so the second $3j$ symbol implies $m_N - m'_N = p$. Since p ranges from -1 to 1, the dipolar coupling changes m_N by 0 or ± 1.

We will often use a slightly more ergonomic notation for the spherical components of the dipole operator, $d^p = T_p^{(1)}(\mathbf{d})$. In terms of the Cartesian components, these are

$$d^0 = d_z, \tag{2.12}$$

$$d^{\pm 1} = \mp\frac{1}{\sqrt{2}}(d_x \pm i d_y). \tag{2.13}$$

2.3.2 Induced dipole moment

With the dipole matrix elements in hand, we can analyze the behavior of equation (2.7) as a function of E. We again assume that $\mathbf{E} = E\hat{\mathbf{z}}$, so only the $p = 0$ term of equation (2.11) is relevant and m_N is preserved. It is also convenient here to introduce the dimensionless field

Matrix element	Value in units of d_{perm}
$\langle 1,0\|d^0\|0,0\rangle$	$1/\sqrt{3}$
$\langle 1,\pm1\|d^{\pm1}\|0,0\rangle$	$1/\sqrt{3}$
$\langle 2,0\|d^0\|1,0\rangle$	$2/\sqrt{15}$
$\langle 2,\pm1\|d^{\pm1}\|1,0\rangle$	$1/\sqrt{5}$

Table 2.2: Some handy dipole matrix elements.

strength $\epsilon = E/E_c$, where $E_c = B_v/d_{\text{perm}}$ is the characteristic field strength for the molecule ($E_c = 3.9$ kV/cm for KRb).

At $\epsilon = 0$, the eigenstates are just the bare rotational states $|N, m_N\rangle$, with energies $E_N = B_v N(N+1)$. For small ϵ, we can calculate the Stark shift in second-order perturbation theory, giving the following simple expression for the energy shifts of the lowest states $|0,0\rangle$ and $|1,0\rangle$,

$$\Delta E^{(2)}_{0,0} = -\frac{\epsilon^2}{6} B_v \tag{2.14}$$

$$\Delta E^{(2)}_{1,0} = \frac{\epsilon^2}{10} B_v, \tag{2.15}$$

and induced dipole moments

$$d^{(2)}_{0,0}(\epsilon) = -\frac{\partial \Delta E^{(2)}_{0,0}}{\partial E} = \frac{\epsilon}{3} d_{\text{perm}} \tag{2.16}$$

$$d^{(2)}_{1,0}(\epsilon) = -\frac{\partial \Delta E^{(2)}_{1,0}}{\partial E} = -\frac{\epsilon}{5} d_{\text{perm}}. \tag{2.17}$$

At higher ϵ, these simple expressions break down as E causes significant mixing of the rotational states. Figure 2.3 shows the energies and induced dipoles ($d = \langle \tilde{N}, m_N | d^0 | \tilde{N}, m_N \rangle$) of the several lowest rotational levels as a function of ϵ (solid lines), obtained by diagonalizing equation (2.7) using states up to $N_{\max} = 8$. The dotted lines are the results from second-order perturbation theory. Note that the stretched states with $|m_N| = \tilde{N}$ all have induced dipoles that increase monotonically with ϵ, since they are the lowest-energy states in each m_N manifold. All of the other states have an initially negative induced dipole, before eventually turning positive. This means, for example, that the direct dipolar interaction strength ($\propto d^2$) between $|\tilde{0}, 0\rangle$ molecules increases monotonically with E, while the interaction between $|\tilde{1}, 0\rangle$ molecules reaches a local maximum near $\epsilon = 1.75$ (roughly $E = 7$ kV/cm for KRb).

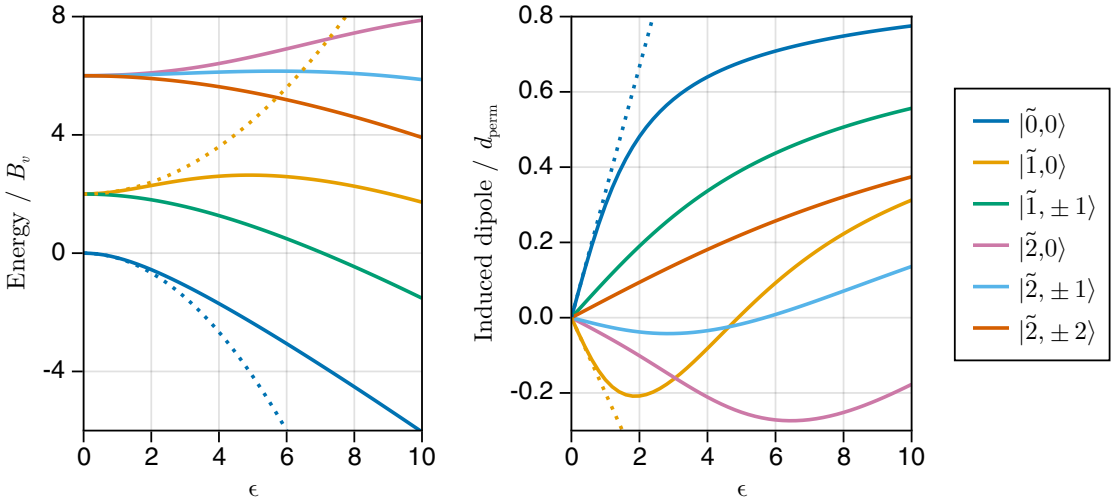

Figure 2.3: Energy and induced dipole moment of the $N \leq 2$ states as a function of the applied electric field. The dotted lines show the second-order perturbation theory results, valid for small ϵ.

Finally, we can plot the state composition of the field-dressed eigenstates $|\tilde{0},0\rangle$ (solid) and $|\tilde{1},0\rangle$ (dashed) in terms of the bare rotational states as a function of ϵ (Figure 2.4A). The state mixing can also be visualized by plotting the wavefunctions of the states at large ϵ as shown in (B). From the mean z-position of the wavefunctions, we can directly see the sign and magnitude of the induced dipole. Notably, at $\epsilon = 2$, the dipole moment of $|\tilde{1},0\rangle$ is negative and more probability is concentrated at $z < 0$, while at $\epsilon = 10$, the situation is reversed.

2.3.3 Transition dipole moments

In the previous section, we looked at the behavior of the induced dipole moments, which are the diagonal matrix elements of d^p. Next, we consider the behavior of the off-diagonal elements (transition dipole moments) $\langle \tilde{N}', m'_N | d^p | \tilde{N}, m_N \rangle$. The transition dipole moments allow us to resonantly couple different rotational states with AC electric fields and lead to dipolar spin-exchange interactions of the molecules (see section 2.6).

We note here that the distinction between the induced and transition dipoles is somewhat artificial — after all, they are both matrix elements of the same operator d^p. When applying a static

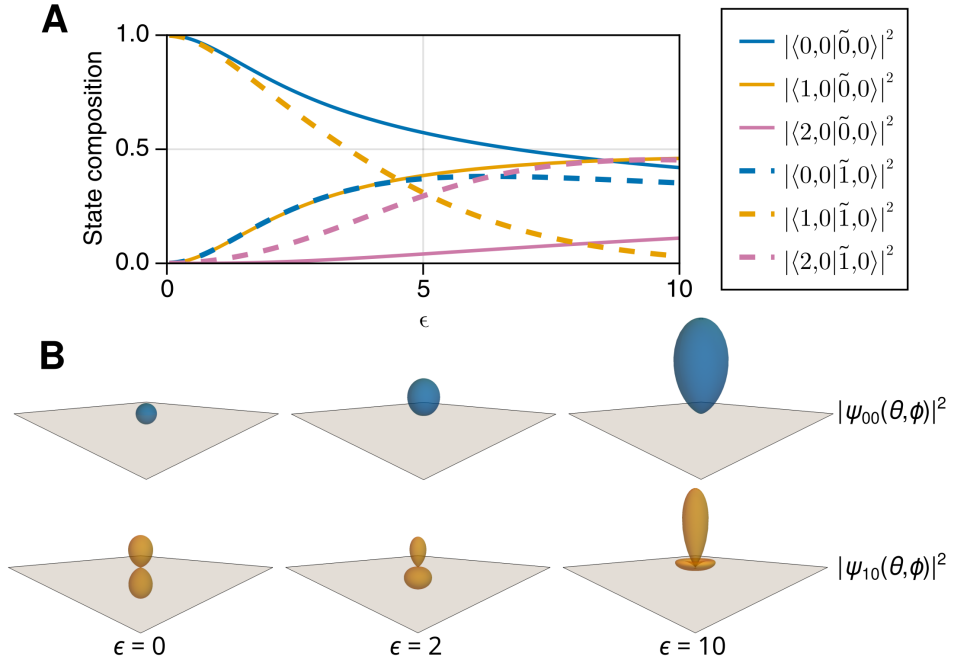

Figure 2.4: (A) The composition of $|\tilde{0},0\rangle$ and $|\tilde{1},0\rangle$ in terms of the bare rotational states as a function of ϵ. (B) Plots of the wavefunctions of $|\tilde{0},0\rangle$ and $|\tilde{1},0\rangle$ at several values of ϵ. The shaded area represents the $z = 0$ plane.

field $\mathbf{E}$, all neighboring states $|\tilde{N}, m_N\rangle$ and $|\tilde{N}+1, m_N\rangle$ are mixed according to the competition between the Stark term and the rotational energy, leading to an induced dipole moment of each state. In contrast, by applying an AC electric field $\mathbf{E}(t) = \mathbf{E}e^{-i\omega t}$, we can resonantly bridge the energy gap between a particular pair of states $|\tilde{N}, m_N\rangle$ and $|\tilde{N}+1, m_N+p\rangle$ to create an isolated two-level system. Since there is a transition dipole moment between the states, their populations undergo Rabi oscillations at an angular frequency $\Omega = \langle \tilde{N}+1, m_N+p|d^p|\tilde{N}, m_N\rangle E_p/\hbar$. Here, $E_{p=0}$ ($E_{p=\pm1}$) is the amplitude of π ($\sigma^{\pm}$) polarization in $\mathbf{E}$.

Having just found the field-dressed eigenstates in the previous section, we can evaluate the transition dipole moments $\langle \tilde{N}', m'_N|d^p|\tilde{N}, m_N\rangle$ as a function of ϵ. Owing to the state mixing shown in Figure 2.4, we would expect that the transition dipole moments for $\tilde{N} \to \tilde{N} \pm 1$ become weaker as the electric field is increased. On the other hand, the initially forbidden couplings $\tilde{N} \to \tilde{N} \pm 2$ (and higher) become weakly allowed as the states become very mixed. This is illustrated by Figure 2.5, which shows the behavior of transition dipole moments from $|\tilde{0},0\rangle$ as a function of ϵ.

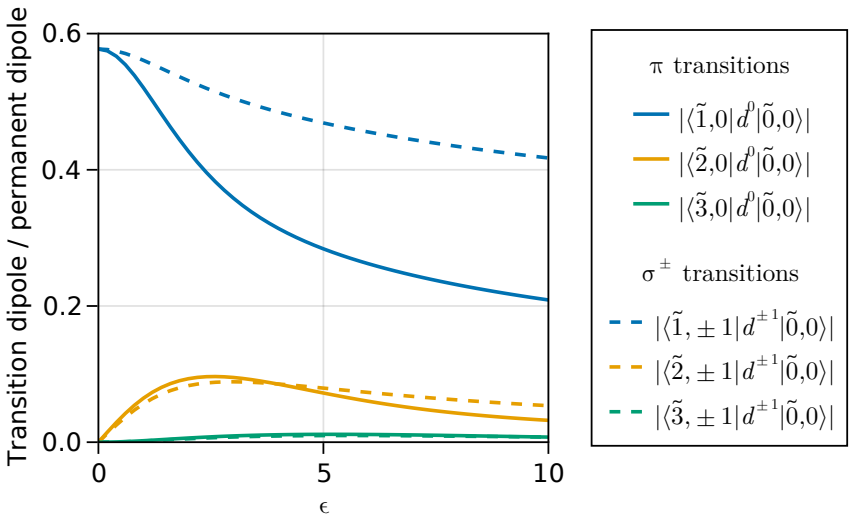

Figure 2.5: Transition dipole moment between $|\tilde{0},0\rangle$ and $|\tilde{N},0\rangle$ or $|\tilde{N},\pm1\rangle$ as a function of ϵ.

Since the transition dipole moments tend to be strongest near $E = 0$, they can be significantly affected by the nuclear electric quadrupole couplings, which are most important at low E. Figure 2.6 shows a calculation for the $\tilde{N} = 1$ states of KRb at $E \leq 1000$ V/cm. The states are colored based on their transition dipole moment with $|g\rangle = |\tilde{0},0,-4,1/2\rangle$, normalized by $d_{\text{perm}}/\sqrt{3}$. Without hyperfine structure, we would expect to only see one allowed transition for each of $p = 0, \pm1$. However, as shown in the plot, mixing due to the nuclear electric quadrupole coupling causes non-negligible coupling to a number of other states, especially in the region below 500 V/cm where there are a number of avoided crossings (see also Figure 2.2). Though these mixings complicate the spectrum, they also enable control of the hyperfine degrees of freedom through their coupling to the rotational states [111].

2.3.4 AC Polarizability

To conclude our discussion of the response of the molecules to external fields, we consider the effect of far off-resonant optical fields. Far red-detuned optical beams exert a dipole force on the molecules due to coupling with electronically excited states, giving an AC Stark shift $U(\mathbf{r}) = -\alpha I(\mathbf{r})$. Dipole traps formed by red-detuned laser beams are a standard technique for

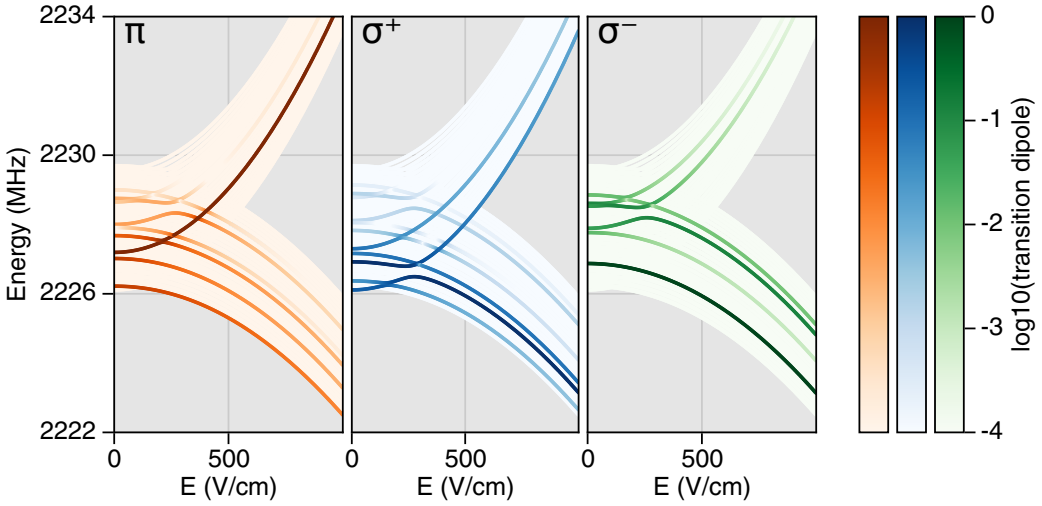

Figure 2.6: Effect of hyperfine structure on transition dipole moments. The plots show the energies of states in $\tilde{N} = 1$ for $E \leq 1000$ V/cm and $B = 545.9$ G, with both fields along $\hat{\mathbf{z}}$. The states are colored by their transition dipole moment with $|\tilde{0}, 0, -4, 1/2\rangle$. Transitions with relative strength $\leq 10^{-4}$ are all colored the same.

ultracold atoms [112], and our optical traps for molecules are based on the same principles. However, molecules have a more complicated light shift due to their anisotropic response to the electric field, which causes a polarization-dependent AC Stark shift [110, 113].

Understanding the AC Stark shift is key for creating long-lived coherent superpositions of the molecular rotations. If the ground and excited states have different AC polarizabilities, they experience different trapping potentials and the resonant transition frequency varies with the position in the trap, shown schematically in Figure 2.7. This inhomogeneous broadening leads to decoherence across the molecular sample. Beyond single particle effects, differential light shifts can also suppress interactions, for example, by detuning the dipolar spin-exchange interactions between molecules in a 3D optical lattice [46].

A similar problem also arises in atomic systems, most notably in optical lattice clocks where differential light shifts are an important source of systematic uncertainty [18]. The solution for clocks is to find a "magic wavelength" where the polarizabilities of the ground and excited states happen to match [114]. In molecules, it is generally harder to find a magic wavelength where

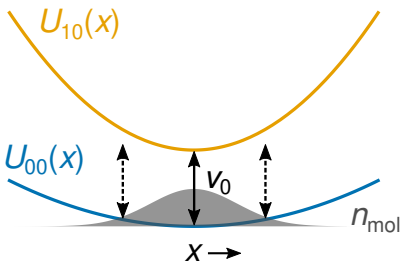

Figure 2.7: Cartoon of differential light shifts in a non-magic trap. The trapping potentials for the two states, $U_{00}(x)$ and $U_{10}(x)$, are different, leading to a variation in the resonant transition frequency as a function of the position in the trap.

losses from off-resonant excitation are also low, due to the dense spectrum of higher excited states [115, 116]. Instead, we can exploit the anisotropic part of the polarizability to find a "magic polarization angle" where the ground and excited states are matched [110, 113].

Let us be more concrete and examine the AC Stark Hamiltonian from Ref. [117],

$$H_{\mathrm{ac}} = -\frac{1}{3}(\alpha_{\parallel} + 2\alpha_{\perp})I_{\mathrm{laser}} - \frac{\sqrt{6}}{3}(\alpha_{\parallel} - \alpha_{\perp})T^{(2)}(\boldsymbol{\epsilon}, \boldsymbol{\epsilon}) \cdot C_2(\omega) I_{\mathrm{laser}}. \tag{2.18}$$

Here, I_{laser} is the light intensity and $\boldsymbol{\epsilon}$ its polarization vector. We assume that the light is linearly polarized, as is the case in our experiments; otherwise, there would also be a vector AC Stark term [113]. The molecular parameters $\alpha_{\parallel}$ and $\alpha_{\perp}$ characterize the frequency-dependent response parallel and perpendicular to the internuclear axis, respectively, and $C_{2p}(\omega) = \mathcal{D}^{(2)}_{p0}(\omega)^*$ is the rotation matrix into the molecular frame.[3] Note that the only off-diagonal matrix elements come from $C_2(\omega)$, which couples states of different N and m_N, weighted by the components of $T^{(2)}(\boldsymbol{\epsilon}, \boldsymbol{\epsilon})$. For typical experimental values of I_{laser}, the AC Stark shifts (on the order of the trap depth, typically several μK) are much smaller than the energy splittings between states of different $\tilde{N}$ (order of $B_v \sim 100$ mK), and we can safely neglect the N-changing part. The explicit form of the matrix elements in terms of $3j$ symbols can be found in Appendix A.

To gain some intuition, let us focus on the states we use most often, $N = 0$ and 1, at $E = 0$. Following Ref. [110], we will assume that we have solved for the molecular eigenstates at $I_{\mathrm{laser}} = 0$

[3] Here, ω represents the Euler angles for rotation to the molecular frame, not to be confused with the angular frequency of the optical field (the dependence of which is assumed to be included in $\alpha_{\parallel}$ and $\alpha_{\perp}$). Ref. [117] uses the notation $C_2(\alpha, \beta)$, where α and β represent the Euler angles, but we use $C_2(\omega)$ in this section to match with the earlier definition of $\mathcal{D}^{(2)}_{pq}(\omega)^*$ and avoid symbol clash with the polarizability α.

before adding $H_{\rm ac}$ as a perturbation. The ground state is isotropic, so its polarizability α_{00} is independent of the polarization,

$$\alpha_{00} = \frac{1}{3}(\alpha_\parallel + 2\alpha_\perp). \tag{2.19}$$

The excited state polarizabilities are determined by the following matrix elements,

$$\langle 1,0|\alpha|1,0\rangle = \frac{1}{3}(\alpha_\parallel + 2\alpha_\perp) - \frac{2}{15}(\alpha_\parallel - \alpha_\perp)(1 - 3\cos^2\theta) \tag{2.20}$$

$$\langle 1,\pm1|\alpha|1,\pm1\rangle = \frac{1}{3}(\alpha_\parallel + \alpha_\perp) + \frac{1}{15}(\alpha_\parallel - \alpha_\perp)(1 - 3\cos^2\theta) \tag{2.21}$$

$$\langle 1,0|\alpha|1,\pm1\rangle = \pm\frac{\sqrt{2}}{5}(\alpha_\parallel - \alpha_\perp)\sin\theta\cos\theta \tag{2.22}$$

$$\langle 1,\pm1|\alpha|1,\mp1\rangle = -\frac{1}{5}(\alpha_\parallel - \alpha_\perp)\sin^2\theta, \tag{2.23}$$

where θ is the angle between $\boldsymbol{\epsilon}$ and $\hat{\mathbf{z}}$.

The importance of the off-diagonal matrix elements depends on the energy splittings between the states. In the simplest case, shown schematically in Figure 2.8A, the three $N = 1$ states are split enough in energy that only the diagonal elements matter. These can be made equal to α_{00} at the "magic angle" where $\cos^2\theta = 1/3$ ($\theta \approx 54.7$ deg). From equation (2.18), it turns out that this is true of every diagonal matrix element, not just for $N = 1$, since they all involve only the $p = 0$ component $T^{(2)}_{p=0}(\boldsymbol{\epsilon},\boldsymbol{\epsilon}) \propto (1 - 3\cos^2\theta)$.

This scenario tends not to be very realistic since, aside from hyperfine structure, the $|\tilde{1},\pm1\rangle$ states are degenerate. Consequently, their mixing by $H_{\rm ac}$ is usually important. Figure 2.8B shows the limiting case where $|\tilde{1},\pm1\rangle$ are exactly degenerate but still separated in energy from $|\tilde{1},0\rangle$. In the basis of $|\tilde{1},-1\rangle$ and $|\tilde{1},1\rangle$, $H_{\rm ac}$ is well-approximated by a simple two-level system with eigenstates given by symmetric and antisymmetric superpositions of $|\tilde{1},\pm1\rangle$. As the energy splitting between $|\tilde{1},-1\rangle$ and $|\tilde{1},1\rangle$ is gradually increased from zero, the green and pink curves in (B) approach the green curve in (A). In the intermediate regime, higher-order terms in $I_{\rm laser}$ (sometimes called "hyperpolarizability") also contribute, since the light shifts the energies of the states and hence also changes the degree of mixing.

Having discussed some limiting cases, we now mention two regimes of particular relevance

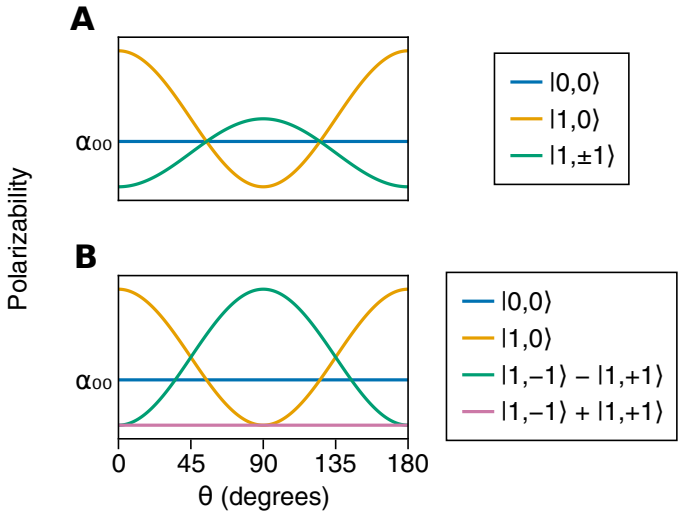

Figure 2.8: Limiting cases of $\alpha(\theta)$. (A) No mixing: the energy splittings of the $N = 1$ states are larger than any AC Stark shifts. The observed polarizabilities are just the diagonal terms of $H_{\rm ac}$. (B) Maximum mixing of $|1, \pm 1\rangle$: $|1, \pm 1\rangle$ are degenerate and split in energy from $|1, 0\rangle$. The two $|m_N| = 1$ states are strongly mixed by the optical field, resulting in symmetric and antisymmetric eigenstates. Both (A) and (B) are computed assuming that the eigenstates at $I_{\rm laser} = 0$ are pure rotational states $|N, m_N\rangle$, and that $\alpha_{\parallel} > \alpha_{\perp} > 0$.

for our experiment. At low E, the $N = 1$ states have small splittings of ~ 100 kHz due to the nuclear electric quadrupole interaction. Since the optical trap depth can be on the order of 100 kHz, AC Stark shifts can mix all three states. The quadrupole interaction also causes some mixing with states of different hyperfine character. The behavior at $E = 0$ was studied experimentally in KRb in Ref. [110], and subsequently in RbCs [118], NaK [119] and NaRb [120], as well as in $^2\Sigma$ CaF molecules [121]. At slightly larger E, the Stark shifts suppress the nuclear quadrupole couplings, and the hyperfine structure decouples from the rotational states. In NaK, this decoupling at moderate E (300 V/cm) was used to suppress the hyperpolarizability term for $|\tilde{1}, 0\rangle$, leading to an enhancement of the coherence time between $|\tilde{0}, 0\rangle$ and $|\tilde{1}, 0\rangle$ [119].

At high E, $|\tilde{1}, 0\rangle$ is much higher in energy than $|\tilde{1}, \pm 1\rangle$ due to the different DC Stark shifts of the states, so the off-diagonal terms are not important for $|\tilde{1}, 0\rangle$. The most notable feature is that the state mixing from E can change the strength of the anisotropic term. As shown theoretically in Ref. [113], this leads to an electric field strength ("magic field") where the polarizabilities of $|\tilde{0}, 0\rangle$

and $|\tilde{1}, 0\rangle$ are matched for all θ. For KRb, the magic field is predicted to occur at $E \approx 10$ kV/cm [113].

Finally, we should mention that magic wavelengths have recently been found for NaK [122] by utilizing a narrow electronic transition [123]. Further theoretical work suggests that this technique can also be extended to simultaneously achieve magic conditions for several rotational states [124].

This concludes our summary of the dipolar characteristics of rigid-rotor molecules in an external electric field. Next, we consider the dipolar interaction between two molecules.

Before moving on, a brief word on notation. So far, it has been helpful to distinguish between the bare and field-dressed states to discuss wavefunction overlaps, matrix elements, etc. However, in experiments, we do not have access to the bare rotational states at any nonzero electric field. For describing the dipolar phenomena that we observe at $E > 0$, we will often only care about the behavior of the field-dressed eigenstates. Because of this, from now on we will drop the tilde on the field-dressed eigenstates, writing them as $|N, m_N\rangle$ when the meaning is clear from context.

2.4 Dipolar interactions – Introduction

Perhaps the most intriguing aspect of ultracold molecules is their dipolar interactions. The long-range and anisotropic nature of these interactions makes polar molecules an exciting setting for studying many body physics [24, 26, 27]. Classically, two dipoles interact according to

$$V_{\mathrm{dd}} = \frac{\mathbf{d}_1 \cdot \mathbf{d}_2 - 3(\mathbf{d}_1 \cdot \hat{\mathbf{r}})(\mathbf{d}_2 \cdot \hat{\mathbf{r}})}{4\pi\epsilon_0 r^3}, \tag{2.24}$$

where $\mathbf{r}$ is the vector separating the dipoles.

In this thesis, we study a range of dipolar phenomena, including dipolar collisions of molecules in a bulk (2D) geometry, resonant shielding arising from dipolar coupling between pairs of internal states, as well as dipolar spin-exchange interactions between separated ensembles of molecules. All of these can be be more or less understood at an intuitive level from a single equation: V_{dd} expressed in terms of spherical tensor operators [45],

$$V_{\mathrm{dd}}(r, \theta, \phi) = -\frac{\sqrt{6}}{4\pi\epsilon_0 r^3} \sum_{p=-2}^{2} (-1)^p C_{2,-p}(\theta, \phi) T_p^{(2)}(\mathbf{d}_1, \mathbf{d}_2), \tag{2.25}$$

where θ and ϕ are the polar and azimuthal angles of $\mathbf{r}$, respectively, and we have assumed that $\mathbf{E}$ points along $\hat{\mathbf{z}}$. As a reminder, the spherical tensor components are [108]

$$T_0^{(2)}(\mathbf{d}_1, \mathbf{d}_2) = \frac{1}{\sqrt{6}} \left(2d_1^0 d_2^0 + d_1^{+1} d_2^{-1} + d_1^{-1} d_2^{+1}\right) \tag{2.26}$$

$$T_{\pm 1}^{(2)}(\mathbf{d}_1, \mathbf{d}_2) = \frac{1}{\sqrt{2}} \left(d_1^{\pm 1} d_2^0 + d_1^0 d_2^{\pm 1}\right) \tag{2.27}$$

$$T_{\pm 2}^{(2)}(\mathbf{d}_1, \mathbf{d}_2) = d_1^{\pm 1} d_2^{\pm 1}. \tag{2.28}$$

Here, d_i^p is just the same dipole operator we studied in section 2.3, acting on the i-th molecule. The angular part is $C_{2,p}(\theta, \phi) = (4\pi/5)^{1/2} Y_{2,p}(\theta, \phi)$, where $Y_{l,m}(\theta, \phi)$ is a spherical harmonic [45].

The interaction V_{dd} depends not only on the internal rotational states of the interacting molecules (through $\mathbf{d}_1$ and $\mathbf{d}_2$), but also on their relative motion (through r, θ, and ϕ). As a result, the qualitative behavior of V_{dd} can be strongly influenced by the external trapping geometry, which determines the accessible motional states. In the next sections, we will consider the behavior of equation (2.25) in two opposite limits where the molecules are either free to move in 3D ("bulk") or pinned to sites in an optical lattice. We will focus primarily on the dipolar interactions between ultracold molecules — other dipolar systems, such as magnetic [125, 126] and Rydberg [127, 128] atoms are exciting areas of active research, but are not discussed in detail here.

2.5 Dipolar interactions – In the bulk

In a bulk 3D geometry, two colliding molecules can be characterized by their collision wavevector k and relative angular momentum state $|L, m_L\rangle$. The collision energy is determined by the temperature T, which sets the average relative velocity of the collision partners. The angular momentum L contributes a centrifugal barrier in the collisions, and there is also an isotropic van der Waals interaction with coefficient C_6, giving a total interaction of [81]

$$V(r, \theta, \phi) = \frac{\hbar^2 L(L+1)}{2\mu r^2} - \frac{C_6}{r^6} + V_{\mathrm{dd}}(r, \theta, \phi), \tag{2.29}$$

where μ is the reduced mass of two colliding molecules.

We need to calculate the matrix elements of V_{dd} to understand equation (2.29) quantitatively. To simplify things, we'll make two assumptions: the molecules are initially in the same field-dressed rotational state $|N, m_N\rangle$, and their internal states are not changed by the interaction. The first assumption is generally true in our experiments since we prepare all of the molecules in a single internal state; otherwise, the molecules are distinguishable and are quickly lost due to s-wave collisions (which have no centrifugal barrier) [32]. The second assumption is generally true since the excited rotational states are typically not energetically accessible — the rotational splitting $B_v \sim 50$ mK is many orders of magnitude higher than our collision energy (set by $T \sim 300$ nK).[4]

Since m_{N1} and m_{N2} cannot change, only the $p = 0$ term of equation (2.25) is relevant, and we get

$$\langle L, m_L | V_{\mathrm{dd}} | L', m'_L \rangle = -\frac{1}{4\pi\epsilon_0 r^3}(-1)^{m_L}\sqrt{(2L+1)(2L'+1)} \times \begin{pmatrix} L & 2 & L' \\ 0 & 0 & 0 \end{pmatrix} \begin{pmatrix} L & 2 & L' \\ -m_L & 0 & m'_L \end{pmatrix} 2(d_{N,m_N})^2, \tag{2.30}$$

where $d_{N,m_N} = \langle N, m_N | d^0 | N, m_N \rangle$ is the induced dipole. The interaction no longer depends on the internal states of the molecule, except through d_{N,m_N}, so we can drop the subscripts and parameterize the interactions with the single parameter d (the induced dipole moment). Also, note that the second $3j$ symbol enforces $m_L = m'_L$.

If the molecules are prepared in the same internal state, then we also have to account for their quantum statistics. For identical fermions (bosons), only odd (even) L are allowed. The centrifugal term in equation (2.29) suppresses the interactions for higher L, so we will primarily be interested in the behavior of the lowest channel ($L = 1$ for fermionic ^{40}K^{87}Rb).

2.5.1 General considerations

Let us start by considering a few limits. At $E = 0$, the induced dipole d is zero and thus $V_{\mathrm{dd}} = 0$. Here, the system is spherically symmetric and both the total angular momentum $N_1 + N_2 + L$

[4] As we will discuss later, the resonant shielding effect occurs when we can engineer the breakdown of this second assumption.

and its projection are conserved. As E is turned on, only cylindrical symmetry about $\hat{\mathbf{z}}$ remains, which leaves the projection $m_{N1} + m_{N2} + m_L$ the only good quantum number — in other words, $V_{\rm dd}$ mixes partial waves. Since $C_2(\theta, \phi)$ couples states with $L' = L \pm 2$, we end up with two sets of coupled partial waves consisting of the even and odd values of L.

We can also use a fixed value of $|d| > 0$ and consider the limits with r. It is helpful to start by extracting some characteristic length scales from $V(r)$. This is done by setting each term equal to the kinetic energy at some separation $r = a_{D,\rm vdW} = 1/k$, giving the dipolar length [129]

$$a_D = \frac{\mu}{\hbar^2} \frac{d^2}{4\pi\epsilon_0} \tag{2.31}$$

and the van der Waals length $a_{\rm vdW} = (2\mu C_6/\hbar^2)^{1/4}$, with k the collision wavevector. At large separations $r \gg a_D, a_{\rm vdW}$, the interaction $V(r)$ is zero and L and m_L are good quantum numbers. On the other hand, at $r \sim a_D$, the states are significantly mixed by $V_{\rm dd}$, causing changes in both the reactive losses and elastic scattering of the molecules.

2.5.2 Reactive losses

Two KRb molecules can be lost in a collision by undergoing an exothermic chemical reaction $2\mathrm{KRb} \rightarrow \mathrm{K_2} + \mathrm{Rb_2}$, which releases about 15 K of energy that propels the products from the trap [32, 79, 34]. The reaction rate can be elegantly described by a quantum threshold model [81], which relates the reaction rate to the probability of tunneling through a potential barrier to reach short range ($r \ll a_{\rm vdW}$) where a reaction can occur. Such a barrier is naturally present for fermionic KRb due to the centrifugal p-wave ($L = 1$) barrier. Turning on $V_{\rm dd}$ alters the height of the barrier and hence changes the probability of tunneling to short range.

Let us first consider the situation with no dipolar interactions. The behavior of $V(r)$ for $d = 0$ and $L = 1$ is shown schematically in Figure 2.9A. There is a p-wave barrier formed by the competition between the centrifugal and van der Waals terms, whose height V_b is much higher than T ($V_b = 24$ μK for KRb). This barrier prevents the molecules from reaching short range (gray region in Figure 2.9A), where the behavior depends sensitively on the details of the unknown

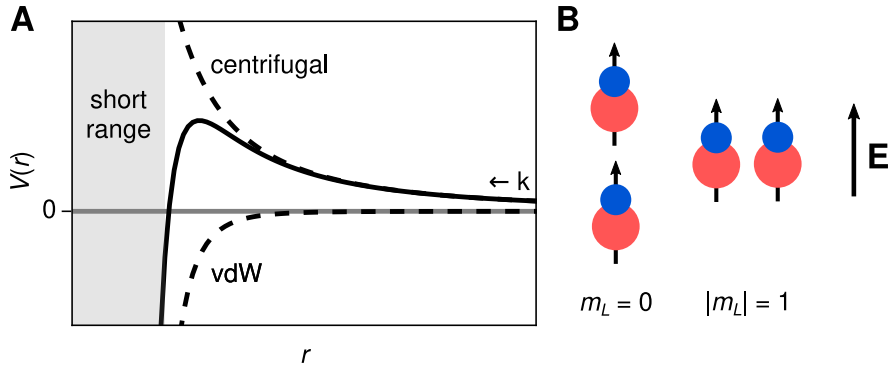

Figure 2.9: (A) Schematic diagram of the p-wave barrier in the absence of dipolar interactions. (B) Relative orientation of the molecules for $L = 1$ collisions with different values of m_L.

short-range potential. For KRb, the experimentally observed loss behavior [32, 79] is well-described by using a perfectly absorbing short range potential (the "black hole model"), which is attributed to the exothermic chemical reactions [82, 83, 81]. As a result, the molecular loss rate is "universal" (determined only by the long range behavior) [82] and set by the rate of tunneling through the p-wave barrier, which occurs with probability $(E_{\rm col}/V_b)^{L+1/2}$ ($E_{\rm col}$ is the collision energy) [81].

Turning on $V_{\rm dd}$ changes the height of V_b and alters the loss rate. To compute the change in V_b, we can make an adiabatic approximation by diagonalizing $V(r)$ at many values of r and stitching together the results [81]. This produces adiabatic energy curves as a function of r, shown in Figure 2.10. For $m_L = 0$ (A), the height of the barrier decreases monotonically with increasing d. In contrast, for $m_L = \pm 1$ (B), V_b is enhanced for moderate $d > 0$, but lowered for larger d.

The qualitative trends can be understood from the form of $V_{\rm dd}$. At small d, the mixing between different L is not too strong, and we only need to consider the diagonal matrix elements. Here, the main feature can be directly seen from equation (2.30): owing to the overall $(-1)^{m_L+1}$ factor, the interaction is attractive for $m_L = 0$ but repulsive for $m_L = \pm 1$. This makes sense classically because an $m_L = 0$ collision corresponds to a head-to-tail approach of the molecules, while an $m_L = \pm 1$ collision is a side-to-side approach (shown schematically in Figure 2.9B). At larger d, where the off-diagonal elements become important, the barriers of all three $L = 1$ states decrease owing to mixing with $L = 3$ (dashed curves in Figure 2.10). This can be understood from

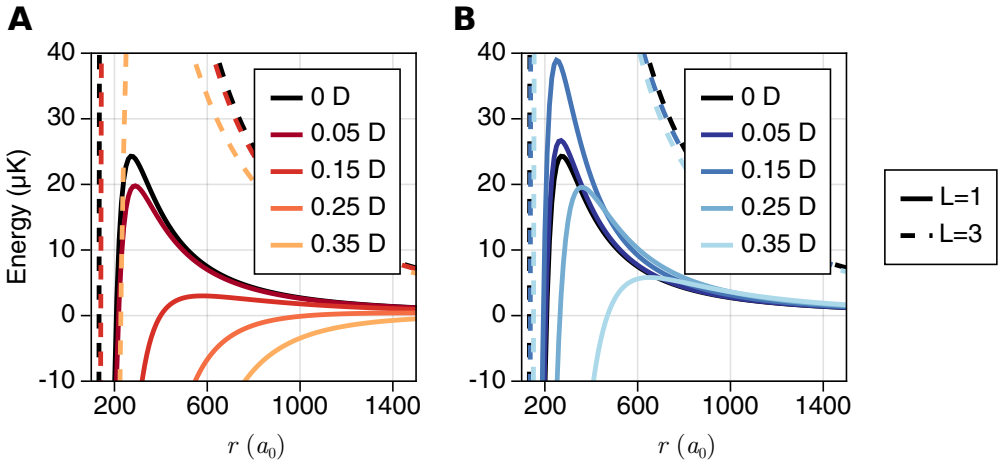

Figure 2.10: Adiabatic energy curves vs d, calculated for KRb. (A) $m_L = 0$. (B) $m_L = \pm 1$. These use $C_6 = 16130$ a.u. [130]. To avoid cluttering the graph, the $L = 3$ curves (dashed lines) are only shown for $d = 0$, 0.15, and 0.35 D.

perturbation theory: $L = 1$, being lower in energy than $L = 3$, is repelled downward in energy by the coupling, hence reducing the barrier.

In 3D, the reduced barrier for $m_L = 0$ leads to a sharply increasing loss rate when d is increased above a critical value. (For KRb, this occurs around $d = 0.1$ D.) Above this corner, the loss rate increases rapidly as d^6 [79, 81], presenting a challenge for studying the dipolar interactions of molecules in 3D. However, the anisotropy of the dipolar interaction means that we can control the loss behavior by controlling the external confinement. In particular, tight confinement in the $\hat{\mathbf{z}}$-direction effectively removes the $m_L = 0$ collisions. Since V_b is initially enhanced for $m_L = \pm 1$, this leads to a suppression of the loss rate in 2D with increasing d, until the mixing with $L = 3$ becomes significant [131, 99, 100, 101, 102, 52]. Our experiments along this direction are described in Chapter 5.

2.5.2.1 Competing length scales in 2D

Here, we make a brief digression to discuss the 2D loss suppression in more detail. We assume molecules are strongly confined into 2D by a harmonic potential along $\hat{\mathbf{z}}$. Further, we assume that

the molecules occupy only the lowest oscillator state in the z-direction, which also implies that $k_B T \ll \hbar\omega$, where ω is the trap frequency along $\hat{\mathbf{z}}$.

The discussion in the previous section provides a simple pertubative explanation of the dipolar loss suppression in 2D. There, we used the 3D form of the interaction from equation (2.30), and assumed that the 2D confinement just controls which incoming m_L states are allowed. Since the collisions still look essentially 3D, we refer to them as being "quasi-2D." However, the long-range nature of the dipolar interaction leads to the breakdown of the quasi-2D picture when d becomes very large — specifically, when the dipolar length a_D becomes larger than the harmonic length $a_{\mathrm{ho}} = \sqrt{\hbar/\mu\omega}$ in the tightly-confined direction. To distinguish from quasi-2d, the $a_D \gg a_{\mathrm{ho}}$ limit is sometimes referred to as "true 2D." The quasi-2D picture suggests that once d becomes sufficiently large, the loss rate in 2D will only increase with larger d owing to coupling with $L = 3$. On the contrary, full theoretical treatments predict that the loss rate eventually becomes highly suppressed when $a_D \gg a_{\mathrm{ho}}$ [100, 101].

To gain more intuition, we calculate the adiabatic energy curves for fermionic KRb in Figure 2.11, following Ref. [100]. Compared to the 3D calculation from Figure 2.10, we add an additional harmonic confinement $(1/2)\mu\omega^2 z^2$ to equation (2.29). First, consider the top panel of Figure 2.11, which corresponds to a moderate dipolar strength in the quasi-2D regime ($a_D = 400a_0$ and $a_{\mathrm{ho}} = 2160a_0$). Here, from our previous argument, we expect to see suppression of loss in the $m_L = \pm 1$ collisions. Only the states satisfying fermionic symmetry have been plotted [100]. The blue solid curves correspond to $m_L = \pm 1$ collisions, while the red dashed curves correspond to $m_L = 0$ collisions. At long distance, the curves connect to harmonic oscillator states of the relative motion, with relative oscillator quanta n and energy $h\nu(n + 1/2)$ (where $\nu = \omega/2\pi$) [100].

We will focus on the behavior of the $n = 0$ state, which corresponds to collisions between two molecules in the ground harmonic oscillator state.[5] The $n = 0$ state connects to $L = 1$, $m_L = \pm 1$ for $r < a_{\mathrm{ho}}$. Thus, as seen in the plot, the dipolar interaction leads to an enhanced barrier for two molecules in the ground state of the 2D potential. On the other hand, $n = 1$, corresponding to an antisymmetric superposition of molecules in the ground and first harmonic oscillator states,

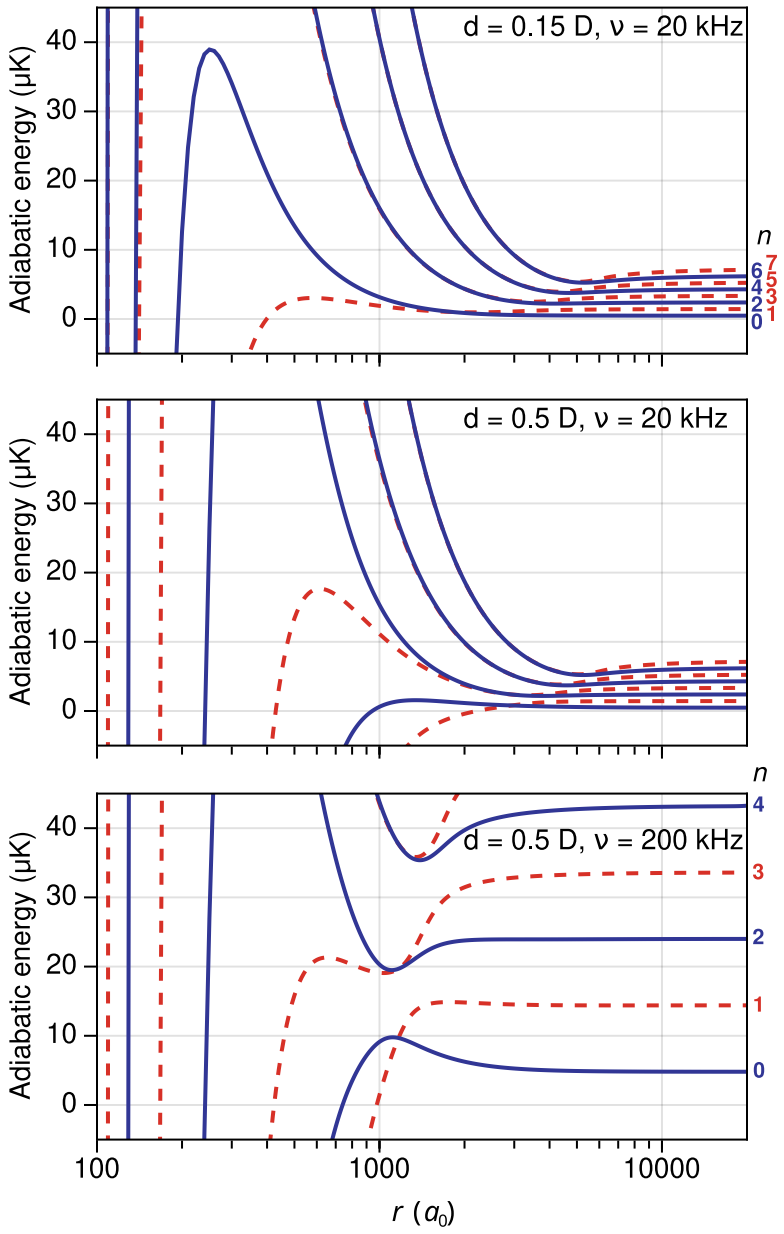

Figure 2.11: Adiabatic energy curves from quasi-2D to 2D, calculated for KRb in $|0,0\rangle$. The vertical trapping frequency is $\nu = \omega/2\pi$. Blue solid curves are $m_L = \pm 1$; red dashed curves are $m_L = 0$. The lowest 8 curves satisfying fermionic symmetry are shown. Top panel: $d = 0.15$ D, $\nu = 20$ kHz, corresponding to $a_D = 400a_0$ and $a_{\rm ho} = 2160a_0$. Middle panel: $d = 0.5$ D, $\nu = 20$ kHz, corresponding to $a_D = 4500a_0$ and $a_{\rm ho} = 2160a_0$. Bottom panel: $d = 0.5$ D, $\nu = 200$ kHz, corresponding to $a_D = 4500a_0$ and $a_{\rm ho} = 680a_0$.

connects to $L = 1$, $m_L = 0$. As shown theoretically in Ref. [100] and experimentally in Ref. [102], this leads to a enhanced loss rate between molecules in different harmonic oscillator states. For the work in Chapter 5, it was thus crucial to load the molecules into the lowest band of the 1D lattice to prevent these lossy $m_L = 0$ collisions.

In the middle panel, d has been increased to 0.5 D, while keeping $\nu = 20$ kHz ($a_D = 4500a_0$ and $a_{\text{ho}} = 2160a_0$). We can see that the barrier for $n = 0$ has decreased owing to coupling with $n = 2$ (which connects to $L = 3$, $m_L = \pm 1$). Thus the quasi-2D picture still holds in this regime, leading to a decrease in the barrier for the lowest $m_L = \pm 1$ channel at large d. This is the same qualitative behavior as seen in 3D (Figure 2.10).

Finally, in the bottom panel, d has been kept at 0.5 D but ν is increased to 200 kHz. Here, the "true 2D" regime is starting to be reached, and the barrier in $n = 0$ has become clearly larger than in the middle panel. From the standpoint of perturbation theory, this makes sense: the coupling between $n = 0$ and 2, which causes the suppression of the barrier for $n = 0$, is weakened as the energy spacing ($\propto h\nu$) is increased. Theoretical calculations show that the $n = 0$ barrier becomes further enhanced as ν is increased [131, 100]. For rigorous calculations of the loss rates in the quasi-2D to 2D crossover, see Refs. [99, 100, 101, 131, 132].

For the experiments in this thesis, we remained in the quasi-2D regime with a maximum dipole of $d = 0.3$ D ($a_D = 1600a_0$) and $\nu = 17$ kHz ($a_{\text{ho}} = 1830a_0$). We could possibly start to explore the crossover by using a much deeper optical lattice confinement, which might allow us to reach a higher elastic to inelastic collision ratio [131]. Experiments on other molecules with larger dipole moments may also start to probe the true 2D regime. For bosonic molecules, it is necessary to reach the true 2D regime to observe the 2D dipolar loss suppression since there is initially no barrier in the collisions [100, 101].

[5] Technically, n labels the relative oscillator state, so $n = 0$ only ensures that the molecules are in the same single-particle oscillator state along z. However, for concreteness, we will stick to the most experimentally relevant case of both molecules in the ground oscillator state.

2.5.3 Elastic scattering

In addition to undergoing reactive losses, the molecules can also scatter elastically, with rate $\Gamma = \langle n\sigma_{\rm el} v\rangle$. Here, n is the molecular density, $\sigma_{\rm el}$ is the elastic cross section, and v is the relative velocity between collision partners. The brackets $\langle\cdot\rangle$ denote the thermal average over the sample.

In atomic physics, we typically think of interactions between ultracold spin-polarized fermions as being very weak. For identical fermions colliding via contact interactions, the collision partners must tunnel through the p-wave barrier to scatter, leading to a cross section that becomes very small at ultralow temperatures ($\sigma_{\rm el} \propto T^2$) [133]. The strategy used to create the first atomic Fermi gas, and still the most commonly used today, is to use a spin mixture of two different hyperfine states, thus enabling s-wave collisions to rethermalize the gas [134].

However, identical *dipolar* fermions can have strong, energy-independent elastic collisions at ultralow temperatures. This has enabled the evaporative cooling of spin-polarized gases of strongly-magnetic fermionic atoms [135], and of KRb [52] and NaK [54] molecules. Within the Born approximation, valid at low collision energies, $\sigma_{\rm el}$ is energy-independent and depends only on a_D for identical dipolar fermions, yielding $\sigma_{\rm el} = (32\pi/15)a_D^2$ [129, 136]. This cross section is universal in that it depends only on the single parameter a_D. Note that in 3D, the reactive losses scale as d^6, while the elastic rate scales as $a_D^2 \propto d^4$, meaning that the loss dominates in 3D in general. On the other hand, in 2D the loss is initially suppressed while $\sigma_{\rm el}$ is increasing. This leads to a favorable ratio $\gamma = \sigma_{\rm el}/\sigma_{\rm reactive}$ of around 200 for KRb at $d = 0.2$ D, enough to experimentally observe evaporative cooling [52].

Finally, we should explain what is meant by the condition that the collision energy is "low". As originally explained in Ref. [129], the dipolar length also defines a characteristic energy scale $E_D = \hbar^2/\mu a_D^2$, which sets the highest collision energy $E_{\rm col}$ where $\sigma_{\rm el}$ is energy-independent. Physically, this can be interpreted as the requirement that the scattering is in the long-wavelength regime, $1/k \gg a_D$, which implies $E_{\rm col} \ll E_D$. For $E_{\rm col} \gg E_D$, $\sigma_{\rm el}$ is no longer energy-independent and falls off as $1/k$ [129].

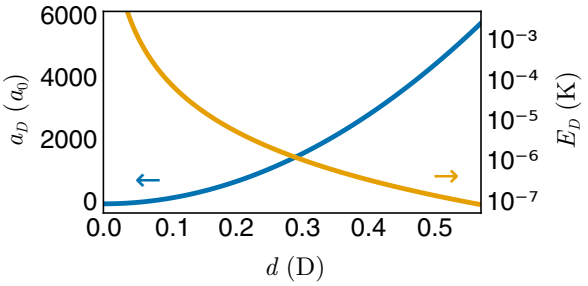

Figure 2.12: a_D (blue, left axis) and E_D (orange, right axis) vs d, calculated with the mass of KRb.

The trends of a_D and E_D as a function of d are shown in Figure 2.12. In our experiments on KRb, we have stayed in (or near the edge of) the universal regime, with $E_D = 570$ nK at our highest dipole moment of $d = 0.35$ D (achieved in 2D [52]) compared to $\langle E_{\text{col}}\rangle/k_B = T \approx 250$ nK. Experiments at higher electric field or in other molecular species with larger d_{perm} will start to probe the edge of the universal regime.

2.5.4 Resonant shielding

So far, we have only seen the effect of the induced dipole moments. We made this restriction somewhat artificially by assuming that the molecule internal states do not change during a collision, though this condition tends to naturally be satisfied since the energy splittings between different rotational states are usually far larger than the other relevant energy scales (collision energy and dipolar interaction energy).

Relaxing this constraint, we can expand V_{dd} in the basis $|N_1, m_{N1}; N_2, m_{N2}; L, m_L\rangle$ to get

$$\begin{aligned}
&\langle N_1, m_{N1}; N_2, m_{N2}; L, m_L|V_{\text{dd}}|N_1', m_{N1}'; N_2', m_{N2}'; L', m_L'\rangle \\
&= -\frac{\sqrt{6}}{4\pi\epsilon_0 r^3}(-1)^{m_L}\sqrt{(2L+1)(2L'+1)}\begin{pmatrix} L & 2 & L' \\ 0 & 0 & 0 \end{pmatrix}\sum_{p=-2}^{p=2}(-1)^p\begin{pmatrix} L & 2 & L' \\ -m_L & -p & m_L' \end{pmatrix} \\
&\qquad \times \langle N_1, m_{N1}; N_2, m_{N2}|T_p^{(2)}(\mathbf{d}_1, \mathbf{d}_2)|N_1', m_{N1}'; N_2', m_{N2}'\rangle. \qquad (2.32)
\end{aligned}$$

We can see that V_{dd} couples different internal states $|N_1, m_{N1}; N_2, m_{N2}\rangle$ via the transition

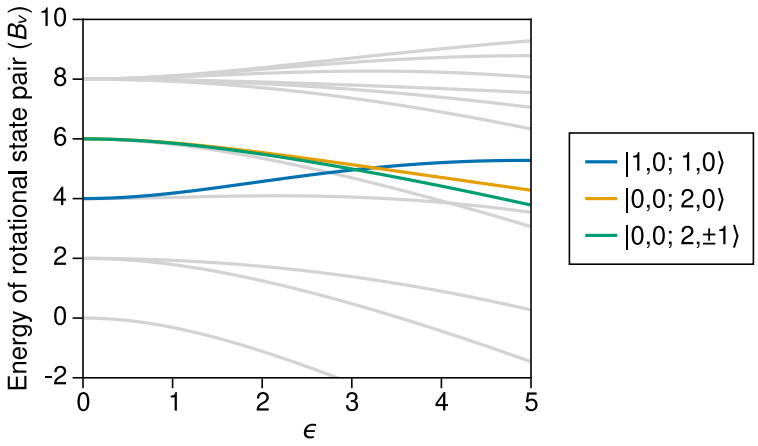

Figure 2.13: Energies of rotational state pairs $|N_1, m_{N1}; N_2, m_{N2}\rangle$ as a function of $\epsilon = E/E_c$. $|1,0;1,0\rangle$ has crossings with $|0,0;2,0\rangle$ and $|0,0;2\pm1\rangle$ near $\epsilon = 3.2$. While $|0,0;2\pm2\rangle$ (gray) also crosses $|1,0;1,0\rangle$ near $\epsilon = 2.8$, the states do not have a strong dipolar coupling since $|1,0\rangle \leftrightarrow |2,\pm2\rangle$ is not dipole-allowed.

dipole moment, although the coupling must overcome the energy cost of changing the internal state. If two pairs of internal states $|N_1, m_{N1}; N_2, m_{N2}\rangle$ and $|N_1', m_{N1}'; N_2', m_{N2}'\rangle$ can be tuned into resonance using E, we might create a situation where the transition dipole moment plays a dominant role in the collisions. This is indeed possible if we initially put the molecules in a rotationally excited state, $|1,0;1,0\rangle$. As shown in Figure 2.13, the energy of $|1,0;1,0\rangle$ crosses that of $|0,0;2,0\rangle$ and $|0,0;2\pm1\rangle$ near $\epsilon \approx 3.2$. These states are strongly coupled through their transition dipole moments, since

$$\langle 0,0;2,0|T_0^{(2)}(\mathbf{d}_1,\mathbf{d}_2)|1,0;1,0\rangle = \frac{2}{\sqrt{6}}\langle 0,0|d^0|1,0\rangle\langle 2,0|d^0|1,0\rangle \tag{2.33}$$

$$\langle 0,0;2,\pm1|T_{\pm1}^{(2)}(\mathbf{d}_1,\mathbf{d}_2)|1,0;1,0\rangle = \frac{1}{\sqrt{2}}\langle 0,0|d^0|1,0\rangle\langle 2,\pm1|d^{\pm1}|1,0\rangle. \tag{2.34}$$

In the vicinity of the crossings, these couplings are near-resonant and the potential experienced by two colliding $|1,0\rangle$ molecules is strongly modified. In particular, the loss rate can be suppressed by an order of magnitude in KRb ("resonant shielding") [137, 138]. This effect is the subject of the experiments in Chapter 6.

2.6 Dipolar interactions – In the lattice

We next consider the behavior with the molecules pinned in sites of a deep 3D optical lattice. Here the motion is completely frozen out, so the angular part $C_2(\theta, \phi)$ just contributes a geometric factor, and the dynamics occur in the internal states of the molecules. Without the relative motion, two molecules in the same single-particle eigenstate $|N, m_N\rangle$ do not show interesting dynamics, and so we need to consider two-particle states with different internal states $|N_1, m_{N1}; N_2, m_{N2}\rangle$. This system can be mapped onto a quantum magnetism model (the "XXZ" model) with long-range and anisotropic interactions that are tunable by experimental control parameters such as external DC or AC microwave fields [45, 24], and can exhibit a wide range of many-body phenomena including dipolar spin liquids [40], spin-orbit coupling [139], and unconventional superfluidity [42].

We first consider two molecules localized in space and separated by a distance r, initially prepared in some superposition of the single-molecule states $|0\rangle \equiv |N = 0, m_N = 0\rangle$ and $|1\rangle \equiv |N = 1, m_N = 0\rangle$. Assuming that there are no other states nearby in energy, the evolution under V_{dd} remains in the subspace of two-particle states spanned by $\{|00\rangle, |01\rangle, |10\rangle, |11\rangle\}$, and only the $p = 0$ term of V_{dd} is relevant. With these constraints, we can simplify equation (2.25) to obtain

$$V_{\mathrm{dd}} = \frac{1 - 3\cos^2\theta}{4\pi\epsilon_0 r^3} \left(d_0^2 |00\rangle\langle 00| + d_1^2 |11\rangle\langle 11| + d_0 d_1 |10\rangle\langle 10| + d_0 d_1 |01\rangle\langle 01| \right. \tag{2.35}$$

$$\left. + d_{01}^2 |01\rangle\langle 10| + d_{01}^2 |10\rangle\langle 01| \right), \tag{2.36}$$

where $d_0 = \langle 0|d^0|0\rangle$ and $d_1 = \langle 1|d^0|1\rangle$ are the induced dipole moments, and $d_{01} = \langle 1|d^0|0\rangle = \langle 0|d^0|1\rangle$ is the transition dipole moment between $|0\rangle$ and $|1\rangle$.

We often talk about this system using the language of magnetism by forming a spin-1/2 system $|\downarrow\rangle \equiv |0\rangle$ and $|\uparrow\rangle \equiv |1\rangle$. By rewriting equation (2.36) in terms of spin-1/2 operators $\mathbf{S}_1$ and $\mathbf{S}_2$, we obtain

$$V_{\mathrm{dd}} = \frac{1 - 3\cos^2\theta}{4\pi\epsilon_0 r^3} \left(J_z S_1^z S_2^z + V + W(S_1^z + S_2^z) + \frac{J_\perp}{2}(S_1^+ S_2^- + \text{c.c.}) \right), \tag{2.37}$$

where $J_z = (d_0 - d_1)^2$, $V = (d_0 + d_1)^2/4$, $W = (d_0^2 - d_1^2)/2$, and $J_\perp = 2d_{01}^2$ [45]. For many particles

confined in an optical lattice, the above equation generalizes to [45]

$$V_{\rm dd} = \frac{1}{2}\sum_{i\neq j} V(\mathbf{r}_i - \mathbf{r}_j)\left(J_z S_i^z S_j^z + V n_i n_j + W(n_i S_j^z + S_i^z n_j) + \frac{J_\perp}{2}\left(S_i^+ S_j^- + \text{c.c.}\right)\right), \qquad (2.38)$$

where $V(\mathbf{r}) = (1 - 3(\hat{\mathbf{r}}\cdot\hat{\mathbf{z}})^2)/4\pi\epsilon_0 r^3$ and n_i is the number of molecules on site i.

We typically work in a deep lattice where the tunneling between sites is negligible. In this case, the V (W) term turns into a static site-to-site energy shift (effective magnetic field). If, for simplicity, we further assume that the lattice has unit filling, then the V and W terms are uniform over the whole lattice, and

$$V_{\rm dd} = \frac{1}{2}\sum_{i\neq j} V(\mathbf{r}_i - \mathbf{r}_j)\left(J_z S_i^z S_j^z + \frac{J_\perp}{2}\left(S_i^+ S_j^- + \text{c.c.}\right)\right). \qquad (2.39)$$

The J_z term gives a long-range and anisotropic Ising interaction, while the $J_\perp$ term gives the dipolar spin-exchange ("flip-flop") interactions, where a molecule in $|\uparrow\rangle$ and one in $|\downarrow\rangle$ trade internal states. The dynamics of equation (2.39) were studied experimentally in Refs. [46, 140] using Ramsey spectroscopy at $E = 0$, where $J_z = 0$ but $J_\perp$ is strong. The main observation was a modulation of the Ramsey contrast as a function of time, with multiple frequency components set by the dipolar energy shifts $J_\perp \times V(\mathbf{r})$ between different pairs of lattice sites. The behavior of the Ramsey contrast was also controlled by the choice of internal state, which affects the strength of the interactions, and the molecule density [140]. In the experiments of Chapter 7, we also studied the spin-exchange interactions between separated ensembles of molecules prepared in different rotational states.

2.6.1 Two-particle calculation

The many-body dynamics of equation (2.39) is of course very complicated, but we can gain some intuition by doing a "toy" two-particle calculation. For two particles, we can write equation (2.39) in the following form,

$$V_{\rm dd}/\hbar = -\frac{J_z}{2}\left(|10\rangle\langle 10| + |01\rangle\langle 01|\right) + \frac{J_\perp}{2}\left(|01\rangle\langle 10| + |10\rangle\langle 01|\right), \qquad (2.40)$$

where we have absorbed some factors into J_z and $J_\perp$ for simplicity, and shifted the zero point of the energy by $-J_z/4$. We can diagonalize $V_{\rm dd}$ by first noting that we have two eigenstates $|00\rangle$ and $|11\rangle$ with zero energy. The remaining bare states $|01\rangle$ and $|10\rangle$ form a two-level system with the same energy offset $-J_z/2$ and coupling $J_\perp/2$, so they form symmetric and antisymmetric eigenstates $|\pm\rangle$ with energies $E_\pm = (1/2)(-J_z \pm J_\perp)$.

Having calculated the eigenstates of $V_{\rm dd}$, we can now write down what happens in a Ramsey sequence. Let us assume that the molecules are initialized in $|00\rangle$. Since $|00\rangle$ is an eigenstate of $V_{\rm dd}$, nothing happens until the first pulse of the Ramsey sequence, with area θ, puts them in an initial superposition

$$|\psi(t=0)\rangle = \left(\cos\frac{\theta}{2}|0\rangle + \sin\frac{\theta}{2}|1\rangle\right) \otimes \left(\cos\frac{\theta}{2}|0\rangle + \sin\frac{\theta}{2}|1\rangle\right) \tag{2.41}$$

$$= \cos^2\frac{\theta}{2}|00\rangle + \sin^2\frac{\theta}{2}|11\rangle + \frac{1}{\sqrt{2}}\sin\theta|+\rangle. \tag{2.42}$$

The molecules then evolve for some time T under $V_{\rm dd}$,

$$|\psi(t=T)\rangle = \cos^2\frac{\theta}{2}|00\rangle + \sin^2\frac{\theta}{2}|11\rangle + \frac{e^{i(J_z-J_\perp)T/2}}{\sqrt{2}}\sin\theta|+\rangle. \tag{2.43}$$

At the two-particle level, the dynamics depends only on the difference $\chi \equiv J_\perp - J_z$.

Finally, a pulse of area $(\pi-\theta)$ and variable phase ϕ closes the interferometer, and we measure the populations in $|0\rangle$ and $|1\rangle$. After some algebra, these are

$$P_0(T,\phi) = \frac{1}{2}\sin^2\theta\left(1 - \cos\theta\cos\phi\sin\frac{\chi T}{2} + \sin\phi\cos\frac{\chi T}{2}\right) \tag{2.44}$$

$$P_1(T,\phi) = 1 - P_0(T,\phi).$$

From equation (2.44), we can see a few interesting limiting cases. First, consider $\theta = \pi/2$ where the populations are initially balanced. Here, $P_0(T,\phi) = (1/2)(\sin\phi\cos\chi T/2)$. In the non-interacting case, $P_0(T,\phi) = (1/2)\sin\phi$, so we see that the interactions lead to a modulation of the contrast $C(T) \propto \cos\chi T/2$. If instead $\theta \neq \pi/2$, then the fringes also shift with a frequency $\propto (\chi/2)\cos\theta$. This frequency shift is linear in the population imbalance $\cos\theta \propto N_0 - N_1$ and is the two-particle analogue of the mean-field shift studied in Chapter 8. Figure 2.14 shows the calculated Ramsey fringes $P_0(T,\phi)$ for two different Bloch sphere tipping angles (A) $\theta = \pi/2$ and (B) $\pi/4$.

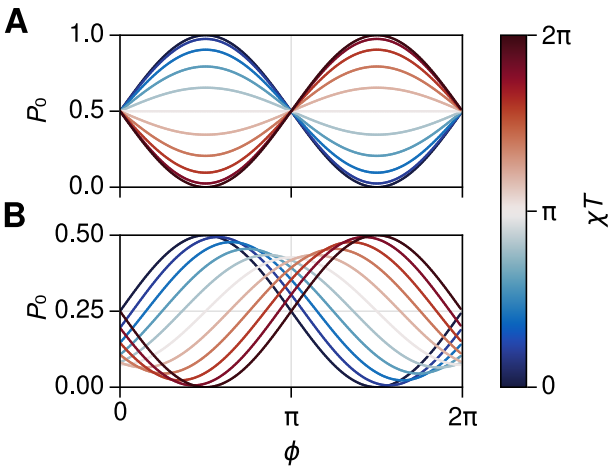

Figure 2.14: Ramsey fringes for two molecules interacting via $V_{\rm dd}$. (A) $\theta = \pi/2$. There is no frequency shift but the contrast oscillates at angular frequency $\chi/2$. (B) $\theta = \pi/4$. There is a frequency shift of $(\chi/2)\cos\theta$.

For two particles, the dynamics can be perfectly cancelled using a dynamical decoupling sequence called the WAHUHA sequence. Ref. [141] gives a detailed explanation of the two-particle case. In an optical lattice with many particles, the WAHUHA sequence removes the dominant oscillation in the contrast, which comes from the nearest-neighbor coupling; however, the wide range of coupling strengths coming from further interaction partners results in an eventual decay of the contrast [46].

2.6.2 Calculating the couplings

The values of the couplings $J_\perp$ and J_z depend on the states that make up our spin-1/2 system $|\downarrow\rangle$, $|\uparrow\rangle$. They can also be tuned over a wide range by changing the external electric field, which changes the induced and transition dipole moments [45, 140]. Figure 2.15 shows the trends of $J_\perp$ and J_z as a function of ϵ for the spin systems formed by $\{|0,0\rangle, |1,0\rangle\}$ (solid lines), $\{|0,0\rangle, |1,\pm1\rangle\}$ (dashed), and $\{|0,0\rangle, |2,0\rangle\}$ (dotted). Note that $\{|0,0\rangle, |1,0\rangle\}$ can be tuned to points where either of $J_\perp$ or J_z is dominant. On the other hand, $J_\perp$ is dominant over the entire plotted range for $\{|0,0\rangle, |1,\pm1\rangle\}$; conversely, J_z is dominant for $\{|0,0\rangle, |2,0\rangle\}$. Finally, note that $J_\perp < 0$ for the $\{|0,0\rangle, |1,\pm1\rangle\}$ system, so switching from there to the $\{|0,0\rangle, |1,0\rangle\}$ system in the middle of a

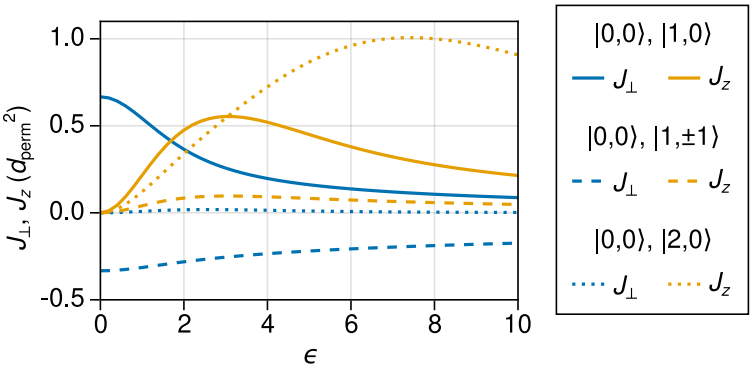

Figure 2.15: Electric field dependence of $J_\perp$ and J_z.

measurement can reverse the evolution of the many-body state [49].

More generally, any externally controlled mixing of the states can be used to control the interaction strengths — for example, by applying a microwave drive to the molecules, we can make one or both of $|\downarrow\rangle$ and $|\uparrow\rangle$ a coherent superposition of bare states. To calculate the interaction parameters, we just need to repeat the analysis of equation (2.36), using our choice of $|\uparrow\rangle$ and $|\downarrow\rangle$ in place of $|0\rangle$ and $|1\rangle$. Several interesting cases are worked out fully in Ref. [45]. A similar effect also occurs naturally due to the avoided crossings at low electric field (Figure 2.2) that mix the $N = 1$ states, with each avoided crossing producing a sharp dip in $J_\perp$. For the density shift measurements in Chapter 8, it was important to take these mixings into account when calculating the expected size of the interaction shift.

2.6.3 Beyond the $p = 0$ term

So far, we have focused solely on the $p = 0$ term of equation (2.25), since the $p \neq 0$ terms are off-resonant and hence highly suppressed. However, in some cases they can be brought to resonance. For example, if the $|1, \pm 1\rangle$ states are made degenerate, then the pair states $|0, 0; 1, 1\rangle$ and $|1, -1; 0, 0\rangle$ are also degenerate and interact resonantly via $T^{(2)}_{\pm 2}(\mathbf{d}_1, \mathbf{d}_2)$. This is the idea behind the spin-orbit coupling proposal of Ref. [139]. The interaction gives a spin-orbit coupling because the total angular momentum projection $m_{N1} + m_{N2} + m_L$ is conserved by V_{dd}, so if $m_{N1} + m_{N2}$

changes by p, then m_L necessarily changes by $-p$. A similar effect can also occur in the resonant shielding when coupling $|1,0;1,0\rangle$ and $|0,0;2,\pm1\rangle$, which interact via the $p = \pm1$ terms.

2.7 Summary

We started this chapter by discussing the relevant energy scales of our diatomic molecules, eventually focusing on the rotational levels of the ground electronic and vibrational state. We showed the full Hamiltonian describing the rotational states in external magnetic and electric fields, including hyperfine couplings, and the complicated energy spectrum that can arise, particularly at low electric fields. Next, we described the induced and transition dipole moments of the molecules, and their changes under an external electric field, as well as the effects of the optical trapping light. Finally, we described aspects of the dipolar interactions between molecules, highlighting a few cases that are especially relevant to the work in this thesis.

Chapter 3

Apparatus and experimental sequence

The experiments in this thesis were conducted on the second-generation JILA KRb machine. The main feature of the new apparatus is the in-vacuum electrode assembly, which allows us to apply large and controllable electric fields to the molecules. The design and initial testing of the apparatus is described in detail in Jacob Covey's thesis [106]. This chapter aims to give an updated overview with a focus on several of the important features that were used to conduct the experiments in this thesis. A complementary discussion, with emphasis on other aspects of the experiment, can be found in William Tobias's thesis [107].

3.1 Overview

Figure 3.1 shows a drawing of the machine, with several regions highlighted for reference in the following discussion. The experiment consists of the following stages:

- Laser cooling: K and Rb atoms are collected in a vapor cell magneto-optical trap (MOT, blue region in Figure 3.1). The relevant atomic transitions are shown in Figure 3.2. After several laser cooling stages, including Λ-enhanced gray molasses cooling for K [142, 143] and Rb [144], atoms are optically pumped to the low-field-seeking stretched states ($|F = 9/2, m_F = 9/2\rangle$ for K and $|2, 2\rangle$ for Rb) and loaded into a magnetic quadrupole trap. At this point, we typically have around 3×10^7 K and 6×10^8 Rb at 100 μK.

- Magnetic transfer and plugged quadrupole evaporation: The magnetic quadrupole coils are mounted on a moveable stage ("Cart" in Figure 3.1), which translates down a differential

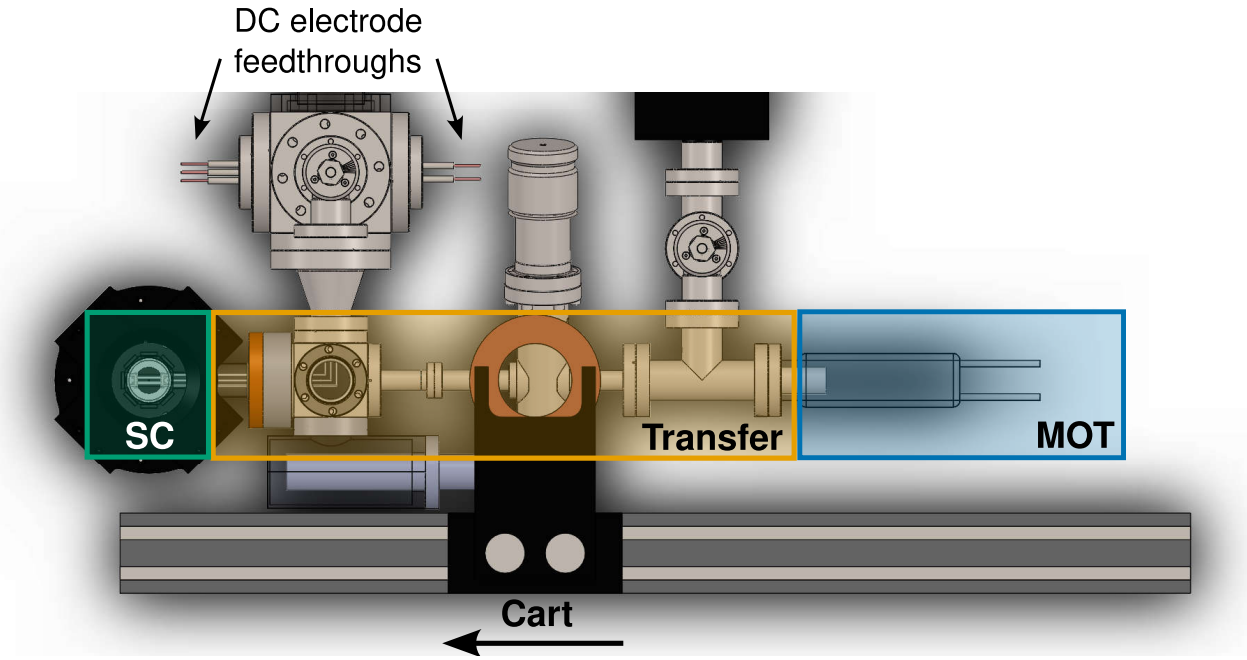

Figure 3.1: Schematic of the JILA KRb machine as viewed from above. SC: Science cell. The ion pumps (toward the top of the image) are not shown. The magnetic transfer cart is shown in the middle of its motion.

pumping tube (orange region) to the science cell (green region), where all subsequent stages of the experiment are performed. After transport, a blue-detuned plug beam is turned on to prevent Majorana spin-flip losses [145]. Radio-frequency (RF) evaporation of Rb is performed on the $|2,2\rangle \rightarrow |1,1\rangle$ transition, and K is sympathetically cooled through collisions with Rb. At this point, we typically have 4×10^6 K and 6×10^6 Rb at 4 μK.

- Optical evaporation: K and Rb are loaded into a crossed optical dipole trap and evaporated by lowering the trap depth. The favorable background K-Rb scattering length ($-185a_0$, where a_0 is the Bohr radius) allows for efficient sympathetic cooling of K through collisions with Rb. Midway through the evaporation, the magnetic field is ramped to 30 G and the atoms are transferred to the Feshbach states ($|9/2,-9/2\rangle$ for K and $|1,1\rangle$ for Rb) using RF adiabatic rapid passage (ARP). Figure 3.3 depicts the relevant atomic hyperfine states. After evaporation, the magnetic field is ramped to 555 G, above the broad interspecies Feshbach resonance at 546.6 G. The atom number and temperature depends on the final evaporation cut, but typical conditions are 5×10^5 K and 1.5×10^5 Rb at around 150 nK.

- Molecule formation and detection: Loosely-bound Feshbach molecules are produced by ramping the magnetic field through the interspecies Feshbach resonance. The molecules are coherently transferred to their ground rovibrational state using stimulated Raman adiabatic passage (STIRAP). Remaining unpaired atoms are removed from the trap using resonant light. For detection, the molecules are mapped back into atoms by reversing the coherent association process, at which point they are detected using standard absorption imaging techniques.

The atomic mixture preparation stages have been described in many group theses [146, 147, 141, 106]. Most of the laser cooling stages and laser setups are still similar to the first-generation apparatus [141], except for the new Λ-enhanced gray molasses and tunable STIRAP setups, which are described in detail in Will Tobias's thesis [107]. The plugged quadrupole setup is fairly similar to the Mainz K-Rb mixture experiment, and the theses of Thorsten Best [148] and Sebastian Will

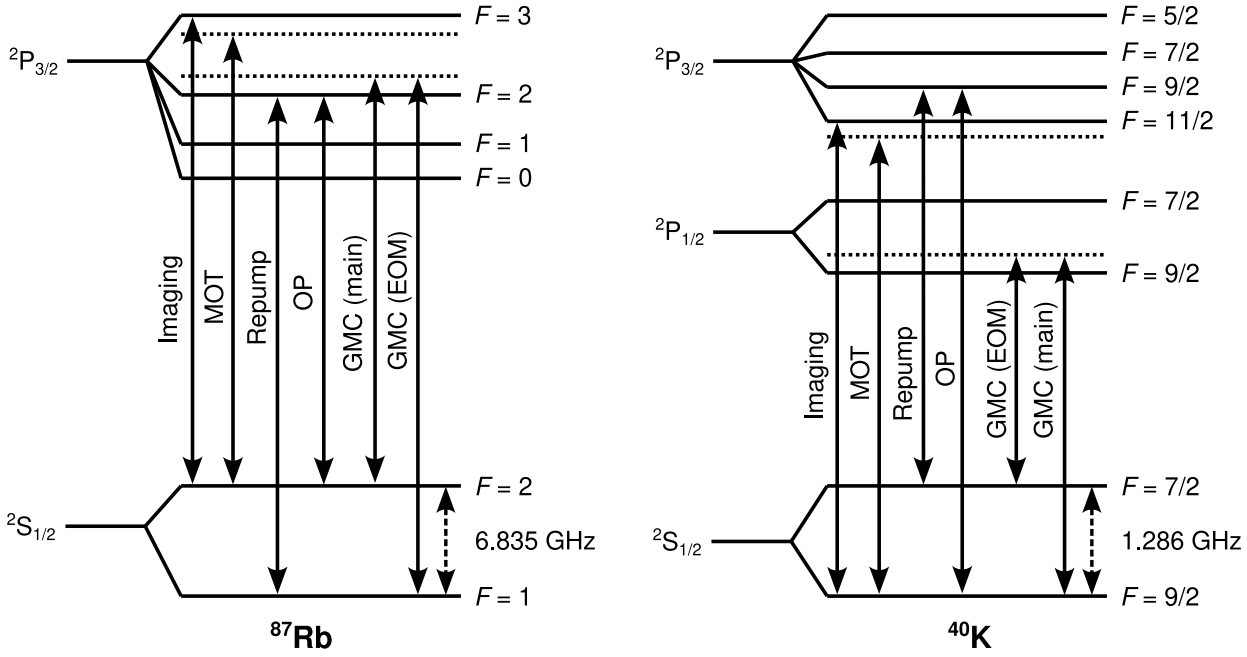

Figure 3.2: Atomic level diagrams for ^{87}Rb (left) and ^{40}K (right). GMC: gray molasses cooling. EOM: electro-optic modulator. The beams labeled "GMC (EOM)" are generated from sidebands on the "GMC (main)" beams using high frequency EOMs at 6.835 and 1.286 GHz.

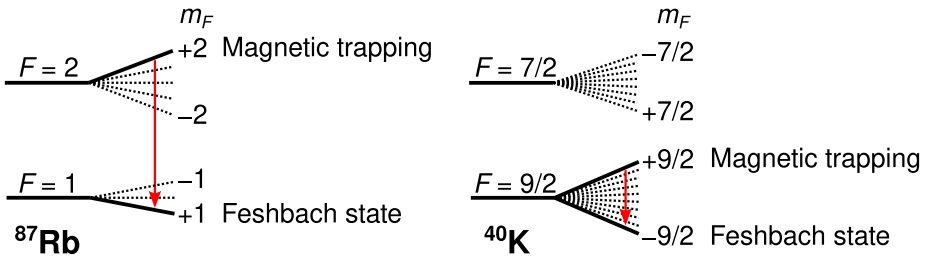

Figure 3.3: Relevant hyperfine states of ^{87}Rb (left) and ^{40}K (right). The red arrows indicate the transitions used for state preparation. For Rb, $|2,2\rangle \rightarrow |1,1\rangle$ is used for the RF evaporation in the plugged quadrupole trap and for state preparation at 30 G. For K, transfer from $|9/2,9/2\rangle$ to $|9/2,-9/2\rangle$ is performed with 9 consecutive ARPs at 30 G.

[149] were very helpful in optimizing our procedure.

The early stages of the experimental sequence consist mostly of standard techniques from the ultracold atom community. We briefly describe the optical trap setup around the science cell, and then focus on some of the subsystems most relevant for the molecule experiments: the electric field control, RF setup, and CCD setup.

3.2 Optical trap setup

Optical dipole traps (ODTs) and lattices are ubiquitous in the AMO community; see Refs. [112, 150] for a detailed introduction. We use traps generated by a high power fiber laser (Nufern NuAmp 50W) at $\lambda = 1064$ nm, which is far red-detuned from any atomic or molecular electronic transitions in our system. This results in a conservative trapping potential,

$$U(\mathbf{r}) = -\alpha I(\mathbf{r}), \tag{3.1}$$

where α is the (species- and wavelength-dependent) polarizability and $I(\mathbf{r})$ is the position-dependent intensity of the trapping beam. Table 3.1 gives the values of α for K and Rb, as well as some of the KRb states used in this work. Note that the polarizability of excited rotational states of KRb also depends on the polarization angle of the trapping light (see section 2.3.4 for an introduction).

Figure 3.4A shows a schematic of the ODTs and imaging paths in the science cell. The plug beam (760 nm, 20 μm waist) is focused on the center of the quadrupole trap to prevent spin-flip losses. After plugged quadrupole evaporation, we load the atoms into a crossed ODT formed by two Gaussian beams at 1064 nm (labeled ODT1 and ODT2). The setup has changed several times over the years, and the following discussion uses the beam parameters used in the lab as of this writing. ODT1 propagates along $-\hat{\mathbf{x}}$ with waists $w_{1,y} = 35$ and $w_{1,z} = 130$ μm. ODT2 propagates along $-\hat{\mathbf{z}}$ with waists $w_{2,y} = 35$ and $w_{2,x} = 175$ μm. Both beams are elliptical with the smaller waist against gravity ($-\hat{\mathbf{y}}$), and together they generate the trapping potential shown in Figure 3.4B. Note that the experimental coordinate system uses $\hat{\mathbf{y}}$ as the vertical direction.

To create a degenerate Bose-Fermi mixture, the atoms are evaporated in the ODT by reducing

Species	α_{1064}/h (Hz/(W/cm^2))	$\omega/\omega_{\mathrm{K}}$	E_R/k_B at $\lambda = 1064$ nm (nK)
K	28	1	211
Rb	32	0.72	97
KRb* (Feshbach)	$\alpha_{\mathrm{K}} + \alpha_{\mathrm{Rb}}$ [151]	0.83	67
KRb ($\|0,0\rangle$ at $\|\mathbf{E}\| = 0$)	55 [110]	0.79	67

Table 3.1: Polarizabilities for K, Rb, KRb* (Feshbach molecules), and KRb at 1064 nm.

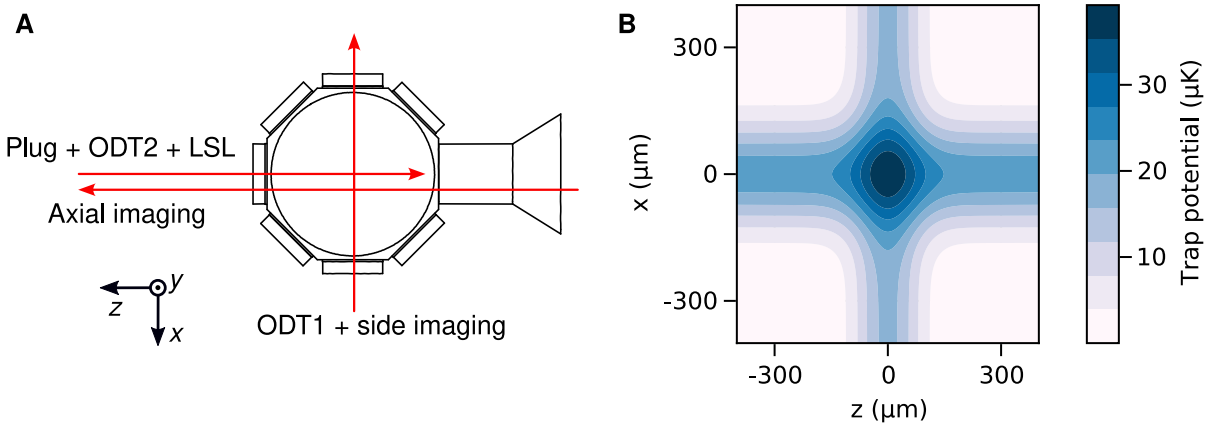

Figure 3.4: Optical trap geometry. (A) Schematic of the plug, optical traps, and imaging paths in the science cell. LSL: large spacing lattice. (B) Crossed ODT potential formed by ODT1 and ODT2, calculated for K in the $y = 0$ plane. The ODT powers for this calculation are the initial values used for loading from the quadrupole trap. Gravity is not included in this calculation.

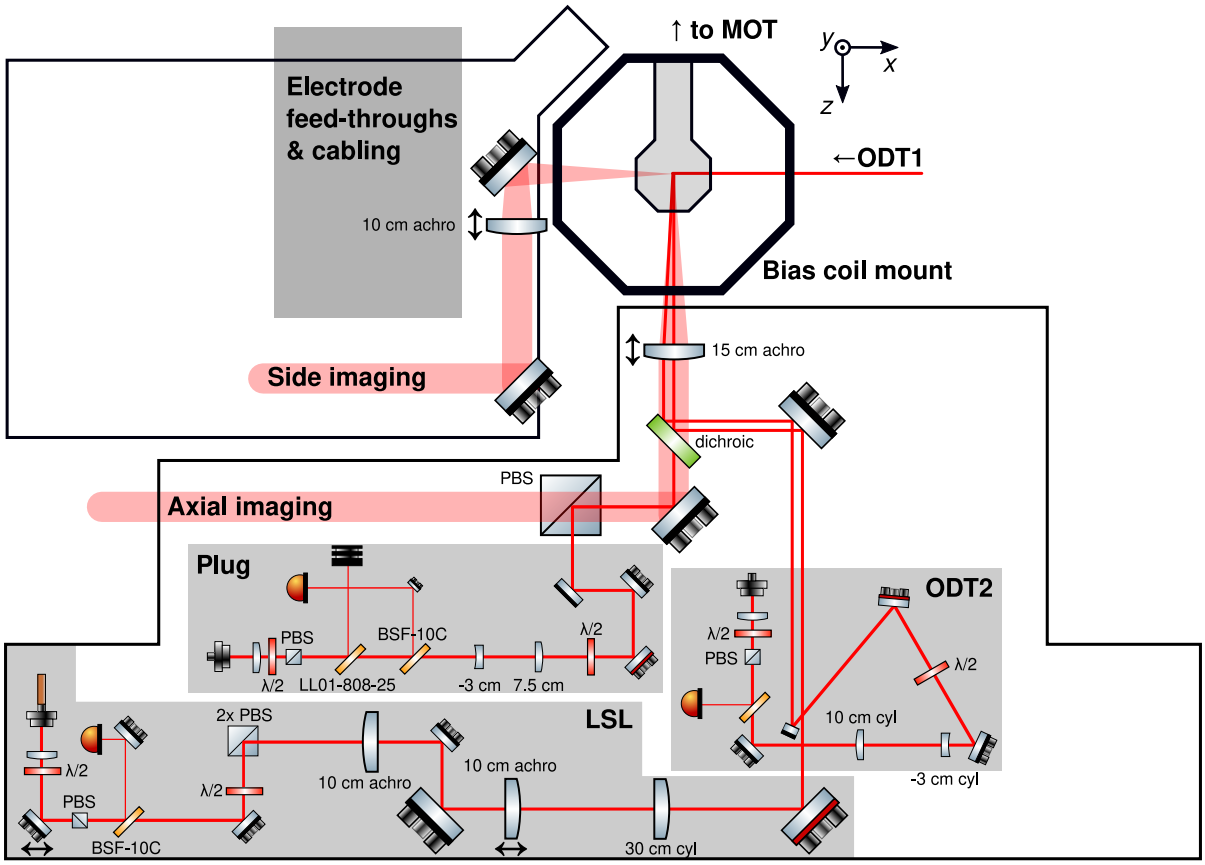

Figure 3.5: Plug, ODT2, LSL, and imaging optics layout. For more details on the LSL optical setup, see section 5.1.1.

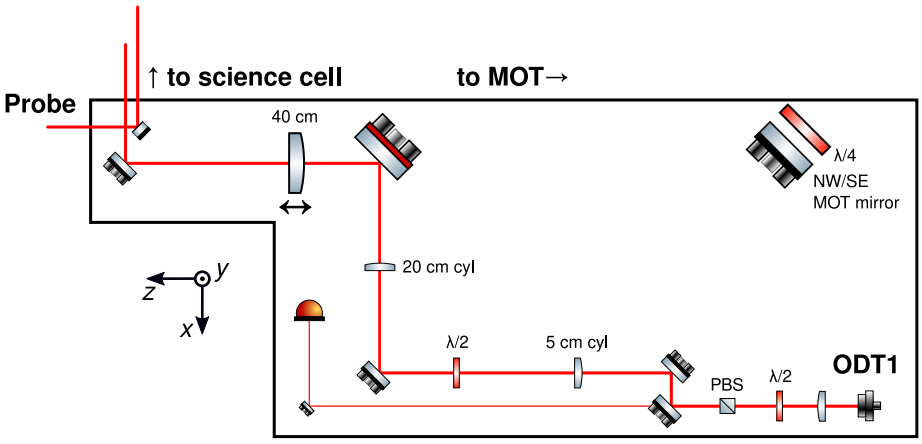

Figure 3.6: ODT1 and side imaging optics layout.

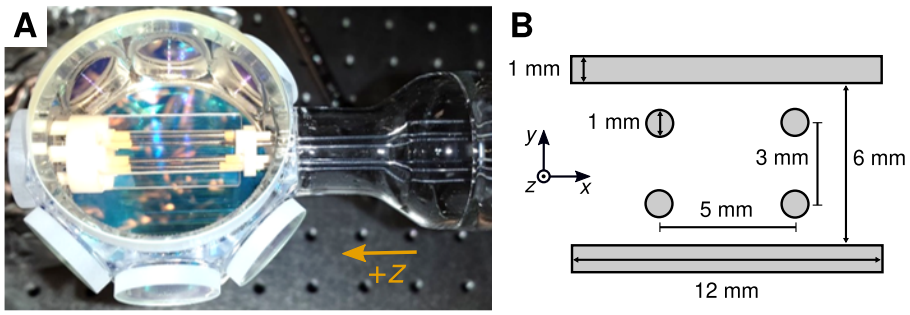

Figure 3.7: Geometry of the electrodes. (A) The science cell with in-vacuum electrode assembly visible inside. (B) Dimensions of the electrode assembly in mm, viewed axially (along $\hat{\mathbf{z}}$). Adapted from Ref. [106].

the optical power over several seconds in two exponential ramps. The large spacing lattice (LSL) and vertical lattice (VL, not shown) traps are used for the 2D experiments and are described in more detail in Chapter 5. The optical layouts for generating the beams in Figure 3.4 are shown in Figures 3.5 and 3.6.

3.3 Electric field control

As introduced in Chapter 2, a key technique for manipulating the molecules is applying an external electric field $\mathbf{E}$. In this section, we will discuss a few high-level considerations, followed by some technical details of the setup. See Will Tobias's thesis [107] for a complementary discussion. In particular, Will's thesis has an in-depth analysis of the electric field stabilization, which is important for understanding the limits to the molecule coherence from $\mathbf{E}$.

The main feature of the second-generation JILA KRb apparatus is the in-vacuum electrode assembly shown in Figure 3.7. The assembly consists of two fused silica plates coated with a transparent conductor (indium tin oxide (ITO)) and four tungsten rods. The transparent plates preserve optical access from the top and bottom, and help to create a homogeneous field. In the most basic field configuration, the plates generate a parallel-plate capacitor field along $\hat{\mathbf{y}}$, while the rods compensate for field gradients arising from edge effects. By independently controlling the six electrodes, we can generate a flexible field configuration with control over the field strength

$|\mathbf{E}|$, its gradients in the $\hat{\mathbf{x}}$ and $\hat{\mathbf{y}}$ directions, and the angle θ in the x-y plane. In-vacuum bias tees on the rods allow for simultaneous application of DC and microwave voltages to the rods. In particular, this allows us to drive rotational transitions of the molecules using the near-field electric field pattern generated by the rods. Jacob Covey's thesis [106] has more details on the design and installation of the electrodes.

3.3.1 Back-of-the-envelope requirements

Let us start by discussing the requirements on the electric fields. We will frame this discussion in terms of two types of experiments that are explored in this thesis:

- Collisions of the molecules at a fixed $\mathbf{E}$ (introduced in section 2.5). We should be able to change the field strength $|\mathbf{E}|$, tilt the field angle θ, and controllably apply or shim out gradients. For the evaporative cooling experiments of Chapter 5, we also needed a tunable curvature of $|\mathbf{E}|$ to controllably lower the trap depth.

- Ramsey spectroscopy to probe dipolar many-body physics in the gas, for example to study the XXZ model [45, 140] (introduced in section 2.6). The interactions can be controlled with the same field parameters ($|\mathbf{E}|$ and field angle). The molecular coherence will be limited by inhomogeneous broadening (e.g., field gradients) and time-varying field noise.

Of course, both of these benefit from a very stable and tunable $\mathbf{E}$, though the precise requirements are different.

3.3.1.1 Field strength and angle

Let us first consider what electric field strengths we need. For collisional experiments, we would like to be able to access a wide range of induced dipole moments to tune interactions in the gas. Owing to the large characteristic field of KRb ($E_c = 3.9$ kV/cm), we need to turn on a large field of ~ 12 kV/cm to get a sizable dipole moment of even 60% of d_{perm} in the $|0,0\rangle$ state (Figure 2.3). The resonant shielding explored in Chapter 6 requires a field of ~ 12.5 kV/cm. A

similar field magnitude is needed to access the regime of the XXZ model where J_z is dominant over $J_\perp$ (Figure 2.15). The first-generation KRb machine had electrodes mounted outside of the glass cell, and experiments at large $|\mathbf{E}|$ were limited by charging of the glass cell, which resulted in a non-repeatable field strength [141, 106]. Our in-vacuum electrodes allowed us to apply large electric fields (up to about 15 kV/cm used in this thesis) without any major problems.

The capability to rotate the angle θ of $\mathbf{E}$ also allows one to manipulate the molecular interactions, especially when combined with confinement into reduced dimensions. For example, by confining the molecules in a 2D plane and changing θ, the dipolar interactions can be changed from all repulsive ($\theta = 0$) to a combination of attractive and repulsive ($\theta = \pi/2$). We used this capability to control the collisions (Chapter 6) as well as the mean-field interaction (Chapter 8).

3.3.1.2 Gradients

Homogeneity of the electric field is also important to consider. At the most basic level, stray gradients can cause molecules to spill from the trap. The force from an electric field gradient along x is $F_x = d(\partial|\mathbf{E}|/\partial x)$, where d is the induced dipole moment. Putting this in experimentally relevant units, we get

$$F_x\,(k_B \times \mathrm{nK}/\mu\mathrm{m}) \approx 2.4 \times [d\,(\mathrm{D})] \times \left[\frac{\partial|\mathbf{E}|}{\partial x}\,\left(\frac{\mathrm{V}}{\mathrm{cm}^2}\right)\right]. \tag{3.2}$$

We can very roughly estimate that the gradients will start to become important when the force times the extent of the cloud is comparable to the temperature. For a typical cloud size of $\sim 20\,\mu$m and $T = 200$ nK, and $d = 0.2$ D, this gives $\sim 20\,\mathrm{V/cm}^2$ as the typical scale of gradient that will cause problems. These numbers are representative for KRb in $|0,0\rangle$ at $|\mathbf{E}| = 4.5$ kV/cm. Gradients become more and more challenging to deal with as $|\mathbf{E}|$ increases, since both d and the electrode voltages are increasing (so the fractional sensitivity is higher).

In Ramsey experiments, gradients across the cloud also contribute an inhomogeneous broadening that lead to decay of the contrast. We can rewrite our expression for F_x in more convenient

units for the spectroscopy,

$$F_x\left(h \times \mathrm{Hz}/\mu\mathrm{m}\right) \approx 50 \times \left[d_{\mathrm{diff}}\left(\mathrm{D}\right)\right] \times \left[\frac{\partial |\mathbf{E}|}{\partial x}\left(\frac{\mathrm{V}}{\mathrm{cm}^2}\right)\right], \tag{3.3}$$

where d_{diff} is the differential dipole moment between the two states being probed. The coherence time is roughly the energy scale of the inhomogeneity over the cloud. Considering $d_{\mathrm{diff}} = 0.2$ D, cloud size of 20 μm, a gradient of $\sim 10\,\mathrm{V/cm}^2$ already gives an inhomogeneity of ~ 2 kHz and limits the coherence to $\sim 1/(2\pi \times 2\ \mathrm{kHz}) \approx 0.1$ ms. Flipping this around, the sensitivity of the Ramsey contrast also makes it the best signal to optimize when trying to shim out gradients of $\mathbf{E}$. For simplicity, we have only considered linear gradients here, although field curvatures will cause similar issues.

Electric field gradients can also detune dipolar spin-exchange interactions [46, 152]. In KRb, these interactions have an energy scale of ~ 100 Hz over 532 nm (a typical lattice spacing) for the $\{|0,0\rangle, |1,0\rangle\}$ system. A field gradient causes a spatially-varying energy shift between $|0,0\rangle$ and $|1,0\rangle$ that suppresses the interaction. From equation (3.3), a gradient of just a few $\mathrm{V/cm}^2$ can significantly detune the spin-exchange over several lattice sites.

3.3.1.3 Noise

Finally, we must consider noise on the electric field. We will make the distinction between two different regimes of noise:

- Low-frequency ("DC") noise that occurs on timescales longer than our typical molecule interrogation time τ ($\tau \sim 10$ ms for a Ramsey experiment). This manifests as a non-repeatable $|\mathbf{E}|$ from shot to shot.

- "AC" noise near the Rabi frequency Ω of our pulses or, if using dynamical decoupling, the delay time between pulses.

Let us first consider the simpler case of DC noise. DC fluctuations of $|\mathbf{E}|$ are largely irrelevant for collision experiments, since the induced dipole moment does not change rapidly with $|\mathbf{E}|$. One

important exception is the shielding resonances studied in Chapter 6, which occur near 12.5 kV/cm and are on the order of 20 V/cm wide. This gives a requirement on the fractional stability of ~ 1600 parts per million (ppm).

Spectroscopy experiments place a much more stringent requirement on the shot-to-shot stability of $|\mathbf{E}|$. Consider a Ramsey experiment probing two states with differential dipole moment d_{diff} for dark time τ. Then the shot-to-shot variation in the phase is $\delta\phi = d_{\text{diff}} \times \delta|\mathbf{E}| \times \tau/\hbar$, where $\delta|\mathbf{E}|$ is the shot-to-shot variation of $|\mathbf{E}|$. Writing this in convenient experimental units, we get

$$\delta\phi\,(\text{deg}) \approx 0.18 \times \left[|\mathbf{E}|\left(\frac{\text{V}}{\text{cm}}\right)\right] \times \left[\frac{\delta|\mathbf{E}|}{|\mathbf{E}|}\,(\text{ppm})\right] \times [d_{\text{diff}}\,(\text{D})] \times [\tau\,(\text{ms})]. \tag{3.4}$$

For concreteness, suppose $|\mathbf{E}| = 1$ kV/cm, where we have a relatively small differential dipole $d_{\text{diff}} = 0.08$ D for $|0,0\rangle \leftrightarrow |1,0\rangle$ for KRb. Plugging in numbers, we see that for $\tau = 1$ ms and a fractional stability of $\delta|\mathbf{E}|/|\mathbf{E}| = 1$ ppm, the shot-to-shot phase deviations are already quite large at $\delta\phi \approx 14$ deg. At higher $|\mathbf{E}|$, d_{diff} can be significantly larger, making the Ramsey phase even more sensitive to $\delta|\mathbf{E}|$. Our electric field stabilization is designed to limit $\delta|\mathbf{E}|$ to the 10 ppm level (see section 3.3.5), and so we typically see that the phase of the Ramsey oscillation becomes scrambled after a few hundred μs.[1]

If the fluctuations of $|\mathbf{E}|$ are slow compared to τ, then we can cancel them completely with a single spin echo pulse. However, if the fluctuations occur on a timescale comparable to τ, then we will need to add additional spin echo pulses to form a dynamical decoupling sequence [154]. In such a sequence, a train of equally-spaced echo pulses forms a bandpass filter for the noise centered at $1/2\tau_{\text{p}}$, where τ_{p} is the pulse spacing [155, 156]. For the measurements in Chapter 8, where $|\mathbf{E}|$ was as large as 9 kV/cm, it was essential to use dynamical decoupling to maintain phase coherence of the molecules with the microwaves. Using the methods of Ref. [155], we could also measure the power spectrum of $|\mathbf{E}(t)|$ through the noise in the molecule spectroscopy, and saw that the

[1] Note that shot-to-shot fluctuations of $|\mathbf{E}|$ cause the relative phase of the molecules and the microwaves to vary shot-to-shot, but they do not affect the coherence between molecules in the sample. By randomizing the phase of the Ramsey pulses and measuring the variance of the populations in the two states, we can still extract the molecule-molecule coherence without requiring a perfectly stable $|\mathbf{E}|$ (e.g., in section 7.2). This is somewhat analogous to a situation that can occur in optical lattice clocks where the atom-atom coherence exceeds the atom-light coherence due to laser phase noise [153].

measured noise was in reasonable agreement with the expected field fluctuations calculated from direct measurements of the electrode voltages with an FFT machine (see Figure 3.11 of Ref. [107])

From this discussion, we can see that the high sensitivity of the molecules to **E** places stringent requirements on the electric field stabilization. One approach to easing these requirements is to reduce the bandwidth of the system, for example by adding low pass filters before the electrodes. A downside is that very rapid changes of **E** are no longer possible. This is not a huge loss — although rapid changes of $|\mathbf{E}|$ could be an interesting way to quench or modulate the dipolar interactions, microwave pulses can also be used to similar effect with less experimental effort. As a result, it often makes sense to limit the bandwidth of **E** as much as possible. At very low bandwidths, timescales associated with the molecular motion and collisions (at or below the trap frequency) can become relevant; for maximum flexibility, the bandwidth of **E** should still remain far above these frequency scales.[2] Experimentally, we found that a bandwidth of a few kHz was a good compromise for strongly suppressing AC noise while still being much larger than the typical transverse trapping frequencies of ~ 40 Hz.

3.3.2 Computing the field distribution

The discussion in the previous section underscores the level of flexibility and control needed for **E**. A convenient model for the field distribution makes it easy to optimize the electrode voltages for any particular experiment. Will Tobias did COMSOL simulations to numerically find the potential $V_i\phi^{(i)}(x,y)$ from applying voltage V_i on the i-th electrode with all others grounded.[3] By summing these, we obtain the total electric potential for any combination of electrode voltages. To make this even easier to work with, we fit the discretized electric potentials to a polynomial in x and y (7th order happened to work well) to obtain a closed-form approximation to the electric potential,

$$V(x,y) = \sum_{i=1}^{6} V_i\phi^{(i)}(x,y) \approx \sum_{i=1}^{6} V_i \sum_{j,k=0}^{7} \alpha_{jk}^{(i)} x^j y^k \tag{3.5}$$

[2] For example, many of our calibrations involve kicking the molecules in the trap using an electric field gradient, which is not possible if the change in **E** is slower than the trap frequency. Methods like Stern-Gerlach imaging of molecules [107] are also difficult to implement if **E** is too slow.

This made it very fast and easy to take derivatives to obtain the electric field and its gradients. Note that we assume the potential is homogeneous along the $\hat{\mathbf{z}}$-direction (the long axis of the electrodes). Experimentally, we found good agreement of the COMSOL model with measurements of the actual $|\mathbf{E}(x, y)|$ obtained by rotational spectroscopy of the molecules at several positions in the science cell (see Figures 3.13 and 3.14 of Ref. [107]).

We use equation (3.5) to optimize the electrode values, with the goal of approximating the desired $\mathbf{E}(x, y)$ based on several target parameters:

- the field strength $|\mathbf{E}|$,
- gradients $\partial|\mathbf{E}|/\partial x$ and $\partial|\mathbf{E}|/\partial y$,
- curvatures $\partial^2|\mathbf{E}|/\partial x^2$ and $\partial^2|\mathbf{E}|/\partial y^2$,
- and angle $\theta = \arctan(E_x/E_y)$ from the $\hat{\mathbf{y}}$ axis.

All target parameters are calculated at the geometrical center of the electrodes, which is where the molecules are located (to the best of our knowledge). The optimization is currently very basic, consisting of a least squares "fit" of the calculated field parameters to the target parameters by varying the electrode voltages.

Note that we have six target parameters, but only five degrees of freedom (since changing all electrodes by an offset voltage does not change $\mathbf{E}$). This means that, in general, our optimization procedure cannot perfectly match the desired $\mathbf{E}$ parameters except for in configurations of high symmetry (such as a homogeneous field oriented along $\hat{\mathbf{y}}$). To get around this, our optimization routine allows us to ignore individual parameters in the fits, which we often need to do when e.g., tilting the field angle θ. For the 1D lattice experiments (along $\hat{\mathbf{y}}$), we often neglect the curvature $\partial^2|\mathbf{E}|/\partial y^2$, since the force from the small residual field curvature is negligible compared to the tight lattice confinement along $\hat{\mathbf{y}}$.

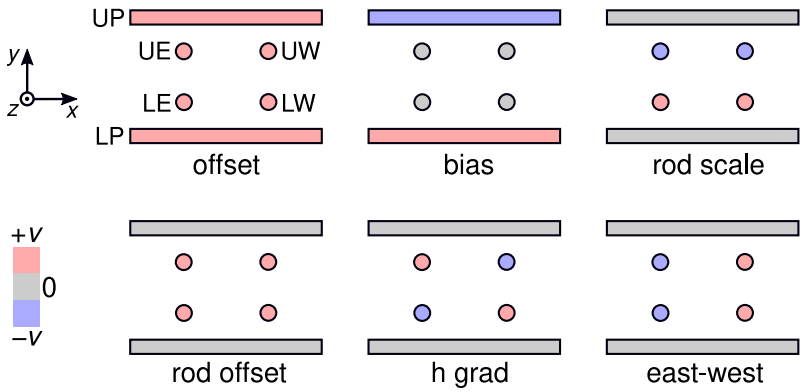

Figure 3.8: Some useful electrode linear combinations.

3.3.3 Useful electrode linear combinations

The optimization routine makes it relatively easy to calculate the required electrode voltages for a desired configuration of **E**. However, it is not very helpful for developing an intuition for what the electrodes are doing. To get a better physical picture, we often decompose the electrode voltages in terms of certain linear combinations. These are illustrated in Figure 3.8. The electrodes are labeled by their spatial arrangement: LP/UP stands for "lower/upper plate", LE for "lower east rod", UW for "upper west rod", etc.

The first combination, labeled "offset", should not affect **E**. The remaining combinations make the most sense in the context of perturbations from a homogeneous field along $\hat{\mathbf{y}}$. To create a bias field along $+\hat{\mathbf{y}}$, we start by applying voltages $\pm V$ to the LP and UP, respectively ("bias" in the figure). If the rods were somehow removed, the electric field strength would be roughly that of a parallel plate capacitor, $|\mathbf{E}| \approx 2V/l$, where $l = 6$ mm is the separation of the plates. The lower and upper rods are set to $\pm\gamma V$, where γ is a scaling factor ("rod scale") that controls the curvatures $\partial^2|\mathbf{E}|/\partial x^2$ and $\partial^2|\mathbf{E}|/\partial y^2$. For our geometry, we find that $\gamma = 0.4225$ cancels both curvatures, and we refer to this as the "flat field" configuration.[4] Starting from the flat field, perturbing with the "rod offset" ("h grad") combination adds a linear y- (x-) gradient. Adding some "east-west" component starts to tilt the field direction away from $\hat{\mathbf{y}}$ and toward $\hat{\mathbf{x}}$.

[3] $\phi^{(i)}(x, y)$ is basically the Green's function for our electrode geometry.

[4] Intuitively, this choice of γ makes the rod voltages approximately equal to what the potential would be at their

3.3.4 Minor imperfections of the electrode geometry

Small imperfections in the electrode geometry can cause gradients of $|\mathbf{E}|$ in the nominally flat field configuration. When we first started using the electric field, we observed a small horizontal gradient that led to loss of the molecules. The gradient scaled linearly with the field strength, with a magnitude of ~ 10 V/cm^2 at 1 kV/cm bias, which would be consistent with a geometric imperfection of the electrodes, and was easily shimmed experimentally by adjusting $\partial|\mathbf{E}|/\partial x$ to maximize the molecule number after a hold time. For the experiments in Chapters 7 and 8, we shimmed the horizontal and vertical gradients more precisely by maximizing the Ramsey coherence of the $|0,0\rangle \leftrightarrow |1,0\rangle$ transition.

A more difficult gradient to fix would be a nonzero $\partial|\mathbf{E}|/\partial z$, since we do not have any way to shim along that direction (the long axis of the electrodes). Such a gradient could occur if, for example, the ITO plates were not parallel. We have observed what seem like small z-gradients on the order of several V/cm^2 at a bias of $|\mathbf{E}| = 4.5$ kV/cm. A z-gradient of this magnitude is small enough that it is difficult to measure reliably, given that we also have no way to controllably change its magnitude. More systematic studies will be needed to gain a clearer picture of the limitations posed by z-gradients in our system.

3.3.5 Controlling the electrode voltages

As mentioned in section 3.3.1, we require roughly 10 ppm stability of the field up to bandwidths of several kHz. This is challenging considering that the electrode voltages can be up to several kV. A block diagram of the high voltage (HV) stabilization system is shown in Figure 3.9. The desired voltage waveforms $V_i(t)$ are calculated using the optimization routine described previously, and sent via USB from our computer control software to an FPGA evaluation board from Opal Kelly (XEM6001). The FPGA programs six 20-bit precision digital-to-analog converters (DACs, Analog Devices AD5791) to output scaled-down waveforms $-V_i(t)/2000$, which provide the

y-positions due the plates at $\pm V$, if the rods were removed. This also means that the parallel plate approximation for $|\mathbf{E}|$ at the center of the electrodes is fairly good (at the $\sim 1\%$ level) in the flat field configuration.

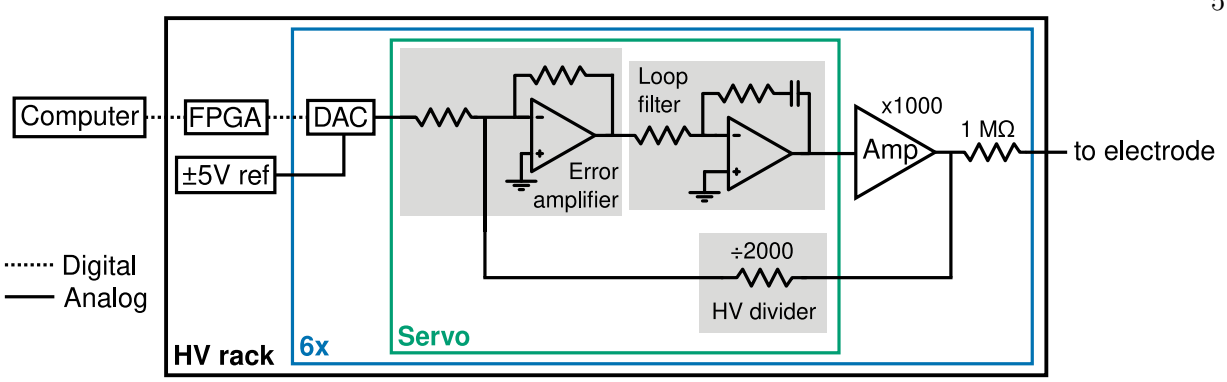

Figure 3.9: Simplified block diagram of the electric field control. For a detailed schematic of the servo, see Refs. [157, 107].

control voltages for the servos. The servos were designed by Terry Brown in the JILA electronics shop. Each servo consists of an error amplifier, which compares the HV after a precision voltage divider with the DAC signal, and a loop filter with three proportional-integral (PI) stages and a differentiator (D) stage. The servo output is sent to an amplifier (Trek 10/10B-HS or Matsusada AMT-5B20-LC), whose output goes through a 1 MΩ current-limiting resistor and is sent to the electrode. The Trek (Matsusada) amplifiers have a maximum output of 10 (5) kV, which gives a maximum field of $|\mathbf{E}| = 33$ kV/cm in the flat field configuration.

Achieving good stability requires a great deal of care with the analog electronics. Will Tobias took the lead on most of the analog aspects, in particular the ±5V reference and DAC output filtering, and his thesis contains a detailed discussion [107]. See also Jamie Shaw's undergraduate honors thesis for some initial testing of the high voltage servos [157], and Appendix A of Will's thesis for a detailed noise analysis of the full system [107]. I worked primarily on the FPGA design and the high voltage cabling and connections, which are described in the following sections.

3.3.6 FPGA control of AD5791 DACs

The computer control system interfaces with the AD5791 DACs via an Opal Kelly XEM6001 evaluation board, which contains a USB microcontroller and Xilinx Spartan 6 FPGA. The XEM6001 was chosen due to familiarity, as it is used extensively in the rest of our control system. For

simplicity, each of the 6 DACs is controlled with an independent process in the FPGA. At the start of each experimental run, the desired sequence of (time, voltage) pairs for each DAC channel is sent from the control system using Opal Kelly's Python SDK and loaded into a RAM block on the FPGA. Each pair is interpreted by the FPGA firmware as the endpoint of a voltage ramp, and the intermediate ramp points are computed as the sequence runs in order to save space in the FPGA RAM. After data transfer, the FPGA waits until it receives a trigger from the main TTL board, at which point it starts to execute the sequence. The AD5791 DACs expose a serial peripheral interface (SPI) bus that is written to by the FPGA to control the DAC output voltage.

Unfortunately, we found that distortions from the ribbon cabling between the FPGA and the DACs limited the fastest reliable SPI clock speed to 4 MHz, significantly lower than the specified maximum clock rate of 25 MHz for the AD5791. This results in a minimum update time of about 8 μs, which is still much faster than the HV response (discussed in the next section). The limited RAM on the FPGA limits the number of sequence points to $2^{10} = 1024$ on each channel. To avoid wasting RAM, the computer control code concatenates adjacent sequence blocks together where the voltage is constant before loading the sequence onto the FPGA.

3.3.7 Cabling and connections

The HV cabling and connections are loosely modeled off the techniques used on the Stark decelerator experiments in JILA. Thanks to Dave Reens of Jun's group and Yomay Shyur of Heather Lewandowski's group for their help. Our experimental voltage and current requirements are far lower than those of Stark decelerators, so some of this is likely overkill.

The output of each HV amplifier is an Amphenol Alden A- (Trek amps) or B- (Matsusada amps) series connector. We use Amphenol Alden A- and B-series cables ($>$ 15 kVDC rated) for the connections within the HV rack from the amplifier output to the servo sense input. The HV feedthroughs on the vacuum chamber use PowerBoot cables from MDC Vacuum Products (20 kV rated). Each cable is fed through a 1/2" or 3/4" diameter Tygon tube surrounded by a grounding braid. The Tygon tubing helps to maintain a greater distance between the cable core and the

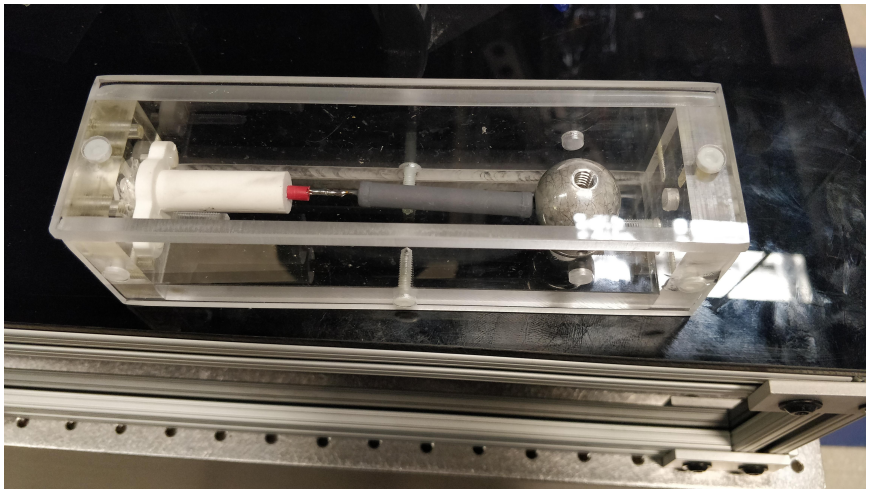

Figure 3.10: Corona sphere for HV connection.

grounding braid to further increase the dielectric breakdown of the cable. The grounding braid is connected to the either the optical table or the HV rack ground to provide a low impedance path in case of a discharge.

The high voltage cabling requires several homemade tees and adapters between the two cable types. Sharp corners or points on any of the conductors should be avoided, as these can cause regions of high electric field that lead to corona discharge [158]. Soldering HV components can thus be quite cumbersome as large solder balls are needed to reduce sharp edges. For greater flexibility in the connections, we use corona spheres to make these connections (Figure 3.10).[5] The corona sphere maintains a smooth outer surface to suppress corona discharge. The cables are inserted through holes drilled in the sphere and clamped down by a set screw to make a good electrical connection. At our highest HV operation of about 5 kV (so far), we have not observed any signs of corona discharge.

The cabling from the high voltage amplifiers to the vacuum feedthroughs has an important impact on the eventual electric field bandwidth. For safety (of both grad students and the apparatus), we have 1 MΩ resistors on the HV output to limit the current to $\leq$ 10 mA. Combined with the capacitance of the cabling, this creates an RC filter that limits the switching time of

[5] Instructions courtesy of Dave Reens: https://www.instructables.com/High-Voltage-Corona-Nuts/

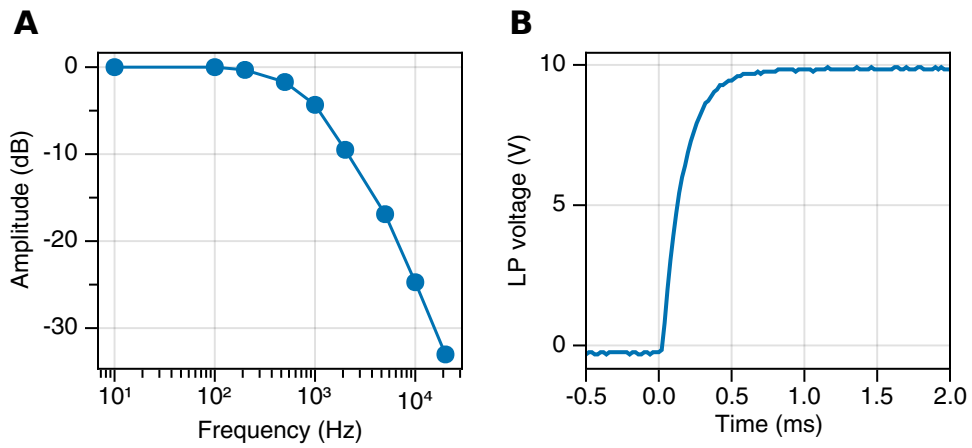

Figure 3.11: Transfer function of the HV cabling. The 1 MΩ resistors on the HV output combine with the capacitance of the cabling to form an RC filter. (A) Measurement of the transfer function of the 1 MΩ resistor + cable. The measured corner frequency is 1.3 kHz, from which we extract a cable capacitance of $C = 120(20)$ pF. (B) Rise time of the LP voltage as measured on an oscilloscope. The fitted exponential rise time is 140 μs, in good agreement with the expected $1/RC = 120\,\mu$s expected from (A). In (B), the cable is connected to the electrode, which is also expected to add a small capacitance, though we estimate it is ~ 1 pF.

the electrodes. As discussed in section 3.3.1.3, this is actually beneficial since it reduces the servo bandwidth required for **E**. Figure 3.11A shows a measurement of the transfer function of one of the HV cables. We extract a cable capacitance of $C = 120(20)$ pF, which is in reasonable agreement with the estimated capacitance from the radii of the cable and the shielding braid [107]. Figure 3.11B shows the rise time of the LP electrode voltage, which has an exponential rise time consistent with the corner frequency measured in (A). We calibrated all 6 electrode setups with this method and found similar results.

3.3.8 High voltage rack

The HV amplifiers were initially set up on the floor of the lab under the main optical table of the experiment to minimize the lengths of cables needed. Unfortunately, this led to excess heating in our 1D optical lattice. The HV amplifiers have large fans that produce vibrations, air currents, and heat. This unwanted environmental noise showed up as heating of the atoms and molecules.

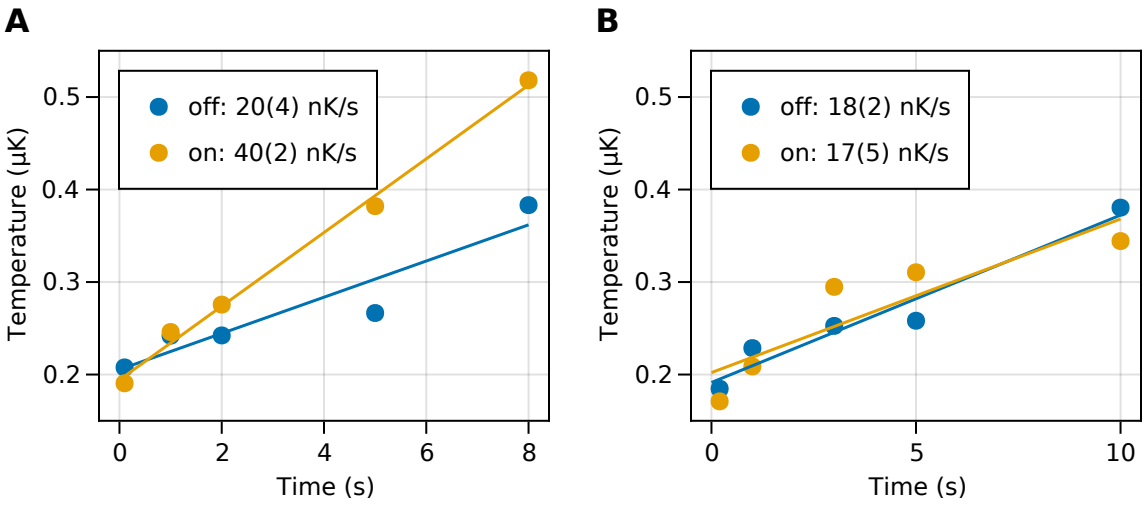

Figure 3.12: Heating rate of a K Fermi gas in the optical lattice from HV amp vibrations. (A) Before moving the amps to the rack. The heating rate with the HV amps off (blue) is much lower than with them on (orange). (B) After moving the amps to the rack. The heating rate does not show any effect from the HV amps.

To characterize this, we produced a spin-polarized Fermi gas of K, loaded it into the 1D lattice, and measured the temperature as a function of hold time (Figure 3.12A). With the HV amps powered off (blue points), we measured a heating rate of 20(4) nK/s, slightly higher than the $\sim$ 10 nK/s expected from off-resonant scattering. With the HV amps on (orange points), the heating rate went up to 40(2) nK/s. This heating was a major barrier to successfully evaporating the molecules.

Our solution was to move the HV electronics into a reconfigurable server rack next to the experiment (Figure 3.13). We mounted the rack directly into the floor using concrete anchors and also placed a thick layer of Viton rubber between the rack and floor to damp the vibrations of the supplies. The fans are mounted on the back of the supplies, so we put panels on the back and sides of the rack to block the air currents from interfering with other laser setups in the lab. We also attached acoustic damping material to the insides of the panels to further suppress vibrations. We left the top and front of the rack open, which keeps the inside of the rack from becoming very hot but also lets some noise and air currents escape. These changes were apparently good enough to fix the vibration problem, since we measured no effect of the HV amps on the heating rate after

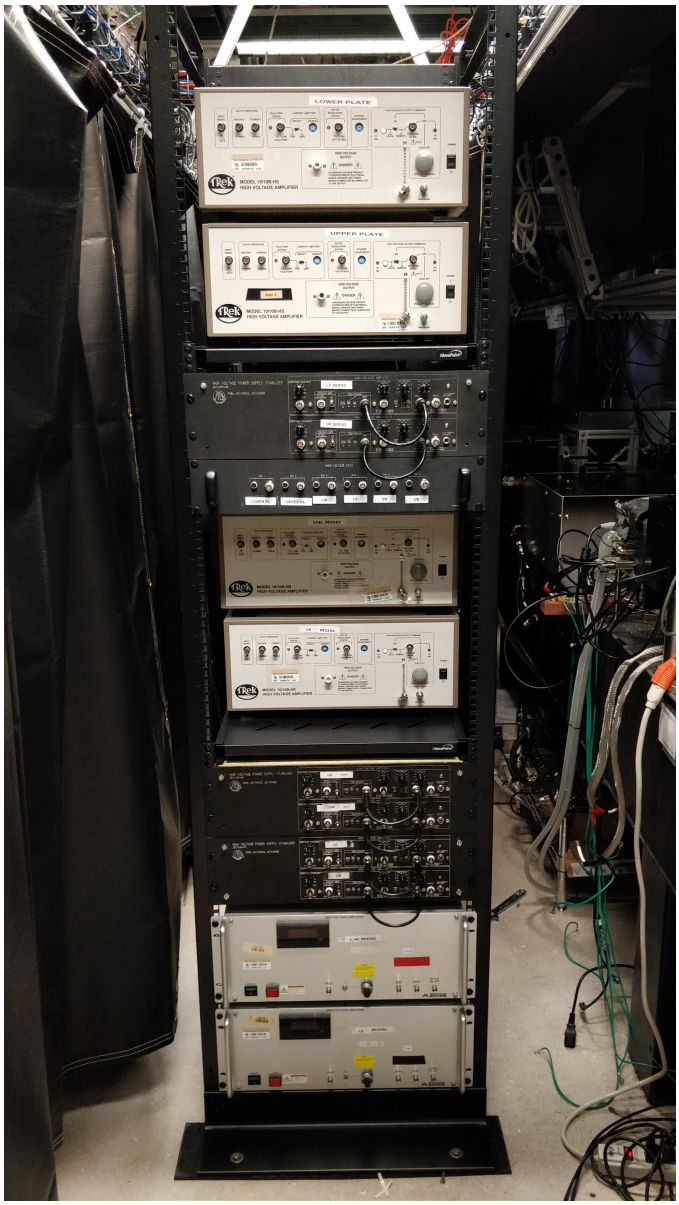

Figure 3.13: High voltage rack holding 6 HV amps, servos, and stable DACs. This picture was taken just after installation of the rack, so many BNC and HV connections are missing.

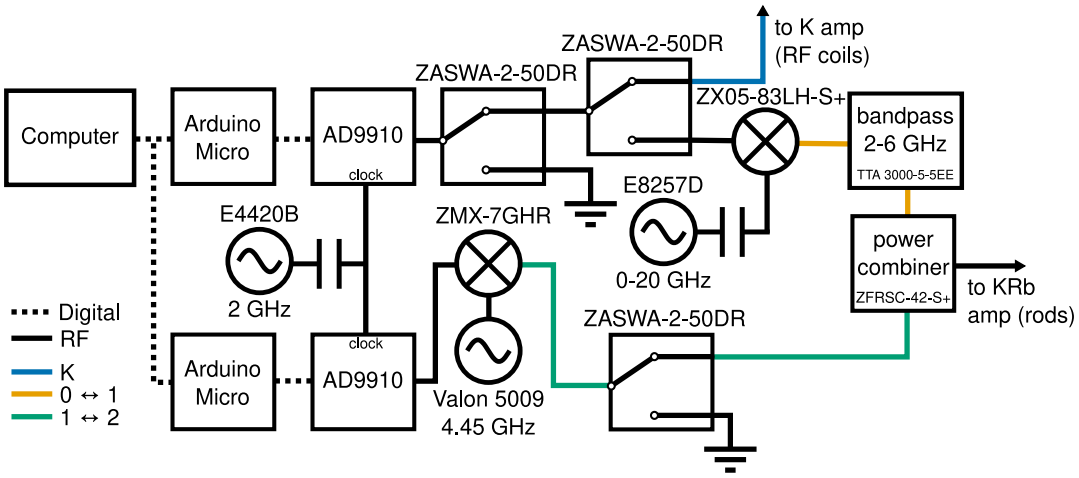

Figure 3.14: Block diagram of the K/KRb RF setup.

moving the supplies (Figure 3.12B). Having all the HV electronics in the same rack also made it easy for us to try several different grounding schemes to improve the noise performance (see Ref. [107] for details). In the future, we should add an air-water heat exchanger inside of the rack, which would allow us to fully enclose it to further reduce the temperature and air current fluctuations.

3.4 Radio-frequency fields

Radio-frequency (RF) fields are an important tool for manipulating ultracold atoms and molecules. We use them for state preparation of the atoms using adiabatic rapid passage (ARPs), as well as for spectroscopy of the molecules. A block diagram of the RF setup for K and KRb is shown in Figure 3.14. The Rb RF system is fairly simple and is not shown in the diagram. The main RF sources are built from a direct digital synthesis (DDS) chip from Analog Devices (AD9910 evaluation board). The DDS evaluation board provides a cheap and flexible synthesizer with frequency (0 to 400 MHz), amplitude, and phase control, which is programmed over serial peripheral interface (SPI) from an Arduino. The Arduino is also connected to a computer over USB, which allows integration with our computer control system.

Our system consists of two Arduino/AD9910 setups:

(1) "K/KRb DDS": used for K state preparation at 10 and 80 MHz, and for driving $N = 0 \leftrightarrow 1$

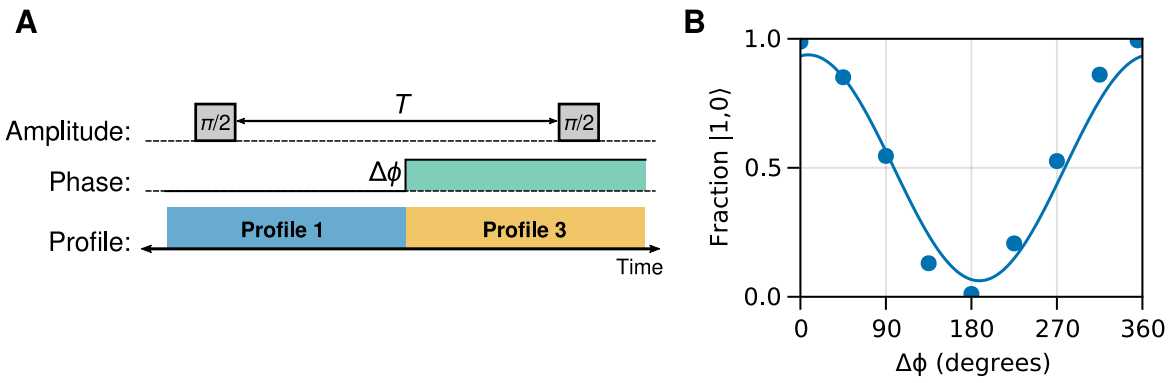

Figure 3.15: Example Ramsey fringe. (A) Schematic of the Ramsey measurement. Two pulses of area $\pi/2$ are spaced by a time T. The first pulse is performed at zero phase offset, which is programmed in (for example) DDS profile 1. The second pulse is performed at a variable phase offset $\Delta\phi$, which is programmed in profile 3. The amplitude is controlled with a switch (ZASWA-2-50DR) to produce square pulses. Amplitude-shaped pulses can also be produced; see section 3.4.1. (B) Experimentally measured Ramsey fringe on the $|0,0\rangle \leftrightarrow |1,0\rangle$ transition of the molecules. This data was taken at a short time ($T = 10\,\mu$s) before there is any measurable decoherence of the fringe.

transitions of the molecule;

(2) "$N = 2$ DDS": used for driving $N = 1 \leftrightarrow 2$ transitions of the molecule.

The three different frequencies are represented by the colored lines in Figure 3.14. Both DDSs have a switch after the output to turn the RF on and off. The K/KRb DDS additionally has a switch to toggle between the low frequency (K) and high frequency (KRb) paths. The K transitions are within the frequency range of the DDS output, which is sent directly to a 20 W amp (Mini Circuits LZY-22). After this amp, there is a high power switch (Mini Circuits MSP2TA-18) that toggles between a non-resonant coil for the ARPs at 30 G and a resonant 80 MHz coil for hiding unpaired K near the Feshbach resonance. The 80 MHz antenna has three loops and is impedance matched using a variable capacitor.

Both of the $N = 0 \leftrightarrow 1$ and $1 \leftrightarrow 2$ frequencies are higher than the DDS can reach (> 2.2 and > 4.4 GHz respectively), so each DDS is mixed with a synthesizer to achieve the desired frequency. The advantage of this setup over simply using the synth output directly is that the DDS's output frequency, amplitude, and phase can be changed much faster than the synth's. A key feature of the

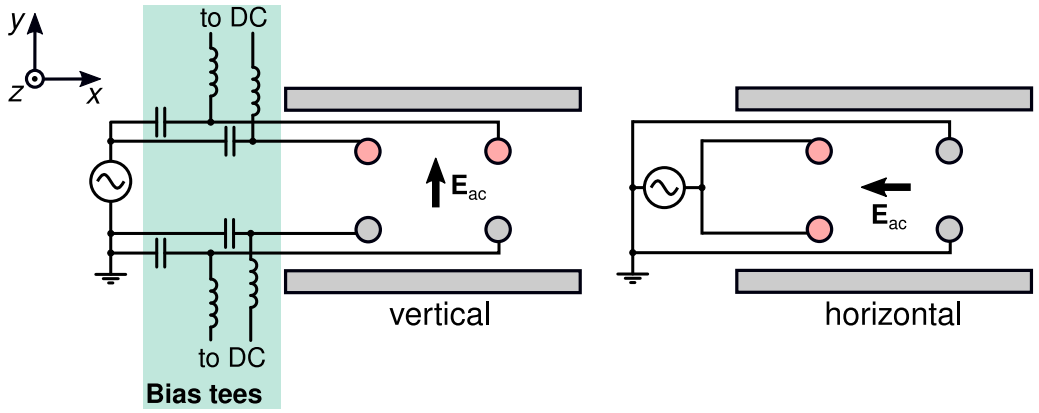

Figure 3.16: AC rod configurations. For simplicity, the in-vacuum bias tees are omitted for the horizontal configuration.

AD9910 is the ability to set preprogrammed "profiles", each of which specifies a frequency, output power, and phase offset. Switching between profiles is fast ($\sim \mu$s) and phase coherent, which allows us to do Ramsey spectroscopy and more complicated dynamical decoupling sequences such as XY8 [154] (Chapter 8). As an example, Figure 3.15 shows how a simple Ramsey sequence is implemented with the AD9910 profiles. The profiles are switched with a TTL signal (not shown) in the middle of the sequence to set the phase offset $\Delta\phi$ for the second pulse. The precise timing of the pulses is controlled by the switch directly after the output of the DDS (Mini Circuits ZASWA-2-50DR, 5 ns typical rise/fall time).

The $N = 0 \leftrightarrow 1$ and $1 \leftrightarrow 2$ frequencies are combined with a power splitter/combiner and sent to a broadband amp (CTT AGM/060-4343, 43 dBm output). The output of the amp is connected to the AC port of the in-vacuum bias tee on the rod electrodes. We can manually switch between the two configurations shown in Figure 3.16, which produce either mostly $\hat{\mathbf{y}}$ (vertical) or mostly $\hat{\mathbf{x}}$ (horizontal) polarization. At our maximum power, we observe π-pulse times of 0.5 to 10 μs for the $|0,0\rangle \leftrightarrow |1,0\rangle$ transition with the rods connected in the vertical configuration. The variation in the Rabi frequency is due to the frequency-dependent couplings to the rods from the bias tees [106]. Some limitations with this setup are described in section 3.4.2.

We had initially used a switch to combine the $N = 0 \leftrightarrow 1$ and $1 \leftrightarrow 2$ frequencies, which gives

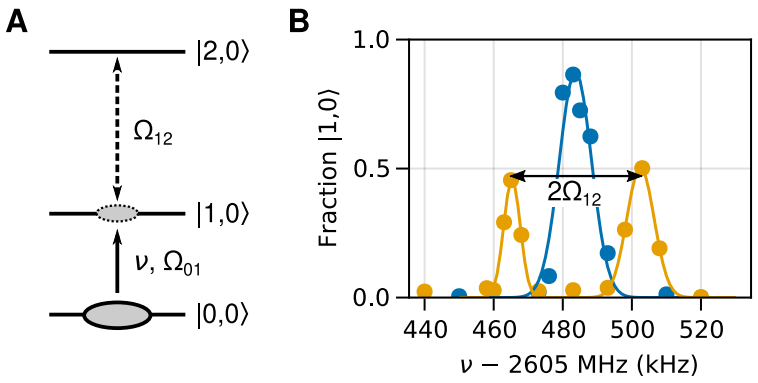

Figure 3.17: Probing $N = 0 \leftrightarrow 1$ while dressing $1 \leftrightarrow 2$. (A) Diagram of the involved rotational levels. The molecules are initially prepared in $|0,0\rangle$. (B) Lineshapes for $|0,0\rangle \leftrightarrow |1,0\rangle$ without (blue) and with (orange) dressing on $|1,0\rangle \leftrightarrow |2,0\rangle$ at $E = 4.56$ kV/cm.

a higher power at the molecules than the power splitter. However, the splitter has the advantage that multiple tones can be applied at the same time. Figure 3.17 shows how we can probe on the $|0,0\rangle \leftrightarrow |1,0\rangle$ transition while dressing with $|1,0\rangle \leftrightarrow |2,0\rangle$. The molecules are initially prepared in $|0,0\rangle$ and are excited to the $|1,0\rangle$ state using a microwave pulse. Scanning the frequency ν of this pulse without the dressing produces a single peak in the transferred fraction (blue points in Figure 3.17). Turning on an additional dressing field resonant with the $|1,0\rangle \leftrightarrow |2,0\rangle$ transition splits the peak into two peaks separated by $2\Omega_{12}$ (orange points), where Ω_{12} is the Rabi frequency of the dressing field. By detuning both drives from one-photon resonance, we can also drive Rabi oscillations directly between $|0,0\rangle$ and $|2,0\rangle$ without populating $|1,0\rangle$. Extending this capability to be able to apply many tones simultaneously may be helpful in the future, for example to control the dipolar interaction using microwave dressing [45] or to implement synthetic dimensions using the rotational states [159].

3.4.1 Amplitude-shaped pulses

The envelope of the RF pulse can add undesired frequency components to the output. For most of the work in this thesis, the pulse envelope was not important and we used square pulses for simplicity. However, for the layer selection (Chapter 7), we used amplitude-shaped pulses to avoid frequency sidebands that could potentially drive molecules in adjacent layers. To implement

this, we added another mixer (Mini Circuits ZFM-2, not shown in Figure 3.14) just before the ZX05-83LH-S+ mixer on the $N = 0 \leftrightarrow 1$ path. A function generator programmed with the desired envelope was connected to the IF port of the new mixer and externally triggered to fire the pulse. To avoid distortion of the pulse, it was important to calibrate the LO and IF powers to remain in the linear regime of the mixer (Figure 3.18A).

For the layer selection, we used Blackman-shaped pulses,

$$A(t) = 0.42 - 0.5\cos\left(\frac{2\pi t}{\tau}\right) + 0.08\cos\left(\frac{4\pi t}{\tau}\right), \tag{3.6}$$

where τ is the total time of the pulse. Note that $A(t)$ reaches a maximum of 1 at $t = \tau/2$. The pulse area is $\int_0^\tau dt\, A(t) = 0.42\tau$, so compared to a square pulse of the same amplitude, the Blackman pulse needs to be longer by a factor of $1/0.42 = 2.38$ to obtain the same pulse area. An example RF pulse with a Blackman envelope is shown in Figure 3.18B. Figure 3.19 shows a comparison of RF lineshapes on the molecules using square (blue) and Blackman (orange) pulses. The prominent sidebands from square pulses are removed by using Blackman pulses.

3.4.2 Limitations of the rods: polarization purity and AC field homogeneity

In principle, driving the microwave fields directly on the rods produces the near-field $\mathbf{E}(t)$ and gives a clean microwave polarization. However, we find in practice that the homemade bias tees (see Ref. [106]) do not provide an equal coupling onto all of the rods, and we can drive all three $\Delta m_N = 0, \pm 1$ transitions with similar Rabi frequencies in the nominally $\hat{\mathbf{y}}$-polarized configuration (Figure 3.16). So far, we have not had a problem addressing individual transitions by resolving them in frequency rather than with polarization. However, well-controlled polarization would be required for some microwave dressing schemes [160] or microwave shielding [161, 162, 105, 54].

We have also observed that the Rabi oscillations of the molecules decay over ~ 25 cycles (Figure 3.20A), which we attribute to an inhomogeneous Rabi frequency Ω caused by the unequal coupling onto the rods. This explanation is consistent with the observation from Figure 3.20B that the oscillation decays slower with decreasing Ω, up until the point where we start to become limited

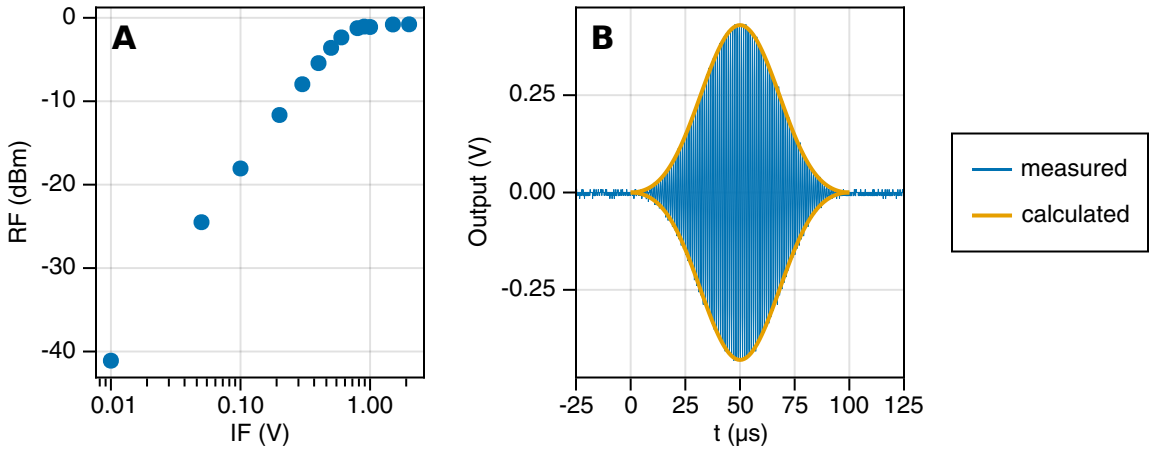

Figure 3.18: Calibration of the amplitude shaping setup. (A) Calibration of the mixer. The part (ZX05-10L) calibrated in this plot was slightly different from what we eventually used (ZFM-2+) in the layer selection measurement. The input at the LO port was 3 dBm at 75 MHz. (B) Blackman-shaped pulse output from the mixer, as measured on an oscilloscope (blue). The input at the LO port was 3 dBm at 21 MHz and the max IF voltage was 0.6 V. The Blackman envelope from equation (3.6) with $\tau = 100\,\mu$s is shown for comparison (orange). The envelope is scaled to match the data.

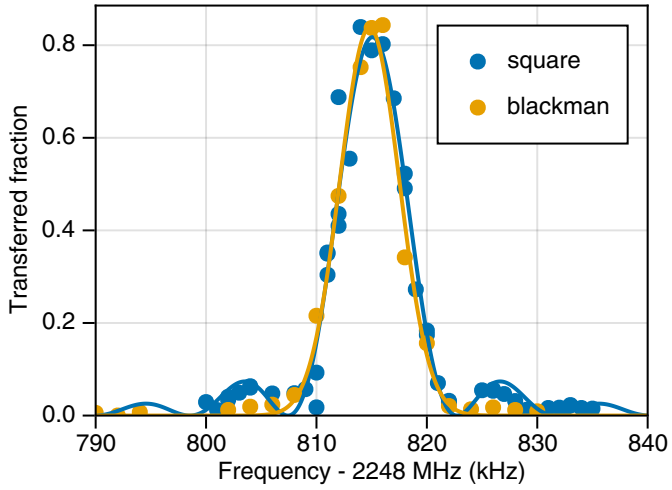

Figure 3.19: Comparison of lineshapes using square (blue) and Blackman (orange) pulses. The lineshapes were obtained by driving $|0,0\rangle \rightarrow |1,0\rangle$ at $|\mathbf{E}| = 1$ kV/cm. The maximum pulse amplitudes were set equal and the duration of the Blackman pulse was chosen to make the pulse areas equal. The square pulse data is fit to a Rabi lineshape (blue line), and the Blackman pulse data is fit to a Gaussian lineshape (orange line).

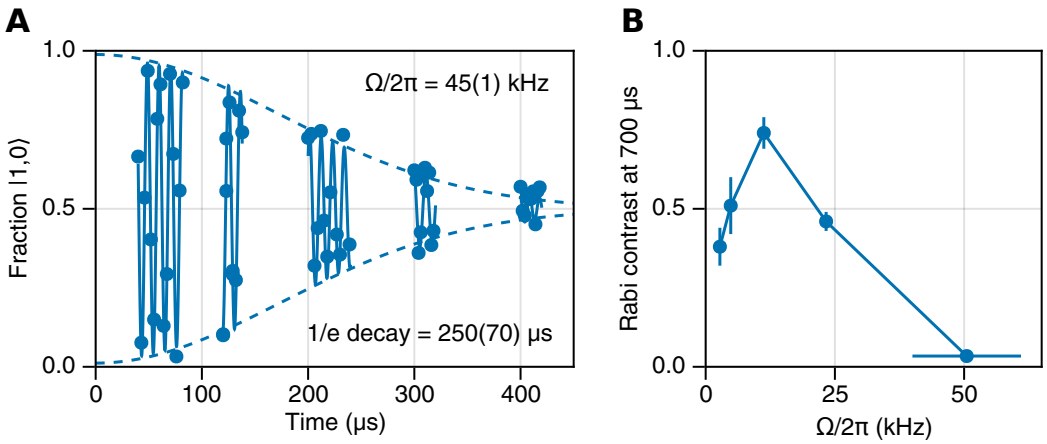

Figure 3.20: Inhomogeneous AC electric field. (A) Rabi oscillations at $|\mathbf{E}| = 4.5$ kV/cm. The oscillations show decay after ~ 25 cycles, indicating an inhomogeneous Rabi frequency across the cloud. (B) Rabi oscillation contrast at the end of a 700 μs pulse as a function of the average Rabi frequency Ω. The contrast is improved for lower Ω, until inhomogeneities of $\mathbf{E}$ start to dominate at the lowest Ω.

by inhomogeneous broadening of the lineshape due to E-field gradients.[6] In simulations, we found that the measured decay is consistent with a $\sim 2\%$ variation of Ω over the 2σ width of the cloud. This data was taken in the vertical configuration of Figure 3.16, where we do expect to have a nonzero gradient of $\mathbf{E}_{\mathrm{ac}}$ owing to the asymmetry between the voltages of the upper and lower rods. However, we calculate that the expected vertical gradient of $\mathbf{E}_{\mathrm{ac}}$ is about a factor of 5 too small to account for the observed inhomogeneity of Ω. A factor of 2 difference in coupling efficiency between the two upper rods, or a fairly large phase shift between them, would explain the observed decay of the Rabi oscillations by creating a horizontal gradient of $\mathbf{E}_{\mathrm{ac}}$.

For this reason, it was important to use the XY8 sequence [154] for the experiments in Chapter 8, which cancels errors in the pulse area to lowest order. The limitations from the unequal coupling could probably be further mitigated by individually phase-shifting and attenuating the signals for each rod to shim the RF field. According to Jun, the JILA eEDM experiment has done extensive work on shimming the RF fields on the eight electrodes that generate their rotating electric field,

[6] The data was taken before carefully shimming this particular field configuration.

so they will be a good resource if we decide to pursue this further.

3.5 CCD calibration

The atoms and molecules are imaged onto a CCD camera using standard absorption imaging (see Refs. [163, 164] for a detailed introduction). We use two Andor iXon Ultra 888 electron-multiplying (EM)CCD cameras; the axial ($\hat{\mathbf{z}}$) and side ($-\hat{\mathbf{x}}$) imaging paths are combined on the first camera (see Figure 3.5), and the top ($-\hat{\mathbf{y}}$) imaging goes to the second camera. An absorption measurement consists of three images: (1) probe light with atoms ("shadow" frame S_{shadow}); (2) probe light without atoms ("light" frame S_{light}); (3) no probe light without atoms ("dark" frame S_{dark}). The optical density (OD) frame is obtained by

$$\text{OD} = -\ln \frac{S_{\text{shadow}} - S_{\text{dark}}}{S_{\text{light}} - S_{\text{dark}}}. \tag{3.7}$$

For low probe light intensity, the OD on a pixel of area A is converted to the number of atoms N on the pixel using $N = (A/\sigma) \times \text{OD}$, where $\sigma = 3\lambda^2/2\pi$ is the resonant absorption cross section at wavelength λ. For higher light intensity, one must account for saturation of the imaging transition [165, 166].

An important noise source in absorption imaging is the photon shot noise of the probe beam. For the density fluctuation measurement in section 4.2.3, it was important to remove the photon shot noise contribution to accurately determine the atom and molecule number fluctuations. A detailed description of the image analysis procedure is given in Refs. [51, 107]. Here, we will focus on one important step, the calibration of the CCD gain. To understand why the CCD gain is important, consider what happens during an exposure. Photons incident on the CCD array are converted to photoelectrons with some quantum efficiency q. If the number of photons is Poisson-distributed with mean N_{photon}, then the number of electrons is also Poisson-distributed with mean $N_e = qN_{\text{photon}}$ [163]. The photoelectrons are then converted to CCD counts according to a (deterministic) gain factor g that depends on the camera model and settings. This results in a mean number of counts $N_{\text{c}} = gN_e$, but a variance $\Delta N_{\text{c}}^2 = g^2 \Delta N_e^2 = g^2 N_e = gN_{\text{c}}$. Thus, N_{c} is

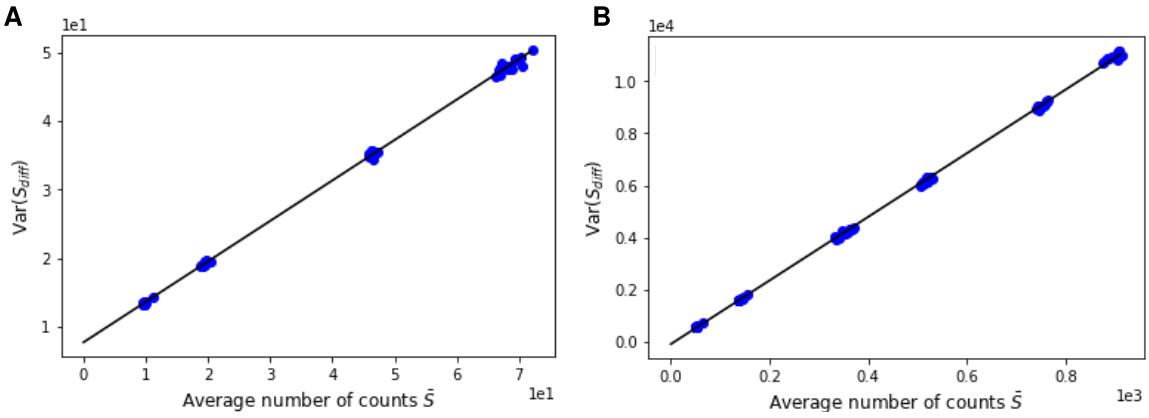

Figure 3.21: Calibration of Andor iXon Ultra 888 CCD. (A) Conventional mode (no EM gain). The linear fit gives $\mathrm{Var}(S_{\mathrm{diff}}) = 0.589(2)\overline{S} + 7.77(9)$. (B) EM mode, with a nominal EM gain of 50. The linear fit gives $\mathrm{Var}(S_{\mathrm{diff}}) = 12.184(25)\overline{S} - 77(14)$.

not Poisson-distributed, but instead is "stretched out" by a factor of g. Measuring the slope of $\Delta N_{\mathrm{c}}^2/N_{\mathrm{c}}$ gives us g and allows us to determine the photon shot noise.

We decided to check the value of g against the specified value from the data sheet following the procedure in Ref. [163]. To do this, we took 60–100 absorption images without atoms present and varied the probe light intensity between a few different values. From the shadow and light frames of each image, we formed the difference image $S_{\mathrm{diff}} = S_{\mathrm{shadow}} - S_{\mathrm{light}}$. We chose a small analysis region near the center of the probe where the intensity of the beam is fairly uniform, and calculated the variance $\mathrm{Var}(S_{\mathrm{diff}})$ over the pixels in this region. If $\overline{S}$ is the average number of counts per pixel in the analysis region (after subtracting the background S_{dark}), then $\mathrm{Var}(S_{\mathrm{diff}})$ should satisfy

$$\mathrm{Var}(S_{\mathrm{diff}}) = 2g\overline{S} + 2(rg)^2, \tag{3.8}$$

where g is the camera gain and r is the readout noise in electrons. The factor of two on both terms comes from the subtraction of S_{shadow} and S_{light}. The second term is missing an additional factor of 2 compared to Ref. [163] because S_{diff} was formed from $(S_{\mathrm{shadow}} - S_{\mathrm{light}})$ instead of $[(S_{\mathrm{shadow}} - S_{\mathrm{dark}}) - (S_{\mathrm{light}} - S_{\mathrm{dark}})]$; the latter contains an extra readout noise contribution from the dark frames.[7]

[7] It looks like the readout noise from S_{dark} should cancel out, since it is perfectly correlated between $(S_{\mathrm{shadow}} -$

According to equation (3.8), we can extract g and r from a linear fit of $\mathrm{Var}(S_{\mathrm{diff}})$ versus $\overline{S}$. The results are shown in Figure 3.21. For conventional CCD mode (no EM gain) in (A), we extracted a gain of $g = 0.295(1)$ counts/electron and readout noise of $r = 6.69(4)$ electrons, reasonably close to the specified values of $g = 1/3.5 = 0.286$ counts/electron and $r = 6.86$ electrons. In units of CCD counts, the readout noise is $rg = 1.97(1)$.

We also calibrated the camera with a nominal EM gain of 50 in (B). The EM amplifier has its own shot noise which doubles the first term in equation (3.8) [167]. The readout noise comes after the EM amplifier and thus is unaffected. This leads to a modified equation

$$\mathrm{Var}(S_{\mathrm{diff}}) = 4Ag\overline{S} + 2(rg)^2, \tag{3.9}$$

where A is the EM gain. Accounting for this extra noise, we obtained $Ag = 3.046(6)$ counts/electron for the data in Figure 3.21B. Using the specified value of $g = 1/16.4$ counts/electron, we extracted $A = 49.9(1)$, which agrees with the nominal EM gain setting.

The fitted offset in Figure 3.21B is slightly negative, which we attribute to the readout noise being too small to measure. This is understandable since the purpose of the EM amplification is to make the readout noise negligible. Plugging in the specified values of $g = 1/16.4$ counts/electron and $r = 25.1$ electrons, we estimate a readout noise contribution of $2(rg)^2 = 4.5$, which is much less than the smallest measured $\mathrm{Var}(S_{\mathrm{diff}})$ of ~ 500 in Figure 3.21B.

S_{dark}) and $(S_{\mathrm{light}} - S_{\mathrm{dark}})$. However, this actually depends on whether fast kinetics is being used. If S_{shadow} and S_{light} are obtained from different regions of the CCD, then readout noise on S_{dark} in those two regions is uncorrelated, giving the additional factor of 2 in the variance.

Chapter 4

Degenerate Fermi gas of molecules in 3D

Creation of a quantum-degenerate molecular gas has been a long-standing goal for the ultracold molecule community. Unfortunately, the complexity of ultracold molecules made this challenging. The highest PSD molecular gases have been formed by associating the molecules from near-degenerate atomic gases using Feshbach resonances. However, low conversion efficiency of atoms into molecules and high losses on the Feshbach resonance prevented attempts to push this technique further to create degenerate molecular gases. Without methods to control the inelastic losses of the molecules while maintaining a high elastic collision rate, direct evaporative cooling of the molecules to higher PSD was also unfeasible.

In our first experiments in the new JILA KRb machine, we started by trying to optimize the Feshbach association stage, encouraged by the much improved atom conditions compared to the previous apparatus. By starting from a deeply-degenerate Bose-Fermi mixture of ^{40}K and ^{87}Rb, with many more fermions than bosons ($N_{\mathrm{K}}/N_{\mathrm{Rb}} \approx 8$), we were able to mitigate the losses on the Feshbach resonance and produce a gas with $N = 30 \times 10^3$ molecules at $T = 50$ nK and $T/T_F = 0.3$ [50], where T_F is the Fermi temperature of the molecular gas. We also observed an intriguing suppression of the reactive loss rate as the molecular gas became degenerate, which is still not fully understood [168, 169]. Finally, we measured the density fluctuations in the gas, which are suppressed by fermionic statistics as the gas becomes degenerate [51]. The density fluctuations gave an alternative measurement of T/T_F that agreed with our measurements of the momentum distribution.

Though our observables were consistent with the molecular gas being initially created in thermal equilibrium, the dynamics while crossing the Feshbach resonance are a complicated competition between inelastic three-body losses and thermalizing elastic collisions. We also studied the elastic collisions between atomic K and the Feshbach molecules (KRb*) and estimated that six elastic collisions occurred per molecule during the Feshbach ramp, facilitating thermalization of KRb* [51].

This chapter is based on Refs. [50, 51]. Since the writing of Ref. [50], there has been a great deal of exciting progress on degenerate molecular gases. Our group demonstrated direct evaporation of molecules in 2D to $T/T_F < 1$ [52] (Chapter 5). In 2021, the Munich group created a DFG of NaK molecules in the Feshbach association stage [53], and subsequently through direct evaporation using microwave shielding [54]. A BEC of homonuclear Cs_2 Feshbach molecules in 2D was also demonstrated by the Chin group in Chicago [170].

4.1 Experimental procedure

The starting point of the experiments is a Bose-Fermi mixture in an optical dipole trap (ODT) formed by two crossed beams at $\lambda = 1064$ nm. In Ref. [50], the beams crossed at 45° and the trap frequencies were $(\omega_x, \omega_y, \omega_z) = 2\pi \times (45, 250, 80)$ Hz for K. In Ref. [51], the beams crossed at 90°, and the trap frequencies were $(\omega_x, \omega_y, \omega_z) = 2\pi \times (60, 240, 60)$ Hz for K. Trap frequencies for Rb, KRb*, and KRb are obtained by scaling the above trap frequencies by 0.72, 0.83, and 0.79, respectively. The experiment coordinate system is defined with $\hat{\mathbf{y}}$ pointing counter to gravity. The magnetic field B is oriented along $\hat{\mathbf{y}}$.

In addition to the ODT, we also used a shallow ($30E_{\mathrm{R}}$ for KRb) lattice along $\hat{\mathbf{y}}$ during molecule production. Before adding the lattice, we noticed a significant slosh of the molecules in $\hat{\mathbf{y}}$ after production, which caused the cloud to heat up. We initially attributed this to differential gravitational sag, which would cause a separation between the Rb and KRb equilibrium positions in the ODT. However, we later realized that the slosh was caused by the momentum kick from the STIRAP transfer, which imparts a momentum of $k_{\mathrm{STIRAP}} = 2\pi \left(\frac{1}{\lambda_{\mathrm{up}}} - \frac{1}{\lambda_{\mathrm{down}}}\right)$, where $\lambda_{\mathrm{up}} = 970$

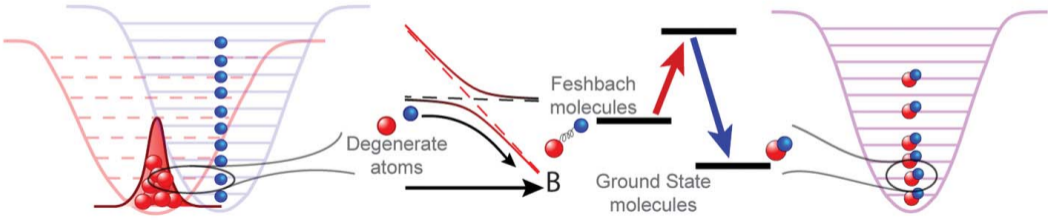

Figure 4.1: Cartoon of molecule production. Starting from an overlapping DFG of K (blue spheres) and BEC of Rb (red spheres) in the ODT, Feshbach molecules are produced by sweeping the magnetic field B across the interspecies Feshbach resonance. Feshbach molecules are then transferred to the ground rovibrational state using STIRAP. Reproduced from Ref. [50].

nm and $\lambda_{\text{down}} = 690$ nm are the wavelengths of the two STIRAP beams (see section 4.3.1 for more details). The shallow lattice completely damped the oscillations, and the lattice was ramped off immediately after molecule production.

The molecule production process is illustrated schematically in Figure 4.1. We started with the atomic mixture at $B = 555$ G, above the broad interspecies K–Rb Feshbach resonance at $B_0 = 546.62$ G (width of 3.04 G) [171]. KRb* was created by adiabatically sweeping B across the Feshbach resonance from 555 G to 546.1 G. The Feshbach sweep was typically performed in 5 ms (see also section 4.3.2). After the Feshbach sweep, molecules were transferred to the ground state using STIRAP [66] with a typical efficiency of 85%. All of the experiments in the chapter were conducted at zero electric field ($|\mathbf{E}| = 0$). Remaining unpaired atoms were removed immediately after STIRAP using resonant light, except for in the K–KRb* collision measurements (section 4.3.1).

By changing the final evaporation cut in the ODT before molecule production, we varied the initial atom numbers N_{K} and N_{Rb} and temperature T, as well as the resulting molecular condition. The results are shown in Figure 4.2. The three columns of Figure 4.2 correspond to the three temperature conditions listed in Table 4.1. At the highest atom number and temperature, Rb was uncondensed (left panel of Figure 4.2). Only about 15% of Rb was converted into molecules, a typical Feshbach conversion efficiency for non-degenerate atomic clouds [172, 151], but owing to the high total atom number we created up to $N = 10^5$ molecules at $T/T_F = 1$. At the coldest

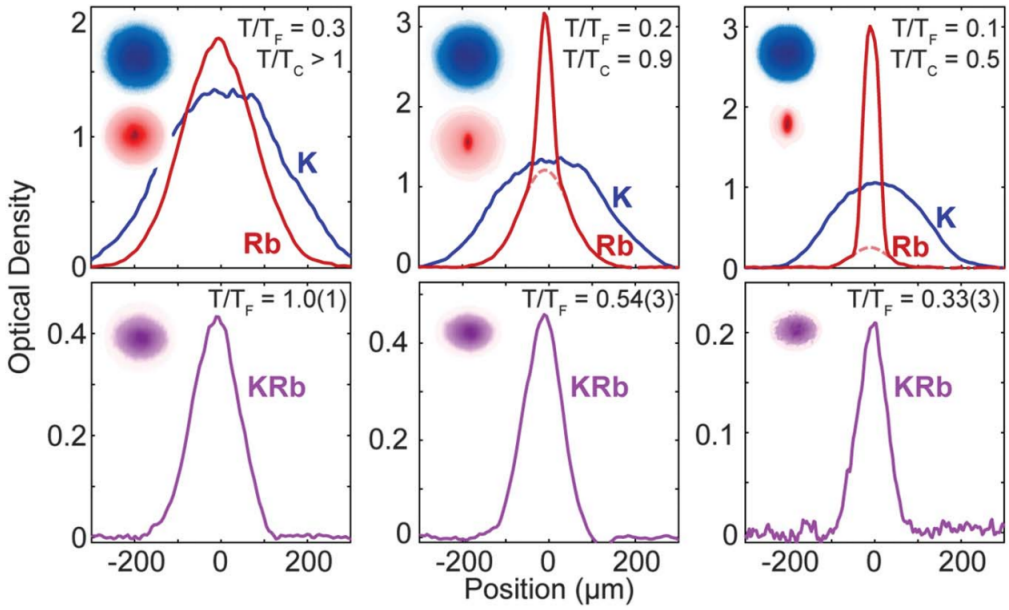

Figure 4.2: Molecule production from a degenerate Bose-Fermi mixture. The plots show vertical slices through the measured atomic (top row) and corresponding molecular (bottom row) distributions in TOF. Insets show the 2D absorption images corresponding to the plotted slices. At the highest atomic evaporation cut (left column), we produce as many as $N = 10^5$ molecules at $T/T_F = 1.0(1)$. At the lowest evaporation cut (right column), we produce around $N = 3 \times 10^4$ molecules at $T/T_F = 0.33(3)$. The atom and molecule numbers and temperatures for these measurements are reported in Table 4.1. Reproduced from Ref. [50].

T (nK)	N_{Rb}	T/T_c	N_{K}	$T/T_{F,\mathrm{K}}$	N_{KRb}	$T/T_{F,\mathrm{KRb}}$
230	6×10^5	> 1	1.2×10^6	0.3	$1.0(1) \times 10^5$	1.0(1)
110	2×10^5	0.9	1×10^6	0.2	$5.0(5) \times 10^4$	0.54(3)
50	7×10^4	0.5	5×10^5	0.1	$3.0(5) \times 10^4$	0.33(3)

Table 4.1: Atom and molecule conditions for Figure 4.2. Reproduced from Ref. [50].

cloud, Rb was about 85% condensed and we converted up to 50% of the Rb, producing a molecular gas at $T/T_F = 0.3$ (right panel of Figure 4.2). The quoted T/T_F is obtained from fitting the cloud to a Fermi-Dirac distribution, described in more detail in the next section. At each evaporation cut, the trap was recompressed to the trap frequencies reported above before producing molecules. This trap depth was found experimentally to improve the density overlap of K and Rb, without increasing the density so much that three-body losses were excessive.

4.2 Properties of the molecular Fermi gas

In this section, we describe our measurements of the molecular Fermi gas. We first measured the molecular distribution in time-of-flight (TOF) expansion to determine the temperature of the molecules. For a degenerate gas, the shape of the distribution is determined by quantum statistics, allowing us to extract the T/T_F of the molecular cloud. We also measured the rate of chemical reactions in the gas [32], and observed a reduction in the chemical reaction rate as the gas became degenerate. Finally, we measured the suppression of density fluctuations in the gas owing to Fermi statistics.

4.2.1 TOF thermometry

Let us start by writing down some of the basic equations for harmonically-trapped ideal Fermi gases [173, 174]. A classical gas (Boltzmann statistics) has a Gaussian density distribution,

$$n_{\mathrm{cl}}(x,y,z) = \frac{N}{(2\pi)^{3/2}\sigma_x\sigma_y\sigma_z}\exp\left(-\frac{x^2}{2\sigma_x^2}-\frac{y^2}{2\sigma_y^2}-\frac{z^2}{2\sigma_z^2}\right), \tag{4.1}$$

where $\sigma_i = \sqrt{k_B T/m\omega_i^2}$ is the thermal size of the cloud along $i \in \{x,y,z\}$. If the particles obey Fermi statistics, they instead follow a Fermi-Dirac distribution,

$$n_{\mathrm{FD}}(x,y,z) = \frac{N}{(2\pi)^{3/2}\sigma_x\sigma_y\sigma_z}\mathrm{Li}_{3/2}\left[-\zeta\exp\left(-\frac{x^2}{2\sigma_x^2}-\frac{y^2}{2\sigma_y^2}-\frac{z^2}{2\sigma_z^2}\right)\right]/\mathrm{Li}_3(-\zeta), \tag{4.2}$$

where $\zeta = e^{\beta\mu}$ is the fugacity, with $\beta = 1/k_B T$ the inverse temperature and μ the chemical potential. The function $\mathrm{Li}_n(-z)$ is a polylogarithm. The fugacity is related to the degeneracy of the gas by

$$\mathrm{Li}_3(-\zeta) = -\frac{1}{6(T/T_F)^3}. \tag{4.3}$$

In a 3D harmonic trap, T_F can also be calculated from

$$T_F = \frac{\hbar\overline{\omega}}{k_B}(6N)^{1/3}, \tag{4.4}$$

where $\overline{\omega} = (\omega_x\omega_y\omega_z)^{1/3}$ is the geometric mean trapping frequency.

To measure the temperature of the cloud, we quickly switch off the ODT to let the gas expand in TOF. After a time t of expansion from a harmonic trap, the density distribution has the same shape but with the sizes scaled according to $\sigma_i \to \sigma_i\sqrt{1+\omega_i^2 t^2}$ [175]. Absorption imaging integrates the signal along the probe axis (here assumed to be $\hat{\mathbf{z}}$), so we fit to the column-integrated distributions

$$n_{\mathrm{cl,int}} = A\exp\left(-\frac{x^2}{2\sigma_x^2} - \frac{y^2}{2\sigma_y^2}\right) \tag{4.5}$$

$$n_{\mathrm{FD,int}} = A \times \mathrm{Li}_2\left[-\zeta\exp\left(-\frac{x^2}{2\sigma_x^2} - \frac{y^2}{2\sigma_y^2}\right)\right]/\mathrm{Li}_2(-\zeta), \tag{4.6}$$

where A is the peak density after time-of-flight. For both the classical and Fermi gas, we extract T from the fitted sizes σ_i according to

$$T = \frac{m\omega_i^2\sigma_i^2}{k_B(1+\omega_i^2 t^2)}. \tag{4.7}$$

Note that at long times $t \gg 1/\omega_i$, the ω_i dependence drops out and $T = m\sigma_i^2/k_B t^2$ — in other words, σ_i expands linearly with velocity $\sqrt{k_B T/m}$. For the Fermi gas, we can also independently extract T/T_F from the fitted fugacity ζ according to equation (4.3).

Figure 4.3A shows a density profile of the molecular DFG after TOF expansion, obtained by an azimuthal average of the full 2D column-integrated absorption image. As shown by the fit residuals (bottom panel), the Fermi-Dirac fit (blue) captures the shape of the cloud better than the classical Gaussian fit (red). From the fitted fugacity, we extract $T/T_F = 0.31(2)$ for this cloud.

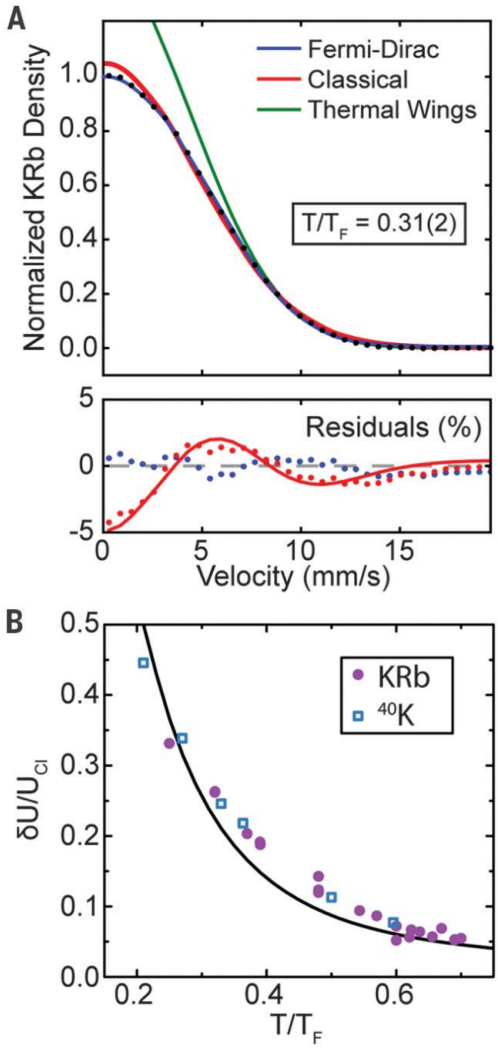

Figure 4.3: TOF thermometry of the molecular DFG. (A) Fit of the molecular density after 10 ms of TOF. The data points (black) are obtained by azimuthally averaging the cloud. The Fermi-Dirac fit (blue) captures the shape of the cloud better than the Gaussian fit (red), as illustrated by the fit residuals (lower panel). A Gaussian fit to the outer wings of the cloud (green) overestimates the density at the center of the cloud. (B) The deviation $\delta U/U_{\rm cl}$ of the internal energy of the gas from the classical prediction as a function of T/T_F. The trends of KRb (purple circles) and K (blue squares) both agree well with the calculation for an ideal Fermi gas (black line). Reproduced from Ref. [50].

A Gaussian fit to the outer wings of the cloud (green) captures the temperature of the cloud but drastically overestimates the density at the center of the distribution.

As the gas becomes deeply degenerate, the average energy per particle U saturates at $(3/4)k_BT_F$ instead of following the classical equipartition value of $U_{\rm cl} = 3k_BT$. Therefore, the deviation $\delta U = U - U_{\rm cl}$ from the classical prediction gives a measure of the degeneracy of the gas. To estimate U, we use $U = 3k_BT_{\rm gauss}$, where $T_{\rm gauss}$ is the temperature obtained from equation (4.7) by fitting the entire cloud to a Gaussian distribution. In Figure 4.3B, we plot the measured $\delta U/U_{\rm cl} = 1 - T/T_{\rm gauss}$ as a function of T/T_F. The internal energy for KRb (purple circles) shows a significant deviation below $T/T_F \approx 0.6$, in agreement with the calculated result for an ideal Fermi gas (black line). For comparison, we also plot the same quantity measured on our ^{40}K atomic Fermi gas (blue squares), which shows the same trend.

4.2.2 Reduced loss rate

As introduced in section 2.5.2, and experimentally studied in Refs. [32, 79, 34], KRb molecules experience losses at ultralow temperatures owing to chemical reactions. Since the molecules are identical fermions, they collide predominantly in p-wave collisions ($L = 1$) at ultracold temperatures. The chemical reaction rate is limited by tunneling through the p-wave barrier to reach short range, which for non-degenerate gases results in the two-body loss rate coefficient β scaling linearly with T. In the absence of heating, the loss is well-modeled by a simple differential equation, $dn/dt = -\beta n^2$, which has solution

$$n(t) = \frac{n_0}{1 + \beta n_0 t}, \tag{4.8}$$

where n is the average molecular density,

$$n = \frac{1}{N}\int dx\, dy\, dz\; n_{\rm cl}(x,y,z)^2 = \frac{N}{8\pi^{3/2}\sigma_x\sigma_y\sigma_z}, \tag{4.9}$$

n_0 is the initial density, and β is the two-body loss rate coefficient that describes the reactive losses. According to equation (4.8), one can estimate β by finding the time $\tau = 1/\beta n_0$ where

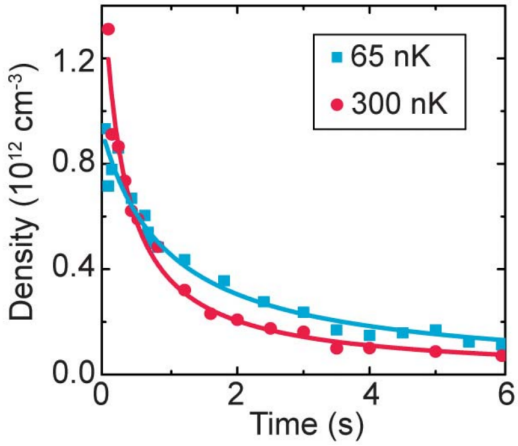

Figure 4.4: Molecular loss measurements at $T = 65$ nK (blue squares) and $T = 300$ nK (red circles). Solid lines are fits to the solution of equation (4.10). Reproduced from Ref. [50].

the density has dropped by half. One can also estimate β by the initial slope of the loss, using $dn/dt \approx -(\beta n_0)n$, which gives a rate $\Gamma = 1/\tau = \beta n_0$.

For a gas in 3D, anti-evaporative heating leads to a more complicated density decay than described by equation (4.8). Owing to the density dependence of the loss, chemical reactions mainly occur in the densest, coldest part of the gas. As a result, the losses cause an effective heating of the gas, referred to as "anti-evaporation" [79], which further lowers the density n. We approximated the temperature evolution by a linear heating rate h, so $T(t) = T_0 + ht$. Experimentally, we measured heating rates of $h = 10 - 30$ nK/s, which are somewhat larger than the value $h = \beta n_0 T_0/12$ predicted by a simple anti-evaporation model [79].

By measuring the average molecular density n after a variable hold time, we obtain loss measurements like the two shown in Figure 4.4. To fit the decay in the presence of heating, we model the loss of the molecules with the following differential equation,

$$\frac{dn}{dt} = -\beta n^2 - \frac{3n}{2T}\frac{dT}{dt}, \tag{4.10}$$

Since $\beta \propto T$, we set $\beta = bT$ in the differential equation to account for changes in the loss rate due to heating. The coefficient b can be calculated using multichannel quantum defect theory (MQDT), which gives $b = 0.8(1) \times 10^{-5}\,\mathrm{cm^3\,s^{-1}\,K^{-1}}$ for KRb [32].

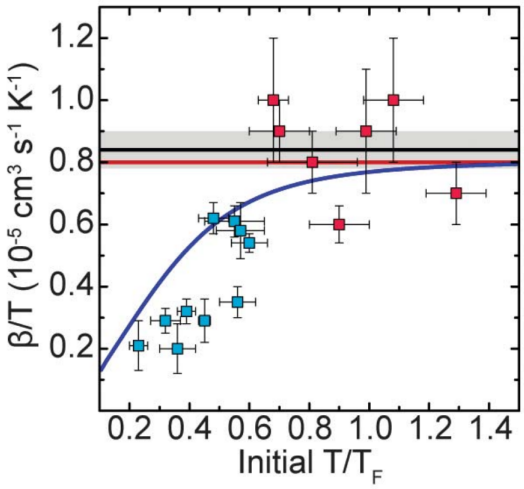

Figure 4.5: Reduction of the chemical reaction rate at low T/T_F. Reproduced from Ref. [50].

The preceding discussion is geared toward thermal gases, but we might expect the behavior to change in quantum degeneracy. At low T/T_F, the collision energy is no longer proportional to T, but rather is determined by the Fermi temperature T_F. Therefore, as $T \to 0$, we might expect the loss rate to saturate at $\beta \sim b \times (E_{\text{avg}}/k_B)$, where $E_{\text{avg}}/k_B = 3T_F/4$ is the average energy in the Fermi gas at $T = 0$ [168].

Experimentally, we saw the opposite trend from what is suggested by this simple physical argument. As shown in Figure 4.5, the fitted loss rate β/T decreased as the initial T/T_F of the cloud was lowered. At $T/T_F > 0.6$ (red points), we measured a constant β/T as a function of the initial T/T_F, in agreement with the classical prediction. The average of those points (black line) gave $\beta/T = 0.84(6) \times 10^{-5}\,\text{cm}^3\,\text{s}^{-1}\,\text{K}^{-1}$, in good agreement with the MQDT prediction (red line). As the gas became degenerate, at $T/T_F < 0.6$ (blue points), we observed a drop in the fitted β/T by nearly a factor of 4. Based on our physical intuition, we thought that this might be due to the reduction in density fluctuations as the gas becomes degenerate. The blue line in Figure 4.5 shows the density fluctuations $\langle \delta n^2(r) \rangle / \langle n(r) \rangle$ scaled by the MQDT value for b. However, later theoretical work found that the density fluctuations play a negligible role in the parameter regime of our experiment [168].

The data points in Figure 4.5 were obtained by fitting loss curves like the ones in Figure 4.4

to the solution of equation (4.10)[1],

$$n(t) = \frac{n_0 h T_0^{3/2}}{(T_0 + ht)(2n_0 T_0^2(\sqrt{T_0} - \sqrt{T_0 + ht})b + h(\sqrt{T_0 + ht} + 2bn_0 t T_0^{3/2}))}. \tag{4.11}$$

The average density n was approximated by fitting the entire cloud in TOF to a Gaussian and calculating n according to equation (4.9) using the expansion temperature T_{gauss} determined from the fit. For our experimental range of T/T_F, we checked numerically that this procedure reproduces n within a few percent of the exact value obtained by integrating the FD distribution (see also Ref. [176]). The temperature T_0 was set to the measured initial temperature of the gas using the FD fit. Note that with this definition, the drop in β/T is even more unexpected, since if β were to depend only on T_F and not T, as in the simple intuitive picture discussed previously, then β/T should diverge as $T \to 0$. We also tried setting T_0 to the expansion energy T_{gauss} of the cloud as a proxy for the energy density of the gas, but saw a similar trend (see Figure 3 of Ref. [168]).

The observation of suppressed losses in the degenerate regime has so far stimulated two related theory works [168, 169]. Ref. [168] found that interactions between molecules and collisional complexes could cause a similar trend to what we observed, although the required molecule–complex cross section is extremely large (even exceeding the s-wave unitary limit). Ref. [169] found new universal relations for gases with two-body losses by computing the contacts of the system, and found a deviation from $\beta \propto T$ behavior at low temperature. More investigation is needed to determine if this effect can explain our measurement. With the creation of a DFG of NaK molecules [53, 54], it will be interesting to see if a similar loss suppression at low T/T_F is observed in a different molecular system.

4.2.3 Density fluctuations

We also measured the density fluctuations of the molecular DFG in Ref. [51]. Owing to Fermi statistics, the density fluctuations become suppressed as the gas becomes degenerate. This

[1] Note that there is a small typo in the Supplementary Material of Ref. [50]. The last term in the denominator of the equation corresponding to (4.11) was missing a factor of t. The equation was correct in the code that we used to analyze the loss curves of the molecules in Ref. [50].

effect was previously studied experimentally in atomic Fermi gases [177, 167]. At high temperature ($T/T_F > 1$), the density fluctuations have a Poissonian distribution, with $\sigma_N^2/\overline{N} = 1$. Here, σ_N^2 and $\overline{N}$ are the variance and mean, respectively, of the molecule number within a certain probe volume. However, for a deeply-degenerate Fermi gas ($T/T_F \ll 1$), the density fluctuations are suppressed by the Pauli exclusion principle and $\sigma_N^2/\overline{N} = (3/2)(T/T_F)$.

More quantitatively, the ratio $\sigma_N^2/\overline{N}$ is given by [167]

$$\frac{\sigma_N^2}{\overline{N}} = \frac{\mathrm{Li}_{1/2}(-\zeta e^{-V(x,y,z)/k_BT})}{\mathrm{Li}_{3/2}(-\zeta e^{-V(x,y,z)/k_BT})}, \tag{4.12}$$

where $V(x, y, z)$ is the 3D harmonic trapping potential. Note that $\sigma_N^2/\overline{N}$ is a local quantity that depends on the position in the gas. Near the center of the gas, the local fugacity $\zeta e^{-V(x,y,z)/k_BT}$ is maximized, and the fluctuations are maximally suppressed. Near the edge of the cloud, the fluctuations approach shot noise, $\sigma_N^2/\overline{N} = 1$. After integrating through the imaging axis (in this case $\hat{\mathbf{y}}$), we obtain the column-integrated expression

$$\frac{\sigma_N^2}{\overline{N}} = \frac{\mathrm{Li}_1(-\zeta e^{-V(x,z)/k_BT})}{\mathrm{Li}_2(-\zeta e^{-V(x,z)/k_BT})}. \tag{4.13}$$

Since the trapping potential is harmonic, expansion for time t in TOF simply rescales the coordinates by $x_i \to x_i/\sqrt{1+\omega_i^2 t^2}$.

We measured density fluctuations in K, KRb*, and KRb gases. Measuring the fluctuations of non-degenerate and degenerate atomic K gases allowed us to benchmark our experimental procedure. Comparing degenerate KRb* and KRb gases revealed the effect of STIRAP, which produces a small number of holes in the KRb distribution owing to its non-unity efficiency.

The procedure for the fluctuation measurement on the molecules was very similar to that used in Ref. [177] on a ^{6}Li DFG. The measurement consisted of taking 50–60 absorption images of atomic or molecular clouds in TOF, prepared with the same sequence. Before imaging, the molecules were dissociated into K atoms by adiabatically ramping across the Feshbach resonance in reverse, in order to accurately determine the molecule number. Each image was subdivided into bins that formed detection sub-volumes. For a given bin i, the j-th image gave a measurement

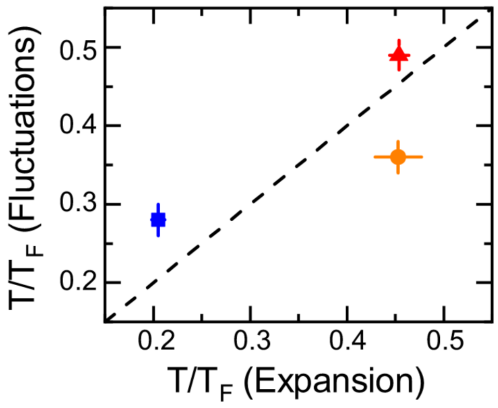

Figure 4.6: Comparison of T/T_F from fluctuations and TOF expansion. Measurements were performed on DFGs of K (blue square), KRb* (orange circle), and KRb (red triangle). The dashed line indicates equal T/T_F from the two methods. Reproduced from Ref. [51].

of the local particle number N_{ij} in that bin on the j-th realization of the gas. By looking at the distribution of N_{ij} over images j, we could obtain σ_N^2 and $\overline{N}$ for bin i. Fitting equation (4.13) over the bins gave a measurement of ζ, which we converted to T/T_F with equation (4.3).

The ratio $\sigma_N^2/\overline{N}$ is ideally unity for a non-degenerate gas, but in practice, it depends on a number of technical factors. The absolute atom or molecule number calibration from absorption imaging directly affects the measured $\sigma_N^2/\overline{N}$, so calibrating the effective absorption cross section and saturation intensity are crucial [165, 166]. The finite resolution of the imaging system can cause smearing of the signal over multiple bins, which reduces the observed fluctuations [177, 167]. Photon shot noise also adds additional fluctuations to the raw images that must be removed to determine the density fluctuations. These experimental details are discussed in detail in Will Tobias's thesis [107] (also see Christian Sanner's thesis [163]). See section 3.5 for details on the CCD calibration, which was needed to determine the photon shot noise contribution.

By measuring the density fluctuations for degenerate gases of K, KRb*, and KRb, we could compare the T/T_F measured from fluctuations and the value measured from FD fits to the cloud in TOF expansion (Figure 4.6). Overall, we obtained good agreement for the two methods for all species. We did observe a higher level of fluctuations for KRb than KRb*, consistent with increased number fluctuations from a non-unity STIRAP efficiency. At $T/T_F = 0.4$, the number of thermal

holes in an ideal Fermi gas is still significant, and we calculate that the lowest-energy state in the trap has an occupation fraction of 0.77. Therefore, fluctuations caused by non-unity STIRAP transfer (85% typical efficiency) do not greatly exceed the thermal fluctuations, and the STIRAP transfer brings the cloud slightly out of equilibrium. However, for lower T/T_F, thermal fluctuations are further suppressed and the relative contribution of STIRAP-induced holes could become very significant. See Ref. [107] or the Supplementary Material of Ref. [51] for more details.

4.3 Feshbach ramp thermalization

In the previous sections, we described our measurements on the KRb DFG. The measurements of the TOF distribution and fluctuations were consistent with a gas in thermal equilibrium. However, the dynamics of crossing the Feshbach resonance can be quite complicated, owing to the competition of strong elastic collisions and rapid three-body losses near resonance.

The K-Rb-KRb* mixture has been previously studied experimentally [178, 179]. Near the Feshbach resonance, the constituents of the loosely-bound Feshbach molecules are indistinguishable from the free atoms, leading to a fermionic suppression of inelastic collisions of KRb* with K and a bosonic enhancement of those with Rb [178]. To minimize inelastic Rb-KRb* losses, we used an initial Bose-Fermi mixture with $N_{\mathrm{K}} \gg N_{\mathrm{Rb}}$. The highest molecule number was produced when the remaining unpaired Rb was no longer condensed after molecule production. After forming molecules, the peak density of K was approximately 10 times larger than Rb, so thermalization of KRb* is expected to occur predominantly through collisions with K.

In this section, we describe measurements of the K-KRb* elastic collision cross section as a function of B near the Feshbach resonance. We also measured the dependence of the molecular T/T_F on the Feshbach ramp rate. We found that the molecular degeneracy saturated as a function of the Feshbach ramp rate, indicating that elastic collisions predominate over inelastic ones.

4.3.1 Collisional damping

To measure the elastic cross section, we studied the damping of KRb* center-of-mass oscillations in the ODT due to collisions with K. The damping rate is proportional to the elastic collision rate $\Gamma = \overline{n}\sigma v_{\mathrm{rel}}$, where $\overline{n} = (1/N_{\mathrm{K}} + 1/N_{\mathrm{KRb}^*}) \int n_{\mathrm{K}} n_{\mathrm{KRb}^*}\, d^3x$ is the overlap density of the two species, σ is the K–KRb* elastic collision cross section, and $v_{\mathrm{rel}} = \sqrt{(8k_B/\pi)(T_{\mathrm{K}}/m_{\mathrm{K}} + T_{\mathrm{KRb}^*}/m_{\mathrm{KRb}^*})}$ is the thermally-averaged relative velocity of the two species [180, 181, 182, 183].

We prepared a mixture of K and KRb* in the ODT with the following sequence. First, we created KRb in the ODT with the Feshbach ramp and STIRAP. The weak lattice is not used for this measurement. Next, pulses of resonant light were used to remove all of the Rb and most of the K. A second STIRAP pulse was used to transfer KRb back to KRb*, producing a mixture of $N_{\mathrm{KRb}^*} = 2 \times 10^4$ at $T_{\mathrm{KRb}^*} = 300$ nK and $N_{\mathrm{K}} = 1.5 \times 10^5$ at $T_{\mathrm{K}} = 600$ nK.

An initial center-of-mass oscillation in $\hat{\mathbf{y}}$ could be selectively excited on KRb* by changing the timing between the STIRAP pulses. As mentioned earlier, each STIRAP sequence imparts a momentum of $k_{\mathrm{STIRAP}} = 2\pi\,(1/\lambda_{\mathrm{up}} - 1/\lambda_{\mathrm{down}})$, where $\lambda_{\mathrm{up}} = 970$ nm and $\lambda_{\mathrm{down}} = 690$ nm are the wavelengths of the two STIRAP beams. The STIRAP beams propagate along $\hat{\mathbf{y}}$. By changing the timing of the two STIRAP pulses relative to the KRb vertical trap period $2\pi/\omega_y = 5.2$ ms, the momentum recoils from the pulses could be made to add up or cancel, giving control over the amplitude of the KRb* oscillation (Figure 4.7). For the oscillation damping measurement, we chose a delay between the STIRAP pulses such that the oscillation amplitude of KRb* was maximized.

After producing the K-KRb* mixture, we ramped B to a target value and measured the KRb* oscillations in $\hat{\mathbf{y}}$. RF spectroscopy on K was used to calibrate B. No oscillation of K was initially excited by the STIRAP pulses, and we did not observe any induced oscillation of K from collisions with KRb*. Example oscillations at $B = 546.1$ G are shown in Figure 4.8. Starting with no K (top panel, $\overline{n} = 0$), the oscillations become increasingly damped with increasing overlap density $\overline{n}$.

From the exponential damping time τ, we could extract the elastic collision cross section σ.

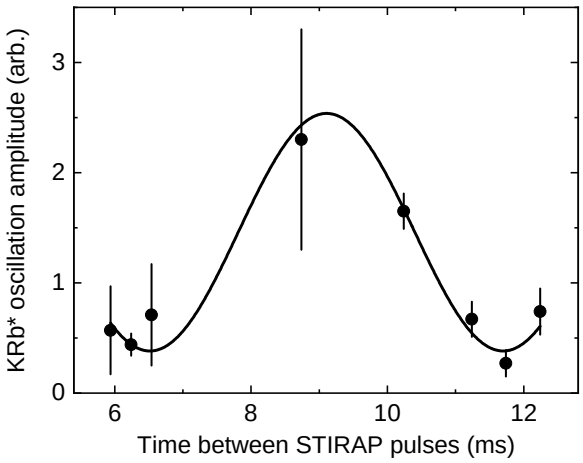

Figure 4.7: STIRAP-induced slosh of KRb*. The solid line is a fit to a sinusoid with the frequency fixed at 190 Hz (the measured $\omega_y/2\pi$ for KRb). Reproduced from Ref. [51].

The damping of the oscillations is described by the following coupled differential equations [183],

$$\ddot{y}_{\mathrm{K}} = -\omega_{\mathrm{K}}^2 y_{\mathrm{K}} - \frac{4}{3}\frac{m_{\mathrm{KRb}}}{M}\frac{N_{\mathrm{KRb}^*}}{N}\Gamma(\dot{y}_{\mathrm{K}} - \dot{y}_{\mathrm{KRb}^*}) \tag{4.14}$$

$$\ddot{y}_{\mathrm{KRb}^*} = -\omega_{\mathrm{KRb}^*}^2 y_{\mathrm{KRb}^*} + \frac{4}{3}\frac{m_{\mathrm{K}}}{M}\frac{N_{\mathrm{K}}}{N}\Gamma(\dot{y}_{\mathrm{K}} - \dot{y}_{\mathrm{KRb}^*}), \tag{4.15}$$

with $M = m_{\mathrm{K}}+m_{\mathrm{KRb}}$ and $N = N_{\mathrm{K}}+N_{\mathrm{KRb}^*}$. For the experimental number ratio ($N_{\mathrm{K}}/N_{\mathrm{KRb}^*} \approx 7.5$) and collision rate, and for initially stationary K, the motion of the two species is nearly uncoupled. Therefore, we approximated the dynamics by

$$\ddot{y}_{\mathrm{KRb}^*} = -\omega_{\mathrm{KRb}^*}^2 y_{\mathrm{KRb}^*} - \frac{4}{3}\frac{m_{\mathrm{K}}}{M}\frac{N_{\mathrm{K}}}{N}\Gamma\dot{y}_{\mathrm{KRb}^*}, \tag{4.16}$$

which gives a damping time τ of

$$\frac{1}{\tau} = \frac{2}{3}\frac{m_{\mathrm{K}}}{M}\frac{N_{\mathrm{K}}}{N}\Gamma. \tag{4.17}$$

We corrected the experimentally measured damping time τ_{exp} to remove the small background damping τ_0 observed at $\overline{n} = 0$, according to $1/\tau = 1/\tau_{\mathrm{exp}} + 1/\tau_0$. From τ, we could extract σ and the s-wave K–KRb* scattering length a_{ad}, using $\sigma = 4\pi a_{\mathrm{ad}}^2/(1 + k_{\mathrm{th}}^2 a_{\mathrm{ad}}^2)$, where $k_{\mathrm{th}} = \sqrt{2\mu k_B T/\hbar^2}$ is the thermal collision wavevector and μ is the K–KRb* reduced mass [22]. A universal prediction gives $a_{\mathrm{ad}} = 1.09a$ for the mass ratio $m_{\mathrm{K}}/m_{\mathrm{Rb}} = 0.46$ of our system, where a is the K–Rb scattering length [184].

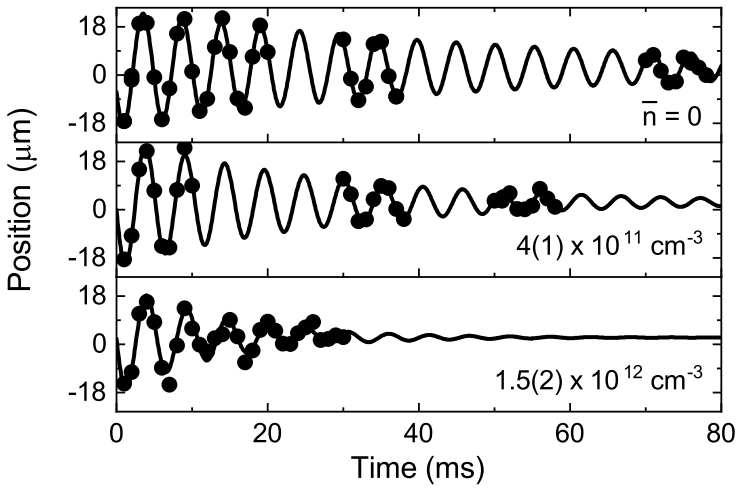

Figure 4.8: Collisional damping from K-KRb* elastic collisions at $B = 546.1$ G, varying the overlap density $\overline{n}$. The K-KRb* scattering lengths $|a_{\rm ad}| = 684(110)a_0$ and $648(88)a_0$ extracted from the middle and bottom panels, respectively, are in good agreement. Reproduced from Ref. [51].

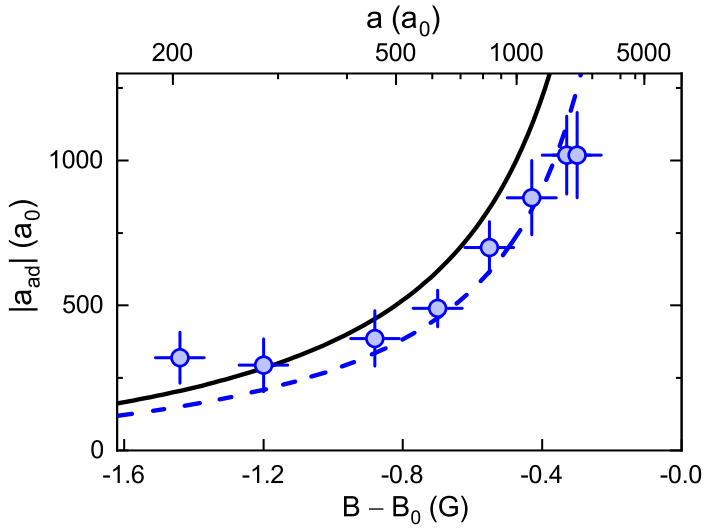

Figure 4.9: Summary of K-KRb* elastic collisions extracted from collisional damping measurements. Reproduced from Ref. [51].

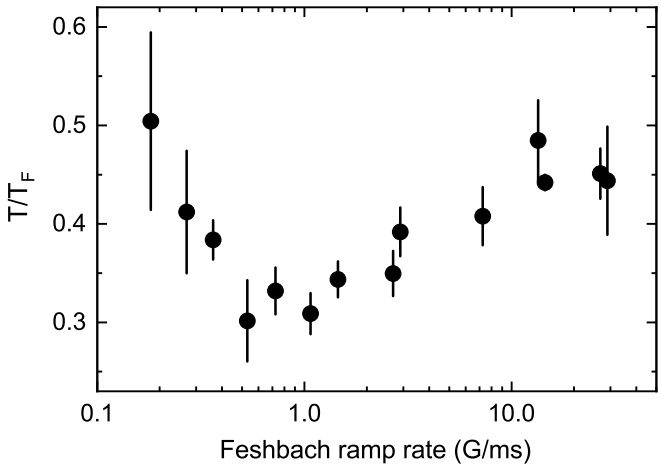

Figure 4.10: KRb T/T_F versus Feshbach ramp rate. Reproduced from Ref. [51].

By measuring the damping rate as a function of B, we obtained a measurement of $|a_{\mathrm{ad}}|$ vs B (Figure 4.9). The dashed line is a fit $|a_{\mathrm{ad}}| = ca$ to a single parameter c, which describes a scaling between a_{ad} and the K–Rb scattering length a. The best fit gave $c = 0.74(5)$. We do not necessarily expect that the universal prediction $a_{\mathrm{ad}} = 1.09a$ holds for the regime of our experiment, owing to the high collision energy and relatively low scattering lengths studied here. Nonetheless, we measured a large K-KRb* elastic cross section near resonance. From the measured K-KRb* elastic cross section, we estimated that about 6 elastic collisions occur during the Feshbach ramp, facilitating thermalization. More details on this calculation can be found in the Supplementary Material of Ref. [51].

4.3.2 Dependence on the Feshbach ramp rate

Varying the Feshbach ramp rate provides an additional method for studying the competition between elastic and inelastic processes [14]. For a very low ramp rate, the inelastic collisions near the Feshbach resonance will result in significant molecule loss; conversely, for a very high ramp rate, the gas may not have enough time to thermalize. We measured this experimentally by monitoring the T/T_F of the KRb gas a function of the Feshbach ramp rate (Figure 4.10). For intermediate ramp rates of 0.5–3 G/ms, the T/T_F reaches a minimum at 0.3. For very slow ramp rates (< 0.5

G/ms), inelastic losses near the Feshbach resonance reduce the molecule number resulting in a sharp increase in T/T_F. We also observe a gradual rise in the T/T_F as the ramp time becomes shorter than the trap oscillation period, while the molecule number remains constant, suggesting that thermalization is hindered for fast ramp speeds.

4.4 Conclusion

In this chapter, we presented experiments on a DFG of molecules. We characterized the degeneracy of the gas both through the momentum distribution in TOF expansion and by measuring the suppression of density fluctuations owing to Fermi statistics. The chemical reaction rate in the gas also became suppressed for $T/T_F < 0.6$, a phenomenon that is still not fully understood. Finally, we discussed measurements of the K-KRb* elastic collision cross section and the dependence of the KRb T/T_F on the Feshbach ramp rate, which allowed us to characterize the thermalization processes during molecule production.

The capability to make a molecular DFG directly at the molecule association stage opens new paths in molecular quantum science. However, an important ingredient that was still missing at the time of Refs. [50, 51] was the ability to turn on elastic dipolar collisions between ground-state KRb while suppressing reactive losses. In the next chapters, we describe two general techniques for doing so.

Chapter 5

Dipolar evaporation of molecules in 2D

In the previous chapter, we produced a degenerate Fermi gas of molecules from two deeply degenerate atomic clouds. However, these initial experiments were ultimately limited by our inability to observe elastic interactions between ground state molecules in the 3D gas. In the absence of an external electric field $\mathbf{E}$, the primary interactions between spin-polarized KRb are p-wave collisions, which are expected to be weak [82]. The rapid dipolar loss in 3D [79] prevented us from ramping up a strong electric field and studying elastic dipolar collisions in the Fermi gas.

As a result, we decided to go to quasi-2D, where previous KRb experiments had demonstrated a reduction of loss at moderate $|\mathbf{E}|$ [102]. As discussed in section 2.5.2, reactive losses are suppressed in 2D thanks to the enhanced barrier from dipolar repulsion in the $m_L = \pm 1$ collisions [99, 100, 101]. We thought we could go beyond Ref. [102] in several areas: we could access higher $|\mathbf{E}|$ to make a more complete map of the loss as a function of d, and with more control over spurious field gradients; we could try to measure the elastic dipolar collisions directly, which had not been previously observed in ultracold molecules; and we could improve the initial PSD of the molecular gas and achieve a high enough density to see evaporative cooling.

More generally, dipolar interactions lead to intriguing phenomena in 2D. The interplay of the $1/r^3$ power law of the interaction with the dimensionality leads to the possibility of true long range order in 2D, in contrast to the usual BKT transition for short-range interactions [185]. In addition, the combination of strong external confinement and the dipolar anisotropy enables control of the system via the orientation of the dipoles (set by $\mathbf{E}$). For example, if $\mathbf{E}$ is oriented perpendicular

to the 2D plane, then all pairs of molecules have the same sign of interaction. But if **E** is rotated into the 2D plane, then molecules experience both attractive and repulsive interactions. This can have a strong effect on the collisions of the molecules (Chapter 6), as well as on the collective spin dynamics when the molecules are driven by a microwave field (Chapter 8).

A high PSD in 2D is necessary for many of these explorations, so trying to demonstrate efficient evaporation of molecules in 2D is a natural first step. Luckily, 2D is not only favorable from a collisional perspective, but also from the basic kinematics of the gas. As described in section 4.2.2, p-wave losses in 3D lead to anti-evaporation, where the coldest and densest portion of the cloud experiences the fastest loss [79]. This effect arises from the competition of the p-wave threshold law ($\beta \propto$ collision energy) with the 3D density distribution in a harmonic trap and results in detrimental heating of the gas. In 2D, the density of states is lower and as a result, theory predicts that there should be no anti-evaporation in 2D for p-wave interactions [186].[1]

This chapter is based on the work in Ref. [52]. First, we describe some technical aspects of preparing a 2D sample of molecules. We next present measurements of the suppressed loss rate and enhanced elastic collision rate that arises from the repulsive dipolar collisions in 2D. The long lifetime of the molecules and strong elastic collisions facilitate direct evaporation of the molecules to as low as $T/T_F = 0.6$, realizing a long-lived and strongly dipolar 2D molecular quantum gas.

5.1 Producing a 2D sample

The experiments in this chapter are performed in the quasi-2D regime. A quasi-2D Fermi gas satisfies $E_F, k_B T \ll \hbar\omega_y$, where ω_y is the vertical trap frequency and $E_F = \hbar\omega_r\sqrt{2N}$, with ω_r the geometric mean trap frequency in the transverse direction. This condition means that the motional energy scales are lower than the harmonic oscillator spacing in $\hat{\mathbf{y}}$, so the particles populate only the lowest oscillator level in the $\hat{\mathbf{y}}$ direction while having a thermal distribution in the radial direction. If the confining potential is a deep optical lattice, then this is equivalent to requiring

[1] This also implies that in a 1D system, or a homogeneous (box) trap, losses can reduce the average kinetic energy of the gas.

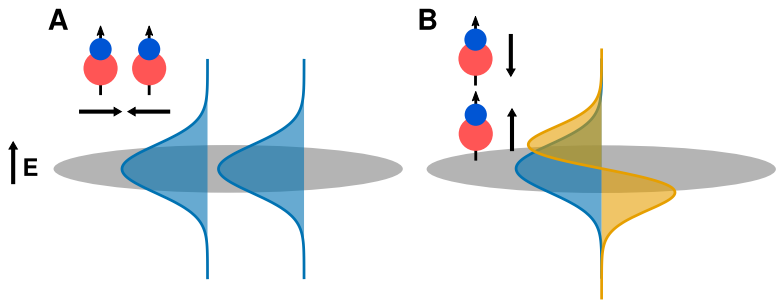

Figure 5.1: Cartoon of intra- (A) vs inter-band (B) collisions. (A) Two molecules in the lowest band collide with $m_L = \pm 1$ due to the strong vertical confinement. (B) A molecule in the lowest band and another in the first excited band can collide with $m_L = 0$. The $m_L = 0$ collisions have a reduced barrier and thus dominate the loss between molecules in different bands.

that the particles occupy only the lowest band.[2]

The 2D dipolar loss suppression relies directly on the quasi-2D nature of the gas. Two molecules in the ground band collide with $m_L = \pm 1$, and enjoy an enhanced barrier to reacting at short range owing to the dipolar repulsion. On the other hand, collisions between molecules in the ground band and first excited band can have $m_L = 0$, and thus have an increased loss rate due to dipolar attraction. This can be seen intuitively by considering the wavefunctions along the y-direction in the harmonic oscillator approximation, as shown in Figure 5.1. More rigorously, this comes from the symmetry requirement that the total wavefunction of a colliding pair of identical fermions must be anti-symmetrized. For collisions with $m_L = 0$, the relative wavefunction is symmetric in the in-plane coordinates, so the molecules must be antisymmetric in their oscillator states in $\hat{\mathbf{y}}$, which is not possible if the molecules are both in the ground band [100, 102]. This can also be seen from the adiabatic energy curves in 2D (see Figure 2.11 or the aforementioned references).

In our experiment, the strong confinement into 2D is created by a 1D optical lattice (Figure 5.2) formed by two $\lambda = 1064$ nm beams (green beams in Figure 5.2) propagating with an angle of 11° from the $\pm\hat{\mathbf{y}}$ axis. At the crossing point, this creates a lattice with spacing $a_{\text{latt}} = 540$ nm

[2] In the context of dipolar interactions, quasi-2D can have another meaning: $a_D < a_{\text{ho}}$, so the collisions "look 3D" (see section 2.5.2.1). In this chapter, we achieved a maximum dipole of $d = 0.3$ D, corresponding to $a_D = 1610a_0$. The harmonic length was $a_{\text{ho}} = \sqrt{\hbar/\mu\omega_y} = 1830a_0$, so our experiments were also quasi-2D with respect to the dipolar collisions.

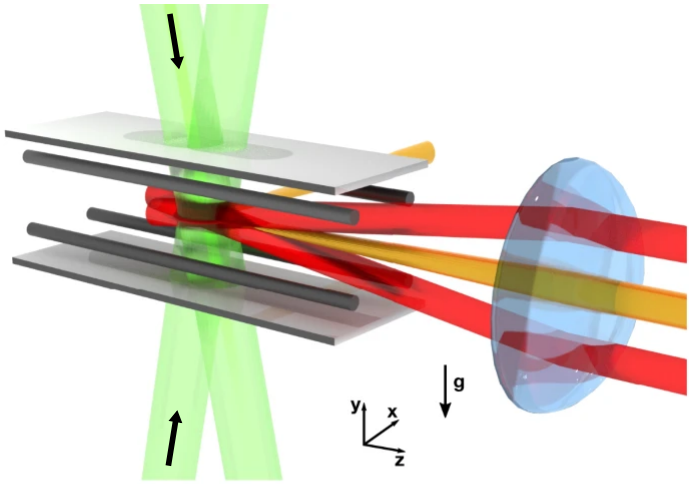

Figure 5.2: Optical trap geometry for 2D work. The atoms are initially trapped in the ODT (orange), then loaded into a single layer of the LSL (red) to squeeze the distribution in the y-direction, and finally loaded into the science lattice (green), which confines the atom into 2D planes with a lattice spacing of 540 nm. Adapted from Ref. [52].

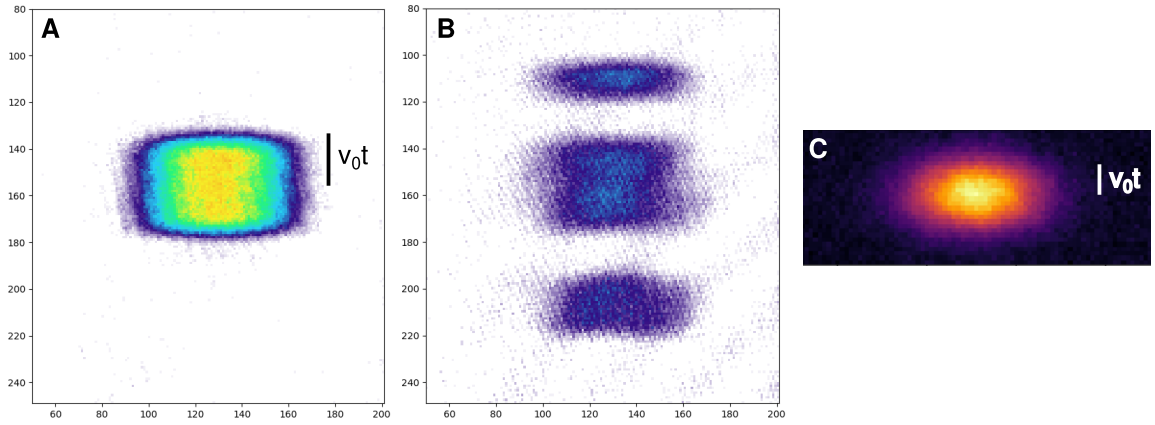

Figure 5.3: Band mapping K and KRb. (A) Image of a K DFG after band mapping from the VL. The width $v_0 t$ of the Brillouin zone after time of flight t is shown for scale, where $v_0 = \hbar(\pi/a_{\text{latt}})/m$ is the velocity at the edge of the Brillouin zone. (B) Band-mapped image of a K DFG after parametric heating. Population is clearly visible in the 2nd excited band. The vertical scales in (A) and (B) are the same. (C) A 2D gas of KRb after band mapping from the VL. The image is the average of 9 measurements. Note that the vertical scale of (C) is not the same as (A) and (B).

that we call the vertical lattice (VL). The beams are angled from the vertical to avoid spurious superlattices formed by reflections off the ITO plates, and are round with waists of 125 μm. We typically operate around $\omega_y/2\pi = 17$ kHz, so $\hbar\omega_y/k_B = 800$ nK, which is larger than the typical temperature of $T = 250$ nK. The lattice frequency ω_y is directly measured using parametric heating of the molecules [187]. To characterize the band populations in the VL, we use the standard technique of band mapping [188, 187]. This is done by ramping down the VL power over $\sim 500\,\mu$s, which shuts off the lattice adiabatically with respect to the band spacing. As a result, the band populations of the atoms or molecules are directly visible after time-of-flight, as shown in Figure 5.3.

To produce molecules in 2D, we first load the atomic mixture from the ODT (orange beams in Figure 5.2) into the large spacing lattice (LSL, red beams). The LSL beams form a lattice along $\hat{\mathbf{y}}$ with 8 μm spacing, which compresses the cloud to improve mode-matching with the VL. Finally, the atoms are loaded into the VL, and molecules are produced with the Feshbach field sweep and STIRAP. In principle, we could have produced molecules in 3D before loading into the lattice, but the molecular losses and lack of thermalizing collisions at $|\mathbf{E}| = 0$ make the timescales challenging.

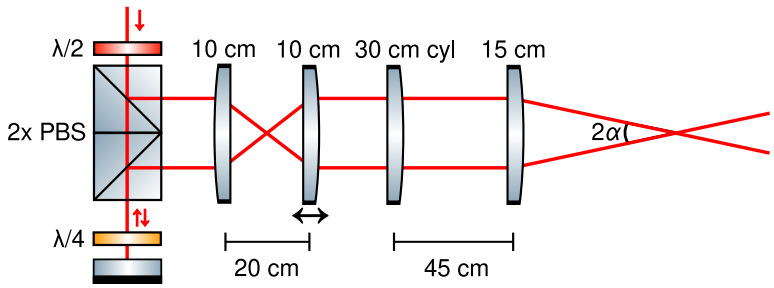

Figure 5.4: LSL optics setup. All of the lenses are achromatic doublets, except the 30 cm cylindrical lens. This diagram is simplified to show the most important optics; the full beam path is shown in Figure 3.5.

Additionally, the initial opening of the band gap when loading the lattice is less favorable for the molecules than the atoms. The initial size of the band gap is given by the photon recoil energy $E_R = \hbar^2 k_{\text{latt}}^2/2m$, where $k_{\text{latt}} = 2\pi/\lambda$. At $\lambda = 1064$ nm, the recoil energies are $E_R^{\text{K}} = 210$ nK and $E_R^{\text{KRb}} = 67$ nK for K and KRb, respectively. Only particles with energy less than E_R can be loaded into the ground band, which imposes a stringent requirement that $T, T_F < E_R/k_B$. Since $E_R^{\text{KRb}} < E_R^{\text{K}}$, this makes it significantly harder to load the molecules directly into the VL [187].

In the following sections, we describe the effect of the LSL on the VL loading, the measurement of the VL layer populations, and the detailed 2D loading procedure.

5.1.1 Large spacing lattice

The LSL is formed by two beams that cross at a shallow half-angle of $\alpha = 4°$, which produces a lattice with $\lambda/(2\sin\alpha) = 8\,\mu$m spacing. The optical setup is shown in Figure 5.4 and is based on the accordion lattice design used in Ref. [189]. The two LSL beams are split from a single input beam using a pair of polarizing beam splitter (PBS) cubes.[3] After the cubes, all optics are common between the two beams. Next, the beams go through a 1-to-1 telescope. The second lens of the telescope is mounted on a micrometer stage, which we adjust to set the crossing point of the beams on the atoms in the z-direction. To avoid compressing the cloud unnecessarily along the horizontal direction, the beams are elliptical at the position of the atoms, with a 50 μm waist in the vertical (y-direction) and 330 μm waist in the horizontal (x-direction). The beam shaping is

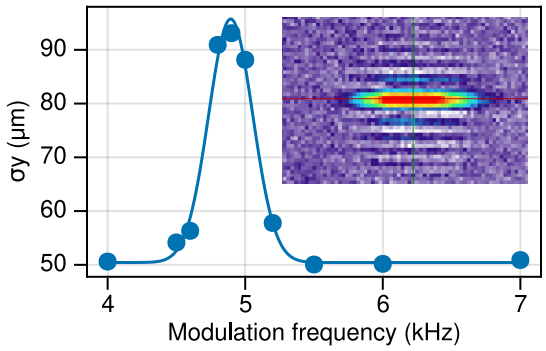

Figure 5.5: Parametric heating in the LSL. The vertical size after TOF of a single LSL layer of Rb is plotted as a function of the modulation frequency of the LSL. Inset: a single layer of KRb in the LSL, imaged in situ.

done with the 30 cm cylindrical lens in Figure 5.4, which is oriented horizontally and positioned about 45 cm away from the final focusing 15 cm (spherical) lens. As a result, the beam is roughly collimated in the horizontal direction after the final lens, but focusing in the vertical direction.

We found that the passive phase stability of the system was good enough that we only needed to optimize the LSL loading one or twice a day. At first, we used a thin piece of glass on one of the two beams before the final lens to adjust the relative phase of the beams (and hence the position of the fringes on the atoms). We eventually found that the step size on our Newport picomotor mirrors was fine enough to optimize the loading using the overall pointing of the two beams, and we removed the glass plate.

We characterized the LSL trap frequency using parametric heating. Figure 5.5 shows the vertical size σ_y of Rb in TOF as a function of the intensity modulation frequency. Rb was initially loaded into a single LSL layer for this measurement. The fitted peak is 2.4 kHz, slightly lower than the calculated value of 2.8 kHz based on the measured beam sizes and powers. For calibration purposes, this measurement was done at a higher LSL trap depth than that used for the molecule experiments. The inset shows a single layer of molecules in the LSL, imaged in situ in the LSL +

[3] We originally tried to use a Wollaston polarizer to create the two LSL beams, following the scheme of Ref. [190]. However, we found that getting the beams to the desired aspect ratio was more challenging with the Wollaston setup than the PBS setup.

VL. To ensure that molecules were produced in a single LSL layer, we also used expansion from the LSL in TOF with matter-wave imaging (see section 5.1.2.1 and Figure 5.8).

Loading the VL directly from the ODT subdivides the cloud into many layers, drastically reducing the PSD in each layer. The LSL spacing is large enough that cloud in the ODT can be loaded into a single LSL layer, which allows us to compress the cloud along $\hat{\mathbf{y}}$ before loading into the VL. Since Rb cloud is much smaller than the K DFG, we can estimate the extent of the molecules by calculating the size of the Rb cloud before loading the lattice. The density distribution of a thermal gas in a harmonic trap is

$$n_{\text{thermal}}(x,y,z) = \frac{N}{(2\pi)^{3/2}\sigma_x\sigma_y\sigma_z}\exp\left[-\frac{x^2}{2\sigma_x^2}-\frac{y^2}{2\sigma_y^2}-\frac{z^2}{2\sigma_z^2}\right], \tag{5.1}$$

where $\sigma_i = \sqrt{k_B T/m\omega_i^2}$. The density distribution for a BEC is

$$n_{\text{BEC}}(x,y,z) = \frac{\mu}{g}\left(1-\frac{x^2}{R_x^2}-\frac{y^2}{R_y^2}-\frac{z^2}{R_z^2}\right), \tag{5.2}$$

where $R_i = \sqrt{2\mu/m\omega_i^2}$ is the Thomas-Fermi radius, $\mu = (\hbar\omega_{\text{ho}}/2)(15Na/a_{\text{ho}})^{2/5}$ is the chemical potential, and $g = 4\pi\hbar^2 a/m$ is the interaction coupling constant. Here $a \approx 100a_0$ is the Rb s-wave scattering length, $\omega_{\text{ho}} = (\omega_x\omega_y\omega_z)^{1/3}$ is the geometric mean trap frequency, and a_{ho} is the oscillator length associated with ω_{ho} [10].

Our typical starting conditions in the ODT were around 1.2×10^5 Rb at $T = 90$ nK with 30% BEC fraction. The ODT trap frequencies are $(\omega_x,\omega_y,\omega_z) = 2\pi\times(40,180,40)$ Hz. Figure 5.6 shows the calculated density distribution along $\hat{\mathbf{y}}$ after integrating in the x- and z-directions (blue line), which can be compared to a_{latt} (green line). This shows that Rb is spread into many layers when loading directly from the ODT. In contrast, using the LSL with a weaker ODT creates a combined trap with $(\omega_x,\omega_y,\omega_z) = 2\pi\times(25,600,25)$ Hz. Typical conditions in the LSL were 9×10^4 Rb at $T = 110$ nK with 30% BEC fraction loaded into a single LSL layer. The distribution in the LSL (orange line) is much narrower than in the ODT, allowing us to squeeze the atoms into fewer layers.

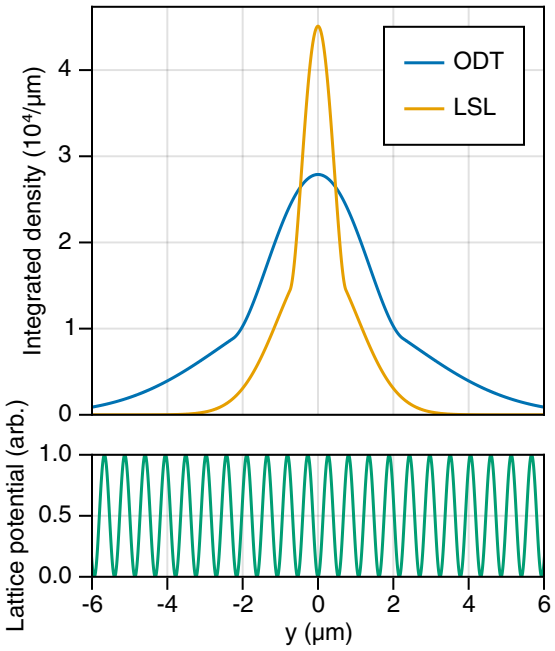

Figure 5.6: Rb density distribution in the ODT (blue) and LSL (orange), compared with the VL spacing (green). Loading the lattice from the LSL subdivides the cloud into fewer lattice sites than loading from the ODT. The plotted density profiles (along $\hat{\mathbf{y}}$) are obtained by integrating the calculated 3D density in the two transverse directions ($\hat{\mathbf{x}}$ and $\hat{\mathbf{z}}$). The Rb number, temperature, and trap frequencies for the calculation are given in the text.

5.1.1.1 Limits of 2D in the LSL

We briefly considered trying to make a 2D sample of molecules in the LSL without using the science lattice. This would be technically challenging, since it would require us to increase the LSL power significantly if we wanted to reach the same ω_y as the VL, though it would allow us to start with all of the molecules contained in a single site. However, we quickly realized that there is a more fundamental problem with this approach. Namely, the quasi-2D requirement imposes a maximum particle number for the Fermi gas,

$$E_F = \hbar\omega_r\sqrt{2N_{\max}} < \hbar\omega_y \implies N_{\max} < \frac{1}{2}\left(\frac{\omega_y}{\omega_r}\right)^2, \tag{5.3}$$

where ω_r is the transverse trapping frequency. This imposes a limitation on the maximum particle number based solely on the geometry of the lattice beams. Plugging in the numbers for our LSL,

we find that this would limit us to $N_{\max} \sim 10^4$ particles per layer. In our current scheme of loading the atoms into 2D first, then making molecules, this would severely limit the initial K number. Considering the low conversion efficiency of K to KRb, this is an especially harsh limitation. Other 2D Fermi gas experiments tend to use a smaller spacing lattice to increase ω_y/ω_r and $N_{\max}$ [191], but we are already using close to our maximum numerical aperture (NA) on the LSL path. As a result, using the LSL as the only source of 2D confinement was not a viable strategy.

5.1.2 Layer counting

The LSL helps to compress the atoms into only a few layers of the VL, at the cost of making it harder to measure the population distribution in the VL layers. At $a_{\text{latt}} = 540$ nm, the VL layers are too closely spaced to optically resolve. Even the vertical width of the cloud in the LSL + VL is below our imaging resolution of $\sim 2\,\mu$m, which means we cannot infer the VL layer populations from the density profile of the cloud in situ. As a result, imaging in situ does not provide much quantitative information, and we instead measure the molecules in TOF after band mapping to accurately determine the total molecule number N and temperature T.

The molecule signal in TOF is a sum over several unequally populated layers, and we need to account for this to quantitatively understand our measured loss and thermalization rates, as well as the fitted T/T_F of the cloud. To do so, we introduce an effective number of layers τ, which we divide the total number N by to estimate the average density in each layer. The precise definition of τ depends on the physical quantity we are measuring, and its value is calculated from our measurement of the Rb layer distribution in the VL (described in the next section).

5.1.2.1 Matter-wave focusing

For the work in this chapter, we were not yet able to spectroscopically address individual layers of the science lattice (as in Chapter 7). To measure the layer populations, we instead used a matter-wave focusing technique to magnify the in situ density distribution in TOF [192, 193]. Specifically, we shut off the science lattice diabatically but leave the ODT on for an additional

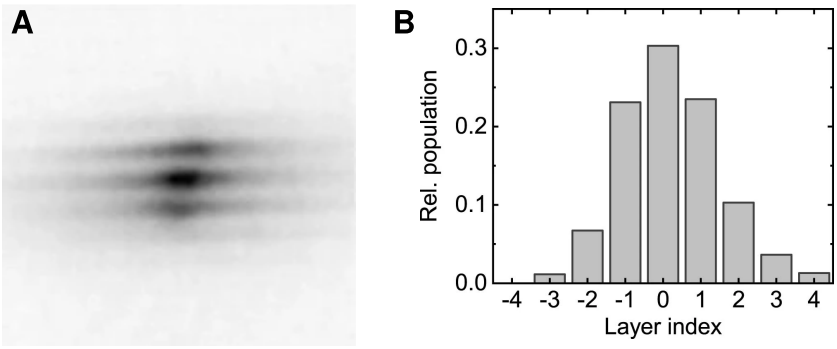

Figure 5.7: Rb layer distribution from matter-wave imaging. (A) Averaged image of 20 measurements of the Rb layer distribution in the VL using matter-wave magnification. (B) Extracted layer distribution for the data in (A). Adapted from Ref. [52].

time $T_{\mathrm{ho}}/4$, where T_{ho} is the trapping period of the ODT in the y-direction. As the atoms evolve in the harmonic potential of the ODT, their distribution in phase space rotates. At $T_{\mathrm{ho}}/4$, the initial position distribution along $\hat{\mathbf{y}}$ is mapped onto the momentum distribution. At this point, we turn off the ODT and let the atoms expand in time-of-flight, which magnifies the in-situ atomic distribution.

Our measurement of the Rb layer distribution is shown in Figure 5.7A. Since the molecules are created within the confines of the Rb distribution, we estimate the final KRb distribution from that of Rb (though the precise distribution of molecules may be slightly different owing to the complicated interplay of loss and molecule formation when crossing the Feshbach resonance). These data were taken with the same number and temperature of Rb as in the molecule experiments.

The layer measurement on Rb involved a few technical challenges. We found that the K–Rb interactions during the phase space rotation caused a significant reduction in the layer contrast, so we removed K for the measurement in Figure 5.7. We checked this explanation by repeating the measurement with the K-Rb mixture at the zero-crossing of the Feshbach resonance, and found that the layer contrast was restored. In addition, the center position of the fringes was not stable shot-to-shot. Since the VL is formed by two separate beams, its phase can drift if the relative phase of the two beams is not actively stabilized (see Ref. [107]). The VL phase was not stabilized for these measurements, and along with small pointing fluctuations of the ODTs, this made the center

of the layers move from shot to shot. As a result, we had to align the images manually by shifting the fringes into alignment. Figure 5.7B shows the extracted layer distribution from the data in (A), obtained by integrating the image in the transverse direction and fitting the resulting 1D profile with a sum of Gaussians with centers displaced by the layer spacing.

5.1.2.2 Determining τ

We would like to estimate several physical quantities, such as the Fermi temperature T_F or two-body loss rate coefficient β, averaged over the layer distribution in Figure 5.7. In TOF, we measure the total molecule number $N = \sum_i N_i$, where N_i is the number in the ith layer, and temperature T. We therefore need to find an effective number of layers τ such that substituting N/τ in our formulas gives the layer-averaged quantity of interest. This explanation is still somewhat nebulous but will hopefully be made clearer by the examples below.

For a fixed molecule distribution, the definition of τ depends on the physical quantity being measured. This is because some of these quantities depend non-linearly on the number in each layer. A simple (linear) quantity of interest is the average number of molecules per layer $\langle N_i \rangle$, where the brackets $\langle \cdot \rangle$ denotes the average with respect to the layer distribution. Using $\tau = N/\langle N_i \rangle$, we obtain $\tau = 4.6(2)$ for the data in the Figure 5.7B.

We also want to measure the layer-averaged Fermi temperature, which is nonlinear in N. Consider the 2D Fermi temperature in the ith layer,

$$T_{F,i} = \frac{\hbar\overline{\omega}}{k_B}\sqrt{2N_i}, \tag{5.4}$$

where $\overline{\omega} = \sqrt{\omega_x \omega_z}$ is the geometric mean trapping frequency. The layer-averaged quantity is $\langle T_{F,i} \rangle = (\hbar\overline{\omega}/k_B)\langle\sqrt{2N_i}\rangle$. By equating $\langle T_{F,i} \rangle$ with the expression for T_F in a single layer but with a reduced number N/τ, $T_F = (\hbar\overline{\omega}/k_B)\sqrt{2N/\tau}$, we obtain $\tau = N/\langle\sqrt{N_i}\rangle^2$. Thus, by using a different definition of τ, we can absorb the nonlinear dependence on N_i into the effective layer number τ.

Extracting $\tau = N/\langle\sqrt{N_i}\rangle^2$ from the data in Figure 5.7B, we find $\tau = 4.9(2)$. Note that the two estimates $N/\langle N_i \rangle$ and $N/\langle\sqrt{N_i}\rangle^2$ give similar values since the layer distribution in the LSL

+ VL is fairly narrow. We used $\tau = 5(1)$ to calculate the molecule T_F in Ref. [52], where the added uncertainty accounts for systematic errors from the non-uniform conversion of Rb to KRb and differences in the evaporation efficiency between the layers.

We also measured the loss rate coefficient β to observe the 2D dipolar loss suppression. In the layered system, the two-body loss is described by the following differential equation,

$$\frac{dn_i}{dt} = -\beta n_i^2, \tag{5.5}$$

with the solution

$$n_i(t) = \frac{n_i(0)}{1 + \beta n_i(0) t}, \tag{5.6}$$

where $n_i(t)$ is the average density in the ith layer. We do not have direct access to the individual layer densities $n_i(t)$, but we can extract $n(t) = \sum_i n_i(t)$ by measuring the total number N and T. We would like to find an effective number of layers τ such that we can fit $n(t)/\tau$ to a layer-averaged two-body loss equation,

$$\frac{d(n/\tau)}{dt} \approx -\beta (n/\tau)^2, \tag{5.7}$$

to accurately extract β.

To determine τ for the loss measurement, we numerically simulated the decay over time of the non-uniform molecule distribution from Figure 5.7B, and compared it to the decay of a gas with a uniform layer distribution and the same N and T. We defined τ as the number of layers of the uniform distribution for which the loss rate matched that of the non-uniform distribution. Owing to the nonlinear nature of the decay in time, this definition of τ also depends on the total measurement time. We modeled the system using the theoretically expected β over our typical measurement time of several seconds, and found $\tau = 8(1)$ for the layer distribution in Figure 5.7B.

5.1.3 Loading procedure

We started with the atomic mixture in the ODT at a magnetic field of 555 G, with trap frequencies of $(\omega_x, \omega_y, \omega_z) = 2\pi \times (40, 180, 40)$ Hz for Rb. The atoms were next loaded into the

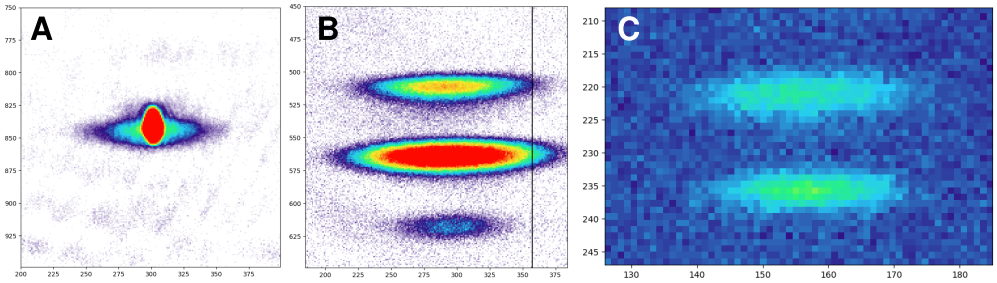

Figure 5.8: Matter-wave magnification of (A) Rb, (B) K, and (C) KRb clouds released from the LSL. All of the Rb is loaded into a single layer, and K is loaded primarily into the central layer. The KRb image in (C) was taken with the LSL intentionally misaligned to show two clear layers of molecules. Note that the region size and color scale are different for all three images.

LSL, with Rb occupying only a single LSL layer, and the ODT was decompressed to reach trap frequencies of $(\omega_x, \omega_y, \omega_z) = 2\pi \times (25, 600, 25)$ for Rb in the combined trap. Finally, the atoms were loaded into the VL and the ODTs were adjusted to reach transverse trap frequencies of $(\omega_x, \omega_z) = 2\pi \times 40$ Hz for KRb. Molecules were then created with the Feshbach field ramp and STIRAP. To ensure that the molecules were created in a single LSL layer, we used the same matter-wave focusing technique discussed in the previous section, but with the LSL playing the role of the VL. This generates images similar to those in Figure 5.8.

In optimizing the loading sequence, we learned that it was important to keep the LSL on after loading the VL to prevent the atoms from tunneling. If the atoms are allowed to tunnel, the number of layers of the molecules will increase. The tunneling element J is approximately given by

$$J/E_R = 1.39666 s^{1.051} e^{-2.12104\sqrt{s}}, \tag{5.8}$$

where s is the lattice depth in units of E_R [194]. At our typical VL depth ($\omega_y = 2\pi \times 17$ kHz for KRb), we calculate $(J_{\mathrm{K}}, J_{\mathrm{Rb}}, J_{\mathrm{KRb}}) = h \times (220, 13, 0.2)$ Hz. Owing to its small mass, K is particularly likely to tunnel. The site-to-site energy shift in the VL from gravity ($h \times 530$ Hz for K) was not enough to fully shut off the tunneling. Keeping the LSL on provided an additional site-to-site shift that completely suppressed the tunneling of the atoms. The LSL was then ramped off after making molecules.

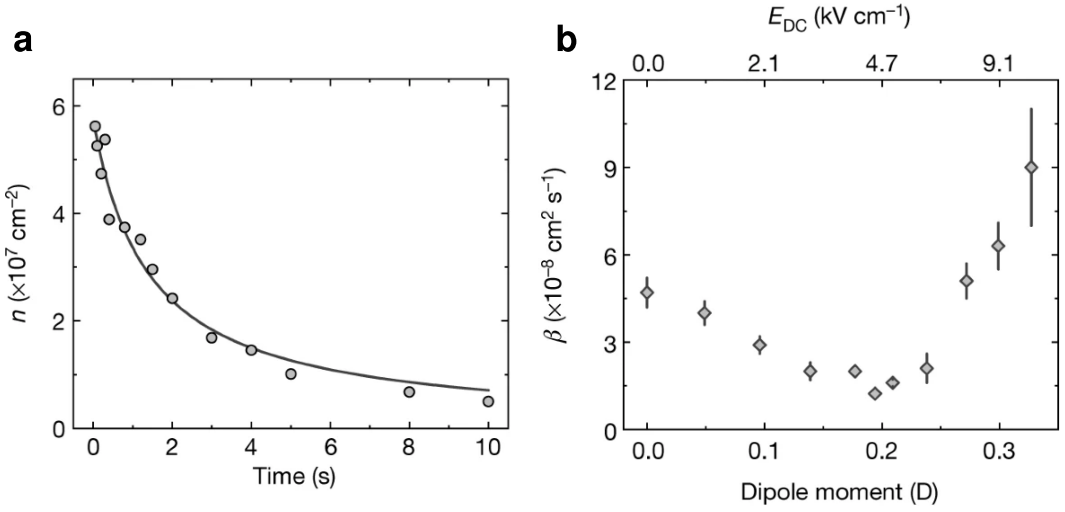

Figure 5.9: Dipolar suppression of loss in 2D. (A) Loss measurement of molecules in quasi-2D at $d = 0.2$ D. The data is fit to equation (5.7) to extract the two-body loss rate coefficient β. (B) Summary of β vs d. Reproduced from Ref. [52].

5.2 Loss suppression

Having produced a 2D molecular gas, we next studied the dipolar loss suppression by measuring the molecular loss rate as a function of $|\mathbf{E}|$. The typical starting conditions for these measurements were $N = 20 \times 10^3$ at $T = 250$ nK, with $\tau = 5$ and $T/T_F = 1.5$. The trap frequencies were $(\omega_x, \omega_y, \omega_z) = 2\pi \times (40, 17 \times 10^3, 40)$ Hz for KRb.

Before measuring the loss rates, we needed to cancel uncompensated electric field gradients, particularly in the loosely trapped x-direction. Strong gradients cause additional one-body loss that could cause us to overestimate the loss rate coefficient β. To fix the gradients, we started by centering the molecules geometrically in the electrodes (discussed in detail in Will Tobias's thesis [107]). Next, we shimmed the horizontal gradient $\partial|\mathbf{E}|/\partial x$ at each field configuration to maximize the molecule number left after a set hold time (typically 100 ms).

After doing this, we were able to observe the 2D dipolar suppression. An example loss measurement at $d = 0.2$ D is shown in Figure 5.9A. Stabilized by repulsive dipolar collisions, the molecules have a very long lifetime and are still detectable after 10 s. The data was fit to equation (5.7) to determine the two-body loss rate coefficient β (solid line). The dependence of β on d is

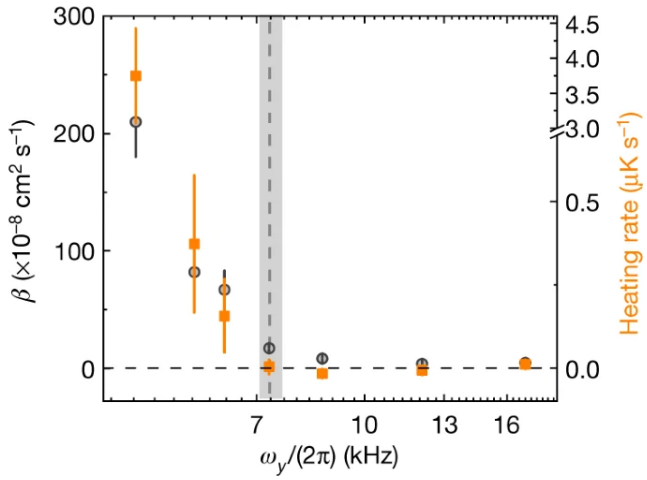

Figure 5.10: Crossover from 3D to quasi-2D. The measured β (gray circles) and heating rate (orange squares) as a function of the vertical trap frequency ω_y. Reproduced from Ref. [52].

shown in part (B). Strikingly, at $d = 0.2$ D, β was suppressed by nearly a factor of 5 below the zero field value. The increase of the loss rate for $d > 0.25$ is consistent with a quasi-2D picture of the dipolar collisions, in which the mixing with $L = 3$ reduces the barrier at large d [81, 100] (see also section 2.5.2).

We also explored the crossover from 3D to quasi-2D at $d = 0.2$ D by varying $\omega_y/2\pi$ from 200 Hz to 17 kHz (Figure 5.10). This was done by lowering the VL power, while adjusting the ODT power to maintain $(\omega_x, \omega_y) = 2\pi \times (40, 40)$. The initial gas temperature $T = 250$ nK was roughly constant as a function of ω_y, and the gas was in 3D for small ω_y. In this regime, the loss rate β (grey) was strongly enhanced by attractive dipolar collisions, similar to previous 3D measurements [79]. As ω_y was increased, the measured β quickly dropped, reaching a plateau for $\omega_y > 2\pi \times 7$ kHz, corresponding to the quasi-2D regime where $\hbar\omega_y > k_B T$. In addition, we observed that the heating rate (orange) in 2D was zero, in agreement with theoretical predictions [186], and in stark contrast to the enormous anti-evaporative heating ($\sim \mu$K/s) observed in 3D [79].

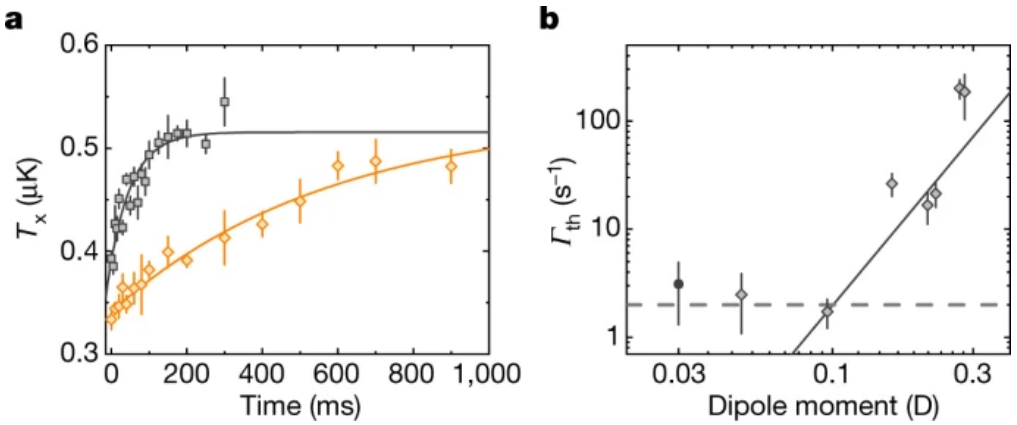

Figure 5.11: Elastic dipolar collisions in quasi-2D. (A) Cross-dimensional thermalization measurements at $d = 0.1$ D (orange diamonds) and 0.21 D (gray squares). Error bars are 1 SE of 5 measurements. (B) Summary of measured thermalization rate Γ_{th} vs induced dipole moment d. The filled point was measured at $d = 0$ D but artificially placed at 0.03 D to be representable on the logarithmic scale. Reproduced from Ref. [52].

5.3 Elastic dipolar collisions

The long lifetime shown in Figure 5.9A gives ample time to measure the elastic collisions via a cross-dimensional thermalization measurement. The elastic collisions occur with rate $\Gamma_{\text{el}} = n\sigma_{\text{el}}v_{\text{th}}$, where n is the average density in 2D, σ_{el} is the elastic cross section, and $v_{\text{th}} = \sqrt{\pi k_B T/2\mu}$ is the thermally-averaged relative velocity of two collision partners, with μ the reduced mass of KRb. The thermalization rate is given by $\Gamma_{\text{th}} = \Gamma_{\text{el}}/\alpha$, where α is the number of collisions to thermalize. Monte-Carlo simulations predict $\alpha = 8$ in the temperature range of our measurements [186].

To measure Γ_{th}, we diabatically increased the power of one of the ODT beams to compress the cloud along $\hat{\mathbf{z}}$. This brought the cloud out of thermal equilibrium and created an imbalance in the thermal energy on the two axes, $T_z > T_x$. Elastic collisions redistributed the excess energy in $\hat{\mathbf{z}}$ to $\hat{\mathbf{x}}$, leading to an increase in T_x over time as the cloud thermalized. We fit the increase in T_x to an exponential curve to extract the thermalization rate Γ_{th}.

Two representative thermalization measurements are shown in Figure 5.11A. Changing d from 0.1 D (orange) to 0.21 D (gray), we measured an increase of Γ_{th} by over a factor of 10. Figure 5.11B shows a summary of the measured Γ_{th} as a function of d, demonstrating that we can tune

the elastic collision rate over at least two orders of magnitude. We attribute the constant Γ_{th} below $d = 0.1$ D to coupling between $\hat{\mathbf{x}}$ and $\hat{\mathbf{z}}$ from the trap anharmonicity, which limited the smallest Γ_{th} we could measure.

By fitting the measured Γ_{th} for $d \geq 0.1$ D (solid line), we extracted $\Gamma_{\text{th}} \propto d^{3.3\pm1.0}$. The fitted dependence is in good agreement with theory, which predicts a crossover between two regimes in the scattering depending on ka_D, where k is the collision wavevector and a_D is the dipolar length [195]. For $ka_D \ll 1$ (low energy regime), Ref. [195] predicts $\sigma_{\text{el}} \propto ka_D^2 \propto kd^4$. For $ka_D \gg 1$ (semiclassical regime), the prediction is $\sigma_{\text{el}} \propto \sqrt{a_D/k} \propto d/\sqrt{k}$. Assuming a collision energy of $E_{\text{col}}/k_B = 450$ nK, we calculate that ka_D ranges from 0.1 to 0.9 over the fitted range of d.

An important figure of merit for evaporative cooling is $\gamma = \sigma_{\text{el}}/\sigma_{\text{inel}}$, the ratio of good to bad collisions. To make a direct connection to our measurements, we can express γ equivalently as $\gamma = \Gamma_{\text{el}}/\Gamma_{\text{inel}} = \alpha\Gamma_{\text{th}}/\Gamma_{\text{inel}}$, where $\Gamma_{\text{inel}} = n_0\beta$ is the initial loss rate and n_0 is the initial average 2D density. Using the theoretically predicted value of $\alpha = 8$ [186], we extracted a maximum value of $\gamma = 200(60)$ at $d = 0.2$ D, indicating that efficient evaporation is possible in our system.

5.4 Direct evaporation of molecules

Thanks to the favorable collision ratio γ measured in the previous sections, we were able to perform efficient evaporation of the molecules to below the Fermi temperature in 2D. To perform evaporation, we leveraged our electric field control to spill the hottest molecules out of the gas by applying an anticurvature of $|\mathbf{E}|$ in the x-direction. The molecular T/T_F after evaporation was obtained from fitting the cloud in time-of-flight, and further supported by measuring the expansion energy of the gas as a function of the final T/T_F. The following subsections discuss the measurement in more detail.

5.4.1 Combined optical + electric potential

Forced evaporative cooling is performed by lowering the trap depth to spill out the hottest molecules. Typically, this is described in terms of the ratio η of the trap depth to the thermal energy

k_BT of the gas (for non-degenerate gases). When holding the gas in the trap without evaporating, one typically needs to keep $\eta \approx 10$ to avoid losing particles.

To evaporate, one lowers η to begin spilling hot particles. We could not lower the VL power to lower η, as is typically done when evaporating in an optical trap, since we needed to maintain a high ω_y for the 2D loss suppression to remain effective. Instead, we applied an anticurvature of $|\mathbf{E}|$ along $\hat{\mathbf{x}}$ to controllably lower the trap depth of the combined optical and electric potential. Calculated trapping potentials along the x-direction are shown in Figure 5.12A, showing how the trap depth can be significantly lowered by the field curvature. Relative to lowering the VL power, this approach also maintains higher transverse trapping frequencies in the center of the cloud. As a result, the thermalization rate could be kept high while the trap depth was lowered.[4]

To quantitatively characterize the combined potential, we measured ω_x in the combined potential as a function of the applied field curvature at $|\mathbf{E}| = 5$ kV/cm (Figure 5.12B). The curvature was controlled by the ratio of r of the rod voltages to the plate voltages (see also section 3.3.3). From knowledge of the VL beam waists and the electrode geometry (section 3.3.2), we calculated the expected behavior of ω_x as a function of r (dashed line) and found good agreement with our measurements (circles).

5.4.2 Evaporation trajectory

To evaporate the molecules, we slowly increased r to spill the hottest molecules from the trap while letting the remaining molecules rethermalize. Figure 5.13A shows r as a function of time for a typical evaporation sequence, with the corresponding calculated trap depth plotted in (B). We started with $\mathbf{E}$ in the "flat field" configuration ($r = 0.4225$), where the anti-trapping from $\mathbf{E}$ is negligible. The sequence consisted of several ramps of r:

(1) An initial fast ramp over 20 ms to start spilling the cloud. We optimized the endpoint of

[4] In principle, using a linear gradient instead of a quadratic one could allow us to maintain an even higher elastic collision rate. Ref. [196] used this scheme in a 3D trap to achieve very fast and efficient evaporation of an atomic Cs gas. We never saw good results by using a gradient instead of anticurvature to evaporate, which we suspect is due to the trap being more smoothly deformed when ramping up the curvature (as opposed to the gradient).

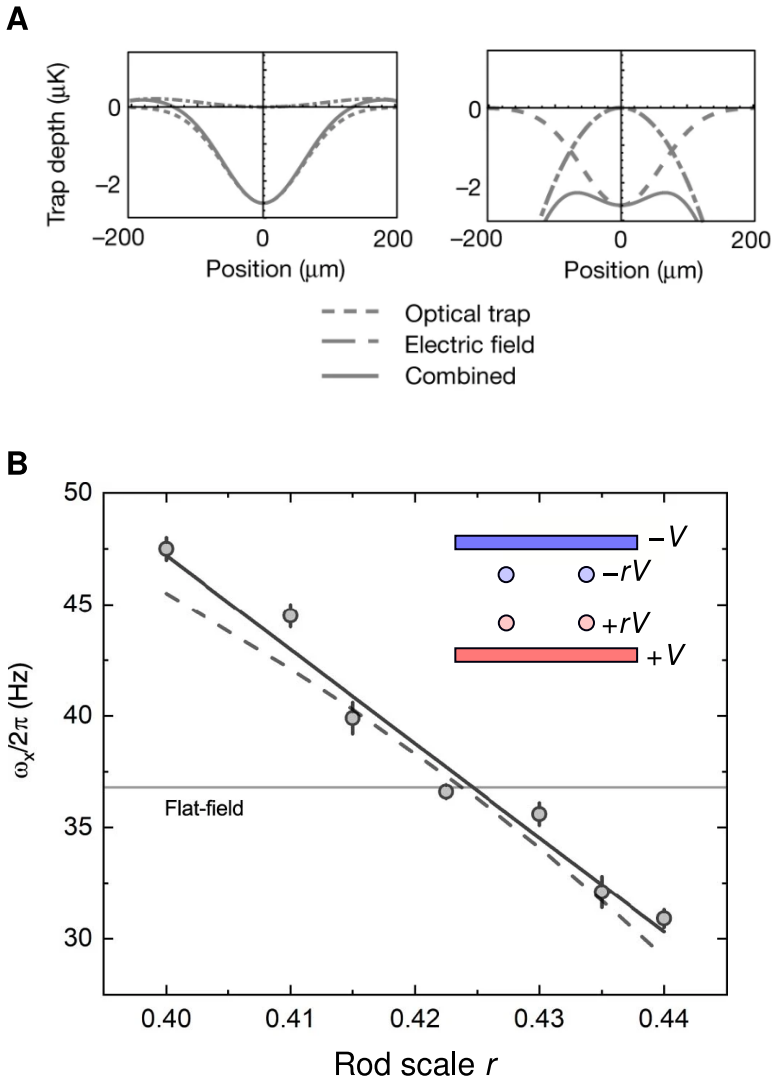

Figure 5.12: Combined optical and electric potential. (A) Combined potentials at the "flat field" configuration (left) and at the end of evaporation (right). (B) Measurements of ω_x in the combined optical and electric potential as a function of the rod scale r. The experimental data (gray circles) show good agreement with the calculated potential (dashed line). The solid gray line is a linear fit to the data. The horizontal line shows the calculated value of ω_x in the flat-field configuration ($r = 0.4225$). Adapted from Ref. [52].

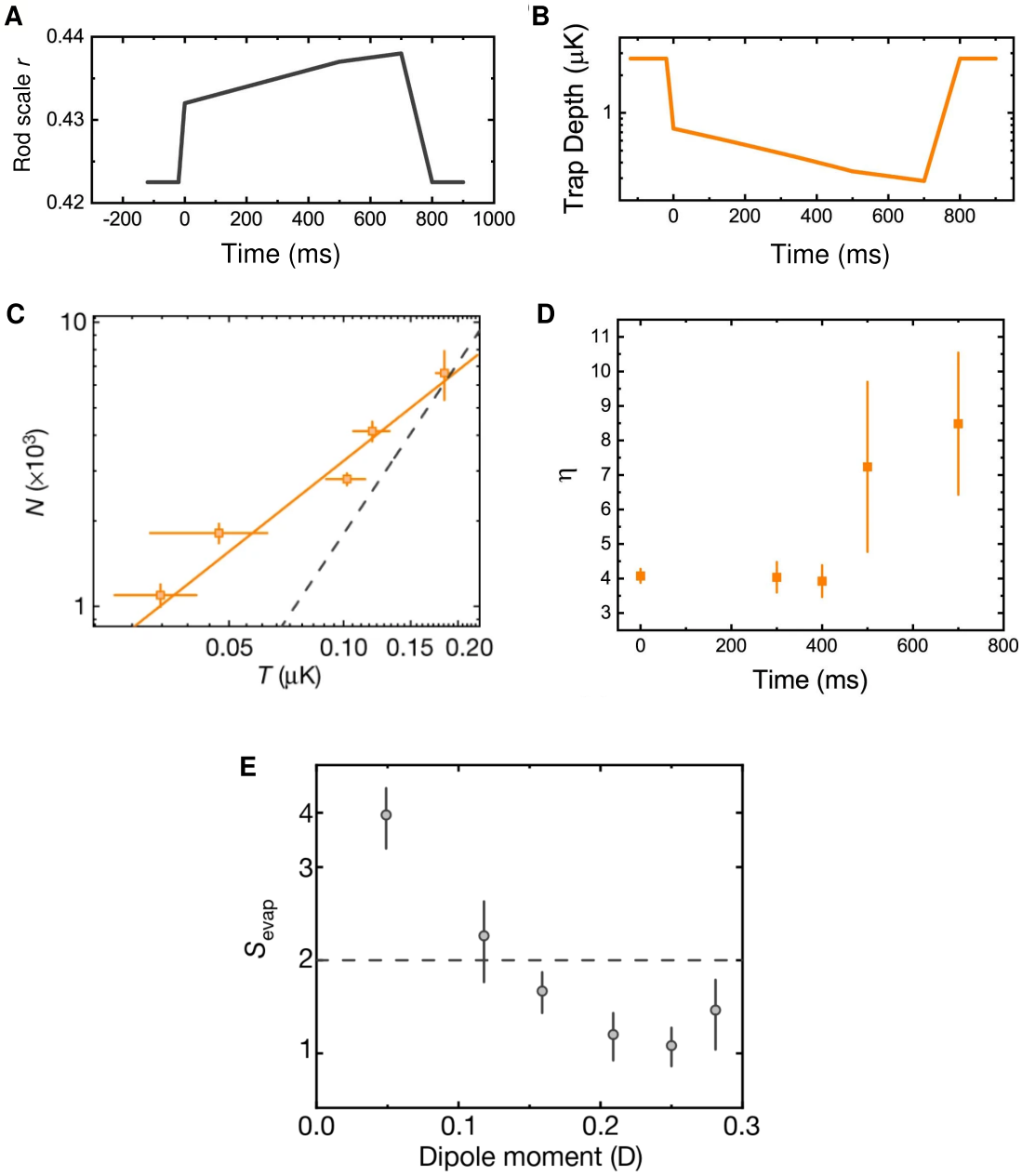

Figure 5.13: Evaporation sequence and trajectory. (A) Value of rod scale r over the evaporation. (B) Calculated trap depth of the combined optical and electric potential over the evaporation. (C) Evaporation trajectory at $|\mathbf{E}| = 6.5$ kV/cm and $d = 0.25$. The fit (orange line) gives $S_{\text{evap}} = 1.06(15)$, significantly better than the threshold of $S_{\text{evap}} = 2$ (dashed line) needed to increase PSD. (D) Calculated η for the evaporation curve shown in (C). (E) Summary of S_{evap} versus the induced dipole moment d. The evaporation is most efficient near $d = 0.2$ to 0.25 D, where γ is the highest. Adapted from Ref. [52].

this ramp to be the point where molecules just started to be lost.

(2) A two-stage evaporation ramp.

(3) A final 100 ms ramp to recompress the trap to its original depth. We compared the PSD with and without evaporation at the same trap frequencies to remove the effects of adiabatic cooling.

By interrupting the evaporation ramps midway through and recompressing to the flat field, we could map out the evaporation trajectory. Figure 5.13C shows an evaporation trajectory at $|\mathbf{E}| = 6.5$ kV/cm ($d = 0.25$ D), showing how the total molecule number N and fitted temperature T evolve over the evaporation. The ratio of the measured molecule temperature T with the calculated trap depth gives an estimate of η over the evaporation trajectory (Figure 5.13D). Our optimized trajectory used $\eta \approx 4$ for the initial stage of evaporation, which is in rough agreement with the expectation from theoretical simulations [186]. This low value of η signals a fairly aggressive evaporation curve, in comparison to typical values of $\eta = 6$–8 for alkali atoms in a harmonic trap [20]. It makes sense intuitively that we need to evaporate quickly, since evaporating too slowly will eventually result in all molecules being lost by reactive collisions.

To characterize the evaporation efficiency, we calculated the evaporation slope S_{evap}, defined by

$$S_{\text{evap}} = \frac{\partial \log N}{\partial \log T}. \tag{5.9}$$

With this definition, a lower S_{evap} is a more efficient evaporation. Since PSD $\propto NT^{-2}$ for a non-degenerate 2D gas, we must have $S_{\text{evap}} < 2$ to increase PSD in 2D. Fitting the evaporation trajectory in Figure 5.13C, we obtain $S_{\text{evap}} = 1.06(15)$ (solid line), significantly better than the threshold of $S_{\text{evap}} = 2$ (dashed line). We optimized the evaporation trajectory at several values of $|\mathbf{E}|$ to measure S_{evap} as a function of d (Figure 5.13E). The best S_{evap} was achieved near $d = 0.2$–0.25 D where γ is maximized.

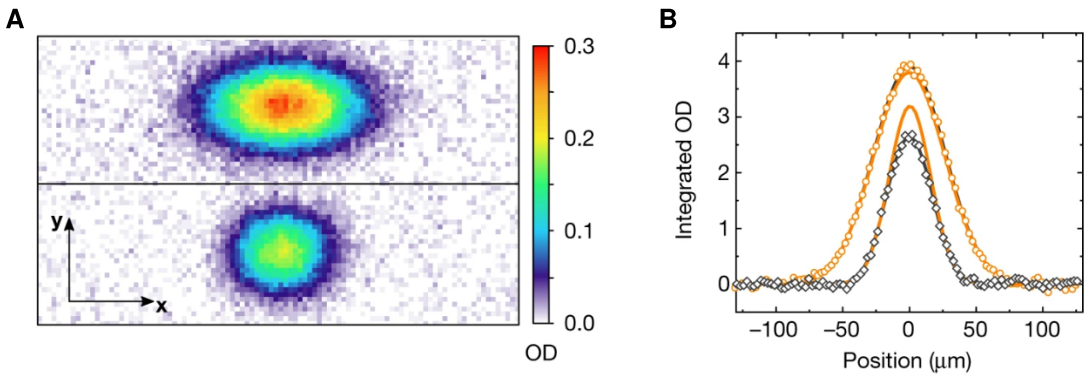

Figure 5.14: 2D Fermi gas of molecules. (A) Absorption images after band mapping from the VL and 5.84 ms of TOF, for a gas at $T/T_F = 2.0(1)$ (top) and $T/T_F = 0.81(15)$ (bottom). (B) Profiles along $\hat{\mathbf{x}}$ after integrating out the y-direction. The profiles are well-fit by the Fermi-Dirac distribution (equation (5.14), black lines). A Gaussian fit to the outer wings of the cloud (orange lines) overestimates the density in the center of the colder cloud, signaling the onset of degeneracy. Reproduced from Ref. [52].

5.4.3 2D Fermi gas of molecules

Since $S_{\text{evap}} < 2$, the evaporative cooling increases the PSD of the molecules and lowers T/T_F. Starting from an initial condition of $T/T_F = 1.5(1)$, we were able to cool the gas below $T/T_F = 1$ and observe the onset of degeneracy in 2D. Our best evaporation gave $N = 1.7(1) \times 10^3$ and $T/T_F = 0.6(2)$.

Figure 5.14A shows images of the molecular gas after band mapping and TOF for $T/T_F = 2.0(1)$ (top) and $T/T_F = 0.81(15)$ (bottom). The colder cloud was produced by evaporation, and shows a clear decrease in the momentum spread along $\hat{\mathbf{x}}$. The momentum spread in the y-direction is limited by the size of the Brillouin zone from the band mapping procedure, so we integrated out the y-direction to obtain the 1D profiles in (B). The molecular T/T_F is determined by fitting the profiles in (B) to the Fermi-Dirac distribution (black lines). Fitting the outer wings of the cloud to a Gaussian (orange lines) produces a good fit for the hotter cloud, but significantly overestimates the density in the center of the colder cloud. This is a hallmark of the onset of quantum degeneracy.

To characterize the change in the momentum distribution as the gas becomes degenerate, we extracted the deviation $\delta U = U - U_{\text{cl}}$ of the energy U of the fermionic gas from the classical energy

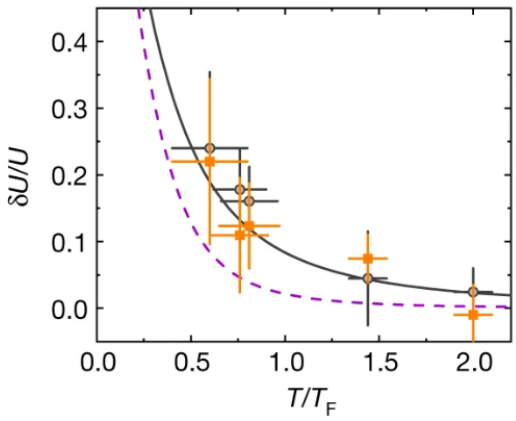

Figure 5.15: Expansion energy of the 2D molecular Fermi gas. The temperature T is determined by the Fermi-Dirac fit to the entire cloud (gray circles) or a Gaussian fit to the outer wings (orange squares). The gray solid and purple dashed curves show the calculated $\delta U/U$ for the 2D and 3D ideal Fermi gases, respectively. Reproduced from Ref. [52].

$U_{\mathrm{cl}} = 2k_BT$. We obtained $U = 2k_BT_{\mathrm{rel}}$ from the width of the momentum distribution by fitting the whole cloud to a Gaussian profile and calculating the release temperature

$$T_{\mathrm{rel}} = \frac{m\omega_x^2\sigma_x^2}{k_B(1+\omega_x^2t^2)}, \tag{5.10}$$

where t is the TOF and σ_x is obtained from the Gaussian fit.

The results are shown in Figure 5.15. A large deviation of $\delta U/U$ is observed below $T/T_F = 1$, in agreement with simulations (gray solid line). The temperature T, which determines the classical energy U_{cl}, was obtained directly from the Fermi-Dirac fit (gray circles) or by fitting a Gaussian to the outer wings of the cloud (orange points). Both methods show good agreement with the expected trend. Note that the effect is much stronger in 2D than in 3D (purple dashed line) owing to the decreased density of states in 2D.

5.4.3.1 Fitting the 2D gas in time-of-flight

Here, we briefly discuss the relevant equations for fitting. The in-situ density distribution of a 2D Fermi gas is

$$n(x,z) = -\frac{1}{\lambda_{\mathrm{db}}^2}\mathrm{Li}_1\left\{-\exp\left[\beta_{\mathrm{th}}\left(\mu - \frac{1}{2}m\omega_x^2x^2 - \frac{1}{2}m\omega_z^2z^2\right)\right]\right\}, \tag{5.11}$$

with $\lambda_{\rm db}$ the thermal deBroghlie wavelength, $\beta_{\rm th} = 1/k_B T$ the inverse temperature, and μ the chemical potential. In 2D, μ is defined by

$$\frac{N}{\tau} = \left(\frac{k_B T}{\hbar \omega_r}\right)^2 \mathrm{Li}_2(-e^{\beta_{\rm th}\mu}). \tag{5.12}$$

The cloud is imaged along $\hat{\mathbf{z}}$, so we see the column-integrated density

$$n_{\rm int}(x) = -\frac{1}{\lambda_{\rm db}^2}\sqrt{\frac{2\pi}{\beta_{\rm th} m\omega_z^2}}\mathrm{Li}_{3/2}\left\{-\exp\left[\beta_{\rm th}\left(\mu - \frac{1}{2}m\omega_x^2 x^2\right)\right]\right\}. \tag{5.13}$$

The imaged cloud after TOF also has a finite extent in the y-direction from the band mapping procedure. We integrate out the y-direction, and fit the resulting 1D profile to

$$n_{\rm int}(x) = A \times \mathrm{Li}_{3/2}\left(-e^{q - x^2/2\sigma_x^2}\right)/\mathrm{Li}_{3/2}(-e^q), \tag{5.14}$$

where $q = \beta_{\rm th}\mu$ is the log fugacity [173]. From the fit, we can extract T/T_F via

$$\left(\frac{T}{T_F}\right)^2 = -\frac{1}{2\mathrm{Li}_2(-e^q)}, \tag{5.15}$$

and T from

$$T = \frac{m\omega_x^2\sigma_x^2}{k_B(1+\omega_x^2 t^2)}, \tag{5.16}$$

where t is the TOF.

We can also determine T by fitting the outer wings of the cloud. To do this, we first fit the entire cloud to extract its Gaussian width σ. Then we fit the cloud again, including only the region beyond 1.5σ from the fitted center of the cloud, which we define as the outer wings of the cloud. The second fit gives a new Gaussian width $\sigma_{\rm out}$ and corresponding temperature $T_{\rm out}$ via equation (5.16).

5.5 Conclusion

In this chapter, we utilized repulsive dipolar collisions in 2D to stabilize the gas against loss while providing a large elastic scattering rate. The favorable ratio $\gamma = 200(60)$ enabled direct evaporation of the molecules to below T_F in 2D. The techniques described here are general and

predicted to work for the other fermionic bialkalis, as well as bosonic molecules at higher d and ω_y [101].

The physics of dipolar gases in 2D is very rich and is ripe for exploration with a 2D Fermi gas of molecules. For example, the collective modes of the system can be modified as the elastic collision rate is tuned by the dipole moment [197]. With the conditions achieved in this work, we should be able to explore the crossover between the collisionless and hydrodynamic regimes. The work in this chapter focused on the direct dipolar interaction between the induced dipole moments, but dipolar spin-exchange can also be brought into play by putting the molecules in a coherent superposition of rotational states (Chapter 8). Owing to the interplay of interactions and dimensionality, interesting phenomena such as spin-orbit coupling [139] or spin-squeezing [49] is predicted to occur. Direct evaporation in 2D will be an important first stage to produce the low-entropy gases needed for these explorations.

Chapter 6

Resonant shielding of molecules in 2D and 3D

In the previous chapter, we showed how the combination of dipolar interactions and tight confinement into 2D could stabilize the molecular gas. This realized a long-lived gas of molecules with strong dipolar interactions, and enabled direct evaporation to below the Fermi temperature in 2D. Those results utilized the induced dipole moment of the molecules to control the collision properties.

In this chapter, we show how the transition dipole moment can enter into the collision process. In particular, we observed resonant collisional shielding of molecules, which caused the loss rate in the $|1,0\rangle$ state to be modulated by nearly three orders of magnitude near a field of $|\mathbf{E}| = 12.5$ kV/cm. At some values of $|\mathbf{E}|$, the loss rate could be suppressed by nearly a factor of 10, and the molecules were shielded from loss. Physically, the shielding arises from a near degeneracy of a pair of molecules in $|1,0\rangle|1,0\rangle$ with another rotational pair $|0,0\rangle|2,\pm1\rangle$ or $|0,0\rangle|2,0\rangle$, which occurs at a certain value of $|\mathbf{E}|$. The two kets denote the (symmetrized) rotational states of the two colliding molecules. Since $|1,0\rangle|1,0\rangle$ is coupled to both $|0,0\rangle|2,\pm1\rangle$ and $|0,0\rangle|2,0\rangle$ through the transition dipole moment (section 2.5.4), the effective intermolecular potential is strongly modified when these rotational state pairs are near-degenerate.

An interesting feature of the shielding, compared to the 2D dipolar repulsion, is that it also works in 3D. After our initial observation in 2D [137], we investigated the properties of the shielding in 3D, including the elastic collisions at the shielding point, and used it to evaporatively cool the molecules in 3D [138].

6.1 Physical mechanism

The idea of shielding molecular collisions with a static **E** was introduced in pioneering theoretical work by Avdeenkov et al. in 2006 [103]. A simple intuitive picture comes from considering the van der Waals interaction between two colliding molecules. In second order perturbation theory, we obtain

$$V_{\mathrm{vdw}}(r) = \sum_{Y} \frac{|\langle Y|V_{\mathrm{dd}}(r)|X\rangle|^2}{E_X - E_Y}. \tag{6.1}$$

Above, $|X\rangle$ represents the incoming channel (internal states of the two molecules as well as partial wave), while Y runs over all other dipole-coupled collision channels. Since $V_{\mathrm{dd}}(r) \propto 1/r^3$, this gives the usual $V_{\mathrm{vdw}}(r) \propto 1/r^6$ scaling.

Equation (6.1) already hints at some of the main features of the shielding. Typically, the energy denominators $E_X - E_Y$ are large[1], suppressing the dipolar coupling between $|X\rangle$ and $|Y\rangle$ except for at very close distances where V_{dd} becomes very strong. However, if we can engineer a situation where some specific state $|Y'\rangle$ becomes nearly degenerate with $|X\rangle$, then the coupling to $|Y'\rangle$ can become the dominant term in V_{vdw} at longer distances.

Let us define V_{shield} as the contribution to V_{vdw} from $|Y'\rangle$,

$$V_{\mathrm{shield}} = \frac{|\langle Y'|V_{\mathrm{dd}}(r)|X\rangle|^2}{\Delta E}, \tag{6.2}$$

with $\Delta E = E_X - E_{Y'}$. We will assume that ΔE is small, so the dipolar coupling is near resonant. If $\Delta E < 0$, then V_{shield} is an attractive potential. On the other hand, if $\Delta E > 0$, then V_{shield} forms a repulsive barrier. Since the reactive loss rate for KRb is directly linked to the rate of tunneling through long-range potential barriers (see section 2.5.2 or Ref. [81]), this implies that the molecular loss can be controlled by ΔE. Also, note that the value of V_{shield} depends on the magnitude of the matrix element $\langle Y'|V_{\mathrm{dd}}|X\rangle$ but not its sign. As long as $\Delta E > 0$, this means that both side-to-side collisions ($m_L = \pm 1$) and head-to-tail collisions ($m_L = 0$) have a repulsive barrier. As a result, the shielding is expected to work in 3D, in contrast to the 2D dipolar loss suppression of Chapter 5.

[1] This is true for KRb and other Σ molecules, but molecules with Λ-doublets in the ground state (e.g., OH [198]) can have small energy denominators even at zero electric field.

In the absence of dipolar interactions, the p-wave barrier keeps the molecules from colliding at short range. The peak of the p-wave ($L = 1$) barrier is located at a distance

$$R_b = \left(\frac{3}{L(L+1)}\right)^{1/4} a_{\mathrm{vdW}} = \left(\frac{3\mu C_6}{\hbar^2}\right)^{1/4}, \tag{6.3}$$

where a_{vdW} is the van der Waals length, with C_6 is the van der Waals coefficient and μ the reduced mass. For KRb, $R_b = 270a_0$ and the height of the barrier is $V_b = 24\,\mu$K.

By calculating $V_{\mathrm{shield}}(R_b)$ as a function of the energy denominator ΔE, we can estimate the effect of the shielding. To make things more concrete, let us plug in $|X\rangle = |1,0\rangle|1,0\rangle$ and $|Y'\rangle = |0,0\rangle|2,0\rangle$, and ignore the motional angular momentum state for simplicity. The order of magnitude of the coupling is $\langle Y'|V_{\mathrm{dd}}(r)|X\rangle \sim d_{21}d_{10}/4\pi\epsilon_0 r^3$, where $d_{21} = \langle 2,0|d^0|1,0\rangle$ and $d_{1,0} = \langle 1,0|d^0|0,0\rangle$ are the transition dipole moments, and we get

$$V_{\mathrm{shield}}(R_b) = \frac{1}{\Delta E}\left(\frac{d_{21}d_{10}}{4\pi\epsilon_0 R_b^3}\right)^2. \tag{6.4}$$

Let us first calculate the effect at $|\mathbf{E}| = 0$, where ΔE is large and V_{shield} should be very small. Here, we have $\Delta E = 2B_v$, where B_v is the rotational constant, and the dipole matrix elements are $d_{10} = d_{\mathrm{perm}}/\sqrt{3}$ and $d_{21} = 2d_{\mathrm{perm}}/\sqrt{15}$ (see Table 2.2). Plugging in numbers for KRb, we obtain $V_{\mathrm{shield}} = -550$ nK at $|\mathbf{E}| = 0$, which is small compared to $V_b = 24\,\mu$K.

However, ΔE can be tuned by $|\mathbf{E}|$. The dependence is shown in Figure 6.1A for KRb; notably, $\Delta E = 0$ at $|\mathbf{E}_{\mathrm{res}}| = 12.505$ kV/cm. The dipolar coupling strength $d_{21}d_{10}$ also changes somewhat with $|\mathbf{E}|$ due to rotational state mixing (Figure 6.1B). With these two quantities, we can calculate how $V_{\mathrm{shield}}(R_b)$ varies with $|\mathbf{E}|$ (Figure 6.1C). For $\Delta E > 0$, $V_{\mathrm{shield}}(R_b)$ is large and positive, forming a repulsive shield for the molecules.

We stress here that the shielding resonances come from the energy degeneracy of the initial scattering state and another free scattering state with different rotational angular momentum. This is in contrast to Feshbach resonances, which arise from bound states. The shielding resonances are essentially Förster resonances — for example, as studied in Rydberg atoms [199, 200, 201] — where two dipole-coupled pairs of states are tuned to resonance with $|\mathbf{E}|$.

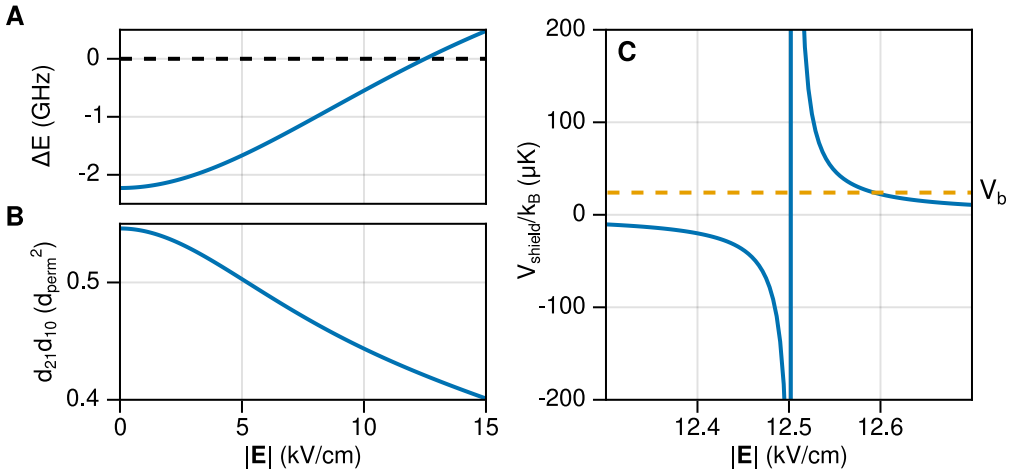

Figure 6.1: $V_{\text{shield}}(R_b)$ as a function of $|\mathbf{E}|$. (A) Energy difference $\Delta E = 2E_{|1,0\rangle} - E_{|2,0\rangle} - E_{|0,0\rangle}$. The dashed line is $\Delta E = 0$. (B) The dipolar coupling strength $d_{21}d_{10}$. (C) The estimated barrier $V_{\text{shield}}(R_b)$, zoomed into the region around $|\mathbf{E}_{\text{res}}|$. Also shown is the height $V_b = 24\,\mu$K of the p-wave barrier (dashed line).

6.1.1 Two-channel picture

When ΔE becomes very small, the perturbative expression from equation (6.1) breaks down. Full quantum scattering calculations are needed to accurately determine the behavior for any ΔE [104]. However, near $\Delta E = 0$, the two coupled states $|1,0\rangle|1,0\rangle$ and $|0,0\rangle|2,0\rangle$ are most important, and one can approximate the system with a two-channel model to estimate the height of the barrier [138, 202]. In this section, we give a brief description of the two-channel model, similar to the explanation given in the supplement of Ref. [138]. For a more rigorous treatment, see the work by our theory collaborators in Ref. [202].

To simplify notation, let us define $|1\rangle \equiv |1,0\rangle|1,0\rangle$ and $|2\rangle \equiv (|0,0\rangle|2,0\rangle + |2,0\rangle|0,0\rangle)/\sqrt{2}$. Note that both $|1\rangle$ and $|2\rangle$ are symmetrized in the molecular internal states. Then at each $|\mathbf{E}|$, we can write down a simplified Hamiltonian in the basis of $|1\rangle$ and $|2\rangle$,

$$H(r) = \begin{pmatrix} H_{11}(r) & H_{12}(r) \\ H_{21}(r) & H_{22}(r) - \Delta E \end{pmatrix}, \tag{6.5}$$

where

$$H_{11}(r) = \frac{\hbar^2 L(L+1)}{2\mu r^2} - \frac{C_6}{r^6} + \langle 1|V_{\rm dd}(r)|1\rangle \tag{6.6}$$

$$H_{22}(r) = \frac{\hbar^2 L(L+1)}{2\mu r^2} - \frac{C_6}{r^6} + \langle 2|V_{\rm dd}(r)|2\rangle \tag{6.7}$$

$$H_{12}(r) = \langle 1|V_{\rm dd}(r)|2\rangle, \tag{6.8}$$

and $\Delta E = 2E_{|1,0\rangle} - E_{|0,0\rangle} - E_{|2,0\rangle}$. The electronic van der Waals coefficient is used $C_6 = 12636$ a.u. [203] to avoid double-counting the rotational contribution. To calculate $\langle i|V_{\rm dd}(r)|j\rangle$, we can use equation (2.32),

$$\begin{aligned}
&\langle N_1, m_{N1}; N_2, m_{N2}; L, m_L|V_{\rm dd}|N_1', m_{N1}'; N_2', m_{N2}'; L', m_L'\rangle \\
&= -\frac{\sqrt{6}}{4\pi\epsilon_0 r^3}(-1)^{m_L}\sqrt{(2L+1)(2L'+1)}\begin{pmatrix} L & 2 & L' \\ 0 & 0 & 0 \end{pmatrix}\begin{pmatrix} L & 2 & L' \\ -m_L & 0 & m_L' \end{pmatrix} \\
&\qquad \times \langle N_1, m_{N1}; N_2, m_{N2}|2d_1^0 d_2^0|N_1', m_{N1}'; N_2', m_{N2}'\rangle.
\end{aligned} \tag{6.9}$$

Above, we have only kept the m_N-preserving term since all the involved rotational states have $m_N = 0$. For simplicity, we neglect the partial wave mixing and keep only terms with $L = L' = 1$, to obtain

$$\langle 1|V_{\rm dd}(r)|1\rangle = \frac{2\sqrt{6}}{4\pi\epsilon_0 r^3} f(L, m_L) d_1^2 \tag{6.10}$$

$$\langle 2|V_{\rm dd}(r)|2\rangle = \frac{2\sqrt{6}}{4\pi\epsilon_0 r^3} f(L, m_L)(d_0 d_2 + d_{02}^2) \tag{6.11}$$

$$\langle 1|V_{\rm dd}(r)|2\rangle = \frac{2\sqrt{6}}{4\pi\epsilon_0 r^3} f(L, m_L)\sqrt{2} d_{21} d_{10}, \tag{6.12}$$

where $d_N = \langle N, 0|d^0|N, 0\rangle$ is the induced dipole moment of $|N, m_N = 0\rangle$ and $d_{NN'} = \langle N, 0|d^0|N', 0\rangle$ is the transition dipole moment between $|N, 0\rangle$ and $|N', 0\rangle$. The angular part is given by

$$f(L, m_L) = (-1)^{m_L+1}(2L+1)\begin{pmatrix} L & 2 & L \\ 0 & 0 & 0 \end{pmatrix}\begin{pmatrix} L & 2 & L \\ -m_L & 0 & m_L \end{pmatrix}. \tag{6.13}$$

For $L = 1$, we have $f(1, \pm 1) = 1/5$ and $f(1, 0) = -2/5$. Since the interaction preserves m_L, we can solve $H(r)$ for each m_L separately.

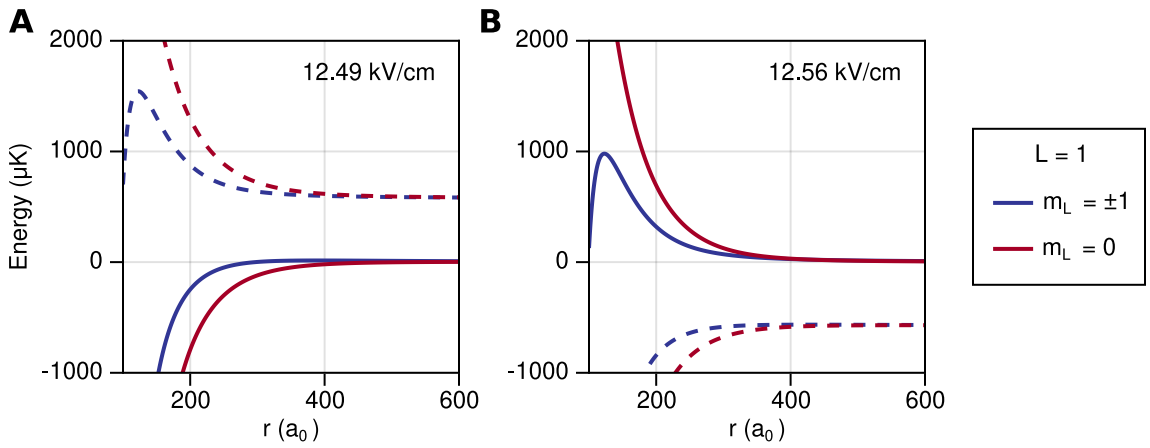

Figure 6.2: Two-channel picture of the shielding, showing adiabatic energy curves calculated from equation (6.5). (A) $|\mathbf{E}| = 12.49$ kV/cm ($|\mathbf{E}| < |\mathbf{E}_{\text{res}}|$). (B) $|\mathbf{E}| = 12.56$ kV/cm ($|\mathbf{E}| > |\mathbf{E}_{\text{res}}|$). In both plots, the solid (dashed) line represent $|1\rangle$ ($|2\rangle$). The curves for $m_L = \pm 1$ (blue) and $m_L = 0$ (red) show similar behavior.

Diagonalizing $H(r)$ at each r yields the adiabatic energy curves shown in Figure 6.2. In both plots, the solid lines represent $|1\rangle$ and the dashed lines represent $|2\rangle$. For $|\mathbf{E}| < |\mathbf{E}_{\text{res}}|$ (A), the effective potential is strongly attractive and the p-wave barrier is completely wiped out. Conversely for $|\mathbf{E}| > |\mathbf{E}_{\text{res}}|$ (B), the potential is strongly repulsive and the molecules are shielded. Note that the qualitative behavior of $m_L = \pm 1$ (blue) and $m_L = 0$ (red) is the same, as we had argued from the form of V_{vdw}. We can also understand the behavior in terms of level repulsion between the states — the upper state is pushed up in energy, thus experiencing a repulsive interaction, while the opposite is true for the lower state. The effect is stronger in $m_L = 0$ since the dipolar interaction is twice as strong as in $m_L = \pm 1$.

From equation (6.5), we can also estimate the width of the shielding features as a function of $|\mathbf{E}|$. The dipolar coupling becomes resonant when $|H_{12}(r)| \geq |\Delta E|$. Since this criterion depends on r, we use $r = R_b$ as an estimate of the relevant length scale for a collision. Plugging in the parameters for KRb, we find that $H_{12}(R_b) \approx h \times 4.2$ MHz at $|\mathbf{E}_{\text{res}}|$. Given the differential Stark shift of $h \times 215$ kHz/(V/cm) between $|1\rangle$ and $|2\rangle$ at $|\mathbf{E}_{\text{res}}|$, this implies a width of roughly 20 V/cm, which is quite narrow compared to $|\mathbf{E}_{\text{res}}|$.

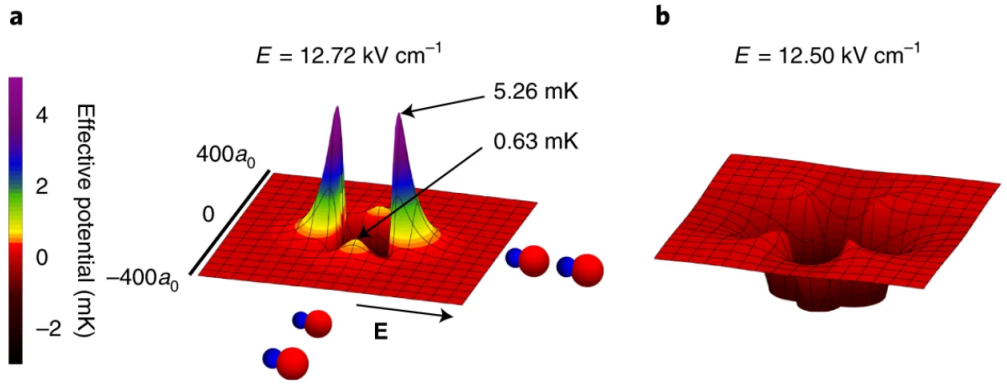

Figure 6.3: Angular dependence of the shielding, demonstrating how the effective intermolecular potential varies as a function of the relative orientation of the molecules at (A) $|\mathbf{E}| = 12.72$ kV/cm ($|\mathbf{E}| > |\mathbf{E}_{\rm res}|$) and (B) $|\mathbf{E}| = 12.50$ kV/cm ($|\mathbf{E}| < |\mathbf{E}_{\rm res}|$). Reproduced from Ref. [138].

As shown in Refs. [138, 202], one can also visualize the dependence of the effective potential on the orientation of the molecules. This is done by leaving the angular part of $V_{\rm dd}$ as a function of θ instead of expanding it in spherical harmonics as we did above. Here, θ is the polar angle of the vector $\mathbf{r}$ between the molecules. For the states considered here, we can do this by simply replacing $f(L, m_L)$ with $(1 - 3\cos^2\theta)/2$ in the equations above. The resulting potential energy maps are shown in Figure 6.3. From these plots, we can clearly see the gaps in the barrier at $\theta = \arccos(\sqrt{3}) \approx 54.7°$ where the dipolar coupling vanishes.

The shielding occurs when the molecules are prepared in the upper branch of the avoided crossing ($|\mathbf{E}| > |\mathbf{E}_{\rm res}|$). Consequently, inelastic collisions that result in decay of $|1\rangle$ to $|2\rangle$ are energetically open and are enhanced very close to $|\mathbf{E}_{\rm res}|$. In our experiment, molecules that undergo inelastic collisions are immediately lost due to reactive s-wave collisions. Thus, the optimal field for shielding is not simply the field with the largest barrier in the adiabatic curves, but rather where the sum of the reactive and inelastic rates is minimized [104].

In the next sections, we will describe the experimental measurements of the shielding in detail. Before moving on, we have two more brief comments. First, while all of the discussion in the section centered on the coupling between $|1,0\rangle|1,0\rangle$ and $|0,0\rangle|2,0\rangle$, similar arguments hold for $|0,0\rangle|2,\pm1\rangle$, which is also coupled to $|1,0\rangle|1,0\rangle$ via dipolar interactions. One interesting difference

is that the dipolar interaction also changes the motional state since the total angular momentum projection must be conserved. Second, the resonant electric field shielding is very general, relying only on the rigid rotor structure of the molecule. Theoretical calculations for the bosonic bialkali molecules [204] and several $^2\Sigma$ molecules [205] all show a strong shielding. Hence, our experimental results should be broadly applicable to other ultracold molecule species.

6.2 Shielding in 2D

Our initial study of the shielding was done in 2D [137]. The procedure for preparing a 2D gas of molecules was similar to the previous 2D work. Typical starting conditions were $N = 2 \times 10^4$ molecules in the $|0,0\rangle$ state at $T = 250$ nK, corresponding to $T/T_F = 1.8$. The molecules were in $\tau = 6$ layers of the VL, with trap frequencies of $(\omega_x, \omega_y, \omega_z) = 2\pi \times (34, 17.7 \times 10^3, 34)$ Hz. Since $k_B T/\hbar\omega_y \approx 0.3$, the gas was in the quasi-2D regime.

The molecules were produced at $|\mathbf{E}_{\mathrm{STIRAP}}| = 4.5$ kV/cm to sidestep the many avoided crossings of the $|1,0\rangle$ state at low electric field (see Figure 2.2). STIRAP initially populates the $|0,0\rangle$ state, and we used a resonant microwave π-pulse at 2.6 GHz (Rabi frequency $\Omega = 2\pi \times 200$ kHz) to transfer the molecules to $|1,0\rangle$ with a typical efficiency of 95%. Any molecules remaining in $|0,0\rangle$ were quickly lost due to s-wave collisions with the majority $|1,0\rangle$ state [32]. After the state preparation, $\mathbf{E}$ was ramped to its target configuration in 60 ms. After a variable hold time t, $\mathbf{E}$ was ramped back to $\mathbf{E}_{\mathrm{STIRAP}}$, and the molecules were transferred back to $|0,0\rangle$ and dissociated for imaging. The average 2D molecular density $n(t)$ was fit to the solution of the two-body loss differential equation $dn/dt = -\beta n^2$ to extract the loss rate coefficient β, same as in the 2D loss measurements in the previous chapter. Since the shielding depends sensitively on $|\mathbf{E}|$, we calibrated the electric field strength to a few parts in 10^4 using microwave spectroscopy of the $|0,0\rangle$ to $|1,0\rangle$ transition.

We first measured β for $|1,0\rangle$ in the region around $|\mathbf{E}_{\mathrm{res}}| = 12.51$ kV/cm to look for the anticipated sharp changes of β near the resonance with $|0,0\rangle|2,0\rangle$. The field was oriented along $\hat{\mathbf{y}}$ for these measurements, so the molecules were colliding with $m_L = \pm 1$. We observed the loss

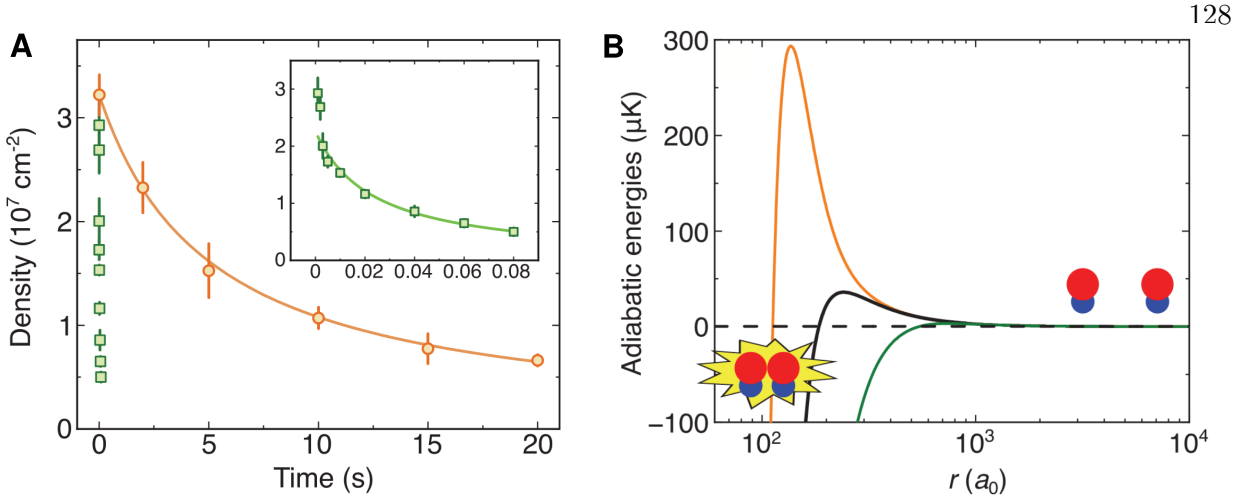

Figure 6.4: Large variation of β near the shielding resonance. (A) Loss measurements at $|\mathbf{E}| = 12.50$ kV/cm (green squares) and 12.67 kV/cm (orange circles). The field is oriented along $\hat{\mathbf{y}}$. The inset shows the 12.50 kV/cm data on an enlarged x-axis. (B) Calculated adiabatic energy curves for $m_L = \pm 1$ collisions of $|1,0\rangle$, corresponding to the values of $|\mathbf{E}|$ in (A). The black curve shows the p-wave + dipolar barrier at 12.67 kV/cm with the resonant dipolar coupling to $|0,0\rangle|2,0\rangle$ removed. Adapted from Ref. [137].

curves shown in Figure 6.4A, which show a two orders-of-magnitude change in β over a 1.4% change in $|\mathbf{E}|$. For $|\mathbf{E}| < |\mathbf{E}_{\text{res}}|$ (green squares), the molecules were lost in tens of milliseconds, while for $|\mathbf{E}| > |\mathbf{E}_{\text{res}}|$ (orange circles), we were able to detect molecules out to 20 seconds. Figure 6.4B shows the adiabatic energy curves for $m_L = \pm 1$ collisions of $|1,0\rangle$ corresponding to the values of $|\mathbf{E}|$ used in (A), calculated by our theory collaborator Goulven Quéméner. The black curve is the diabatic contribution from the p-wave centrifugal barrier and the $m_L = \pm 1$ dipolar repulsion ($d = -0.08$ D), which ignores the effect of the resonant dipolar coupling. In the shielded case (orange line), the molecules experience a 300 μK barrier in the effective potential, which strongly suppresses the tunneling to short range. Conversely, in the anti-shielded case (green), the molecules experience a strong attraction that completely overwhelms the diabatic barrier, leading to rapid loss.

From the physical picture described in the previous section, we would expect to see two sharp features in β arising from the crossings of $|0,0\rangle|2,\pm 1\rangle$ and $|0,0\rangle|2,0\rangle$ with $|1,0\rangle|1,0\rangle$ (Figure 6.5A). These crossings occur at electric fields of $|\mathbf{E}_1| = 11.72$ kV/cm and $|\mathbf{E}_2| = 12.51$ kV/cm, respectively. Measuring β as a function of $|\mathbf{E}|$ revealed the two sharp features shown in Figure

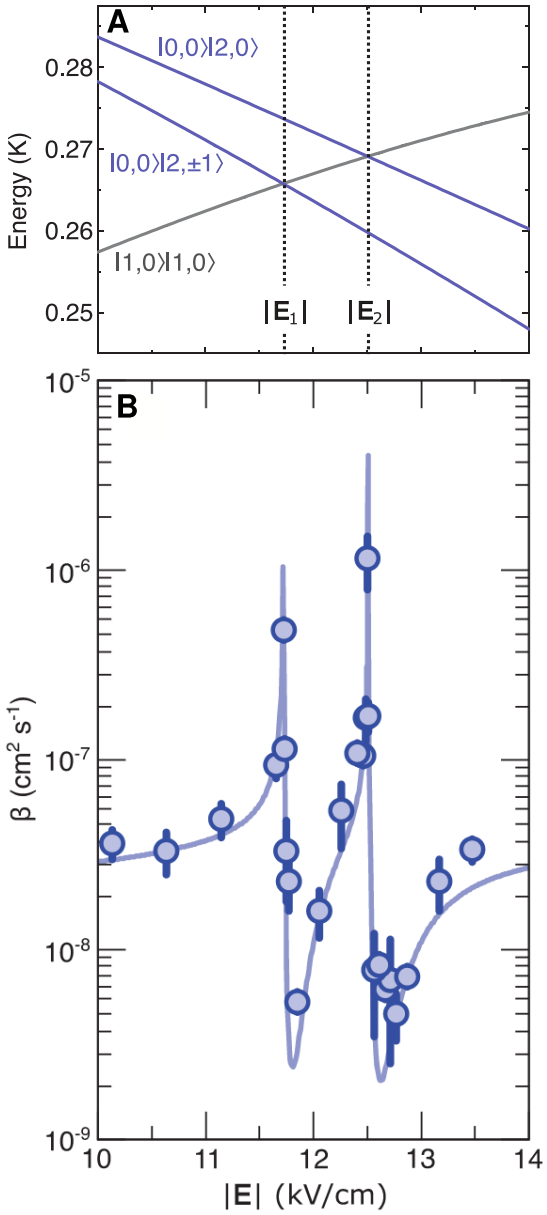

Figure 6.5: Measurement of the shielding resonances. (A) Energies of $|1,0\rangle|1,0\rangle$ (gray), and $|0,0\rangle|2,0\rangle$ and $|0,0\rangle|2,\pm1\rangle$ (blue) as a function of $|\mathbf{E}|$. The two state crossings at $|\mathbf{E}_1|$ and $|\mathbf{E}_2|$ are clearly visible. (B) Summary of β measurements near $|\mathbf{E}_1|$ and $|\mathbf{E}_2|$. The data agree well with the theoretical calculation (solid line) with no free parameters, using the experimentally measured T and ω_y. The field is oriented along $\hat{\mathbf{y}}$ for these measurements. Adapted from Ref. [137].

6.5B, showing the extreme tunability of the reactive loss by almost three orders of magnitude near the crossings. In particular, we measured a factor of 8(3) suppression in β between the shielded (12.77 kV/cm) and background (10.13 kV/cm) loss rates, realizing a collisionally-shielded and long-lived gas of molecules at a high electric field. The solid lines in (B) are theoretical calculations for $m_L = \pm 1$ collisions with no free parameters, using the experimental T and ω_y. The calculations were performed in 3D and scaled to quasi-2D using $\beta_{2\mathrm{D}} = \beta_{3D}/\sqrt{\pi} a_{\mathrm{ho}}$ [102], where a_{ho} is the harmonic oscillator length along $\hat{\mathbf{y}}$.

6.3 Probing the collision anisotropy

The measurements described so far had $\mathbf{E}$ oriented along $\hat{\mathbf{y}}$, so the molecules collided with $m_L = \pm 1$ as in the previous 2D work. Thanks to our highly controllable electric field (section 3.3), we are also able to rotate the electric field in the x-y plane by an angle θ away from $\hat{\mathbf{y}}$. Changing θ, in conjunction with the 2D confinement, allows us to probe the anisotropy of the collisions. At $\theta = 0°$, $\mathbf{E}$ is perpendicular to the 2D pancakes (x-z plane) and the molecules only meet in side-to-side collisions ($m_L = \pm 1$). However at $\theta = 90°$, $\mathbf{E}$ lies within the pancakes and the molecules have both head-to-tail ($m_L = 0$) and side-to-side ($m_L = \pm 1$) collisions, as shown schematically in Figure 6.6A. Note that in this section, we define m_L and m_N as the projections of L and N onto the quantization axis $\mathbf{E}$, instead of onto the fixed axis $\hat{\mathbf{y}}$. Since the dipoles are aligned along $\mathbf{E}$, this means that the usual picture of a head-to-tail (side-to-side) approach corresponding to a $m_L = 0$ (± 1) collision still holds as θ is varied.

6.3.1 Contribution of m_L states vs θ

By rotating $\mathbf{E}$, we can measure the loss rate β_0 in the $m_L = 0$ channel and compare it with the loss rate $\beta_{\pm 1}$ in the $m_L = \pm 1$ channels, which maps out the shielding as a function of the relative orientation of the molecules. A rigorous treatment of the collisions of tilted dipoles in quasi-2D can be found in Ref. [206]. In this work, we approximated the collisions by considering only the lowest three angular momentum states $m_L = 0, \pm 1$. Since the dipolar interactions are

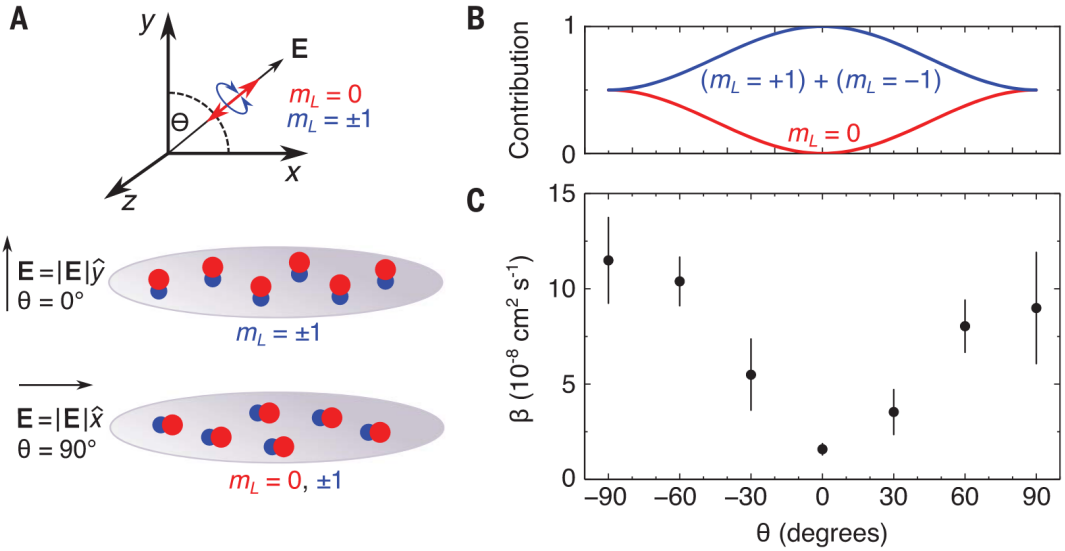

Figure 6.6: Collisions in quasi-2D with tilted **E**. (A) Schematic diagram of the collisions. The angular momentum states are defined with respect to **E**, which sets the quantization axis. At $\theta = 0°$, the molecules only experience $m_L = \pm 1$ collisions. At $\theta = 90°$, the molecules experience all three of $m_L = 0, \pm 1$. (B) Normalized contributions of the various m_L states to the scattering as θ is varied. The lines are the weighting factors from equations (6.17) and (6.18). (C) Measured loss rate β of $|1, 0\rangle$ molecules at $|\mathbf{E}| = 7.09$ kV/cm as a function of θ. Reproduced from Ref. [137].

relatively weak (except for in a narrow range of $|\mathbf{E}|$ near resonance[2]), the dipolar length a_D is small compared to the harmonic oscillator length $a_{\rm ho} = \sqrt{\hbar/\mu\omega_y}$, and the collisions can be treated as 3D. For the largest induced dipole $|d| \approx 0.1$ D studied here, we obtain $a_D = 180a_0$ compared to $a_{\rm ho} = 1800a_0$. The dipolar interactions are weak enough that different L are not strongly mixed, and hence we consider only the lowest manifold $L = 1$.

Rotating the field mixes the angular momentum states $|L = 1, m_L\rangle$ together. The initially allowed states at $\theta = 0$ are $m_L = \pm 1$ owing to the 2D confinement. These states transform under $\theta \neq 0$ according to the Wigner rotation matrices [108],

$$|L = 1, m_L = 1\rangle \to |\psi_{+1}(\theta)\rangle = \frac{1 + \cos\theta}{2}|1, 1\rangle - \frac{\sin\theta}{\sqrt{2}}|1, 0\rangle + \frac{1 - \cos\theta}{2}|1, -1\rangle \tag{6.14}$$

$$|L = 1, m_L = -1\rangle \to |\psi_{-1}(\theta)\rangle = \frac{1 - \cos\theta}{2}|1, 1\rangle + \frac{\sin\theta}{\sqrt{2}}|1, 0\rangle + \frac{1 + \cos\theta}{2}|1, -1\rangle. \tag{6.15}$$

Roughly speaking, we want to figure out the probability $P_{m_L}(\theta)$ of scattering with m_L as a function

[2] We can estimate the effect of the dipolar coupling between the channels directly on resonance by calculating $a_D \sim \mu d_{21} d_{10}/4\pi\epsilon_0\hbar^2 = 1040a_0$, corresponding to a dipole moment $d \sim \sqrt{d_{21}d_{10}} = 0.24$ D.

of θ,

$$P_{m_L}(\theta) = \frac{|\langle 1, m_L|\psi_{+1}(\theta)\rangle|^2}{2} + \frac{|\langle 1, m_L|\psi_{-1}(\theta)\rangle|^2}{2} \tag{6.16}$$

$$P_{-1}(\theta) = P_{+1}(\theta) = \frac{1+\cos^2\theta}{4} \tag{6.17}$$

$$P_0(\theta) = \frac{\sin^2\theta}{2} \tag{6.18}$$

The total loss rate β is the sum over the rates β_{m_L} in each m_L, weighted by $2P_{m_L}(\theta)$. The factor of 2 comes from the fact that the total loss rate is the sum over the individual loss rates in each channel, not the average. This yields the following expression for β,

$$\beta(\theta) = \beta_0 \sin^2\theta + (\beta_{-1} + \beta_{+1})\frac{1+\cos^2\theta}{2}. \tag{6.19}$$

As a check, note that $\beta(0^\circ) = \beta_{-1} + \beta_{+1}$ and $\beta(90^\circ) = \beta_0 + (1/2)(\beta_{-1} + \beta_{+1})$, which matches our intuition from Figure 6.6A. The full dependence on θ is shown in Figure 6.6B, which plots $P_0(\theta)$ (red line) and $P_1(\theta) + P_{-1}(\theta)$ (blue line). By combining measurements at $\theta = 0^\circ$ and $\theta = 90^\circ$, we can obtain β_0 and $\beta_1 + \beta_{-1}$ separately.

Figure 6.6C shows the measured β for $|1,0\rangle$ molecules at $|\mathbf{E}| = 7.09$ kV/cm, as a function of θ. At $\theta = 0^\circ$, β is minimized due to the repulsive $m_L = \pm 1$ dipolar collisions ($d = -0.12$ at this field). As θ is changed away from 0°, attractive $m_L = 0$ collisions enter the scattering and β increases. At $\theta = 90^\circ$, β is increased by an order of magnitude over $\theta = 0^\circ$.

Leaving the resonant shielding for a moment, let us briefly discuss the collisions of tilted dipoles. The data in Figure 6.6C was taken at $|\mathbf{E}| = 7.09$ kV/cm, where $|d|$ is maximized for $|1,0\rangle$ (in our range of accessible $|\mathbf{E}|$), in order to maximize the change of β with θ. However, we should see an even bigger effect of θ using the $|0,0\rangle$ state, which has a much larger d. The combination of a large d and tilted $\mathbf{E}$ is predicted to cause some interesting effects — for example, molecules may be excited to higher bands in the lattice during a collision when their dipoles are tilted [206]. We have taken some preliminary data with $|0,0\rangle$ that shows a rapid increase of the loss when the dipoles are tilted by even a few degrees (Figure 6.7), though more systematic studies are needed to say anything more.

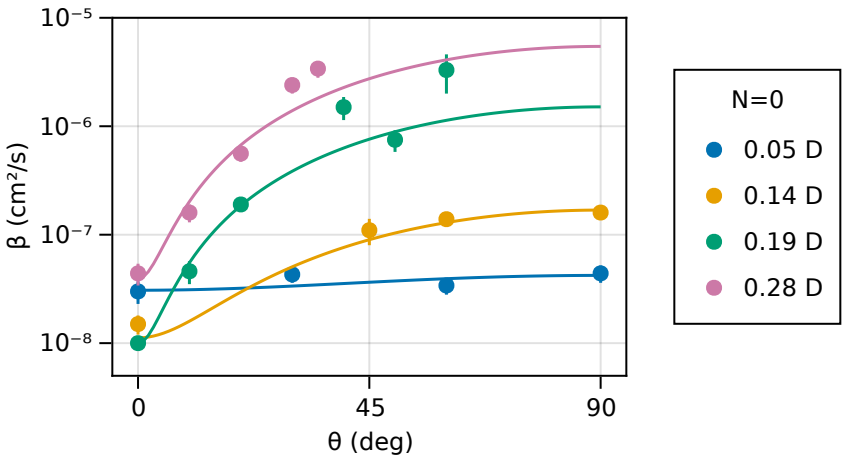

Figure 6.7: Collisions of $|0,0\rangle$ in tilted $\mathbf{E}$. Points are experimental data, lines are fits to equation (6.19) with fitting parameters β_0 and $(\beta_{-1}+\beta_{+1})$. For larger d, a sharp rise in β is observed when θ is changed away from 0°. The values of β at $\theta = 0°$ follow the trend in Figure 5.9B: as d is increased, β is initially suppressed before increasing again at high d (owing to the quasi-2D nature of the system).

6.3.2 Shielding in $m_L = 0$

As explained in the previous section we can extract $\beta_{\pm1} \equiv \beta_{-1} + \beta{+}1$ and β_0 by combining measurements at $\theta = 0°$ and 90°. We measured $\beta_{\pm1}$ (A) and β_0 (B) over a wide range of $|\mathbf{E}|$ to map out the shielding resonances, shown in Figure 6.8. In the background region away from the resonances, we observed $\beta_0 > \beta_{\pm1}$, consistent with the picture of dipolar attraction ($m_L = 0$) or repulsion ($m_L = \pm1$) from Ref. [52]. Near resonance, we observed sharp features at $|\mathbf{E}_1|$ and $|\mathbf{E}_2|$ in both angular momentum states. In particular, in the $m_L = 0$ channel, we observed a variation of β_0 by a factor of 1000(400) near the features, and a suppression of β_0 by a factor of 23(10) at the maximum shielding (11.84 kV/cm) compared to the background loss rate (at 11.32 kV/cm). The experimental measurements agree well with theoretical calculations (solid lines) with no free parameters.

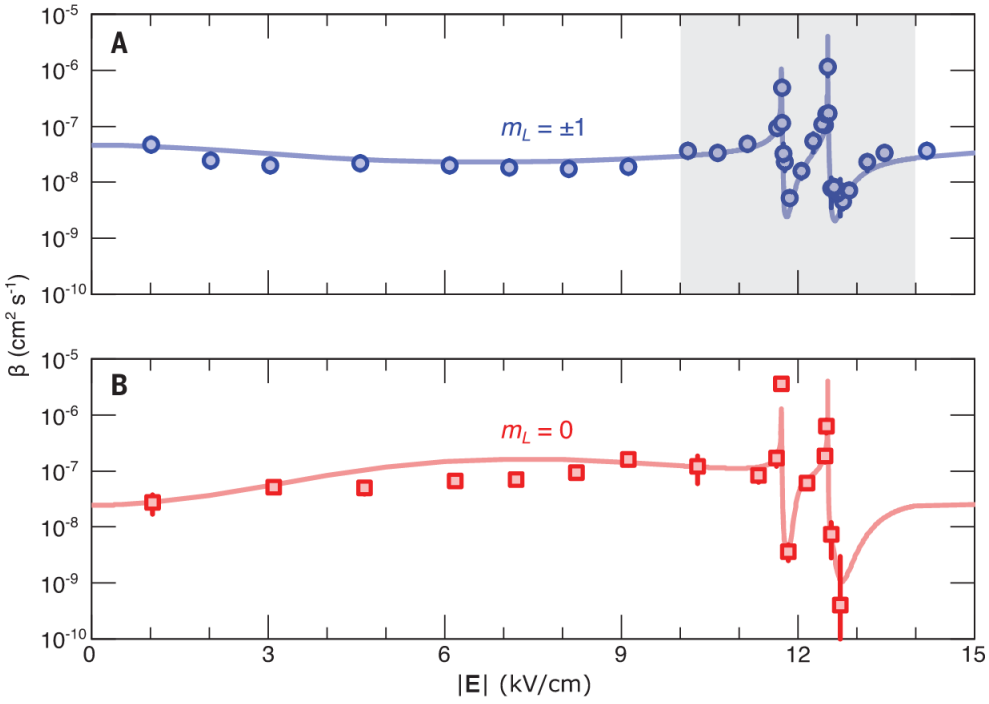

Figure 6.8: Summary of 2D shielding. (A) $\beta_{\pm 1}$ as a function of $|\mathbf{E}|$. (B) β_0 as a function of $|\mathbf{E}|$. The solid lines are theoretical calculations with no free parameters, using the experimental T and ω_y. The gray shaded region in (A) is the same as Figure 6.5B. Reproduced from Ref. [137].

6.4 Shielding in 3D

Figure 6.8 shows that the shielding is indeed effective in all three of $m_L = 0, \pm 1$, as expected from theoretical predictions [104] and the arguments in section 6.1. Next, we explored the shielding in 3D and elastic collisions at the shielding field ($|\mathbf{E}_s| = 12.72$ kV/cm) [138]. For KRb, we observed that the elastic collisions are nearly unaffected at $|\mathbf{E}_s|$, displaying the same anisotropy expected for pure dipolar scattering [136, 207]. We were also able to perform efficient evaporative cooling at $|\mathbf{E}_s|$ to increase the PSD of the molecules. These results demonstrate tunable dipolar interactions in a long-lived 3D gas of molecules.

For the 3D loss measurements, we followed a similar procedure to the 2D shielding measurements, except the molecules were created in the ODT without the LSL or VL. Typical starting conditions for the measurements were $N = 15 \times 10^3$ molecules at $T = 330$ nK. The ODT trap frequencies were $(\omega_x, \omega_y, \omega_z) = 2\pi \times (45, 250, 45)$ Hz for $|1, 0\rangle$ at $|\mathbf{E}_{\mathrm{STIRAP}}| = 4.5$ kV/cm, with a

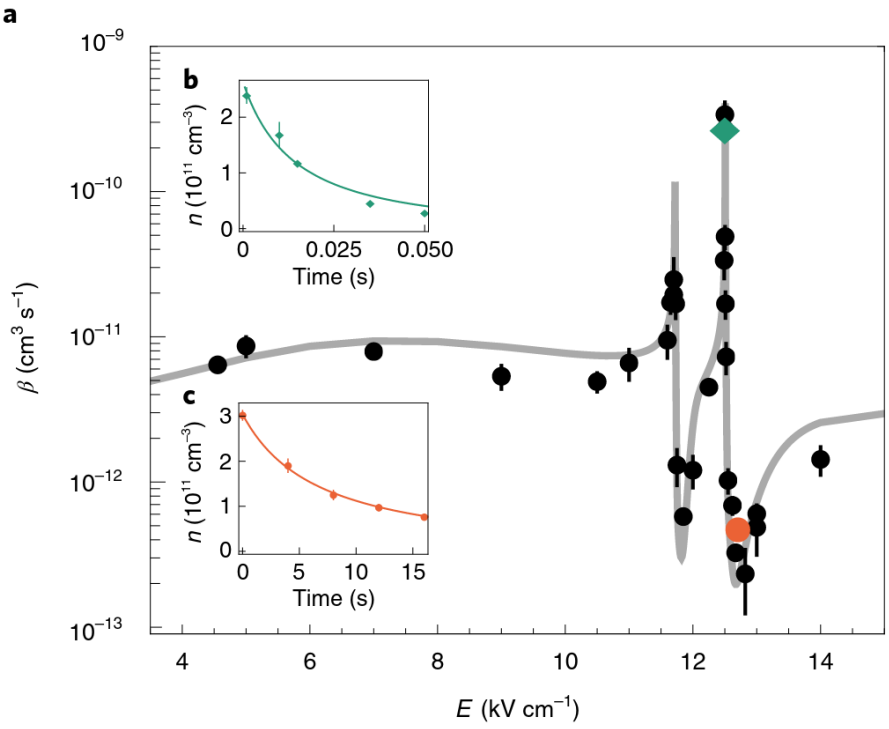

Figure 6.9: Resonant shielding in 3D. (A) Measured 3D loss rate coefficient β as a function of $|\mathbf{E}|$. The data agree well with a theoretical calculation (solid line) at $T = 330$ nK with no free parameters. (B) Molecule loss measurement at $|\mathbf{E}| = 12.50$ kV/cm. (C) Molecule loss measurement at $|\mathbf{E}_s| = 12.72$ kV/cm. Reproduced from Ref. [138].

weak dependence on $|\mathbf{E}|$ [113]. We fit the average 3D molecular density n as a function of hold time to a differential equation that incorporates two-body loss and heating [79, 50],

$$\frac{dn}{dt} = -\beta n^2 - \frac{3n}{2T}\frac{dT}{dt}, \tag{6.20}$$

where β is the two-body loss rate coefficient.

Figure 6.9 shows the measured β as a function of $|\mathbf{E}|$. The shielding resonances at $|\mathbf{E}_1|$ and $|\mathbf{E}_2|$ are again strikingly sharp. At $|\mathbf{E}_s|$ (orange point in (A), and inset (C)), the molecules had a long lifetime ~ 10 s, realizing a long-lived 3D gas at high electric field.

6.4.1 Elastic collisions at the shielding field

The long shielded lifetime of the molecules provided an opportunity to study the elastic collisions of KRb in 3D for the first time. One question we had was whether the shielding would

substantially modify the dipolar elastic collisions. For fermionic dipoles at low temperature, neglecting the resonant shielding, $\sigma_{\rm el}$ is given by the universal prediction $\sigma_{\rm el} = (32\pi/15)a_D^2$, where a_D is the dipolar length [129, 136]. The resonant shielding modifies the effective intermolecular potential and hence also affects the elastic collisions. Numerical calculations from Ref. [104] predict that $\sigma_{\rm el}$ is sharply enhanced very close to the resonances, where the loss is also maximized, but is only slightly modified from the universal value at $|\mathbf{E}_s|$. At $|\mathbf{E}_s|$, KRb in the $|1,0\rangle$ state has $d = -0.08$ D, corresponding to a universal prediction of $\sigma_{\rm el} = 2.8 \times 10^{-12}$ cm^2.

In addition to changing the total cross section $\sigma_{\rm el}$, the shielding could also conceivably alter the anisotropy of the collisions. We measured both $\sigma_{\rm el}$ and the collision anisotropy using cross-dimensional thermalization measurements. The trap intensity was modulated at a frequency of $2\omega_y$ to parametrically heat the molecules along the $\hat{\mathbf{y}}$ direction. We then monitored the temperatures T_x and T_y along $\hat{\mathbf{x}}$ and $\hat{\mathbf{y}}$ as a function of the hold time. The molecules thermalized with a rate $\Gamma_{\rm th} = \Gamma_{\rm el}/N_{\rm coll}$, where $\Gamma_{\rm el} = n\sigma_{\rm el}v_{\rm th}$ is the elastic collision rate and $v_{\rm th}$ the thermally-averaged relative velocity. The parameter $N_{\rm coll}$ is the number of collisions required to thermalize, which characterizes how efficiently the collisions redistribute energy between the axes. For contact interactions, $N_{\rm coll} = 2.7$ for s-wave collisions and 4.1 for p-wave collisions. Since the dipolar interactions are anisotropic, $N_{\rm coll}$ depends on the relative angle θ between the excitation direction $\hat{\mathbf{y}}$ and the dipole orientation (parallel to $\mathbf{E}$) [136]. Anisotropic rethermalization of dipoles was previously studied in fermionic [208] and bosonic [209] gases of strongly magnetic atoms.

We performed cross-dimensional thermalization measurements at $|\mathbf{E}_s|$ and several values of θ to measure the dependence of $N_{\rm coll}$ on θ. Experimentally, θ was varied by rotating $\mathbf{E}$ in the x-y plane. The cloud was parametrically heated for 50–100 ms to achieve an initial temperature imbalance of $T_y \approx 2.5T_x$, then allowed to rethermalize during a variable hold time. Panels (A) and (B) of Figure 6.10 show thermalization measurements at $\theta = 45°$ and $\theta = 90°$, respectively, demonstrating the large variation in $\Gamma_{\rm th}$ that can be observed by rotating θ.

To analyze these data quantitatively, the measured n, T_x, and T_y were fit to the following set

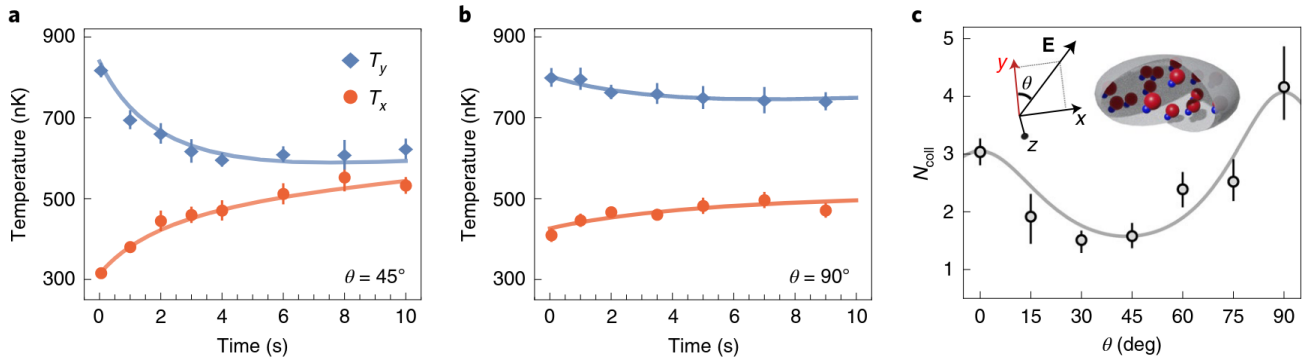

Figure 6.10: Thermalization measurements at $|\mathbf{E}_s|$. (A) and (B) show cross-dimensional thermalization measurements at $\theta = 45°$ and $90°$, respectively. (C) Summary of N_{coll} vs θ. Reproduced from Ref. [138].

of coupled differential equations,

$$\frac{dn}{dt} = -K_L(T_y + 2T_x)n^2 - \frac{n}{2T_y}\frac{dT_y}{dt} - \frac{n}{2T_x}\frac{dT_x}{dt} \tag{6.21}$$

$$\frac{dT_y}{dt} = \frac{n}{4}K_L(-T_y + 2T_x)T_y - \frac{2\Gamma_{\text{th}}}{3}(T_y - T_x) + c_y \tag{6.22}$$

$$\frac{dT_x}{dt} = \frac{n}{4}K_L T_y T_x + \frac{\Gamma_{\text{th}}}{3}(T_y - T_x) + c_x, \tag{6.23}$$

which capture the complicated interplay of loss, anti-evaporation, and rethermalization in the system [79]. Above, c_x and c_y are background heating rates and K_L represents the two-body loss per spatial direction. (In equilibrium, $\beta = 3K_L T$.) In Γ_{th}, $v_{\text{th}} = \sqrt{8k_B(2T_x + T_y)/3\pi\mu}$ is defined using the average temperature. The equations assume that the temperatures along the two unmodulated directions, T_x and T_z, remain equal throughout the thermalization process.

By fitting the thermalization rates at each θ, we could extract N_{coll} as a function of θ (Figure 6.10C). From the cross-dimensional thermalization measurement, we cannot independently determine σ_{el} and N_{coll}, so we assumed the universal value for σ_{el}. We observed a strong dependence of N_{coll} on θ, a direct consequence of the anisotropy of the collisions. Near $\theta = 45°$, $N_{\text{coll}} = 1.6^{+0.2}_{-0.1}$ was lower than the value of 2.7 for s-wave collisions, signalling very efficient thermalization. The experimental data agrees well with theoretical calculations for purely dipolar scattering from Reuben Wang and John Bohn (solid line) [207], demonstrating that the dipolar character of the elastic collisions is preserved at $|\mathbf{E}_s|$.

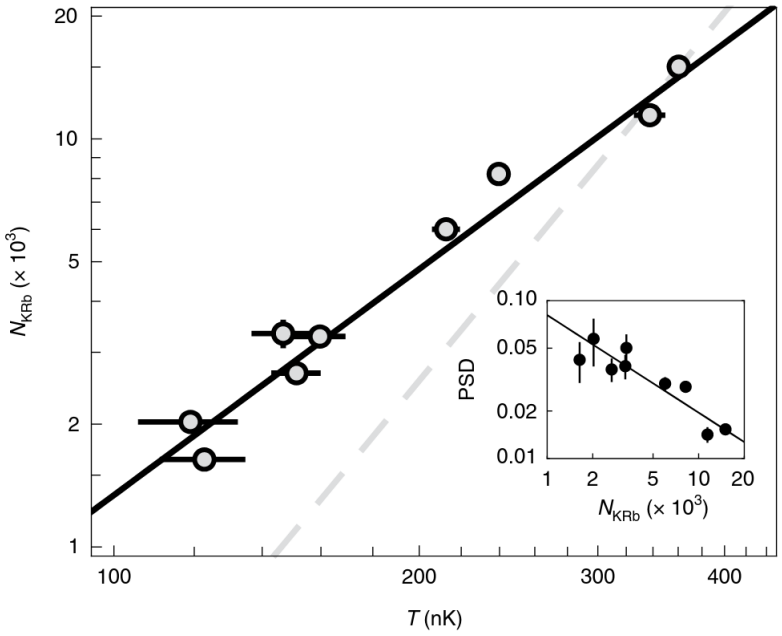

Figure 6.11: Evaporation of molecules in 3D. The main panel shows the trajectory of N and T during the evaporation. We extract a slope $S_{\text{evap}} = 1.84(9)$ (solid line), indicating efficient evaporation. For comparison, a slope of $S_{\text{evap}} = 3$ (dashed line) does not increase PSD. The inset shows the increase of PSD during the evaporation as the total molecule number is reduced. Reproduced from Ref. [138].

6.4.2 Direct evaporation of molecules in 3D

From the measured loss rates, we extract a ratio of good to bad collisions $\gamma = \sigma_{\text{el}}/\sigma_{\text{re}} = 12(1)$, where $\sigma_{\text{re}} = \beta/v_{\text{th}}$ is the cross section for reactive collisions, so elastic collisions dominate in the system. While this ratio is not as favorable as the $\gamma = 200(60)$ that we found for $|0,0\rangle$ molecules in 2D, it was still high enough for us to see dipolar evaporation of the molecules in 3D for the first time. Figure 6.11 shows the evaporation trajectory, obtained by lowering the ODT power at $|\mathbf{E}_s|$ and $\theta = 0°$. The solid line shows the fitted $S_{\text{evap}} = \partial \log N/\partial \log T = 1.84(9)$, compared to the upper threshold of $S_{\text{evap}} = 3$ (dashed line) to increase PSD in 3D. The inset shows that the PSD increased by roughly a factor of 4, from 0.014(1) to 0.06(2), corresponding to a reduction in T/T_F from 2.3(1) to 1.4(2).

The best T/T_F reached by evaporation in 3D was still higher than the conditions of $N = 25 \times 10^3$ and $T/T_F = 0.3$ in our previous 3D work [50]. We attribute most of this discrepancy to the

additional technical challenges involved with preparing the molecules in $|1,0\rangle$ at $|\mathbf{E}_s|$. In particular, losses during the ramp from $\mathbf{E}_{\mathrm{STIRAP}}$ to $\mathbf{E}_s$ limit the initial molecule number for evaporation. After some upgrades to our STIRAP lasers, we now have the ability to create molecules directly at $\mathbf{E}_s$ (see Ref. [107]), which should allow us to improve the initial evaporation condition and reach a lower T/T_F.

6.5 Conclusion

The resonant shielding is a powerful technique for controlling molecular losses by leveraging the transition dipole moments of the molecules. It is highly general in terms of molecular species [104, 205, 204] and geometry, working in 2D and 3D. For species with larger dipole moments than KRb, the achievable γ is expected to be as high as 10^6 [204], which should facilitate highly efficient evaporation. Our measurements of N_{coll} showed that the elastic collisions at $|\mathbf{E}_s|$ are very similar to those of pure dipoles, suggesting that the resonant shielding could be an excellent setting for studying 3D dipolar phenomena such as Fermi surface deformation [210] and sound propagation [211, 212].

In the previous chapter, we discussed the 2D loss suppression from repulsive dipolar collisions, which realized a non-resonant collisional shielding. Together with the resonant shielding, these techniques form a powerful toolbox for controlling molecular losses while retaining strong elastic collisions. In addition, the Harvard CaF [105] and Munich NaK [54] groups recently demonstrated microwave shielding [161, 213], in which the $N = 0$ and $N = 1$ states are coupled using a blue-detuned microwave drive. The microwave photons supply the necessary energy to make the dipolar interactions between these states near-resonant, similar to the role played by $|\mathbf{E}|$ in the resonant shielding, resulting in shielding from loss. An advantage of microwave shielding, as opposed to resonant shielding, is that the additional degree of freedom (Rabi frequency and detuning, as opposed to only the detuning for resonant shielding) allows one to also enhance the elastic collision rate. Ref. [54] was able to leverage this to perform efficient evaporative cooling to a degenerate Fermi gas in 3D. One advantage of the resonant shielding, however, is the ability to easily tune the

dipole orientation by tilting **E**. In contrast, for microwave shielding the quantization axis is set by the microwave polarization, which may be more difficult to rotate.

There have also been exciting recent advances in controlling atom-molecule collisions. For the NaLi + Na system, $\gamma > 50$ was achieved, enabling sympathetic cooling of NaLi by Na [214]. Additionally, atom-molecule Feshbach resonances have been observed in NaK + K [96] and NaLi + Na [98], even allowing the association of loosely-bound triatomic molecules [97]. For KRb, Ref. [215] observed an anomalously long lifetime of KRb + Rb complexes, which may suggest that it is possible to find Feshbach resonances in this system as well. However, the complexes were observed to be destroyed by the 1064 nm trapping light, so such explorations might need to be done in a box trap [94].

Chapter 7

Single-layer control of molecules in a 1D optical lattice

In the previous two chapters, we discussed two different methods for protecting the molecules from unwanted reactive losses. With the losses under control, we renewed our focus on studying 2D dipolar physics. As previously mentioned, dipolar interactions in 2D provide a very interesting setting for studying many-body physics. The interplay of the long-range interaction with reduced dimensionality leads to new phenomena in 2D, such as condensation of rotational excitations [185, 216, 217]. In addition, the combination of the dipolar anisotropy and strong confinement makes the many-body behavior of the system highly tunable with the dipole orientation [45, 218]. These elements combine to lead to intriguing phenomena in 2D such as topological superfluidity [42, 43], spin liquids [40], and spin-squeezing [49].

For many of these proposals, a single 2D layer of molecules is required. Since the dipolar interactions are long ranged, molecules in adjacent 2D layers can interact, potentially competing with the intralayer interactions. We can also flip this statement around — by controlling the internal state of the molecules in a layer-resolved manner, we can gain control of the interlayer interactions and thus enable a new level of control over the molecules.

In this chapter, we show how to prepare molecules in a single 2D layer by performing microwave spectroscopy in an electric field gradient. The gradient causes a layer-to-layer shift of the $|0,0\rangle$ to $|1,0\rangle$ transition, which allows us to individually address each layer. A similar technique is used in ultracold atom experiments to select 2D planes, for example in quantum gas microscopes [219, 220], but with a magnetic field rather than electric field. The capability of layer-resolved

internal state control allows us to observe interlayer dipolar exchange interactions by putting adjacent layers in different (dipole-coupled) rotational states. The interlayer interactions manifest as an enhancement of the reactive loss rate, allowing layer-to-layer control of the chemical reactions mediated by the dipolar interactions.

This chapter is based on the work in Ref. [152]. We will focus mainly on the high-level results here, but getting the layer selection to work well required solving a number of technical challenges on the experiment. Will Tobias led much of these efforts and his thesis covers those aspects in detail [107].

7.1 Addressing a single layer

For the experiments in this chapter, we created molecules in 2D in the VL. The procedure was similar to Chapter 5, but without using the LSL. The LSL was removed to purposefully load many layers in VL, in order to make the center of the layer distribution very homogeneous. This was advantageous for our studies of three isolated layers, where we wanted to make the molecule number in each as similar as possible. Typical starting conditions for the experiments were $N = 20 \times 10^3$ molecules at $T = 350$ nK in about 15–20 layers of the VL. Owing to the large number of populated layers, $T/T_F \approx 3.5$ for these studies. Molecules were produced using STIRAP at $|\mathbf{E}_{\text{bias}}| = 1$ kV/cm. The combined trap frequencies of the ODT + VL were $(\omega_x, \omega_y, \omega_z) = 2\pi \times (42, 17 \times 10^3, 48)$ Hz for $|0, 0\rangle$ molecules at $|\mathbf{E}_{\text{bias}}|$.

The molecules were imaged in situ in the VL by dissociating the ground state molecules with STIRAP and imaging the Feshbach molecules. The VL layers are too closely spaced to be optically resolvable, so our measurements gave the total number of molecules in each internal state, summed over the populated layers. Since STIRAP is state-selective, we could measure the number of molecules in each rotational state $|N\rangle \equiv |N, m_N = 0\rangle$, allowing us to normalize by the total molecule number when desired. However, we found that the $|0\rangle$ imaging pulse caused a significant loss of $|1\rangle$ molecules by excitation to a different intermediate state. Since we did not observe the same loss in $|2\rangle$, we solved this problem by shelving $|1\rangle$ in the $|2\rangle$ state during the $|0\rangle$ imaging pulse.

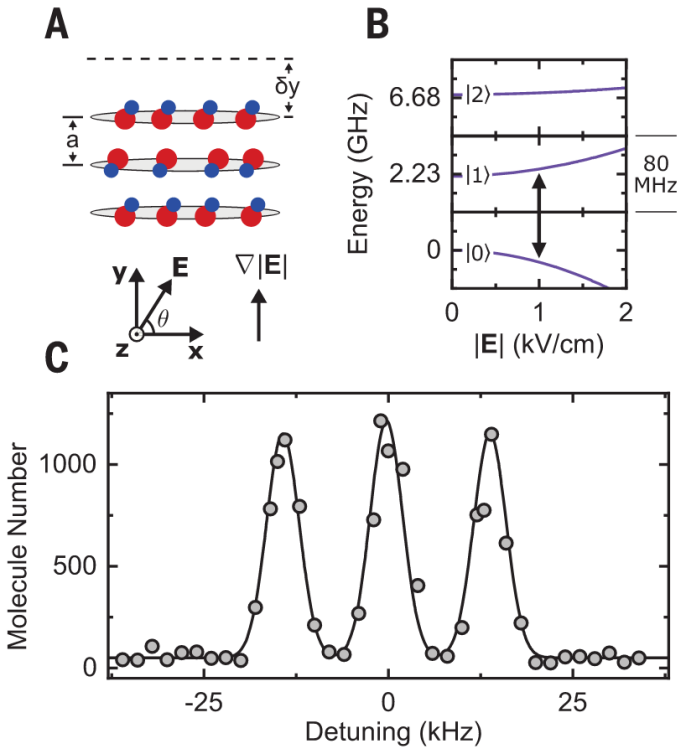

Figure 7.1: Layer-resolved spectroscopy. (A) Schematic of the molecules in several layers of the VL. A strong vertical field gradient $\nabla|\mathbf{E}|$ parallel to $\hat{\mathbf{y}}$ is used to create a site-to-site shift of the $|0\rangle \leftrightarrow |1\rangle$ transition frequency. (B) Energy shifts of rotational states with $|\mathbf{E}|$ near $|\mathbf{E}_{\text{bias}}| = 1$ kV/cm. (C) Spectroscopy of a trilayer of molecules. A gradient of $\partial|\mathbf{E}|/\partial y = 6.4(2)\,\text{kV/cm}^2$ was used, giving a layer-to-layer shift of $\Delta = h \times 14$ kHz. Reproduced from Ref. [152].

The basic principle of the layer selection is shown in Figure 7.1A. The molecules are held in the VL with a layer spacing of $a = 540$ nm along $\hat{\mathbf{y}}$. We apply a bias electric field of strength $|\mathbf{E}_{\text{bias}}|$ and variable tilt θ to cancel differential AC Stark shifts [113, 110]. In contrast to the previous chapter, the tilt angle θ is defined between $\mathbf{E}$ and the VL polarization (along $\hat{\mathbf{x}}$). By applying a gradient $\nabla|\mathbf{E}| = \hat{\mathbf{y}}(\partial|\mathbf{E}|/\partial y)$, we induce a site-to-site Stark shift of the rotational transition from $|0\rangle$ to $|1\rangle$. The DC Stark shifts of $|0\rangle$, $|1\rangle$, and $|2\rangle$ near 1 kV/cm are shown in (B), demonstrating the shift of the $|0\rangle \leftrightarrow |1\rangle$ transition with $|\mathbf{E}|$. At $|\mathbf{E}_{\text{bias}}|$, the differential dipole moment is $(d_0 - d_1)/h = 40$ kHz/(V/cm).

The vertical gradient $\partial|\mathbf{E}|/\partial y$ leads to a site-to-site transition shift

$$\Delta = \left(\frac{d_1 - d_0}{h}\right)\frac{\partial|\mathbf{E}|}{\partial y}a, \tag{7.1}$$

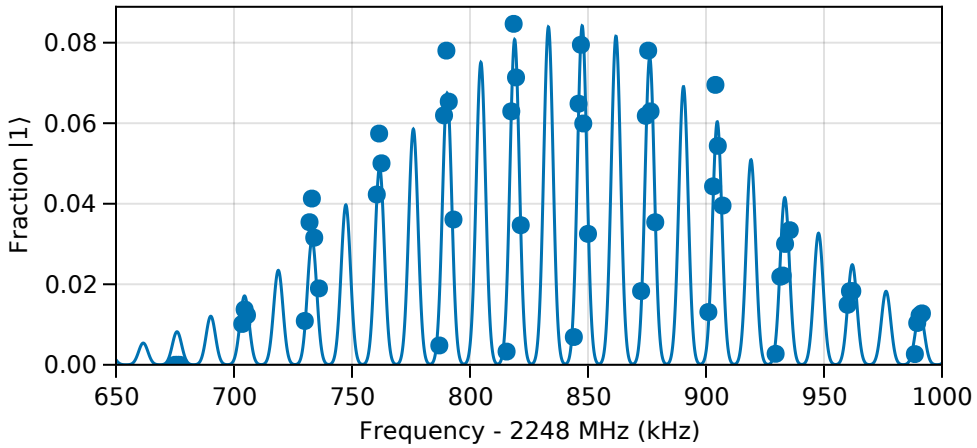

Figure 7.2: Spectroscopy on many layers. A narrow microwave π-pulse is scanned on a sample with ~ 20 layers, at $\partial|\mathbf{E}|/\partial y = 6.4$ kV/cm^2. By fitting the spectrum to a sum of Gaussian lineshapes with an overall Gaussian envelope, we extract the layer number $\tau = N/\langle N_i \rangle = 19(1)$. This data was taken in slightly different conditions from Ref. [152] (which had $\tau \approx 12$).

where d_N is the induced dipole moment of $|N\rangle$ at $|\mathbf{E}_{\text{bias}}|$ and $(\partial|\mathbf{E}|/\partial y)a$ is the change in the electric field between two neighboring sites. We typically used a gradient of $\partial|\mathbf{E}|/\partial y = 6.4\,\text{kV/cm}^2$, leading to a site-to-site shift of $\Delta = 14$ kHz. Figure 7.1C shows a microwave spectrum of three isolated layers (a "trilayer") with a field gradient of $\partial|\mathbf{E}|/\partial y = 6.4(2)$ kV/cm^2. Using a narrow microwave pulse, we cleanly resolved the three layers spectroscopically, showing that we could individually address and manipulate 2D layers.

This technique, combined with state-selective molecule removal, was used to initially prepare the trilayer system probed in Figure 7.1 from the initial distribution with many populated layers. Figure 7.2 shows a layer spectroscopy scan on an initial sample with 19 layers. The molecules were initially in the $|0\rangle$ state and were transferred to $|1\rangle$ with a narrow microwave π-pulse. The quantity on the y-axis is the number of $|1\rangle$ molecules divided by the total number of molecules. For Figure 7.2, we probed only every second occupied layer to reduce the data acquisition time. The data is fit (solid line) to a sum of Gaussian lineshapes representing the signal from each VL layer, with an overall Gaussian envelope to capture the layer distribution.

To prepare a trilayer as in Figure 7.1, we started with the molecules initialized in $|0\rangle$ and

many layers populated (as in Figure 7.2). We transferred only the three central layers to $|1\rangle$, and used resonant light from one of the STIRAP beams (690 nm) to blast away the untransferred molecules in $|0\rangle$. During the blast, the $|1\rangle$ layers were shelved in $|2\rangle$ to avoid excitation by the blast light. By further combining layer selective pulses on $|0\rangle \leftrightarrow |1\rangle$, global π-pulses on $|0\rangle \leftrightarrow |1\rangle$ and $|1\rangle \leftrightarrow |2\rangle$, and global optical blasts, we could prepare an arbitrary pattern of layers in $|0\rangle$, $|1\rangle$ and $|2\rangle$.

In this section, we glossed over many of the technical details required to make the layer selection work. The phase of the VL must be well-stabilized to the electrode assembly to keep the y-position (and thus transition frequency) of the layers stable from shot-to-shot. In addition, the axis of the VL must be well-aligned to the direction of the electric field gradient. Owing to the large radial extent of the cloud, we calculated that even small tilts of the VL of $< 1^\circ$ degree would completely wash out the layer structure. And of course, $|\mathbf{E}|$ must be stable enough to allow the necessary spectroscopic resolution to see individual layers. These technical aspects of the measurement are discussed in depth in Will Tobias's thesis [107]. One other important technical detail, the use of Blackman shaped pulses to minimize RF sidebands on the layer selection pulses, is discussed in section 3.4.1.

7.2 Magic angle electric field

An important prerequisite for the layer selection was reducing the inhomogeneous broadening from the different lattice potentials felt by $|0\rangle$ and $|1\rangle$. As discussed qualitatively in section 2.3.4, $|0\rangle$ and $|1\rangle$ experience a differential AC Stark shift from the trapping light that depends on the angle θ between the $\mathbf{E}$ and the light polarization. The differential shift leads to an inhomogeneous broadening of the lineshape on each layer, making the layers more difficult to spectroscopically resolve. In our experiments, the VL polarization is fixed along $\hat{\mathbf{x}}$, but we can rotate $\mathbf{E}$ to change θ. The polarizabilities of $|0\rangle$ and $|1\rangle$ are expected to be matched at the "magic angle" $\theta_\mathrm{m} = 54.7^\circ$ [113, 110], corresponding to the condition $\cos^2\theta_\mathrm{m} = 1/3$.

In this chapter, we used the experimentally determined value of $\theta_\mathrm{m} = 57^\circ$, found by measuring

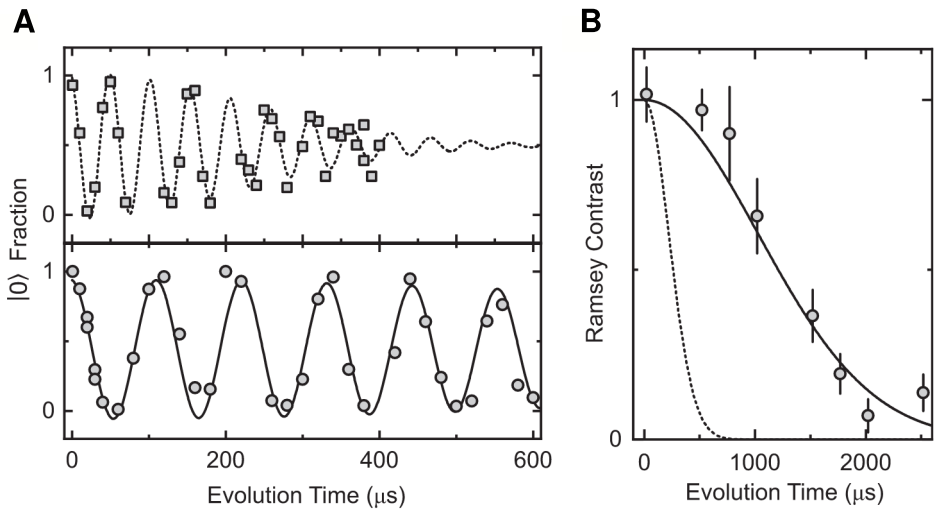

Figure 7.3: Rotational coherence of $|0\rangle$ and $|1\rangle$. (A) Comparison of Ramsey fringes for $\theta = 90°$ (top panel) and $\theta = \theta_{\mathrm{m}}$ (bottom panel). (B) Ramsey contrast decay at $\theta = \theta_m$. The decay is fit to a Gaussian envelope e^{-t^2/τ^2}, which gives a coherence time of $\tau = 1450(80)\,\mu$s. For comparison, the dashed line shows the fitted coherence decay for the non-magic ($\theta = 90°$) configuration from (A). Reproduced from Ref. [152].

the shift of the $|0\rangle \leftrightarrow |1\rangle$ transition as a function of the VL power at several values of θ. We also rotated the polarizations of the ODT beams such that their polarizations formed an angle of θ_{m} with $\mathbf{E}$. This configuration was used in the layer selection measurements (Figures 7.1 and 7.2) to maximize the layer contrast.

To characterize the differential AC Stark shift, we prepared a single layer of molecules and studied the coherence with Ramsey spectroscopy. Ramsey fringes for short evolution times are shown in Figure 7.3A, showing a clear difference between $\theta = 90°$ (top panel) and $\theta = \theta_{\mathrm{m}}$ (bottom panel). We fit both fringes to a sinusoid with a Gaussian envelope e^{-t^2/τ^2}, where t is the evolution time. At $\theta = 90°$, the differential polarizability is large, leading to a short coherence time $\tau = 310(30)\,\mu$s. In contrast, τ is significantly increased at θ_{m}. Figure 7.3B shows the envelope of the Ramsey contrast at θ_{m} as a function of evolution time t. For $t > 600\,\mu$s, the Ramsey oscillation phase became scrambled by slight shot-to-shot changes in $|\mathbf{E}|$ at the few 10s of ppm level. Thus, to extract the coherence at long times, we randomized the phase of the second Ramsey pulse and used the variance of the measured $|0\rangle$ and $|1\rangle$ populations to extract the contrast. Fitting the

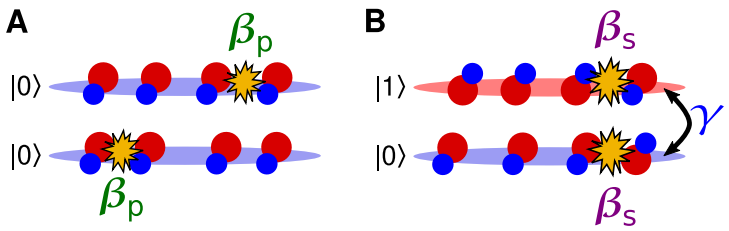

Figure 7.4: Cartoon of dipolar exchange induced losses. (A) Two adjacent layers are populated with molecules in the same state state $|0\rangle$. Each layer experiences slow p-wave losses at rate β_p. (B) Two adjacent layers are populated with $|1\rangle$ and $|0\rangle$, respectively. Interlayer dipolar exchange with rate γ causes a small population admixture in each layer, which is quickly lost via s-wave interactions at rate β_s. The intralayer p-wave loss β_p is not shown, but is also present in (B).

contrast decay, we extract $\tau = 1450(80)\,\mu$s at $\theta_{\rm m}$, a factor of 5 improvement over $\theta = 90°$ (dashed line). After the experiments of Ref. [152], we recalibrated $\theta_{\rm m}$ and found a slightly different value of $\theta_{\rm m} = 54°$, closer to the theoretical value of 54.7°. We attribute the discrepancy to small background gradients of $\mathbf{E}$ that were present when initially calibrating $\theta_{\rm m}$. With the updated value of $\theta_{\rm m}$, we were able to achieve Ramsey coherence times of about 4 ms, described in the next chapter.

7.3 Interlayer dipolar spin-exchange interactions

As introduced in section 2.6, a molecule in $|0\rangle$ and another in $|1\rangle$ can undergo dipolar spin-exchange and trade rotational angular momentum states [45, 46]. This interaction can be quite strong, since it arises from the transition dipole moment d_{01} between $|0\rangle$ and $|1\rangle$ ($d_{01} = d_{\rm perm}/\sqrt{3}$ at $|\mathbf{E}| = 0$), and it is a resonant process since the pair states $|0\rangle|1\rangle$ and $|1\rangle|0\rangle$ have the same energy. Our ability to prepare each 2D layer in a different rotational state allows us to explore and control these interactions in a layer-resolved manner. For example, we can imagine preparing a system with several adjacent layers populated in $|0\rangle$, except for the center layer which is initialized in $|1\rangle$. Ignoring losses for the moment, we would expect that the initial rotational excitation on the central layer diffuses to the adjacent layers through dipolar exchange. Perhaps the rate of diffusion could be changed with disorder (e.g., from an optical speckle pattern [221]) or a potential gradient [222, 223], allowing the study of localization in the system [224, 225].

In our bulk 2D layers, with no transverse lattices to suppress collisions, the most immediate effect of the spin-exchange interactions is an enhanced loss rate. This is depicted schematically in Figure 7.4. Consider two adjacent layers in the state $|0\rangle$, as in (A). Since all molecules are identical, the collisions within the layer are p-wave and the losses are relatively slow with rate β_p. However, if an adjacent layer is populated with molecules in $|1\rangle$, as in (B), then the layers are coupled via dipolar exchange interactions. This leads to a small admixture of $|1\rangle$ impurities in the predominantly $|0\rangle$ layer (and vice versa). Since impurities are distinguishable from the majority population, they are quickly lost in s-wave collisions with rate β_s. The spin-exchange rate γ is expected to be much faster than β_p but much slower than β_s, so the overall loss rate is limited by γ. This physical system was treated theoretically in Ref. [226] and in the Supplementary Material of Ref. [152].

To probe this effect, we created a trilayer of molecules and studied the loss by measuring the number N of molecules remaining in the central layer after a variable hold time (Figure 7.5A), with $\partial|\mathbf{E}|/\partial y = 0$. We fit the data to the solution of $dN/dt = -\beta N^2$ to extract the two-body loss rate coefficient β. Note that β has different units here than in the rest of this thesis. For convenience, we will refer to the trilayer configurations according to $N_1N_2N_3$, where N_i is the rotational quantum number of the ith layer. For example, 101 refers to a central layer of $|0\rangle$ between two layers of $|1\rangle$.

We started by measuring β_p and β_s as a baseline. To measure β_p, we prepared 000 and 111 trilayers, and found $\beta_p = 2.99(17) \times 10^{-3}\,\mathrm{s}^{-1}$ for $|0\rangle$ and $|1\rangle$ (green squares). We found a slightly different value $\beta_p = 1.78(24) \times 10^{-3}\,\mathrm{s}^{-1}$ for $|2\rangle$, which we attributed to a slightly smaller van der Waals coefficient for $|2\rangle$, though more measurements are needed to understand this. To measure β_s, we prepared a 000 trilayer and then applied a $\pi/2$ pulse to create a 50/50 mixture of $|0\rangle$ and $|1\rangle$. Fitting the decay of $|0\rangle$, we measured $\beta_s = 2.0(3) \times 10^{-1}\,\mathrm{s}^{-1}$ (purple triangles in inset), about two orders of magnitude higher than β_p [32].

For a 101 trilayer (blue circles), we observed an order of magnitude faster loss than in 111 (green squares). This demonstrates the strong enhancement of loss from the interlayer dipolar interactions. Using our rotational state control, we could also probe configurations where spin-

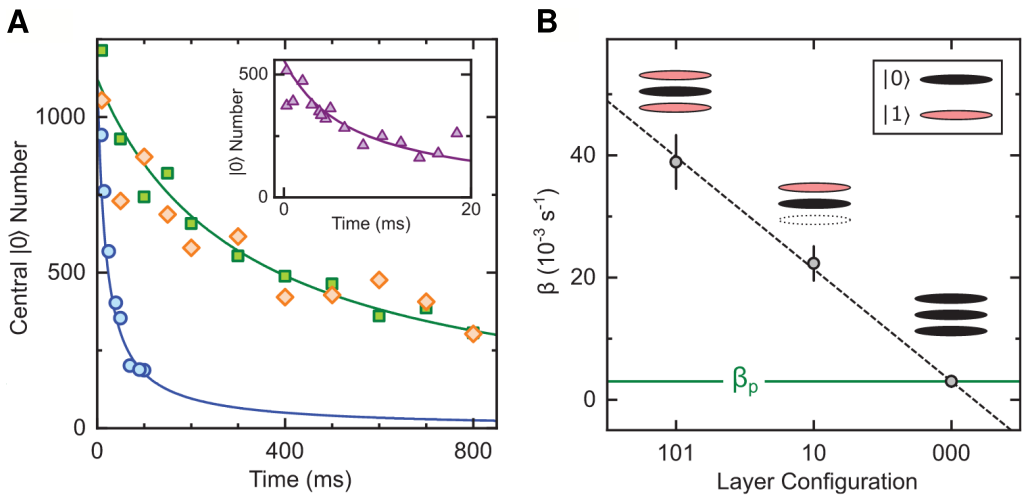

Figure 7.5: Losses induced by interlayer dipolar exchange. (A) Comparison of losses with and without dipolar exchange. In a 000 (green) or 202 trilayer (orange), dipolar exchange is forbidden and the molecule number decays slowly at β_p. The loss rate for a 101 trilayer (blue) shows a marked enhancement from interlayer dipolar interactions. Inset: loss measurement for a 50/50 mixture of $|0\rangle$ and $|1\rangle$, used to obtain β_s. (B) Density dependence of the dipolar exchange. The loss rate for a layer of $|0\rangle$ molecules shows a linear increase with the number of adjacent $|1\rangle$ layers. Reproduced from Ref. [152].

exchange is forbidden due to selection rules. For example, neglecting the small state mixing at $|\mathbf{E}_{\text{bias}}|$, the electric dipole transition between $|0\rangle$ and $|2\rangle$ is forbidden since N changes by two. Accordingly, a 202 trilayer (orange diamonds) experiences no interlayer dipolar exchange, and thus showed no enhancement of the loss rate above β_p. By changing the layer configuration, we could also vary the effective density of interacting molecules. Figure 7.5B shows that the exchange-induced loss rate between $|0\rangle$ and $|1\rangle$ was approximately doubled when doubling the number of adjacent layers, since the molecules in $|0\rangle$ have twice as many partners for exchange.

As mentioned before, dipolar spin-exchange is a resonant process. Thus, we were interested to see whether it could be suppressed by reintroducing the site-to-site transition shift Δ used for the layer selection. Note that Δ is precisely the detuning of the interlayer exchange from resonance. To study this quantitatively, we fit the measured loss curves to a rate equation that models the effects of β_p, β_s, and γ on the rotational populations in each layer, where γ is the average rate of spin-exchange in the gas [152]. This allowed us to extract γ as a function of Δ.

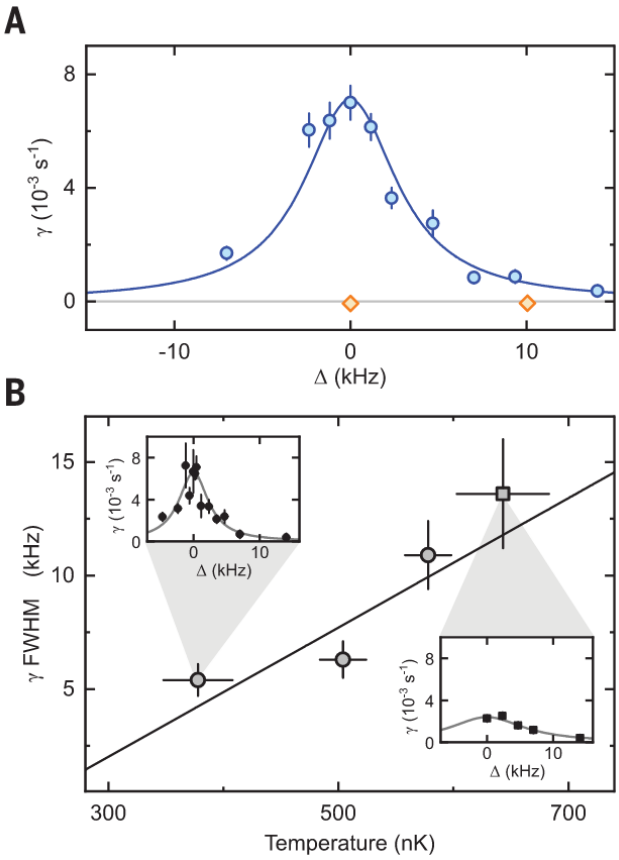

Figure 7.6: Dependence of the interlayer dipolar exchange on the site-to-site shift Δ. (A) Spin exchange rate γ versus Δ at $\theta = 90°$ and $T = 334(30)$ nK. The 101 trilayer (blue circles) shows a broad feature in $\gamma(\Delta)$, while the 202 trilayer (orange diamonds) are consistent with $\gamma = 0$ across the range of measured Δ. (B) FWHM of $\gamma(\Delta)$ for a 101 trilayer as T is varied, at $\theta = \theta_{\mathrm{m}}$. The insets show measurements of $\gamma(\Delta)$ at $T = 378(30)$ nK (circles, left inset) and 643(40) nK (squares, right inset). Reproduced from Ref. [152].

An example measurement of $\gamma(\Delta)$ is shown in Figure 7.6A. From a maximum value at $\Delta = 0$ of $\gamma = 7.0(6) \times 10^{-3}$ s^{-1}, γ was reduced with increasing $|\Delta|$ for 101 (blue circles). Measurements of the spin-exchange forbidden 202 system (orange diamonds) were consistent with $\gamma = 0$ over the full range of measured Δ. Perhaps surprisingly, $\gamma(\Delta)$ was quite broad for the 101 trilayer, with a full width at half maximum (FWHM) of 6.4(6) kHz, which is much larger than the ~ 50 Hz interactions between neighboring layers [46]. The measured FWHM is similar to the molecule temperature $k_B T/h \approx 7$ kHz, and follows an approximately linear trend with T (Figure 7.6B). This suggests that two molecules undergoing dipolar exchange can also change their motional states

in the harmonic trap, thereby changing their kinetic energy to compensate for Δ. Two-particle calculations by Thomas Bilitewski and Ana Maria Rey support this physical picture [152]. The interlayer dipolar interactions in this system lead to a complicated interplay of dipolar exchange, reactive losses, and external motion.

7.4 Conclusion

In this chapter, we showed how to prepare a single 2D layer of molecules from an initial distribution of many layers. We utilized our electric field control to reduce inhomogeneous broadening by minimizing the differential AC Stark shift with θ. The ability to control the rotational state of the molecules with single layer resolution allowed us to study the interlayer dipolar interactions in a controllable way. Changing the layer-to-layer detuning Δ revealed a complex interplay of dipolar interactions and harmonic mode-changing collisions.

Looking forward, the preparation of single 2D molecular systems opens a path to studying a wide range of 2D dipolar physics, from collective oscillations [197] to spin squeezing [49]. With $\mathbf{E}$ oriented perpendicular to the layer, all pairs of molecules in the system have the same sign of dipolar interaction, which can lead to highly collective behavior. If the s-wave losses are suppressed by a shallow 3D optical lattice, the many-layer system could also be used to study transport and localization between planes [224]. Recently, theory [222] and experiments on trapped ions [223] have shown that a form of many-body localization can arise from a linear potential gradient (like our layer selection gradient) in the absence of disorder, and perhaps in the future our system would be well-suited for studying similar localization physics. Our theory collaborators Thomas Bilitewski and Ana Maria Rey have also suggested that the layered system naturally realizes a multi-mode squeezing Hamiltonian, similar to two-mode squeezing observed in spinor BECs [227, 228], which could be an interesting future direction to explore.

Chapter 8

Dipolar density shifts in 2D

In the previous chapter, we used microwave spectroscopy to address single 2D layers in our optical lattice. By putting neighboring layers in different rotational states, we were able to look at the effect of interlayer dipolar interactions on the reactive loss.

In this chapter, we instead explore the intralayer interactions between molecules in a coherent superposition of rotational states. By mapping rotational states $|\downarrow\rangle = |N = 0, m_N = 0\rangle$ and $|\uparrow\rangle = |1, 0\rangle$ or $|\uparrow'\rangle = |1, -1\rangle$ onto a spin–1/2 degree of freedom, we realize a 2D quantum spin system with long-range and anisotropic interactions. In contrast to earlier work where molecules were pinned to sites of a 3D optical lattice [46], here the molecules are free to move in the 2D layers, resulting in an itinerant system where coherent collective spin dynamics compete with collisions. At lowest order, the dipolar interactions cause a mean-field shift of the transition frequency between $|\downarrow\rangle$ and $|\uparrow\rangle$ [229], which we detect using Ramsey spectroscopy. At lower T/T_F, the dipolar interactions in 2D are predicted to generate spin-squeezed states [49].

Long range, anisotropic, and highly tunable dipolar interactions make ultracold molecules an attractive platform for explorations of quantum spin systems [24, 26, 27], which are central to many questions at the intersection of condensed matter physics, materials science, and quantum information [230, 231, 232]. Here, we leveraged our control of $\mathbf{E}$ to demonstrate aspects of this tunability. While Ref. [46] operated at $\mathbf{E} = 0$, we studied the dynamics over a large range of $|\mathbf{E}|$ from 0 to 9 kV/cm, allowing us to vary the relative strength between the Ising and spin-exchange interactions and explore the full spin-1/2 Hamiltonian [140]. Additionally, we varied the angle α of

$\mathbf{E}$ from $\hat{\mathbf{y}}$ to rotate the orientation of the dipoles in the 2D plane.[1] This changed the interactions from purely repulsive at $\alpha = 0°$ to (on average) attractive at $\alpha = 90°$. By choosing $|\uparrow\rangle = |1, 0\rangle$ or $|\uparrow'\rangle = |1, -1\rangle$, we could also change the sign and magnitude of the dipolar interactions. Taking advantage of this fact, we dynamically reversed the sign of the couplings in the underlying spin Hamiltonian by switching from $|\uparrow'\rangle$ to $|\uparrow\rangle$ in the middle of a measurement, leading to a reversal of the Ramsey phase accumulation. This is a key capability needed for performing a time-reversal or "untwisting" protocol on a spin squeezed state [49], which allows one to enjoy a metrological gain from spin squeezing without requiring detection at the single particle level [233].

This chapter is based on a manuscript which is still in preparation [234], and some of this work is still preliminary. I will mainly focus on giving a high-level summary of what we have seen so far. The experiments were done in 2D using a similar procedure to Chapter 7. Typical starting conditions were $N = 20 \times 10^3$ at $T = 400$ nK in about 20 layers of the VL. The combined trap frequencies in the ODT + VL were $(\omega_x, \omega_y, \omega_z) = 2\pi \times (45, 17 \times 10^3, 45)$ Hz for $|0, 0\rangle$ at $|\mathbf{E}| = 0$. The molecules were in the quasi-2D regime ($k_B T/\hbar\omega_y = 0.5$) and predominantly occupied the lowest harmonic level in $\hat{\mathbf{y}}$. Molecules were produced directly at the target $\mathbf{E}$ for each measurement using our tunable STIRAP setup [107].

8.1 Spin Hamiltonian

Let us start by introducing the collective spin Hamiltonian used to analyze the system. Since the molecules are free to move in the 2D planes, the single particle states are described by a spin part times a motional part. The motional eigenfunctions are given by the harmonic oscillator modes in the trap. This is illustrated schematically in Figure 8.1. The interlayer interactions described in the previous chapter are weak on the timescales used for these measurements, so we can approximate neighboring 2D layers as being uncoupled.

In the limit of few elastic collisions, the motional states are effectively frozen and do not

[1] Note that the field angle α is denoted θ in the previous chapters. We change notation here to avoid symbol clash with the Bloch sphere polar angle θ.

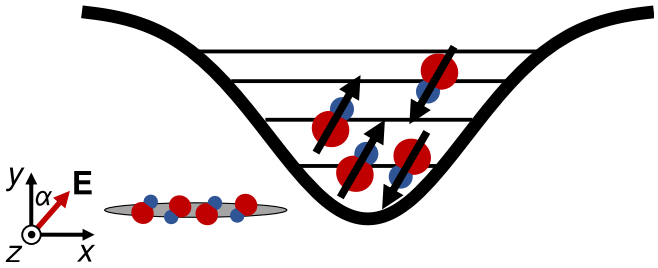

Figure 8.1: Cartoon of the spin Hamiltonian. In a 2D layer, each single particle eigenstate can be decomposed into the product of a spin-1/2 degree of freedom and a motional state in the harmonic trap. The dynamics are controlled by $|\mathbf{E}|$ and the angle α between $\mathbf{E}$ and $\hat{\mathbf{y}}$. Reproduced from Ref. [234].

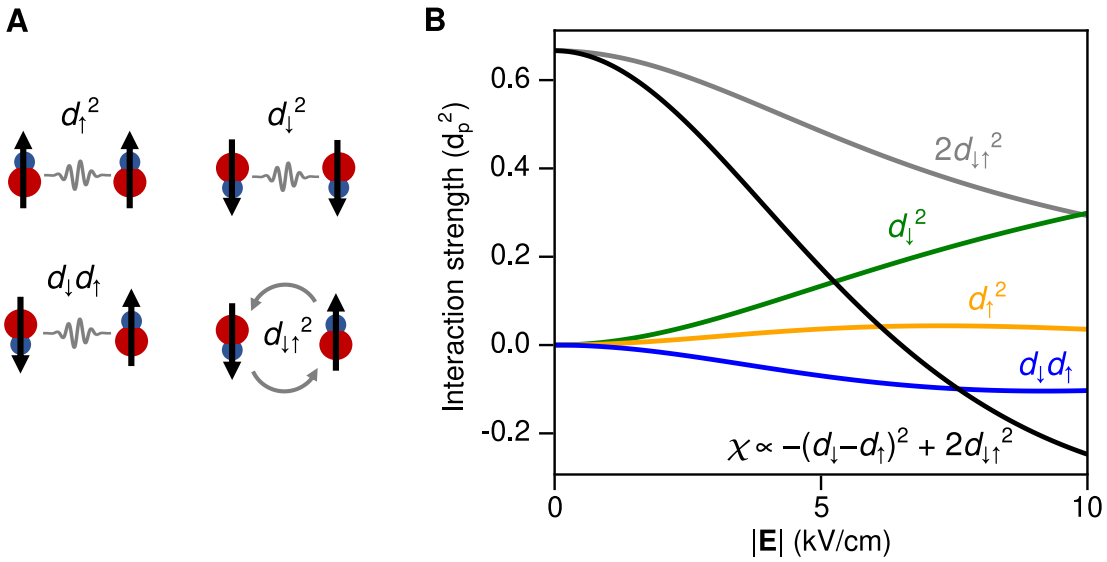

Figure 8.2: Dependence of χ on $|\mathbf{E}|$. (A) Dipolar interactions between $|\downarrow\rangle$ and $|\uparrow\rangle$. The molecules interact via their induced dipole moments ($d_\uparrow$ and $d_\downarrow$), as well as the transition dipole moment ($d_{\downarrow\uparrow} = \langle\downarrow|d|\uparrow\rangle = \langle\uparrow|d|\downarrow\rangle$). (B) Strengths of these dipolar interaction terms plotted as a function of $|\mathbf{E}|$ for $|\downarrow\rangle = |0,0\rangle$ and $|\uparrow\rangle = |1,0\rangle$ of KRb. The dipolar coupling strength is given in units of d_p, the permanent dipole moment (0.574 D for KRb). The black line shows the dependence of χ, which controls the magnitude of the density shift, on $|\mathbf{E}|$. Adapted from Ref. [234].

participate in the dynamics [49, 235, 236, 237]. In this "frozen mode" approximation, the dynamics take place only in the spin degrees of freedom,

$$\mathcal{H} = \frac{1}{2}\sum_{ij}\left[J_{ij}^{z}s_i^z s_j^z + J_{ij}^{\perp}\left(s_i^x s_j^x + s_i^y s_j^y\right)\right] + \sum_i s_i^z h_i^z, \tag{8.1}$$

where the indices i and j label the occupied harmonic oscillator modes in the trap. Above, $s_i^{\{x,y,z\}}$ is a spin-1/2 operator acting on a particle in harmonic mode i. This theory has successfully modeled the spin dynamics of p-wave interacting fermions in optical lattice clocks [235, 236], and described dynamical phase transitions in a ^{40}K Fermi gas [237]. For our system, the couplings J_{ij}^z, $J_{ij}^{\perp}$, and h_i^z depend on the induced dipole moments $d_\downarrow$ and $d_\uparrow$ and the transition dipole moment $d_{\downarrow\uparrow}$ (shown in Figure 8.2A), as well as the matrix element of the spatial part of the dipolar interaction with respect to oscillator modes i and j [49].

Assuming that these matrix elements do not depend too strongly on i and j, the spin model can be approximated by a collective spin Hamiltonian,

$$H = J_\perp S^2 + \chi S_z^2 + h_z S_z, \tag{8.2}$$

where $S_\alpha = \sum_i s_i^\alpha$ is the collective spin operator obtained by summing the individual spin–1/2 operators. The couplings $J_\perp$, $\chi = J_z - J_\perp$, and h_z are obtained by averaging the mode-dependent couplings in equation (8.1) over the occupied harmonic modes. In contrast to the 3D lattice system, the couplings J_{ij}^z and $J_{ij}^{\perp}$ are relatively homogeneous for the bulk system and thus the collective approximation is expected to be valid [49]. The first term $J_\perp S^2$ protects the system from decoherence, since processes that would decohere a molecule necessarily change the value of S, and are thus suppressed by the many-body gap $J_\perp$ [236]. The second term gives one-axis twisting with coupling strength χ, which generates spin squeezing [4, 6, 238]. The third term gives an effective magnetic field h_z from the background field generated by the spins.

At the mean-field level, $\chi S_z^2 \approx 2\chi\langle S_z\rangle S_z$, which produces a spin-dependent external field that shifts the transition frequency between the two spin states by an amount proportional to the spin

imbalance $\langle S_z \rangle = (N_\uparrow - N_\downarrow)/2$. For Ramsey spectroscopy, this manifests as a phase shift

$$\Delta\phi = N\chi T \cos\theta, \tag{8.3}$$

where T is the Ramsey evolution time and $\cos\theta = (N_\uparrow - N_\downarrow)/N = 2\langle S_z \rangle/N$ is the normalized population imbalance ($N = N_\downarrow + N_\uparrow$ is the total molecule number). Thus, χ is responsible for the dipolar density shift in our system. Physically, we expect that $\Delta\phi$ scales not only with the total number N but with the average density n of molecules. This dependence is actually already present in equation (8.3) since χ implicitly depends on the transverse trapping frequencies and temperature, which determine the populated modes in equation (8.1). To make the density dependence more explicit, we redefine χ such that

$$\frac{\Delta\phi}{2\pi} = n\chi T \cos\theta, \tag{8.4}$$

where now χ has units of Hz per 2D density.

The value of χ depends on the dipole moments according to

$$\chi \propto -(d_\downarrow - d_\uparrow)^2 + \eta d_{\downarrow\uparrow}^2, \tag{8.5}$$

and, as a result, χ is tunable by $|\mathbf{E}|$ (Figure 8.2B). The factor η depends on the rotational angular momentum projections of $|\downarrow\rangle$ and $|\uparrow\rangle$: $\eta = 2$ for the $\{|0,0\rangle, |1,0\rangle\}$ system, while $\eta = -1$ for $\{|0,0\rangle, |1,\pm1\rangle\}$.[2] At small $|\mathbf{E}|$, the largest contribution to χ is from the transition dipole $d_{\downarrow\uparrow}$, while at large $|\mathbf{E}|$, the contribution of the induced dipoles $d_\downarrow$ and $d_\uparrow$ are stronger. Since χ depends on the averaged relative orientation of interacting molecule pairs, it is also tunable by the angle α between $\mathbf{E}$ and $\hat{\mathbf{y}}$.

[2] This can be seen from equation (2.25). The molecules are interacting through $T_0^{(2)}(\mathbf{d}_1, \mathbf{d}_2)$, which generates spin-exchange between $|0,0\rangle$ and $|1,0\rangle$ ($|0,0\rangle$ and $|1,\pm1\rangle$) through the $2d_1^0 d_2^0$ ($d_1^\pm d_2^\mp$) term. This explains the factor of 2; the negative sign can also be obtained by calculating the matrix elements. Classically, two molecules interacting in a superposition of $|0,0\rangle$ and $|1,0\rangle$ look like two dipoles oscillating along the quantization axis. Two molecules in a superposition of $|0,0\rangle$ and $|1,\pm1\rangle$ look like dipoles rotating in the plane perpendicular to the quantization axis. Owing to the dipolar anisotropy, the time-averaged interaction in the second case picks up a factor of $(1/2\pi)\int_0^{2\pi} d\theta\,(1 - 3\cos^2\theta) = -1/2$.

8.1.1 More discussion of χ

Before moving on to discuss the experimental measurements, we try to develop some intuition for the form of χ. For concreteness, we assume $|\downarrow\rangle = |0,0\rangle$ and $|\uparrow\rangle = |1,0\rangle$ in this section. Let $\epsilon_\downarrow$ and $\epsilon_\uparrow$ be the interaction energy per particle of $|\downarrow\rangle$ and $|\uparrow\rangle$, respectively. First, consider a molecule in $|\downarrow\rangle$. It feels an energy shift proportional to $d_\downarrow^2 N_\downarrow$ ($d_\downarrow d_\uparrow N_\uparrow$) from interactions with $|\downarrow\rangle$ ($|\uparrow\rangle$) through the induced dipole moment. It also feels an interaction from the transition dipole moment, $d_{\downarrow\uparrow}^2 N_\uparrow$, giving a total interaction energy of

$$\epsilon_\downarrow \propto d_\downarrow^2 N_\downarrow + d_\downarrow d_\uparrow N_\uparrow + d_{\downarrow\uparrow}^2 N_\uparrow. \tag{8.6}$$

These terms are depicted schematically in Figure 8.2A. Classically, the proportionality factor is given by the integral of the dipolar interaction $V(r)$ times the molecular density distribution. A similar argument for $|\uparrow\rangle$ gives

$$\epsilon_\uparrow \propto d_\uparrow^2 N_\uparrow + d_\downarrow d_\uparrow N_\downarrow + d_{\downarrow\uparrow}^2 N_\uparrow. \tag{8.7}$$

In Ramsey spectroscopy, we are only sensitive to the energy difference $\epsilon_\uparrow - \epsilon_\downarrow$,

$$\epsilon_\uparrow - \epsilon_\downarrow \propto d_\uparrow^2 N_\uparrow - d_\downarrow^2 N_\downarrow + \left(d_\downarrow d_\uparrow + d_{\downarrow\uparrow}^2\right)(N_\downarrow - N_\uparrow). \tag{8.8}$$

We make the substitutions

$$N_\downarrow = \left(\frac{N_\downarrow + N_\uparrow}{2} + \frac{N_\downarrow - N_\uparrow}{2}\right), \tag{8.9}$$

$$N_\uparrow = \left(\frac{N_\downarrow + N_\uparrow}{2} - \frac{N_\downarrow - N_\uparrow}{2}\right), \tag{8.10}$$

to obtain

$$\epsilon_\uparrow - \epsilon_\downarrow \propto (d_\uparrow^2 - d_\downarrow^2)\left(\frac{N_\downarrow + N_\uparrow}{2}\right) - (d_\downarrow^2 + d_\uparrow^2)\left(\frac{N_\downarrow - N_\uparrow}{2}\right) + \left(d_\downarrow d_\uparrow + d_{\downarrow\uparrow}^2\right)(N_\downarrow - N_\uparrow) \tag{8.11}$$

$$= (d_\uparrow^2 - d_\downarrow^2)\left(\frac{N_\downarrow + N_\uparrow}{2}\right) + \left(\frac{N_\downarrow - N_\uparrow}{2}\right)\left[-(d_\downarrow - d_\uparrow)^2 + 2d_{\downarrow\uparrow}^2\right]. \tag{8.12}$$

The first term depends on the total number of molecules, so it is a constant shift that ends up being canceled by our decoupling pulses. However, the second term is proportional to the imbalance $\langle S_z \rangle$

and the dipolar dependence of χ from equation (8.5), directly giving us the mean field shift $\chi\langle S_z\rangle$. This calculation can be generalized to the $\{|0,0\rangle, |1,\pm1\rangle\}$ system by replacing the spin-exchange terms $d_{\downarrow\uparrow}^2 N_\uparrow \to (\eta/2) d_{\downarrow\uparrow}^2 N_\uparrow$ in $\epsilon_\downarrow$ (and similarly for the corresponding term in $\epsilon_\uparrow$).

Some intuition can also be gained from basic two-particle Ramsey calculation in section 2.6.1. Though that calculation assumed that the molecules were pinned in space, the form of χ was the same as in equation (8.5). Figure 2.14B shows that there is a shift in the Ramsey fringes over time for $N_\downarrow \neq N_\uparrow$, which is the two-particle analogue of the density shift studied in this chapter.

8.1.2 Validity of the spin model

Elastic collisions between molecules couple the motional states in the trap. Therefore, the reduction to the pure spin model in equation (8.1) depends crucially on the elastic collision rate being low. However, molecules placed in a rotational superposition have strong dipolar interactions that could potentially lead to a high elastic collision rate. Consider two molecules in a symmetric superposition,

$$|+\rangle = \frac{1}{2}\left(|\downarrow\rangle + |\uparrow\rangle\right) \otimes \left(|\downarrow\rangle + |\uparrow\rangle\right) = \frac{1}{2}\left(|\downarrow\downarrow\rangle + |\downarrow\uparrow\rangle + |\uparrow\downarrow\rangle + |\uparrow\uparrow\rangle\right), \tag{8.13}$$

which is the state of a pair of molecules just after the initial Ramsey pulse (section 2.6.1). At $|\mathbf{E}| = 0$, this gives a dipolar interaction strength of

$$\langle +|2d_1^0 d_2^0|+\rangle = \frac{1}{2}\left(\langle\downarrow\uparrow|\, d_1^0 d_2^0 |\uparrow\downarrow\rangle + \langle\uparrow\downarrow|\, d_1^0 d_2^0 |\downarrow\uparrow\rangle\right) = d_{\downarrow\uparrow}^2. \tag{8.14}$$

Comparing the value above to the same expression calculated for two induced dipoles d (which gives $2d^2$), the effective dipole moment for interactions of the equal superposition is $d_{\downarrow\uparrow}/\sqrt{2}$ [239]. For $|\mathbf{E}| = 0$, $|\downarrow\rangle = |0,0\rangle$, $|\uparrow\rangle = |1,0\rangle$, this gives a large dipole moment of $d_{\downarrow\uparrow}/\sqrt{2} = d_{\mathrm{perm}}/\sqrt{6}$, corresponding to a dipolar length of $a_D = 990 a_0$ for KRb at $|\mathbf{E}| = 0$. Of course, this analysis only holds while the molecules are fully coherent; otherwise, the assumption that the molecules collide in $|+\rangle$ is no longer valid.

Experimental measurements are ongoing in the lab to try to understand the role of elastic dipolar collisions between molecules in the spin dynamics. Physically, we would expect that the spin

model is still valid at short times before the molecules have a chance to collide, even if it breaks down at longer times. By scaling the elastic collision rate measured in Ref. [52] for the dipole moment ($d_{\mathrm{perm}}/\sqrt{6}$) and temperature used here (450 nK), we estimate an elastic collision rate $\Gamma \sim 100\ \mathrm{s}^{-1}$ at the highest molecular densities studied here. For the density shift measurements, we use an interrogation time on the order of 1 ms, much shorter than the estimated collision time, and thus we expect that the spin model is still a good description of the system.

8.2 Dynamical decoupling

To measure the density shift, we require sufficiently long coherence time to measure the phase shift $\Delta\phi$. For our parameters, we estimate a frequency shift on the order of $\Delta\nu = n\chi \approx 100$ Hz. Thus if we want to see a $\Delta\phi$ of a few degrees, we require a coherence time on the order of about 1 ms. This is longer than the coherence time of a few hundred μs observed when the trap is non-magic [110, 152].

In the previous chapter, we showed that the coherence between $|\downarrow\rangle = |0,0\rangle$ and $|\uparrow\rangle = |1,0\rangle$ could be increased to above 1 ms by bringing $\mathbf{E}$ to the experimentally-measured magic angle $\theta_{\mathrm{m}} = 57°$. After that work, we more carefully characterized the differential AC Stark shifts from our lattice and found an updated value of $\theta_{\mathrm{m}} = 54°$, closer to the theoretically predicted 54.7° [113]. Figure 8.3 shows the decay of the Ramsey contrast as a function of time at $|\mathbf{E}| = 1$ kV/cm and θ_{m} (gray circles), from which we extract a $1/e$ coherence time of $\tau_c = 4.0(4)$ ms. This measurement was taken with no spin echo pulses, so τ_c could be limited by gradients of $\mathbf{E}$ or a small residual differential AC polarizability.

Since the polarization of the VL is constrained to lie in the x-z plane, reaching magic trapping conditions requires tilting $\mathbf{E}$ to θ_m. This poses a limitation for fully mapping out the behavior of χ. For example, we would like to observe the dependence of χ on the field angle α, which necessarily involves tilting the field away from the magic angle. We would also like to measure χ as a function of $|\mathbf{E}|$. At $|\mathbf{E}| = 0$, the trap is non-magic since the quantization axis is set by the magnetic field along $+\hat{\mathbf{y}}$, and we observed that the Ramsey coherence was sharply reduced to 0.24(1) ms (black

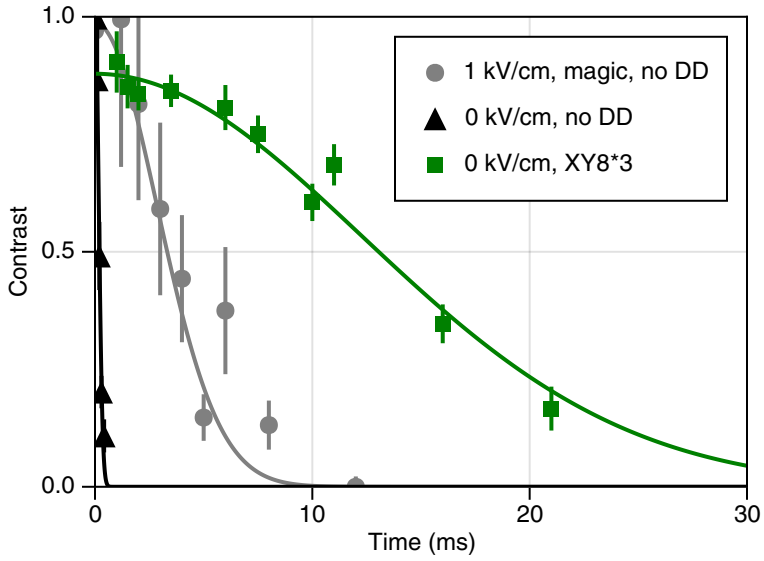

Figure 8.3: Contrast decay between $|\downarrow\rangle$ and $|\uparrow\rangle$ with and without dynamical decoupling. At $|\mathbf{E}| = 1$ kV/cm and θ_{m} (gray circles), the fitted $1/e$ coherence time with no spin echo pulses is $\tau_c = 4.0(4)$ ms. Moving the electric field to $|\mathbf{E}| = 0$ (black triangles), away from the magic trapping condition, decreases the coherence time to $\tau_c = 0.24(1)$ ms without decoupling pulses. At the non-magic condition, using the XY8*3 DD sequence (green squares) improves the coherence time to $\tau_c = 17(1)$ ms for a low density of molecules. All fits are to e^{-t^2/τ_c^2}. Adapted from Ref. [234].

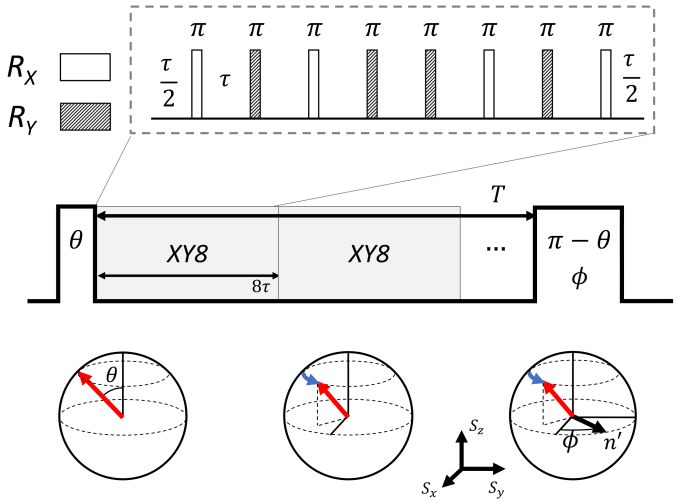

Figure 8.4: Dynamical decoupling sequence. The standard Ramsey sequence (no DD) consists of an initial pulse of area θ about $\hat{\mathbf{y}}$ (in spin space), followed by an evolution time T, and finally a pulse of area $\pi - \theta$ about an axis $\hat{\mathbf{n}}' = \hat{\mathbf{x}}\cos\phi + \hat{\mathbf{y}}\sin\phi$. To add DD, we insert one or more XY8 sequences during T. One XY8 sequence (zoomed region) consists of 8 π-pulses about $\hat{\mathbf{x}}$ or $\hat{\mathbf{y}}$ spaced by time τ, for a total duration of 8τ. XY8*n refers to n XY8 sequences concatenated, for a total interrogation time of $T = 8n\tau$. Reproduced from Ref. [234].

triangles in Figure 8.3).

To bypass this limitation, we implemented a dynamical decoupling (DD) pulse sequence [154]. DD sequences consist of many successive spin echo pulses, spaced by time τ. The pulse train forms a bandpass filter that rejects noise outside of a narrow bandwidth around $f_0 = 1/2\tau$ [155, 156]. DD is a standard technique in fields such as NMR [240] and NV centers [241, 242] for increasing the coherence time T_2^* limited by technical noise toward the intrinsic coherence limit T_2 of the quantum system. In our system, the DD sequence removes inhomogeneous broadening from differential AC Stark shifts and gradients of $\mathbf{E}$, as well as time-dependent noise on $\mathbf{E}$.

Specifically, we implemented the XY8 pulse sequence [154, 243], depicted in Figure 8.4. The XY8 sequence consists of an initial delay $\tau/2$, followed by 8 π-pulses spaced by τ, and a final $\tau/2$ delay at the end of the sequence. The total duration is 8τ. The Bloch sphere rotation axis of the pulses alternate between $\hat{\mathbf{x}}$ and $\hat{\mathbf{y}}$ to reduce sensitivity to errors in the pulse area. The sequence is also time-symmetric for more effective noise suppression [244]. The XY8 sequence also serves as a building block for creating longer sequences (denoted XY8*n) by concatenation. Technical details of the RF system used to generate the pulses can be found in section 3.4.

Using the XY8*3 sequence (green squares in Figure 8.3) vastly improved the coherence time at $|\mathbf{E}| = 0$ by almost two orders of magnitude, from $\tau_c = 0.24(1)$ ms to 17(1) ms. The measurement was taken at a low molecule density $n = 0.14(2) \times 10^7$ cm^{-2} to avoid interaction effects. With a coherence time on the order of 10 ms, we could move on to systematically study the dipolar density shift as a function of $|\mathbf{E}|$ and α.

8.3 Density shift

The measurement of the density shift proceeded in several stages. At a fixed density n, we conducted Ramsey experiments between $|\downarrow\rangle$ and $|\uparrow\rangle$ using an XY8*3 DD sequence, with a typical total evolution time of $T = 1.2$ ms. By scanning the phase ϕ of the final Ramsey pulse, we measured Ramsey fringes like those shown in Figure 8.5A and determined the phase shift $\Delta\phi$ for each fringe. We took fringes at several different values of the initial pulse area θ to vary the strength of the

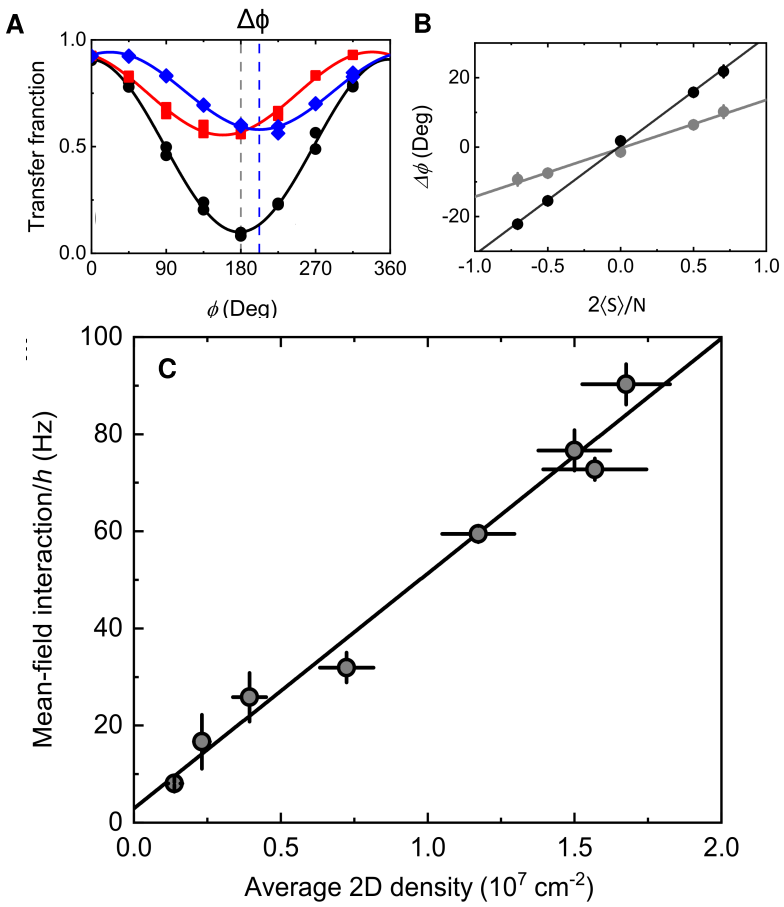

Figure 8.5: Measurement of the dipolar density shift for the $\{|\downarrow\rangle, |\uparrow\rangle\}$ spin manifold with a total evolution time of $T = 1.2$ ms. (A) Example Ramsey fringes taken with an XY8*3 sequence at $|\mathbf{E}| = 0$. The initial pulse areas are $\theta = \pi/4$ (red), $\pi/2$ (black), and $3\pi/4$ (blue). The phase shift $\Delta\phi$ is extracted for each fringe by a fit to a sinusoid. (B) Plots of $\Delta\phi$ versus $2\langle S_z\rangle/N = \cos\theta$ for two different densities $n = 1.4(1) \times 10^7$ cm^{-2} (black) and $0.65(7) \times 10^7$ cm^{-2} (gray). Solid lines are linear fits. The slope of $\Delta\phi/T$ versus $2\langle S_z\rangle/N$ gives the mean-field interaction shift $\Delta\nu$. (C) Mean-field interaction $\Delta\nu$ versus average density n. For each n, a set of Ramsey fringes are taken to obtain $\Delta\nu$. A linear fit to the data directly gives χ. Reproduced from Ref. [234].

mean-field shift, which is proportional to the population imbalance $\cos\theta$. The red, black, and blue data in Figure 8.5A correspond to $\theta = \pi/4$, $\pi/2$, and $3\pi/4$, respectively. According to equation (8.4), the mean-field interaction $\Delta\nu = (1/2\pi)\Delta\phi/T$ is linear with $2\langle S_z\rangle/N = \cos\theta$. Thus, fitting the slope of $\Delta\phi$ versus $2\langle S_z\rangle/N$ allows us to extract $\Delta\nu$. Figure 8.5B shows $\Delta\phi$ versus $2\langle S_z\rangle/N$ for two different values of n. The lower density measurement (gray) shows a shallower slope, and thus lower $\Delta\nu$, than the higher density measurement (black).

In principle, we can extract χ from a measurement of $\Delta\nu$ at a single density n by assuming that equation (8.4) holds. Instead of making this assumption, we measured $\Delta\nu$ at several values of n to experimentally determine the dependence on n (Figure 8.5C). We observed the expected linear trend, and from a linear fit (solid line) we extract $\chi = 4.9(3) \times 10^{-6}$ Hz/cm^{-2}.

8.4 Tuning the interactions

Using the procedure of the previous section, we measured χ as a function of $\mathbf{E}$ to demonstrate the high degree of tunability of our molecular spin system. By varying $|\mathbf{E}|$, with fixed $\alpha = 0°$, we could probe the effects of rotational state mixing on the mean-field interactions. As shown in Figure 8.2B, dipolar spin-exchange is the dominant interaction at low $|\mathbf{E}|$. As $|\mathbf{E}|$ increases, the increasing strength of the direct (Ising) interactions from the induced dipoles competes with the spin-exchange to cause a reduction in χ, leading to $\chi = 0$ near $|\mathbf{E}| \approx 7$ kV/cm. For even higher $|\mathbf{E}|$, the direct interactions are dominant and χ is negative. We experimentally measured χ over a wide range of $|\mathbf{E}|$ to observe this trend (Figure 8.6A). In particular, at the highest field of 8.9 kV/cm, χ was negative, demonstrating the high degree of tunability with $|\mathbf{E}|$. The solid line shows the expected dependence of χ, given by $A[-(d_\downarrow - d_\uparrow)^2 + 2d_{\downarrow\uparrow}^2]$, which is fit to the experimental data with the overall scaling factor A. The small dips in the fitted curve at low $|\mathbf{E}|$ are caused by avoided crossings of $|\uparrow\rangle$ with other hyperfine states in $N = 1$, as calculated for KRb at $B = 545.9$ G and including the optical fields of the VL and ODT.

The combination of the reduced dimensions with the dipolar anisotropy can also be used to control χ via the angle α between $\mathbf{E}$ and $\hat{\mathbf{y}}$ (the tightly confined direction). In Figure 8.6B, we measured χ as a function of α at fixed $|\mathbf{E}| = 1.02$ kV/cm. At $\alpha = 0°$, all pairs of molecules interact repulsively, leading to a large and positive χ. In contrast, at $\alpha = 90°$, the dipoles lie in the plane and the molecules experience both attractive and repulsive interactions. Owing to the form of the dipolar anisotropy, the interactions are attractive on average, resulting in a negative χ. Assuming that the trapping potential is symmetric in the x-z plane, the interaction strength has a simple angular dependence $A(3\cos^2\alpha - 1)$ [234]. The solid line in Figure 8.6B is a fit to this functional

form.

The choice of internal states used to form the spin-1/2 system offers another knob for tuning dipolar interactions. Figure 8.7 shows a measurement of the mean-field interaction between $|\downarrow\rangle$ and $|\uparrow'\rangle = |1,-1\rangle$ at $|\mathbf{E}| = 0$ (green squares). The measurement of the $\{|\downarrow\rangle, |\uparrow\rangle\}$ system from Figure 8.5C (black circles) is shown for comparison. Using $|\uparrow'\rangle$ instead of $|\uparrow\rangle$ changes the magnitude of χ and reverses its sign, and we measured $\chi' = -2.3(8) \times 10^{-6}$ Hz/cm^{-2} for the $\{|\downarrow\rangle, |\uparrow'\rangle\}$ system. The experimental ratio of χ'/χ is consistent with $-1/2$, the value expected from equation (8.5) at $|\mathbf{E}| = 0$. Interaction control via the internal state allows us to rapidly change the coupling strengths in the spin Hamiltonian, since the duration of an RF pulse is much shorter than the experimental limit of several ms for smoothly changing $|\mathbf{E}|$ or α.

8.5 Dynamically reversing the evolution

The ability to switch the parameters of the spin Hamiltonian allows us to dynamically control the evolution of the many-body state. In particular, by switching the excited state from $|\uparrow'\rangle$ to $|\uparrow\rangle$ in the middle of the Ramsey evolution, the spin Hamiltonian couplings are instantaneously changed by a factor of -2 at $|\mathbf{E}| = 0$. This reverses the many-body dynamics, a key ingredient for studying quantities such as out-of-time-ordered correlators [245]. Such time-reversal schemes are also useful for approaching the Heisenberg limit of measurement sensitivity without requiring single particle detection [233].

Here, we demonstrate the reversal of the mean-field interaction shift, a first step toward realizing such a many-body echo in our dipolar spin system. The measurement consisted of three stages (Figure 8.8A). The first and third stages consisted of evolution in a coherent superposition of $\{|\downarrow\rangle, |\uparrow'\rangle\}$ or $\{|\downarrow\rangle, |\uparrow\rangle\}$, respectively, using XY8 to protect the spin coherence. The middle stage consisted of a sequence of three pulses (denoted R in Figure 8.8A) that swapped the excited state population from $|\uparrow'\rangle$ to $|\uparrow\rangle$ with a duration of 70 μs. We measured the phase difference $\Delta\Phi$ between the Ramsey fringes obtained for $\theta = \pi/4$ and $\theta = 3\pi/4$, in order to reject systematics such as extra shifts caused by frequency switching of the microwave source.

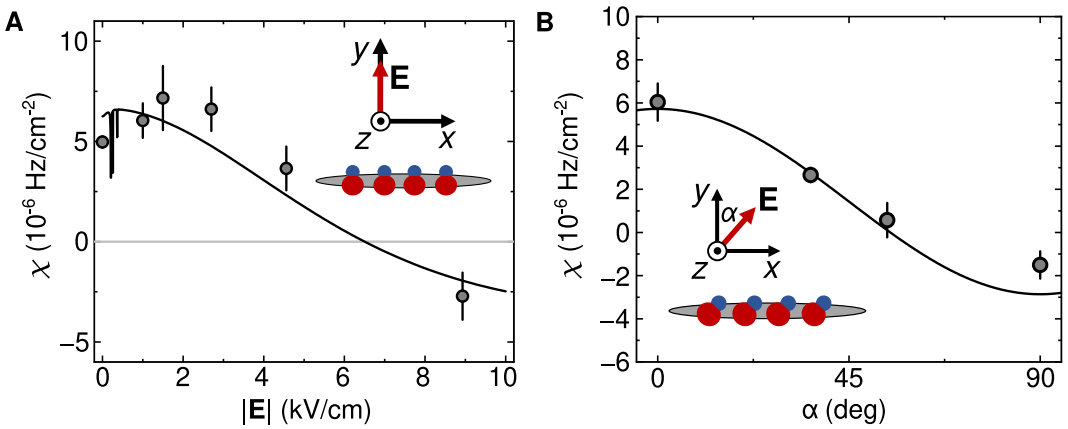

Figure 8.6: Tuning χ with $|\mathbf{E}|$ and α for the $\{|\downarrow\rangle, |\uparrow\rangle\}$ spin manifold. (A) Dependence on $|\mathbf{E}|$. Initially large and positive at low $|\mathbf{E}|$, χ passes through zero near $|\mathbf{E}| = 7$ kV/cm, and becomes negative for higher $|\mathbf{E}|$. The change in sign of χ is a direct manifestation of the competition between the interactions arising from the transition and induced dipoles, see equation (8.5). The solid line is the calculated $\chi(|\mathbf{E}|)$ including hyperfine structure, scaled to the experimental data. (B) Dependence on the field angle α. Owing to the dipolar anisotropy, χ depends strongly on the orientation of the electric field set by α. The solid line is a fit to $A(3\cos^2\alpha - 1)$. Adapted from Ref. [234].

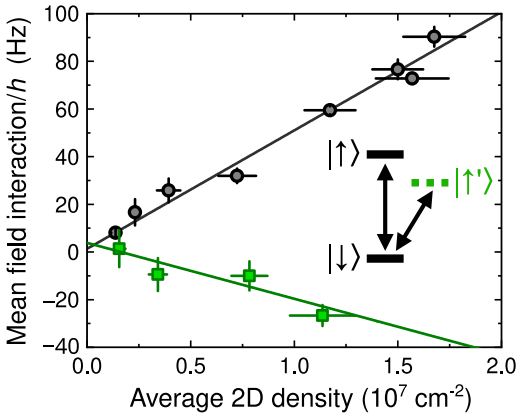

Figure 8.7: Internal state dependence of χ. The mean-field interaction is measured for $\{|\downarrow\rangle, |\uparrow\rangle\}$ (black circles, same data as Figure 8.5C) as well as $\{|\downarrow\rangle, |\uparrow'\rangle\}$ (green squares) spin manifolds at $|\mathbf{E}| = 0$. The slope of the mean field interaction versus density gives χ for each system. The measured for $\{|\downarrow\rangle, |\uparrow\rangle\}$ is consistent with a factor of 2 larger $|\chi|$ than $\{|\downarrow\rangle, |\uparrow'\rangle\}$, and opposite interaction sign. Adapted from Ref. [234].

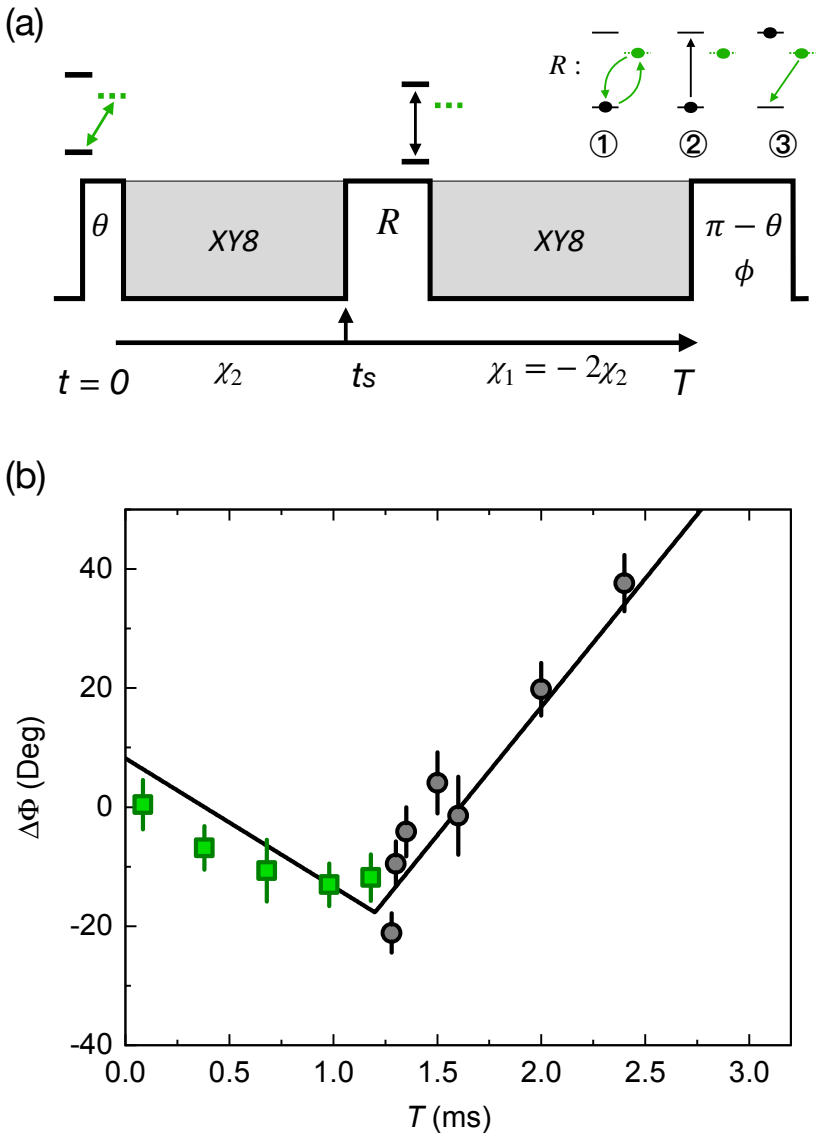

Figure 8.8: Reversing the spin Hamiltonian. (A) Experimental pulse sequence used to measure the reversal. An initial pulse of area θ creates a superposition of $|\downarrow\rangle$ and $|\uparrow'\rangle$. After a hold time t_s, during which an XY8 sequence is used to suppress decoherence, the excited state population is coherently transferred from $|\uparrow'\rangle$ to $|\uparrow\rangle$ using a composite pulse R. The remaining $T - t_s$ hold time is spent in a superposition of $|\downarrow\rangle$ and $|\uparrow\rangle$, with another XY8 pulse sequence again suppressing decoherence. A final pulse of area $\pi - \theta$ and variable phase ϕ is used to measure the populations in $|\downarrow\rangle$ and $|\uparrow\rangle$. (B) The differential phase shift $\Delta\Phi$ measured between $\theta = \pi/4$ and $\theta = 3\pi/4$ versus the total time T. Green squares: phase accumulation in $\{|\downarrow\rangle, |\uparrow'\rangle\}$. Black circles: phase accumulation in $\{|\downarrow\rangle, |\uparrow\rangle\}$. The black line is the piecewise linear fit described in the text. The density is $n = 1.1(1) \times 10^7$ cm^{-2}. Reproduced from Ref. [234].

The full sequence in (A) was used for each measurement of $\Delta\Phi$, though the lengths of the first stage (duration t_s) and third stage could be independently varied to map out the evolution of $\Delta\Phi$ before and after the reversal R as a function of the total time T (Figure 8.8B). For $T \leq 1.2$ ms, we kept the third stage (in $\{|\downarrow\rangle, |\uparrow\rangle\}$) as short as possible and scanned the time t_s of the first stage. This let $\Delta\Phi$ accumulate from interactions in the $\{|\downarrow\rangle, |\uparrow'\rangle\}$ spin manifold (green squares). For $T > 1.2$ ms, we kept the time of the first stage fixed at $t_s = 1.2$ ms, and scanned the time of the third stage. We observed a change in the slope of $\Delta\Phi$ versus T from negative to positive at $T = 1.2$ ms, indicating a reversal in the sign of the mean-field interaction. The data is well-fit by a piecewise linear function where the slopes before and after the reversal have a ratio of -2, as expected from Figure 8.7. These results demonstrate reversal of the spin Hamiltonian at $|\mathbf{E}| = 0$, paving the way for future studies of dynamic engineering of the many-body state.

8.6 Conclusion

In this chapter, we described initial explorations of the collective spin physics of dipolar molecules in 2D. With the help of dynamical decoupling sequences to suppress single-particle decoherence, we observed the mean-field interaction shift from the dipolar interactions. By changing $|\mathbf{E}|$, the field angle α, or the internal state, we could change the magnitude and sign of the density shift. Finally, we showed that by changing the internal state we could reverse the sign of the couplings in the spin Hamiltonian, which we observed through a reversal of the mean-field shift. This itinerant dipolar spin system opens many exciting future directions, which are discussed in more detail in the following concluding remarks.

Chapter 9

Conclusion and Outlook

In this thesis, I described our work over the past six years on the JILA KRb experiment. After making molecules in the new machine in early 2018, we were able to leverage the improved atom conditions to create a DFG of molecules in the ODT at $T/T_F = 0.3$ (Chapter 4). The Fermi statistics were apparent from the distribution in TOF expansion and the density fluctuations of the cloud. However, turning on a large electric field to polarize the molecules and induce strong dipolar interactions led to rapid losses in 3D. We therefore explored two different methods for protecting the molecules from loss while maintaining elastic collisions. Confining the molecules into 2D, with the dipoles oriented perpendicular to the plane, allowed us to exploit the interaction anisotropy to stabilize the gas while also turning on strong elastic dipolar collisions (Chapter 5). This enabled direct evaporative cooling of the molecules through dipolar collisions to $T/T_F < 1$ in 2D. Alternatively, by putting the molecules in an excited rotational state, we could observe resonant collisional shielding of the chemical reactions near Förster resonances tuned by the external electric field (Chapter 6). The resonant shielding was effective in both 2D and 3D, and enabled studies of elastic dipolar collisions and direct evaporation in 3D. Both of these methods are highly general and are expected to be applicable to other polar molecule species. Complementary work at Harvard [105] and Munich [54] also demonstrated suppressed loss rates and enhanced elastic collision rates using microwave shielding.

With improved control over the collisions, we shifted our focus from two-body physics of molecular collisions toward the mean-field (and in the future, many-body) dynamics of the dipolar

gas. A single 2D layer is an ideal setting for studying the collective behavior of dipoles, so we leveraged our precise electric field control to spectroscopically address and select single 2D pancakes (Chapter 7). Our layer-resolved rotational state control led to the observation of a long-range collision process where two molecules in adjacent layers could scatter by exchanging their rotational state while also changing motional states in the trap, enabling control of the chemical reaction rate through the internal state of molecules in a neighboring 2D layer. Finally, in our most recent work, we have started to tune the collective spin dynamics of molecules prepared in a superposition of rotational states (Chapter 8). Through the strength and orientation of the electric field or the choice of rotational states, we showed that we can tune the magnitude and sign of mean-field dipolar shifts in the system.

The 2D dipolar spin system promises to open many new scientific explorations. The mean-field shift studied in Chapter 8 is a first manifestation of the S_z^2 term of the collective Hamiltonian, which also generates spin squeezing [49]. Thus, in the near future it will be exciting to start measuring the spin noise in the system. Perhaps one day, squeezing generated by dipolar interactions could be used to enhance the sensitivity of next-generation precision measurements with molecular quantum gases [246]. One can also envision further engineering the Hamiltonian by using different rotational states or adding microwave dressing to tailor the interactions [41, 45, 160]. Spin-orbit coupling arising from dipolar interactions, either using the scheme of Ref. [139] or possibly by exploiting the shielding resonances, could also extend the already rich dynamics in 2D. Additionally, the competition between the coherent spin dynamics and collisions in this itinerant spin system provides an interesting area for further exploration. At one extreme, the dipolar collisions can be strong enough to enter the hydrodynamic regime in 2D [197]. At the other extreme, transverse lattices can be added to protect the spin dynamics by fully suppressing reactive losses and elastic collisions.

More generally, it will be exciting to look for new and creative ways to push the limits on control of the molecules. Most of the experiments in this thesis relied on one main technical advance (in addition to our capability of preparing a quantum gas of molecules): the ability to produce a

large and highly controllable electric field for the molecules. It is fun to think about how our electric field control can be combined with other innovations from around the ultracold community to further enhance our experimental capabilities. Single molecule control, either in tweezers [86, 74] or in a quantum gas microscope [247], brings new opportunities. Our experiment was designed to be compatible with high resolution imaging if we decide to explore this direction [106]. A magic wavelength trap for the $|0,0\rangle \leftrightarrow |1,0\rangle$ rotational transition, as demonstrated in NaK [122], could also significantly simplify our experiments. For KRb, the corresponding transition is near 1020 nm [123]. Theory predicts that the magic condition could even be met for multiple rotational states simultaneously [124], facilitating (for example) studies of synthetic dimensions encoded in the ladder of rotational states [159]. Blue-detuned box traps [94] for KRb could facilitate more collisional studies, for example in higher rotational levels or in the non-reactive Rb-KRb mixture [215], by removing the influence of the trapping light [91, 92]. Dipolar interaction strengths could be boosted by sub-wavelength trapping [248] to facilitate pairing and superfluidity [249, 43], and dispersive imaging techniques could allow for sensitive and non-destructive detection of molecules [250, 251]. Adding periodic driving [252] could enable Floquet engineering of polar molecule systems to realize novel states of matter [253]. Hybrid systems of polar molecules and Rydberg atoms also promise new opportunities by combining the advantages of both subsystems [254, 255, 256]. The future of molecular quantum science is bright!

Bibliography

[1] J. I. Cirac and P. Zoller. Quantum Computations with Cold Trapped Ions. Phys. Rev. Lett., 74:4091–4094, May 1995.

[2] C. Monroe, D. M. Meekhof, B. E. King, W. M. Itano, and D. J. Wineland. Demonstration of a Fundamental Quantum Logic Gate. Phys. Rev. Lett., 75:4714–4717, Dec 1995.

[3] M. H. Devoret and R. J. Schoelkopf. Superconducting Circuits for Quantum Information: An Outlook. Science, 339(6124):1169–1174, 2013.

[4] Ian D. Leroux, Monika H. Schleier-Smith, and Vladan Vuletić. Implementation of Cavity Squeezing of a Collective Atomic Spin. Phys. Rev. Lett., 104:073602, Feb 2010.

[5] J. Aasi, J. Abadie, B. P. Abbott, et al. Enhanced sensitivity of the LIGO gravitational wave detector by using squeezed states of light. Nature Photonics, 7(8):613–619, Aug 2013.

[6] Luca Pezzè, Augusto Smerzi, Markus K. Oberthaler, Roman Schmied, and Philipp Treutlein. Quantum metrology with nonclassical states of atomic ensembles. Rev. Mod. Phys., 90:035005, Sep 2018.

[7] Immanuel Bloch, Jean Dalibard, and Sylvain Nascimbène. Quantum simulations with ultracold quantum gases. Nature Physics, 8(4):267–276, Apr 2012.

[8] Christian Gross and Immanuel Bloch. Quantum simulations with ultracold atoms in optical lattices. Science, 357(6355):995–1001, 2017.

[9] Florian Schäfer, Takeshi Fukuhara, Seiji Sugawa, Yosuke Takasu, and Yoshiro Takahashi. Tools for quantum simulation with ultracold atoms in optical lattices. Nature Reviews Physics, 2(8):411–425, Aug 2020.

[10] Franco Dalfovo, Stefano Giorgini, Lev P. Pitaevskii, and Sandro Stringari. Theory of Bose-Einstein condensation in trapped gases. Rev. Mod. Phys., 71:463–512, Apr 1999.

[11] Stefano Giorgini, Lev P. Pitaevskii, and Sandro Stringari. Theory of ultracold atomic Fermi gases. Rev. Mod. Phys., 80:1215–1274, Oct 2008.

[12] D. Jaksch, C. Bruder, J. I. Cirac, C. W. Gardiner, and P. Zoller. Cold Bosonic Atoms in Optical Lattices. Phys. Rev. Lett., 81:3108–3111, Oct 1998.

[13] Markus Greiner, Olaf Mandel, Tilman Esslinger, Theodor W. Hänsch, and Immanuel Bloch. Quantum phase transition from a superfluid to a Mott insulator in a gas of ultracold atoms. Nature, 415(6867):39–44, Jan 2002.

[14] Markus Greiner, Cindy A. Regal, and Deborah S. Jin. Emergence of a molecular Bose–Einstein condensate from a Fermi gas. Nature, 426(6966):537–540, Dec 2003.

[15] M. W. Zwierlein, J. R. Abo-Shaeer, A. Schirotzek, C. H. Schunck, and W. Ketterle. Vortices and superfluidity in a strongly interacting Fermi gas. Nature, 435(7045):1047–1051, Jun 2005.

[16] S. Jochim, M. Bartenstein, A. Altmeyer, G. Hendl, S. Riedl, C. Chin, J. Hecker Denschlag, and R. Grimm. Bose-Einstein Condensation of Molecules. Science, 302(5653):2101–2103, 2003.

[17] T. Bourdel, L. Khaykovich, J. Cubizolles, J. Zhang, F. Chevy, M. Teichmann, L. Tarruell, S. J. J. M. F. Kokkelmans, and C. Salomon. Experimental Study of the BEC-BCS Crossover Region in Lithium 6. Phys. Rev. Lett., 93:050401, Jul 2004.

[18] Andrew D. Ludlow, Martin M. Boyd, Jun Ye, E. Peik, and P. O. Schmidt. Optical atomic clocks. Rev. Mod. Phys., 87:637–701, Jun 2015.

[19] Tobias Bothwell, Colin J. Kennedy, Alexander Aeppli, Dhruv Kedar, John M. Robinson, Eric Oelker, Alexander Staron, and Jun Ye. Resolving the gravitational redshift across a millimetre-scale atomic sample. Nature, 602(7897):420–424, Feb 2022.

[20] Wolfgang Ketterle and N.J. Van Druten. Evaporative Cooling of Trapped Atoms. volume 37 of Advances In Atomic, Molecular, and Optical Physics, pages 181–236. Academic Press, 1996.

[21] Eric Cornell, J Ensher, and C Wieman. Experiments in Dilute Atomic Bose-Einstein Condensation. Proceedings of the International School of Physics Enrico Fermi, Varenna on Lake Como, IT, 1999-11-01 1999.

[22] Cheng Chin, Rudolf Grimm, Paul Julienne, and Eite Tiesinga. Feshbach resonances in ultracold gases. Rev. Mod. Phys., 82:1225–1286, Apr 2010.

[23] Lincoln D Carr, David DeMille, Roman V Krems, and Jun Ye. Cold and ultracold molecules: science, technology and applications. New Journal of Physics, 11(5):055049, May 2009.

[24] M. A. Baranov, M. Dalmonte, G. Pupillo, and P. Zoller. Condensed Matter Theory of Dipolar Quantum Gases. Chemical Reviews, 112(9):5012–5061, 2012. PMID: 22877362.

[25] Goulven Quéméner and Paul S. Julienne. Ultracold Molecules under Control! Chemical Reviews, 112(9):4949–5011, 2012. PMID: 22921011.

[26] Bryce Gadway and Bo Yan. Strongly interacting ultracold polar molecules. Journal of Physics B: Atomic, Molecular and Optical Physics, 49(15):152002, jun 2016.

[27] John L. Bohn, Ana Maria Rey, and Jun Ye. Cold molecules: Progress in quantum engineering of chemistry and quantum matter. Science, 357(6355):1002–1010, 2017.

[28] N. Balakrishnan. Perspective: Ultracold molecules and the dawn of cold controlled chemistry. The Journal of Chemical Physics, 145(15):150901, 2016.

[29] Jutta Toscano, H. J. Lewandowski, and Brianna R. Heazlewood. Cold and controlled chemical reaction dynamics. Phys. Chem. Chem. Phys., 22:9180–9194, 2020.

[30] A. B. Henson, S. Gersten, Y. Shagam, J. Narevicius, and E. Narevicius. Observation of Resonances in Penning Ionization Reactions at Sub-Kelvin Temperatures in Merged Beams. Science, 338(6104):234–238, 2012.

[31] Tim de Jongh, Matthieu Besemer, Quan Shuai, Tijs Karman, Ad van der Avoird, Gerrit C. Groenenboom, and Sebastiaan Y. T. van de Meerakker. Imaging the onset of the resonance regime in low-energy NO-He collisions. Science, 368(6491):626–630, 2020.

[32] S. Ospelkaus, K.-K. Ni, D. Wang, M. H. G. de Miranda, B. Neyenhuis, G. Quéméner, P. S. Julienne, J. L. Bohn, D. S. Jin, and J. Ye. Quantum-State Controlled Chemical Reactions of Ultracold Potassium-Rubidium Molecules. Science, 327(5967):853–857, 2010.

[33] Joschka Wolf, Markus Deiß, Artjom Krükow, Eberhard Tiemann, Brandon P. Ruzic, Yujun Wang, José P. D'Incao, Paul S. Julienne, and Johannes Hecker Denschlag. State-to-state chemistry for three-body recombination in an ultracold rubidium gas. Science, 358(6365):921–924, 2017.

[34] M.-G. Hu, Y. Liu, D. D. Grimes, Y.-W. Lin, A. H. Gheorghe, R. Vexiau, N. Bouloufa-Maafa, O. Dulieu, T. Rosenband, and K.-K. Ni. Direct observation of bimolecular reactions of ultracold KRb molecules. Science, 366(6469):1111–1115, 2019.

[35] Yu Liu, Ming-Guang Hu, Matthew A Nichols, Dongzheng Yang, Daiqian Xie, Hua Guo, and Kang-Kuen Ni. Precision test of statistical dynamics with state-to-state ultracold chemistry. Nature, 593(7859):379–384, 2021.

[36] William B. Cairncross, Daniel N. Gresh, Matt Grau, Kevin C. Cossel, Tanya S. Roussy, Yiqi Ni, Yan Zhou, Jun Ye, and Eric A. Cornell. Precision Measurement of the Electron's Electric Dipole Moment Using Trapped Molecular Ions. Phys. Rev. Lett., 119:153001, Oct 2017.

[37] V. Andreev, D. G. Ang, D. DeMille, J. M. Doyle, G. Gabrielse, J. Haefner, N. R. Hutzler, Z. Lasner, C. Meisenhelder, B. R. O'Leary, C. D. Panda, A. D. West, E. P. West, X. Wu, and A. C. M. E. Collaboration. Improved limit on the electric dipole moment of the electron. Nature, 562(7727):355–360, Oct 2018.

[38] Edmund R. Meyer, John L. Bohn, and Michael P. Deskevich. Candidate molecular ions for an electron electric dipole moment experiment. Phys. Rev. A, 73:062108, Jun 2006.

[39] A.E. Leanhardt, J.L. Bohn, H. Loh, P. Maletinsky, E.R. Meyer, L.C. Sinclair, R.P. Stutz, and E.A. Cornell. High-resolution spectroscopy on trapped molecular ions in rotating electric fields: A new approach for measuring the electron electric dipole moment. Journal of Molecular Spectroscopy, 270(1):1–25, 2011.

[40] N. Y. Yao, M. P. Zaletel, D. M. Stamper-Kurn, and A. Vishwanath. A quantum dipolar spin liquid. Nature Physics, 14(4):405–410, Apr 2018.

[41] H. P. Büchler, E. Demler, M. Lukin, A. Micheli, N. Prokof'ev, G. Pupillo, and P. Zoller. Strongly Correlated 2D Quantum Phases with Cold Polar Molecules: Controlling the Shape of the Interaction Potential. Phys. Rev. Lett., 98:060404, Feb 2007.

[42] N. R. Cooper and G. V. Shlyapnikov. Stable Topological Superfluid Phase of Ultracold Polar Fermionic Molecules. Phys. Rev. Lett., 103:155302, Oct 2009.

[43] A. K. Fedorov, S. I. Matveenko, V. I. Yudson, and G. V. Shlyapnikov. Novel p-wave superfluids of fermionic polar molecules. Scientific Reports, 6(1):27448, Jun 2016.

[44] A. Micheli, G. K. Brennen, and P. Zoller. A toolbox for lattice-spin models with polar molecules. Nature Physics, 2(5):341–347, May 2006.

[45] Alexey V. Gorshkov, Salvatore R. Manmana, Gang Chen, Eugene Demler, Mikhail D. Lukin, and Ana Maria Rey. Quantum magnetism with polar alkali-metal dimers. Phys. Rev. A, 84:033619, Sep 2011.

[46] Bo Yan, Steven A. Moses, Bryce Gadway, Jacob P. Covey, Kaden R. A. Hazzard, Ana Maria Rey, Deborah S. Jin, and Jun Ye. Observation of dipolar spin-exchange interactions with lattice-confined polar molecules. Nature, 501(7468):521–525, Sep 2013.

[47] S. L. Campbell, R. B. Hutson, G. E. Marti, A. Goban, N. Darkwah Oppong, R. L. McNally, L. Sonderhouse, J. M. Robinson, W. Zhang, B. J. Bloom, and J. Ye. A Fermi-degenerate three-dimensional optical lattice clock. Science, 358(6359):90–94, 2017.

[48] Alexander Aeppli, Anjun Chu, Tobias Bothwell, Colin J. Kennedy, Dhruv Kedar, Peiru He, Ana Maria Rey, and Jun Ye. Hamiltonian engineering of spin-orbit coupled fermions in a Wannier-Stark optical lattice clock. https://arxiv.org/abs/2201.05909, 2022.

[49] Thomas Bilitewski, Luigi De Marco, Jun-Ru Li, Kyle Matsuda, William G. Tobias, Giacomo Valtolina, Jun Ye, and Ana Maria Rey. Dynamical Generation of Spin Squeezing in Ultracold Dipolar Molecules. Phys. Rev. Lett., 126:113401, Mar 2021.

[50] Luigi De Marco, Giacomo Valtolina, Kyle Matsuda, William G. Tobias, Jacob P. Covey, and Jun Ye. A degenerate Fermi gas of polar molecules. Science, 363(6429):853–856, 2019.

[51] William G. Tobias, Kyle Matsuda, Giacomo Valtolina, Luigi De Marco, Jun-Ru Li, and Jun Ye. Thermalization and Sub-Poissonian Density Fluctuations in a Degenerate Molecular Fermi Gas. Phys. Rev. Lett., 124:033401, Jan 2020.

[52] Giacomo Valtolina, Kyle Matsuda, William G. Tobias, Jun-Ru Li, Luigi De Marco, and Jun Ye. Dipolar evaporation of reactive molecules to below the Fermi temperature. Nature, 588(7837):239–243, 2020.

[53] Marcel Duda, Xing-Yan Chen, Andreas Schindewolf, Roman Bause, Jonas von Milczewski, Richard Schmidt, Immanuel Bloch, and Xin-Yu Luo. Transition from a polaronic condensate to a degenerate Fermi gas of heteronuclear molecules. https://arxiv.org/abs/2111.04301, 2021.

[54] Andreas Schindewolf, Roman Bause, Xing-Yan Chen, Marcel Duda, Tijs Karman, Immanuel Bloch, and Xin-Yu Luo. Evaporation of microwave-shielded polar molecules to quantum degeneracy. https://arxiv.org/abs/2201.05143, 2022.

[55] M. D. Di Rosa. Laser-cooling molecules. The European Physical Journal D - Atomic, Molecular, Optical and Plasma Physics, 31(2):395–402, Nov 2004.

[56] Benjamin K. Stuhl, Brian C. Sawyer, Dajun Wang, and Jun Ye. Magneto-optical Trap for Polar Molecules. Phys. Rev. Lett., 101:243002, Dec 2008.

[57] J. F. Barry, D. J. McCarron, E. B. Norrgard, M. H. Steinecker, and D. DeMille. Magneto-optical trapping of a diatomic molecule. Nature, 512(7514):286–289, Aug 2014.

[58] Loïc Anderegg, Benjamin L. Augenbraun, Eunmi Chae, Boerge Hemmerling, Nicholas R. Hutzler, Aakash Ravi, Alejandra Collopy, Jun Ye, Wolfgang Ketterle, and John M. Doyle. Radio Frequency Magneto-Optical Trapping of CaF with High Density. Phys. Rev. Lett., 119:103201, Sep 2017.

[59] S. Truppe, H. J. Williams, M. Hambach, L. Caldwell, N. J. Fitch, E. A. Hinds, B. E. Sauer, and M. R. Tarbutt. Molecules cooled below the Doppler limit. Nature Physics, 13(12):1173–1176, Dec 2017.

[60] Alejandra L. Collopy, Shiqian Ding, Yewei Wu, Ian A. Finneran, Loïc Anderegg, Benjamin L. Augenbraun, John M. Doyle, and Jun Ye. 3D Magneto-Optical Trap of Yttrium Monoxide. Phys. Rev. Lett., 121:213201, Nov 2018.

[61] Ivan Kozyryev, Louis Baum, Kyle Matsuda, and John M. Doyle. Proposal for Laser Cooling of Complex Polyatomic Molecules. ChemPhysChem, 17(22):3641–3648, 2016.

[62] Ivan Kozyryev, Louis Baum, Kyle Matsuda, Benjamin L. Augenbraun, Loic Anderegg, Alexander P. Sedlack, and John M. Doyle. Sisyphus Laser Cooling of a Polyatomic Molecule. Phys. Rev. Lett., 118:173201, Apr 2017.

[63] Debayan Mitra, Nathaniel B. Vilas, Christian Hallas, Loïc Anderegg, Benjamin L. Augenbraun, Louis Baum, Calder Miller, Shivam Raval, and John M. Doyle. Direct laser cooling of a symmetric top molecule. Science, 369(6509):1366–1369, 2020.

[64] Yewei Wu, Justin J. Burau, Kameron Mehling, Jun Ye, and Shiqian Ding. High Phase-Space Density of Laser-Cooled Molecules in an Optical Lattice. Phys. Rev. Lett., 127:263201, Dec 2021.

[65] Nikolay V. Vitanov, Andon A. Rangelov, Bruce W. Shore, and Klaas Bergmann. Stimulated Raman adiabatic passage in physics, chemistry, and beyond. Rev. Mod. Phys., 89:015006, Mar 2017.

[66] K.-K. Ni, S. Ospelkaus, M. H. G. de Miranda, A. Pe'er, B. Neyenhuis, J. J. Zirbel, S. Kotochigova, P. S. Julienne, D. S. Jin, and J. Ye. A High Phase-Space-Density Gas of Polar Molecules. Science, 322(5899):231–235, 2008.

[67] Tetsu Takekoshi, Lukas Reichsöllner, Andreas Schindewolf, Jeremy M. Hutson, C. Ruth Le Sueur, Olivier Dulieu, Francesca Ferlaino, Rudolf Grimm, and Hanns-Christoph Nägerl. Ultracold Dense Samples of Dipolar RbCs Molecules in the Rovibrational and Hyperfine Ground State. Phys. Rev. Lett., 113:205301, Nov 2014.

[68] Peter K. Molony, Philip D. Gregory, Zhonghua Ji, Bo Lu, Michael P. Köppinger, C. Ruth Le Sueur, Caroline L. Blackley, Jeremy M. Hutson, and Simon L. Cornish. Creation of Ultracold $^{87}Rb^{133}Cs$ Molecules in the Rovibrational Ground State. Phys. Rev. Lett., 113:255301, Dec 2014.

[69] Jee Woo Park, Sebastian A. Will, and Martin W. Zwierlein. Ultracold Dipolar Gas of Fermionic $^{23}Na^{40}K$ Molecules in Their Absolute Ground State. Phys. Rev. Lett., 114:205302, May 2015.

[70] Frauke Seeßelberg, Nikolaus Buchheim, Zhen-Kai Lu, Tobias Schneider, Xin-Yu Luo, Eberhard Tiemann, Immanuel Bloch, and Christoph Gohle. Modeling the adiabatic creation of ultracold polar $^{23}Na^{40}K$ molecules. Phys. Rev. A, 97:013405, Jan 2018.

[71] Lan Liu, De-Chao Zhang, Huan Yang, Ya-Xiong Liu, Jue Nan, Jun Rui, Bo Zhao, and Jian-Wei Pan. Observation of interference between resonant and detuned stirap in the adiabatic creation of $^{23}Na^{40}K$ molecules. Phys. Rev. Lett., 122:253201, Jun 2019.

[72] Mingyang Guo, Bing Zhu, Bo Lu, Xin Ye, Fudong Wang, Romain Vexiau, Nadia Bouloufa-Maafa, Goulven Quéméner, Olivier Dulieu, and Dajun Wang. Creation of an Ultracold Gas of Ground-State Dipolar $^{23}Na^{87}Rb$ Molecules. Phys. Rev. Lett., 116:205303, May 2016.

[73] Timur M. Rvachov, Hyungmok Son, Ariel T. Sommer, Sepehr Ebadi, Juliana J. Park, Martin W. Zwierlein, Wolfgang Ketterle, and Alan O. Jamison. Long-Lived Ultracold Molecules with Electric and Magnetic Dipole Moments. Phys. Rev. Lett., 119:143001, Oct 2017.

[74] William B. Cairncross, Jessie T. Zhang, Lewis R. B. Picard, Yichao Yu, Kenneth Wang, and Kang-Kuen Ni. Assembly of a Rovibrational Ground State Molecule in an Optical Tweezer. Phys. Rev. Lett., 126:123402, Mar 2021.

[75] Ian Stevenson, Aden Z. Lam, Niccolò Bigagli, Claire Warner, Weijun Yuan, Siwei Zhang, and Sebastian Will. Ultracold Gas of Dipolar NaCs Ground State Molecules. https://arxiv.org/abs/2206.00652, 2022.

[76] Vincent Barbé, Alessio Ciamei, Benjamin Pasquiou, Lukas Reichsöllner, Florian Schreck, Piotr S. Żuchowski, and Jeremy M. Hutson. Observation of Feshbach resonances between alkali and closed-shell atoms. Nature Physics, 14(9):881–884, Sep 2018.

[77] Alaina Green, Hui Li, Jun Hui See Toh, Xinxin Tang, Katherine C. McCormick, Ming Li, Eite Tiesinga, Svetlana Kotochigova, and Subhadeep Gupta. Feshbach Resonances in p-Wave Three-Body Recombination within Fermi-Fermi Mixtures of Open-Shell ^{6}Li and Closed-Shell ^{173}Yb Atoms. Phys. Rev. X, 10:031037, Aug 2020.

[78] A. Guttridge, Matthew D. Frye, B. C. Yang, Jeremy M. Hutson, and Simon L. Cornish. Two-photon photoassociation spectroscopy of CsYb: Ground-state interaction potential and interspecies scattering lengths. Phys. Rev. A, 98:022707, Aug 2018.

[79] K.-K. Ni, S. Ospelkaus, D. Wang, G. Quéméner, B. Neyenhuis, M. H. G. de Miranda, J. L. Bohn, J. Ye, and D. S. Jin. Dipolar collisions of polar molecules in the quantum regime. Nature, 464(7293):1324–1328, Apr 2010.

[80] Paul S. Julienne. Ultracold molecules from ultracold atoms: a case study with the KRb molecule. Faraday Discuss., 142:361–388, 2009.

[81] Goulven Quéméner and John L. Bohn. Strong dependence of ultracold chemical rates on electric dipole moments. Phys. Rev. A, 81:022702, Feb 2010.

[82] Zbigniew Idziaszek and Paul S. Julienne. Universal Rate Constants for Reactive Collisions of Ultracold Molecules. Phys. Rev. Lett., 104:113202, Mar 2010.

[83] Zbigniew Idziaszek, Goulven Quéméner, John L. Bohn, and Paul S. Julienne. Simple quantum model of ultracold polar molecule collisions. Phys. Rev. A, 82:020703, Aug 2010.

[84] Amodsen Chotia, Brian Neyenhuis, Steven A. Moses, Bo Yan, Jacob P. Covey, Michael Foss-Feig, Ana Maria Rey, Deborah S. Jin, and Jun Ye. Long-Lived Dipolar Molecules and Feshbach Molecules in a 3D Optical Lattice. Phys. Rev. Lett., 108:080405, Feb 2012.

[85] Kaden R. A. Hazzard, Bryce Gadway, Michael Foss-Feig, Bo Yan, Steven A. Moses, Jacob P. Covey, Norman Y. Yao, Mikhail D. Lukin, Jun Ye, Deborah S. Jin, and Ana Maria Rey. Many-Body Dynamics of Dipolar Molecules in an Optical Lattice. Phys. Rev. Lett., 113:195302, Nov 2014.

[86] Loïc Anderegg, Lawrence W. Cheuk, Yicheng Bao, Sean Burchesky, Wolfgang Ketterle, Kang-Kuen Ni, and John M. Doyle. An optical tweezer array of ultracold molecules. Science, 365(6458):1156–1158, 2019.

[87] Piotr S. Żuchowski and Jeremy M. Hutson. Reactions of ultracold alkali-metal dimers. Phys. Rev. A, 81:060703, Jun 2010.

[88] Xin Ye, Mingyang Guo, Maykel L. González-Martínez, Goulven Quéméner, and Dajun Wang. Collisions of ultracold $^{23}Na^{87}Rb$ molecules with controlled chemical reactivities. Science Advances, 4(1):eaaq0083, 2018.

[89] Mingyang Guo, Xin Ye, Junyu He, Maykel L. González-Martínez, Romain Vexiau, Goulven Quéméner, and Dajun Wang. Dipolar Collisions of Ultracold Ground-State Bosonic Molecules. Phys. Rev. X, 8:041044, Dec 2018.

[90] Michael Mayle, Goulven Quéméner, Brandon P. Ruzic, and John L. Bohn. Scattering of ultracold molecules in the highly resonant regime. Phys. Rev. A, 87:012709, Jan 2013.

[91] Arthur Christianen, Martin W. Zwierlein, Gerrit C. Groenenboom, and Tijs Karman. Photoinduced Two-Body Loss of Ultracold Molecules. Phys. Rev. Lett., 123:123402, Sep 2019.

[92] Yu Liu, Ming-Guang Hu, Matthew A. Nichols, David D. Grimes, Tijs Karman, Hua Guo, and Kang-Kuen Ni. Photo-excitation of long-lived transient intermediates in ultracold reactions. Nature Physics, 16(11):1132–1136, Nov 2020.

[93] Philip D. Gregory, Jacob A. Blackmore, Sarah L. Bromley, and Simon L. Cornish. Loss of Ultracold $^{87}Rb^{133}Cs$ Molecules via Optical Excitation of Long-Lived Two-Body Collision Complexes. Phys. Rev. Lett., 124:163402, Apr 2020.

[94] Roman Bause, Andreas Schindewolf, Renhao Tao, Marcel Duda, Xing-Yan Chen, Goulven Quéméner, Tijs Karman, Arthur Christianen, Immanuel Bloch, and Xin-Yu Luo. Collisions of ultracold molecules in bright and dark optical dipole traps. Phys. Rev. Research, 3:033013, Jul 2021.

[95] Philipp Gersema, Kai K. Voges, Mara Meyer zum Alten Borgloh, Leon Koch, Torsten Hartmann, Alessandro Zenesini, Silke Ospelkaus, Junyu Lin, Junyu He, and Dajun Wang. Probing Photoinduced Two-Body Loss of Ultracold Nonreactive Bosonic $^{23}Na^{87}Rb$ and $^{23}Na^{39}K$ Molecules. Phys. Rev. Lett., 127:163401, Oct 2021.

[96] Huan Yang, De-Chao Zhang, Lan Liu, Ya-Xiong Liu, Jue Nan, Bo Zhao, and Jian-Wei Pan. Observation of magnetically tunable Feshbach resonances in ultracold $^{23}Na^{40}K + ^{40}K$ collisions. Science, 363(6424):261–264, 2019.

[97] Huan Yang, Xin-Yao Wang, Zhen Su, Jin Cao, De-Chao Zhang, Jun Rui, Bo Zhao, Chun-Li Bai, and Jian-Wei Pan. Evidence for the association of triatomic molecules in ultracold 23Na40K + 40K mixtures. Nature, 602(7896):229–233, Feb 2022.

[98] Hyungmok Son, Juliana J. Park, Yu-Kun Lu, Alan O. Jamison, Tijs Karman, and Wolfgang Ketterle. Control of reactive collisions by quantum interference. Science, 375(6584):1006–1010, 2022.

[99] Andrea Micheli, Zbigniew Idziaszek, Guido Pupillo, Mikhail A. Baranov, Peter Zoller, and Paul S. Julienne. Universal Rates for Reactive Ultracold Polar Molecules in Reduced Dimensions. Phys. Rev. Lett., 105:073202, Aug 2010.

[100] Goulven Quéméner and John L. Bohn. Dynamics of ultracold molecules in confined geometry and electric field. Phys. Rev. A, 83:012705, Jan 2011.

[101] Goulven Quéméner, John L. Bohn, Alexander Petrov, and Svetlana Kotochigova. Universalities in ultracold reactions of alkali-metal polar molecules. Phys. Rev. A, 84:062703, Dec 2011.

[102] M. H. G. de Miranda, A. Chotia, B. Neyenhuis, D. Wang, G. Quéméner, S. Ospelkaus, J. L. Bohn, J. Ye, and D. S. Jin. Controlling the quantum stereodynamics of ultracold bimolecular reactions. Nature Physics, 7(6):502–507, Jun 2011.

[103] Alexander V. Avdeenkov, Masatoshi Kajita, and John L. Bohn. Suppression of inelastic collisions of polar $^1\Sigma$ state molecules in an electrostatic field. Phys. Rev. A, 73:022707, Feb 2006.

[104] Gaoren Wang and Goulven Quéméner. Tuning ultracold collisions of excited rotational dipolar molecules. New J. Phys., 17:035015, 2015.

[105] Loïc Anderegg, Sean Burchesky, Yicheng Bao, Scarlett S. Yu, Tijs Karman, Eunmi Chae, Kang-Kuen Ni, Wolfgang Ketterle, and John M. Doyle. Observation of microwave shielding of ultracold molecules. Science, 373(6556):779–782, 2021.

[106] Jacob Covey. Enhanced optical and electric manipulation of a quantum gas of KRb molecules. PhD thesis, University of Colorado Boulder, 2017.

[107] William G. Tobias. Degenerate Polar Molecules with Controlled Interactions and Reactivity. PhD thesis, University of Colorado Boulder, 2022.

[108] John M. Brown and Alan Carrington. Rotational Spectroscopy of Diatomic Molecules. Cambridge Molecular Science. Cambridge University Press, 2003.

[109] J. Aldegunde, Ben A. Rivington, Piotr S. Żuchowski, and Jeremy M. Hutson. Hyperfine energy levels of alkali-metal dimers: Ground-state polar molecules in electric and magnetic fields. Phys. Rev. A, 78:033434, Sep 2008.

[110] B. Neyenhuis, B. Yan, S. A. Moses, J. P. Covey, A. Chotia, A. Petrov, S. Kotochigova, J. Ye, and D. S. Jin. Anisotropic Polarizability of Ultracold Polar $^{40}K^{87}Rb$ Molecules. Phys. Rev. Lett., 109:230403, Dec 2012.

[111] S. Ospelkaus, K.-K. Ni, G. Quéméner, B. Neyenhuis, D. Wang, M. H. G. de Miranda, J. L. Bohn, J. Ye, and D. S. Jin. Controlling the Hyperfine State of Rovibronic Ground-State Polar Molecules. Phys. Rev. Lett., 104:030402, Jan 2010.

[112] Rudolf Grimm, Matthias Weidemüller, and Yurii B. Ovchinnikov. Optical Dipole Traps for Neutral Atoms. volume 42 of Advances In Atomic, Molecular, and Optical Physics, pages 95–170. Academic Press, 2000.

[113] Svetlana Kotochigova and David DeMille. Electric-field-dependent dynamic polarizability and state-insensitive conditions for optical trapping of diatomic polar molecules. Phys. Rev. A, 82:063421, Dec 2010.

[114] Jun Ye, H. J. Kimble, and Hidetoshi Katori. Quantum State Engineering and Precision Metrology Using State-Insensitive Light Traps. Science, 320(5884):1734–1738, 2008.

[115] S. Kotochigova and E. Tiesinga. Controlling polar molecules in optical lattices. Phys. Rev. A, 73:041405, Apr 2006.

[116] R. Vexiau, D. Borsalino, M. Lepers, A. Orbán, M. Aymar, O. Dulieu, and N. Bouloufa-Maafa. Dynamic dipole polarizabilities of heteronuclear alkali dimers: optical response, trapping and control of ultracold molecules. International Reviews in Physical Chemistry, 36(4):709–750, 2017.

[117] Ming Li, Alexander Petrov, Constantinos Makrides, Eite Tiesinga, and Svetlana Kotochigova. Pendular trapping conditions for ultracold polar molecules enforced by external electric fields. Phys. Rev. A, 95:063422, Jun 2017.

[118] Philip D. Gregory, Jacob A. Blackmore, Jesus Aldegunde, Jeremy M. Hutson, and Simon L. Cornish. ac Stark effect in ultracold polar $^{87}Rb^{133}Cs$ molecules. Phys. Rev. A, 96:021402, Aug 2017.

[119] Frauke Seeßelberg, Xin-Yu Luo, Ming Li, Roman Bause, Svetlana Kotochigova, Immanuel Bloch, and Christoph Gohle. Extending Rotational Coherence of Interacting Polar Molecules in a Spin-Decoupled Magic Trap. Phys. Rev. Lett., 121:253401, Dec 2018.

[120] Junyu Lin, Junyu He, Xin Ye, and Dajun Wang. Anisotropic polarizability of ultracold ground-state $^{23}Na^{87}Rb$ molecules. Phys. Rev. A, 103:023332, Feb 2021.

[121] Sean Burchesky, Loïc Anderegg, Yicheng Bao, Scarlett S. Yu, Eunmi Chae, Wolfgang Ketterle, Kang-Kuen Ni, and John M. Doyle. Rotational Coherence Times of Polar Molecules in Optical Tweezers. Phys. Rev. Lett., 127:123202, Sep 2021.

[122] Roman Bause, Ming Li, Andreas Schindewolf, Xing-Yan Chen, Marcel Duda, Svetlana Kotochigova, Immanuel Bloch, and Xin-Yu Luo. Tune-Out and Magic Wavelengths for Ground-State $^{23}Na^{40}K$ Molecules. Phys. Rev. Lett., 125:023201, Jul 2020.

[123] J. Kobayashi, K. Aikawa, K. Oasa, and S. Inouye. Prospects for narrow-line cooling of KRb molecules in the rovibrational ground state. Phys. Rev. A, 89:021401, Feb 2014.

[124] Q. Guan, Simon L. Cornish, and S. Kotochigova. Magic conditions for multiple rotational states of bialkali molecules in optical lattices. Phys. Rev. A, 103:043311, Apr 2021.

[125] J. Stuhler, A. Griesmaier, T. Koch, M. Fattori, T. Pfau, S. Giovanazzi, P. Pedri, and L. Santos. Observation of Dipole-Dipole Interaction in a Degenerate Quantum Gas. Phys. Rev. Lett., 95:150406, Oct 2005.

[126] Lauriane Chomaz, Igor Ferrier-Barbut, Francesca Ferlaino, Bruno Laburthe-Tolra, Benjamin L. Lev, and Tilman Pfau. Dipolar physics: A review of experiments with magnetic quantum gases. https://arxiv.org/abs/2201.02672, 2022.

[127] M. Saffman, T. G. Walker, and K. Mølmer. Quantum information with Rydberg atoms. Rev. Mod. Phys., 82:2313–2363, Aug 2010.

[128] G. Semeghini, H. Levine, A. Keesling, S. Ebadi, T. T. Wang, D. Bluvstein, R. Verresen, H. Pichler, M. Kalinowski, R. Samajdar, A. Omran, S. Sachdev, A. Vishwanath, M. Greiner, V. Vuletić, and M. D. Lukin. Probing topological spin liquids on a programmable quantum simulator. Science, 374(6572):1242–1247, 2021.

[129] J L Bohn, M Cavagnero, and C Ticknor. Quasi-universal dipolar scattering in cold and ultracold gases. New Journal of Physics, 11(5):055039, May 2009.

[130] Svetlana Kotochigova. Dispersion interactions and reactive collisions of ultracold polar molecules. New Journal of Physics, 12(7):073041, Jul 2010.

[131] Goulven Quéméner and John L. Bohn. Electric field suppression of ultracold confined chemical reactions. Phys. Rev. A, 81:060701, Jun 2010.

[132] Paul S. Julienne, Thomas M. Hanna, and Zbigniew Idziaszek. Universal ultracold collision rates for polar molecules of two alkali-metal atoms. Phys. Chem. Chem. Phys., 13:19114–19124, 2011.

[133] B. DeMarco, J. L. Bohn, J. P. Burke, M. Holland, and D. S. Jin. Measurement of p-Wave Threshold Law Using Evaporatively Cooled Fermionic Atoms. Phys. Rev. Lett., 82:4208–4211, May 1999.

[134] B. DeMarco and D. S. Jin. Onset of Fermi Degeneracy in a Trapped Atomic Gas. Science, 285(5434):1703–1706, 1999.

[135] K. Aikawa, A. Frisch, M. Mark, S. Baier, R. Grimm, and F. Ferlaino. Reaching Fermi Degeneracy via Universal Dipolar Scattering. Phys. Rev. Lett., 112:010404, Jan 2014.

[136] John L. Bohn and Deborah S. Jin. Differential scattering and rethermalization in ultracold dipolar gases. Phys. Rev. A, 89:022702, Feb 2014.

[137] Kyle Matsuda, Luigi De Marco, Jun-Ru Li, William G. Tobias, Giacomo Valtolina, Goulven Quéméner, and Jun Ye. Resonant collisional shielding of reactive molecules using electric fields. Science, 370(6522):1324–1327, 2020.

[138] Jun-Ru Li, William G. Tobias, Kyle Matsuda, Calder Miller, Giacomo Valtolina, Luigi De Marco, Reuben R. W. Wang, Lucas Lassablière, Goulven Quéméner, John L. Bohn, and Jun Ye. Tuning of dipolar interactions and evaporative cooling in a three-dimensional molecular quantum gas. Nature Physics, 17(10):1144–1148, Oct 2021.

[139] Sergey V. Syzranov, Michael L. Wall, Victor Gurarie, and Ana Maria Rey. Spin–orbital dynamics in a system of polar molecules. Nature Communications, 5(1):5391, Nov 2014.

[140] Kaden R. A. Hazzard, Salvatore R. Manmana, Michael Foss-Feig, and Ana Maria Rey. Far-from-Equilibrium Quantum Magnetism with Ultracold Polar Molecules. Phys. Rev. Lett., 110:075301, Feb 2013.

[141] Steven Moses. A quantum gas of polar molecules in an optical lattice. PhD thesis, University of Colorado Boulder, 2016.

[142] G. Salomon, L. Fouché, P. Wang, A. Aspect, P. Bouyer, and T. Bourdel. Gray-molasses cooling of ^{39}K to a high phase-space density. EPL (Europhysics Letters), 104(6):63002, dec 2013.

[143] Franz Sievers, Norman Kretzschmar, Diogo Rio Fernandes, Daniel Suchet, Michael Rabinovic, Saijun Wu, Colin V. Parker, Lev Khaykovich, Christophe Salomon, and Frédéric Chevy. Simultaneous sub-doppler laser cooling of fermionic ^{6}Li and ^{40}K on the D_1 line: Theory and experiment. Phys. Rev. A, 91:023426, Feb 2015.

[144] Sara Rosi, Alessia Burchianti, Stefano Conclave, Devang S. Naik, Giacomo Roati, Chiara Fort, and Francesco Minardi. Λ-enhanced grey molasses on the D2 transition of Rubidium-87 atoms. Scientific Reports, 8(1):1301, Jan 2018.

[145] K. B. Davis, M. O. Mewes, M. R. Andrews, N. J. van Druten, D. S. Durfee, D. M. Kurn, and W. Ketterle. Bose-Einstein Condensation in a Gas of Sodium Atoms. Phys. Rev. Lett., 75:3969–3973, Nov 1995.

[146] Joshua Zirbel. Ultracold Fermionic Feshbach Molecules. PhD thesis, University of Colorado Boulder, 2008.

[147] Kang-Kuen Ni. A Quantum Gas of Polar Molecules. PhD thesis, University of Colorado Boulder, 2009.

[148] Thorsten Best. Interacting Bose-Fermi mixture in optical lattices. PhD thesis, Johannes Gutenberg-Universität Mainz, 2011.

[149] Sebastian Will. Interacting bosons and fermions in three-dimensional optical lattice potentials: From atom optics to quantum simulation. PhD thesis, Johannes Gutenberg-Universität Mainz, 2011.

[150] Markus Greiner. Ultracold quantum gases in three-dimensional optical lattice potentials. PhD thesis, Ludwig-Maximilians-Universität München, 2003.

[151] J. J. Zirbel, K.-K. Ni, S. Ospelkaus, T. L. Nicholson, M. L. Olsen, P. S. Julienne, C. E. Wieman, J. Ye, and D. S. Jin. Heteronuclear molecules in an optical dipole trap. Phys. Rev. A, 78:013416, Jul 2008.

[152] William G. Tobias, Kyle Matsuda, Jun-Ru Li, Calder Miller, Annette N. Carroll, Thomas Bilitewski, Ana Maria Rey, and Jun Ye. Reactions between layer-resolved molecules mediated by dipolar spin exchange. Science, 375(6586):1299–1303, 2022.

[153] G. Edward Marti, Ross B. Hutson, Akihisa Goban, Sara L. Campbell, Nicola Poli, and Jun Ye. Imaging Optical Frequencies with 100 μHz Precision and 1.1 μm Resolution. Phys. Rev. Lett., 120:103201, Mar 2018.

[154] Mustafa Ahmed Ali Ahmed, Gonzalo A. Álvarez, and Dieter Suter. Robustness of dynamical decoupling sequences. Phys. Rev. A, 87:042309, Apr 2013.

[155] M. Bishof, X. Zhang, M. J. Martin, and Jun Ye. Optical Spectrum Analyzer with Quantum-Limited Noise Floor. Phys. Rev. Lett., 111:093604, Aug 2013.

[156] Michael J. Martin. Quantum Metrology and Many-Body Physics: Pushing the Frontier of the Optical Lattice Clock. PhD thesis, University of Colorado Boulder, 2013.

[157] Jamie C. Shaw. External electric fields: A new tool for controlling ultracold polar molecules. B.S. thesis, University of Colorado Boulder, 2015.

[158] Yomay Shyur. Stark deceleration methods for cold molecule experiments. PhD thesis, University of Colorado Boulder, 2018.

[159] Bhuvanesh Sundar, Bryce Gadway, and Kaden R. A. Hazzard. Synthetic dimensions in ultracold polar molecules. Scientific Reports, 8(1):3422, Feb 2018.

[160] David Peter, Norman Y. Yao, Nicolai Lang, Sebastian D. Huber, Mikhail D. Lukin, and Hans Peter Büchler. Topological bands with a Chern number $C = 2$ by dipolar exchange interactions. Phys. Rev. A, 91:053617, May 2015.

[161] Tijs Karman and Jeremy M. Hutson. Microwave Shielding of Ultracold Polar Molecules. Phys. Rev. Lett., 121:163401, Oct 2018.

[162] Tijs Karman. Microwave shielding with far-from-circular polarization. Phys. Rev. A, 101:042702, Apr 2020.

[163] Christian Sanner. Fluctuations in Quantum Degenerate Fermi Gases. PhD thesis, University of Colorado Boulder, 2012.

[164] George Edward Marti. Scalar and Spinor Excitations in a Ferromagnetic Bose-Einstein Condensate. PhD thesis, University of California, Berkeley, 2014.

[165] G. Reinaudi, T. Lahaye, Z. Wang, and D. Guéry-Odelin. Strong saturation absorption imaging of dense clouds of ultracold atoms. Optics Letters, 32(21):3143–3145, Nov 2007.

[166] Klaus Hueck, Niclas Luick, Lennart Sobirey, Jonas Siegl, Thomas Lompe, Henning Moritz, Logan W. Clark, and Cheng Chin. Calibrating high intensity absorption imaging of ultracold atoms. Opt. Express, 25(8):8670–8679, Apr 2017.

[167] Torben Müller, Bruno Zimmermann, Jakob Meineke, Jean-Philippe Brantut, Tilman Esslinger, and Henning Moritz. Local Observation of Antibunching in a Trapped Fermi Gas. Phys. Rev. Lett., 105:040401, Jul 2010.

[168] Peiru He, Thomas Bilitewski, Chris H. Greene, and Ana Maria Rey. Exploring chemical reactions in a quantum degenerate gas of polar molecules via complex formation. Phys. Rev. A, 102:063322, Dec 2020.

[169] Mingyuan He, Chenwei Lv, Hai-Qing Lin, and Qi Zhou. Universal relations for ultracold reactive molecules. Science Advances, 6(51):eabd4699, 2020.

[170] Zhendong Zhang, Liangchao Chen, Kai-Xuan Yao, and Cheng Chin. Transition from an atomic to a molecular Bose–Einstein condensate. Nature, 592(7856):708–711, Apr 2021.

[171] C. Klempt, T. Henninger, O. Topic, M. Scherer, L. Kattner, E. Tiemann, W. Ertmer, and J. J. Arlt. Radio-frequency association of heteronuclear Feshbach molecules. Phys. Rev. A, 78:061602, Dec 2008.

[172] E. Hodby, S. T. Thompson, C. A. Regal, M. Greiner, A. C. Wilson, D. S. Jin, E. A. Cornell, and C. E. Wieman. Production Efficiency of Ultracold Feshbach Molecules in Bosonic and Fermionic Systems. Phys. Rev. Lett., 94:120402, Mar 2005.

[173] W. Ketterle and M. W. Zwierlein. Making, probing and understanding ultracold Fermi gases. La Rivista del Nuovo Cimento, 31(5):247–422, May 2008.

[174] Cindy Regal. Experimental realization of BCS–BEC crossover physics with a Fermi gas of atoms. PhD thesis, University of Colorado Boulder, 2006.

[175] Georg M. Bruun and Charles W. Clark. Ideal gases in time-dependent traps. Phys. Rev. A, 61:061601, May 2000.

[176] Brian DeMarco. Quantum Behavior of an Atomic Fermi Gas. PhD thesis, University of Colorado Boulder, 2001.

[177] Christian Sanner, Edward J. Su, Aviv Keshet, Ralf Gommers, Yong-il Shin, Wujie Huang, and Wolfgang Ketterle. Suppression of Density Fluctuations in a Quantum Degenerate Fermi Gas. Phys. Rev. Lett., 105:040402, Jul 2010.

[178] J. J. Zirbel, K.-K. Ni, S. Ospelkaus, J. P. D'Incao, C. E. Wieman, J. Ye, and D. S. Jin. Collisional Stability of Fermionic Feshbach Molecules. Phys. Rev. Lett., 100:143201, Apr 2008.

[179] Ruth S. Bloom, Ming-Guang Hu, Tyler D. Cumby, and Deborah S. Jin. Tests of Universal Three-Body Physics in an Ultracold Bose-Fermi Mixture. Phys. Rev. Lett., 111:105301, Sep 2013.

[180] P. Maddaloni, M. Modugno, C. Fort, F. Minardi, and M. Inguscio. Collective Oscillations of Two Colliding Bose-Einstein Condensates. Phys. Rev. Lett., 85:2413–2417, Sep 2000.

[181] S. D. Gensemer and D. S. Jin. Transition from Collisionless to Hydrodynamic Behavior in an Ultracold Fermi Gas. Phys. Rev. Lett., 87:173201, Oct 2001.

[182] G. Ferrari, M. Inguscio, W. Jastrzebski, G. Modugno, G. Roati, and A. Simoni. Collisional Properties of Ultracold K-Rb Mixtures. Phys. Rev. Lett., 89:053202, Jul 2002.

[183] F Ferlaino, R J Brecha, P Hannaford, F Riboli, G Roati, G Modugno, and M Inguscio. Dipolar oscillations in a quantum degenerate Fermi Bose atomic mixture. Journal of Optics B: Quantum and Semiclassical Optics, 5(2):S3–S8, apr 2003.

[184] D. S. Petrov. Three-body problem in Fermi gases with short-range interparticle interaction. Phys. Rev. A, 67:010703, Jan 2003.

[185] D. Peter, S. Müller, S. Wessel, and H. P. Büchler. Anomalous Behavior of Spin Systems with Dipolar Interactions. Phys. Rev. Lett., 109:025303, Jul 2012.

[186] Bihui Zhu, Goulven Quéméner, Ana M. Rey, and Murray J. Holland. Evaporative cooling of reactive polar molecules confined in a two-dimensional geometry. Phys. Rev. A, 88:063405, Dec 2013.

[187] Brian Neyenhuis. Ultracold Polar KRb Molecules in Optical Lattices. PhD thesis, University of Colorado Boulder, 2012.

[188] Markus Greiner, Immanuel Bloch, Olaf Mandel, Theodor W. Hänsch, and Tilman Esslinger. Exploring Phase Coherence in a 2D Lattice of Bose-Einstein Condensates. Phys. Rev. Lett., 87:160405, Oct 2001.

[189] J. L. Ville, T. Bienaimé, R. Saint-Jalm, L. Corman, M. Aidelsburger, L. Chomaz, K. Kleinlein, D. Perconte, S. Nascimbène, J. Dalibard, and J. Beugnon. Loading and compression of a single two-dimensional bose gas in an optical accordion. Phys. Rev. A, 95:013632, Jan 2017.

[190] Chen-Lung Hung. In situ probing of two-dimensional quantum gases. PhD thesis, University of Chicago, 2011.

[191] M. G. Ries, A. N. Wenz, G. Zürn, L. Bayha, I. Boettcher, D. Kedar, P. A. Murthy, M. Neidig, T. Lompe, and S. Jochim. Observation of Pair Condensation in the Quasi-2D BEC-BCS Crossover. Phys. Rev. Lett., 114:230401, Jun 2015.

[192] P. A. Murthy, D. Kedar, T. Lompe, M. Neidig, M. G. Ries, A. N. Wenz, G. Zürn, and S. Jochim. Matter-wave Fourier optics with a strongly interacting two-dimensional Fermi gas. Phys. Rev. A, 90:043611, Oct 2014.

[193] S. Tung, G. Lamporesi, D. Lobser, L. Xia, and E. A. Cornell. Observation of the Presuperfluid Regime in a Two-Dimensional Bose Gas. Phys. Rev. Lett., 105:230408, Dec 2010.

[194] Ana Maria Rey. Ultracold bosonic atoms in optical lattices. PhD thesis, University of Maryland, 2004.

[195] Christopher Ticknor. Two-dimensional dipolar scattering. Phys. Rev. A, 80:052702, Nov 2009.

[196] Chen-Lung Hung, Xibo Zhang, Nathan Gemelke, and Cheng Chin. Accelerating evaporative cooling of atoms into Bose-Einstein condensation in optical traps. Phys. Rev. A, 78:011604, Jul 2008.

[197] Mehrtash Babadi and Eugene Demler. Collective excitations of quasi-two-dimensional trapped dipolar fermions: Transition from collisionless to hydrodynamic regime. Phys. Rev. A, 86:063638, Dec 2012.

[198] Benjamin K. Stuhl, Matthew T. Hummon, Mark Yeo, Goulven Quéméner, John L. Bohn, and Jun Ye. Evaporative cooling of the dipolar hydroxyl radical. Nature, 492(7429):396–400, Dec 2012.

[199] G. Günter, H. Schempp, M. Robert de Saint-Vincent, V. Gavryusev, S. Helmrich, C. S. Hofmann, S. Whitlock, and M. Weidemüller. Observing the Dynamics of Dipole-Mediated Energy Transport by Interaction-Enhanced Imaging. Science, 342(6161):954–956, 2013.

[200] Sylvain Ravets, Henning Labuhn, Daniel Barredo, Lucas Béguin, Thierry Lahaye, and Antoine Browaeys. Coherent dipole–dipole coupling between two single Rydberg atoms at an electrically-tuned Förster resonance. Nature Physics, 10(12):914–917, Dec 2014.

[201] R. Faoro, B. Pelle, A. Zuliani, P. Cheinet, E. Arimondo, and P. Pillet. Borromean three-body FRET in frozen Rydberg gases. Nature Communications, 6(1):8173, Sep 2015.

[202] Lucas Lassablière and Goulven Quéméner. Model for two-body collisions between ultracold dipolar molecules around a Förster resonance in an electric field. https://arxiv.org/abs/2204.02885, 2022.

[203] M. Lepers, R. Vexiau, M. Aymar, N. Bouloufa-Maafa, and O. Dulieu. Long-range interactions between polar alkali-metal diatoms in external electric fields. Phys. Rev. A, 88:032709, Sep 2013.

[204] Maykel L. González-Martínez, John L. Bohn, and Goulven Quéméner. Adimensional theory of shielding in ultracold collisions of dipolar rotors. Phys. Rev. A, 96:032718, Sep 2017.

[205] Goulven Quéméner and John L. Bohn. Shielding $^2\Sigma$ ultracold dipolar molecular collisions with electric fields. Phys. Rev. A, 93:012704, Jan 2016.

[206] Goulven Quéméner, Maxence Lepers, and Olivier Dulieu. Dynamics of ultracold dipolar particles in a confined geometry and tilted fields. Phys. Rev. A, 92:042706, Oct 2015.

[207] Reuben R. W. Wang and John L. Bohn. Anisotropic thermalization of dilute dipolar gases. Phys. Rev. A, 103:063320, Jun 2021.

[208] K. Aikawa, A. Frisch, M. Mark, S. Baier, R. Grimm, J. L. Bohn, D. S. Jin, G. M. Bruun, and F. Ferlaino. Anisotropic Relaxation Dynamics in a Dipolar Fermi Gas Driven Out of Equilibrium. Phys. Rev. Lett., 113:263201, Dec 2014.

[209] Yijun Tang, Andrew Sykes, Nathaniel Q. Burdick, John L. Bohn, and Benjamin L. Lev. s-wave scattering lengths of the strongly dipolar bosons ^{162}Dy and ^{164}Dy. Phys. Rev. A, 92:022703, Aug 2015.

[210] K. Aikawa, S. Baier, A. Frisch, M. Mark, C. Ravensbergen, and F. Ferlaino. Observation of Fermi surface deformation in a dipolar quantum gas. Science, 345(6203):1484–1487, 2014.

[211] Ching-Kit Chan, Congjun Wu, Wei-Cheng Lee, and S. Das Sarma. Anisotropic-Fermi-liquid theory of ultracold fermionic polar molecules: Landau parameters and collective modes. Phys. Rev. A, 81:023602, Feb 2010.

[212] Shai Ronen and John L. Bohn. Zero sound in dipolar Fermi gases. Phys. Rev. A, 81:033601, Mar 2010.

[213] Lucas Lassablière and Goulven Quéméner. Controlling the Scattering Length of Ultracold Dipolar Molecules. Phys. Rev. Lett., 121:163402, Oct 2018.

[214] Hyungmok Son, Juliana J. Park, Wolfgang Ketterle, and Alan O. Jamison. Collisional cooling of ultracold molecules. Nature, 580(7802):197–200, Apr 2020.

[215] Matthew A. Nichols, Yi-Xiang Liu, Lingbang Zhu, Ming-Guang Hu, Yu Liu, and Kang-Kuen Ni. Detection of Long-Lived Complexes in Ultracold Atom-Molecule Collisions. Phys. Rev. X, 12:011049, Mar 2022.

[216] M. P. Kwasigroch and N. R. Cooper. Bose-Einstein condensation and many-body localization of rotational excitations of polar molecules following a microwave pulse. Phys. Rev. A, 90:021605, Aug 2014.

[217] M. P. Kwasigroch and N. R. Cooper. Synchronization transition in dipole-coupled two-level systems with positional disorder. Phys. Rev. A, 96:053610, Nov 2017.

[218] N. Y. Yao, A. V. Gorshkov, C. R. Laumann, A. M. Läuchli, J. Ye, and M. D. Lukin. Realizing Fractional Chern Insulators in Dipolar Spin Systems. Phys. Rev. Lett., 110:185302, Apr 2013.

[219] Jacob F. Sherson, Christof Weitenberg, Manuel Endres, Marc Cheneau, Immanuel Bloch, and Stefan Kuhr. Single-atom-resolved fluorescence imaging of an atomic Mott insulator. Nature, 467(7311):68–72, Sep 2010.

[220] G. J. A. Edge, R. Anderson, D. Jervis, D. C. McKay, R. Day, S. Trotzky, and J. H. Thywissen. Imaging and addressing of individual fermionic atoms in an optical lattice. Phys. Rev. A, 92:063406, Dec 2015.

[221] Juliette Billy, Vincent Josse, Zhanchun Zuo, Alain Bernard, Ben Hambrecht, Pierre Lugan, David Clément, Laurent Sanchez-Palencia, Philippe Bouyer, and Alain Aspect. Direct observation of anderson localization of matter waves in a controlled disorder. Nature, 453(7197):891–894, Jun 2008.

[222] M. Schulz, C. A. Hooley, R. Moessner, and F. Pollmann. Stark Many-Body Localization. Phys. Rev. Lett., 122:040606, Jan 2019.

[223] W. Morong, F. Liu, P. Becker, K. S. Collins, L. Feng, A. Kyprianidis, G. Pagano, T. You, A. V. Gorshkov, and C. Monroe. Observation of Stark many-body localization without disorder. Nature, 599(7885):393–398, Nov 2021.

[224] N. Y. Yao, C. R. Laumann, S. Gopalakrishnan, M. Knap, M. Müller, E. A. Demler, and M. D. Lukin. Many-Body Localization in Dipolar Systems. Phys. Rev. Lett., 113:243002, Dec 2014.

[225] Rahul Nandkishore and David A. Huse. Many-Body Localization and Thermalization in Quantum Statistical Mechanics. Annual Review of Condensed Matter Physics, 6(1):15–38, 2015.

[226] A. Pikovski, M. Klawunn, A. Recati, and L. Santos. Nonlocal state swapping of polar molecules in bilayers. Phys. Rev. A, 84:061605, Dec 2011.

[227] H. Pu and P. Meystre. Creating Macroscopic Atomic Einstein-Podolsky-Rosen States from Bose-Einstein Condensates. Phys. Rev. Lett., 85:3987–3990, Nov 2000.

[228] B. Lücke, M. Scherer, J. Kruse, L. Pezzé, F. Deuretzbacher, P. Hyllus, O. Topic, J. Peise, W. Ertmer, J. Arlt, L. Santos, A. Smerzi, and C. Klempt. Twin Matter Waves for Interferometry Beyond the Classical Limit. Science, 334(6057):773–776, 2011.

[229] Kaden R. A. Hazzard, Alexey V. Gorshkov, and Ana Maria Rey. Spectroscopy of dipolar fermions in layered two-dimensional and three-dimensional lattices. Phys. Rev. A, 84:033608, Sep 2011.

[230] Elbio Dagotto. Correlated electrons in high-temperature superconductors. Rev. Mod. Phys., 66:763–840, Jul 1994.

[231] Leon Balents. Spin liquids in frustrated magnets. Nature, 464(7286):199–208, Mar 2010.

[232] Subir Sachdev. Quantum magnetism and criticality. Nature Physics, 4(3):173–185, Mar 2008.

[233] Emily Davis, Gregory Bentsen, and Monika Schleier-Smith. Approaching the Heisenberg Limit without Single-Particle Detection. Phys. Rev. Lett., 116:053601, Feb 2016.

[234] Jun-Ru Li et al. in preparation, 2022.

[235] A. M. Rey, M. J. Martin, M. D. Swallows, M. Bishof, C. Benko, S. Blatt, J. Von Stecher, A. Gorshkov, and J. Ye. Probing many-body spin interactions with an optical lattice clock. In 2012 IEEE International Frequency Control Symposium Proceedings, pages 1–1, 2012.

[236] M. J. Martin, M. Bishof, M. D. Swallows, X. Zhang, C. Benko, J. von Stecher, A. V. Gorshkov, A. M. Rey, and Jun Ye. A Quantum Many-Body Spin System in an Optical Lattice Clock. Science, 341(6146):632–636, 2013.

[237] Scott Smale, Peiru He, Ben A. Olsen, Kenneth G. Jackson, Haille Sharum, Stefan Trotzky, Jamir Marino, Ana Maria Rey, and Joseph H. Thywissen. Observation of a transition between dynamical phases in a quantum degenerate fermi gas. Science Advances, 5(8):eaax1568, 2019.

[238] Christian Gross. Spin squeezing, entanglement and quantum metrology with bose–einstein condensates. Journal of Physics B: Atomic, Molecular and Optical Physics, 45(10):103001, may 2012.

[239] Tijs Karman, Zoe Z. Yan, and Martin Zwierlein. Resonant and first-order dipolar interactions between ultracold $^1\Sigma$ molecules in static and microwave electric fields. Phys. Rev. A, 105:013321, Jan 2022.

[240] L. M. K. Vandersypen and I. L. Chuang. NMR techniques for quantum control and computation. Rev. Mod. Phys., 76:1037–1069, Jan 2005.

[241] G. de Lange, Z. H. Wang, D. Ristè, V. V. Dobrovitski, and R. Hanson. Universal dynamical decoupling of a single solid-state spin from a spin bath. Science, 330(6000):60–63, 2010.

[242] L. M. Pham, N. Bar-Gill, C. Belthangady, D. Le Sage, P. Cappellaro, M. D. Lukin, A. Yacoby, and R. L. Walsworth. Enhanced solid-state multispin metrology using dynamical decoupling. Phys. Rev. B, 86:045214, Jul 2012.

[243] Hagai Edri, Boaz Raz, Gavriel Fleurov, Roee Ozeri, and Nir Davidson. Observation of nonlinear spin dynamics and squeezing in a BEC using dynamic decoupling. New Journal of Physics, 23(5):053005, May 2021.

[244] Alexandre M. Souza, Gonzalo A. Álvarez, and Dieter Suter. Robust dynamical decoupling for quantum computing and quantum memory. Phys. Rev. Lett., 106:240501, Jun 2011.

[245] Martin Gärttner, Justin G. Bohnet, Arghavan Safavi-Naini, Michael L. Wall, John J. Bollinger, and Ana Maria Rey. Measuring out-of-time-order correlations and multiple quantum spectra in a trapped-ion quantum magnet. Nature Physics, 13(8):781–786, Aug 2017.

[246] Ivan Kozyryev and Nicholas R. Hutzler. Precision Measurement of Time-Reversal Symmetry Violation with Laser-Cooled Polyatomic Molecules. Phys. Rev. Lett., 119:133002, Sep 2017.

[247] Jason S. Rosenberg, Lysander Christakis, Elmer Guardado-Sanchez, Zoe Z. Yan, and Waseem S. Bakr. Observation of the Hanbury Brown and Twiss Effect with Ultracold Molecules. https://arxiv.org/abs/2111.09426, 2021.

[248] Andreas Kruckenhauser, Lukas M. Sieberer, Luigi De Marco, Jun-Ru Li, Kyle Matsuda, William G. Tobias, Giacomo Valtolina, Jun Ye, Ana Maria Rey, Mikhail A. Baranov, and Peter Zoller. Quantum many-body physics with ultracold polar molecules: Nanostructured potential barriers and interactions. Phys. Rev. A, 102:023320, Aug 2020.

[249] A. Pikovski, M. Klawunn, G. V. Shlyapnikov, and L. Santos. Interlayer Superfluidity in Bilayer Systems of Fermionic Polar Molecules. Phys. Rev. Lett., 105:215302, Nov 2010.

[250] D. Wang, B. Neyenhuis, M. H. G. de Miranda, K.-K. Ni, S. Ospelkaus, D. S. Jin, and J. Ye. Direct absorption imaging of ultracold polar molecules. Phys. Rev. A, 81:061404, Jun 2010.

[251] Qingze Guan, Michael Highman, Eric J. Meier, Garrett R. Williams, Vito Scarola, Brian DeMarco, Svetlana Kotochigova, and Bryce Gadway. Nondestructive dispersive imaging of rotationally excited ultracold molecules. Phys. Chem. Chem. Phys., 22:20531–20544, 2020.

[252] Christof Weitenberg and Juliette Simonet. Tailoring quantum gases by Floquet engineering. Nature Physics, 17(12):1342–1348, Dec 2021.

[253] Thomas Schuster, Felix Flicker, Ming Li, Svetlana Kotochigova, Joel E. Moore, Jun Ye, and Norman Y. Yao. Realizing Hopf Insulators in Dipolar Spin Systems. Phys. Rev. Lett., 127:015301, Jun 2021.

[254] Elena Kuznetsova, Seth T. Rittenhouse, H. R. Sadeghpour, and Susanne F. Yelin. Rydberg-atom-mediated nondestructive readout of collective rotational states in polar-molecule arrays. Phys. Rev. A, 94:032325, Sep 2016.

[255] M. Zeppenfeld. Nondestructive detection of polar molecules via Rydberg atoms. EPL (Europhysics Letters), 118(1):13002, apr 2017.

[256] Kenneth Wang, Conner P. Williams, Lewis R. B. Picard, Norman Y. Yao, and Kang-Kuen Ni. Enriching the quantum toolbox of ultracold molecules with Rydberg atoms. https://arxiv.org/abs/2204.05293, 2022.

[257] Jeff Bezanson, Alan Edelman, Stefan Karpinski, and Viral B Shah. Julia: A fresh approach to numerical computing. SIAM review, 59(1):65–98, 2017.

[258] Simon Danisch and Julius Krumbiegel. Makie.jl: Flexible high-performance data visualization for Julia. Journal of Open Source Software, 6(65):3349, 2021.

[259] Jacob A. Blackmore, Philip D. Gregory, Jeremy M. Hutson, and Simon L. Cornish. Diatomic-py: A python module for calculating the rotational and hyperfine structure of $^1\Sigma$ molecules. https://arxiv.org/abs/2205.05686, 2022.

Appendix A

KRb energy levels in external fields

We will start by summarizing a few of the important equations in Chapter 2, following Chapter 5 of Ref. [108].

Let $\mathcal{D}^{(k)}_{pq}(\omega)^*$ be the rank k rotation matrix, with ω the Euler angles for rotating from the molecule frame to the lab frame. This has matrix elements

$$\langle J, m_J, \Omega | \mathcal{D}^{(k)}_{pq}(\omega)^* | J', m'_J, \Omega' \rangle = (-1)^{m_J - \Omega} \sqrt{(2J+1)(2J'+1)} \begin{pmatrix} J & k & J' \\ -\Omega & q & \Omega' \end{pmatrix} \begin{pmatrix} J & k & J' \\ -m_J & p & m'_J \end{pmatrix}. \tag{A.1}$$

The index p is associated with the lab frame while the index q is associated with the molecule frame. This also gives a helpful mnemonic for remembering the matrix elements, since the molecule frame index q appears alongside Ω and the lab frame index p appears alongside M_J in the $3j$ symbols.

To get a tensor $T^{(k)}_q(\mathbf{A})$ from the molecule frame to the lab frame, we contract it with $\mathcal{D}^{(k)}_{pq}(\omega)^*$,

$$T^{(k)}_p(\mathbf{A}) = \sum_q \mathcal{D}^{(k)}_{pq}(\omega)^* T^{(k)}_q(\mathbf{A}). \tag{A.2}$$

In terms of the Cartesian components of $\mathbf{A}$, the rank 1 tensor $T^{(1)}_p(\mathbf{A})$ is

$$T^{(1)}_0(\mathbf{A}) = A_z, \tag{A.3}$$

$$T^{(1)}_{\pm 1}(\mathbf{A}) = \mp \frac{1}{\sqrt{2}}(A_x \pm i A_y). \tag{A.4}$$

The rank 2 tensor $T_p^{(2)}(\mathbf{u},\mathbf{v})$ is given by

$$T_0^{(2)}(\mathbf{u},\mathbf{v}) = \frac{1}{\sqrt{6}}(2u_z v_z - u_x v_x - u_y v_y) \tag{A.5}$$

$$T_{\pm1}^{(2)}(\mathbf{u},\mathbf{v}) = \mp\frac{1}{2}\left(u_x v_z + u_z v_x \pm i(u_y v_z + u_z v_y)\right) \tag{A.6}$$

$$T_{\pm2}^{(2)}(\mathbf{u},\mathbf{v}) = \frac{1}{2}\left(u_x v_x - u_y v_y \pm i(u_x v_y + u_y v_x)\right). \tag{A.7}$$

In terms of $3j$ symbols, the Wigner-Eckart theorem is

$$\langle j,m|T_p^{(k)}(\mathbf{A})|j',m'\rangle = (-1)^{j-m}\begin{pmatrix} j & k & j' \\ -m & p & m' \end{pmatrix}\langle j||T^{(k)}(\mathbf{A})||j'\rangle. \tag{A.8}$$

Here are a few useful reduced matrix elements:

$$\langle j||T^{(1)}(\mathbf{J})||j'\rangle = \delta_{jj'}\sqrt{j(j+1)(2j+1)} \tag{A.9}$$

$$\langle j||T^{(2)}(\mathbf{J},\mathbf{J})||j'\rangle = \delta_{jj'}\frac{j(2j-1)}{\sqrt{6}}\begin{pmatrix} J & 2 & J \\ -J & 0 & J \end{pmatrix}^{-1} \tag{A.10}$$

$$\langle I||T^{(2)}(\mathbf{Q})||I'\rangle = \delta_{II'}\frac{eQ}{2}\begin{pmatrix} I & 2 & I \\ -I & 0 & I \end{pmatrix}^{-1}. \tag{A.11}$$

$T^{(2)}(\mathbf{Q})$ above is the nuclear quadrupole tensor, needed for calculating the nuclear electric quadupole interaction.

A.1 Molecular Hamiltonian

Following Ref. [109], the molecular Hamiltonian in the presence of $\mathbf{B}$ and $\mathbf{E}$ is

$$H = H_{\rm rot} + H_{\rm S} + H_{\rm hf} + H_{\rm Z} \tag{A.12}$$

$$H_{\rm rot} = B_v \mathbf{N}^2 \tag{A.13}$$

$$H_{\rm S} = -\mathbf{d}\cdot\mathbf{E} \tag{A.14}$$

$$H_{\rm hf} = \sum_{i={\rm K,Rb}} \mathbf{V}_i\cdot\mathbf{Q}_i + \sum_{i={\rm K,Rb}} c_i\mathbf{N}\cdot\mathbf{I}_i + c_3\mathbf{I}_{\rm K}\cdot\mathbf{T}\cdot\mathbf{I}_{\rm Rb} + c_4\mathbf{I}_{\rm K}\cdot\mathbf{I}_{\rm Rb} \tag{A.15}$$

$$H_{\rm Z} = -g_r\mu_N\mathbf{N}\cdot\mathbf{B} - \sum_{i={\rm K,Rb}} g_i\mu_N\mathbf{I}_i\cdot\mathbf{B}(1-\sigma_i). \tag{A.16}$$

Above, we have ignored the centrifugal distortion term $D_v\mathbf{N}^2\mathbf{N}^2$, which is negligible for the lowest rotational states.

The physical meaning of individual terms of H and coupling constants for KRb are discussed in section 2.2. Here, we will write down the relevant matrix elements. We work in the uncoupled basis $|N, m_N, m_1, m_2\rangle$, where m_1 (m_2) is the K (Rb) nuclear angular momentum projection. The rotation term is already diagonal in the uncoupled basis, and the Stark term is discussed in detail in section 2.3.1. The Zeeman term is already diagonal if $\mathbf{B} = B\mathbf{z}$. However, it might be useful in the future to vary the angle between $\mathbf{B}$ and $\mathbf{E}$, so let us work out the general case for $\mathbf{B}$. All of the terms of H_Z have the same form (up to swapping $\mathbf{N}$ for $\mathbf{I}_i$), so we can just focus on the $\mathbf{N}\cdot\mathbf{B}$ term,

$$\begin{aligned}\langle N, m_N|\mathbf{N}\cdot\mathbf{B}|N', m'_N\rangle &= \sum_{p=-1}^{1}(-1)^p\langle N, m_N|T_p^{(1)}(\mathbf{N})T_{-p}^{(1)}(\mathbf{B})|N', m'_N\rangle \\ &= (-1)^{N-m_N}\sum_{p=-1}^{1}(-1)^pT_{-p}^{(1)}(\mathbf{B})\begin{pmatrix} N & 1 & N' \\ -m_N & p & m'_N\end{pmatrix}\langle N||T_p^{(1)}(\mathbf{N})||N\rangle \\ &= (-1)^{N-m_N}\delta_{NN'}\sqrt{N(N+1)(2N+1)}\sum_{p=-1}^{1}(-1)^pT_{-p}^{(1)}(\mathbf{B})\begin{pmatrix} N & 1 & N' \\ -m_N & p & m'_N\end{pmatrix}.\end{aligned} \tag{A.17}$$

The orientation of $\mathbf{E}$ can also be allowed to vary by generalizing the Stark term to

$$H_\mathrm{S} = -\sum_p(-1)^pd^pT_{-p}^{(1)}(\mathbf{E}). \tag{A.18}$$

The hyperfine Hamiltonian is the most complicated. The first term (nuclear electric quadrupole)

is calculated explicitly in Brown and Carrington, pg. 476:

$$\sum_{p=-2}^{2}\langle N,m_N,I_i,m_i|(-1)^p T_p^{(2)}(\mathbf{V}_i)T_{-p}^{(2)}(\mathbf{Q}_i)|N',m'_N,I'_i,m'_i\rangle$$

$$=\frac{q}{2}\sum_p(-1)^p(-1)^{-m_N}\sqrt{(2N+1)(2N'+1)}\begin{pmatrix}N & 2 & N'\\ 0 & 0 & 0\end{pmatrix}\begin{pmatrix}N & 2 & N'\\ -m_N & p & m'_N\end{pmatrix}$$

$$\times(-1)^{I_i-m_i}\begin{pmatrix}I_i & 2 & I'_i\\ -m_i & -p & m'_i\end{pmatrix}\langle I_i||T^{(2)}(\mathbf{Q}_i)||I'_i\rangle$$

$$=\delta_{I_iI'_i}\frac{(eqQ_i)}{2}\sum_p(-1)^p(-1)^{-m_N}\sqrt{(2N+1)(2N'+1)}\begin{pmatrix}N & 2 & N'\\ 0 & 0 & 0\end{pmatrix}\begin{pmatrix}N & 2 & N'\\ -m_N & p & m'_N\end{pmatrix}$$

$$\times(-1)^{I_i-m_i}\begin{pmatrix}I_i & 2 & I_i\\ -m_i & -p & m'_i\end{pmatrix}\begin{pmatrix}I_i & 2 & I_i\\ -I_i & 0 & I_i\end{pmatrix}^{-1}.$$

Note that the N-dependent part is the matrix element of $\mathcal{D}^{(k)}_{p,q=0}(\omega)^* = \sqrt{4\pi/(2N+1)}Y_{2p}(\omega) = C_{2p}(\omega)$, which explains the correspondence between the form that is used in Ref. [109] versus Ref. [117, 124]. For KRb, the $c_4\mathbf{I}_1\cdot\mathbf{I}_2$ term is the next largest, with matrix elements

$$\langle m_1,m_2|\mathbf{I}_1\cdot\mathbf{I}_2|m'_1,m'_2\rangle=\sum_{p=-1}^{1}(-1)^p\langle m_1,m_2|T_p^{(1)}(\mathbf{I}_1)T_{-p}^{(1)}(\mathbf{I}_2)|m'_1,m'_2\rangle$$

$$=\sum_{p=-1}^{1}(-1)^p(-1)^{I_1-m_1}\begin{pmatrix}I_1 & 1 & I_1\\ -m_1 & p & m'_1\end{pmatrix}\langle I_1||T^{(1)}(\mathbf{I}_1)||I_1\rangle$$

$$\times(-1)^{I_2-m_2}\begin{pmatrix}I_2 & 1 & I_2\\ -m_2 & -p & m'_2\end{pmatrix}\langle I_2||T^{(1)}(\mathbf{I}_2)||I_2\rangle$$

$$=\sum_{p=-1}^{1}(-1)^p(-1)^{I_1+I_2-m_1-m_2}\sqrt{I_1(I_1+1)(2I_1+1)}\sqrt{I_2(I_2+1)(2I_2+1)}$$

$$\times\begin{pmatrix}I_1 & 1 & I_1\\ -m_1 & p & m'_1\end{pmatrix}\begin{pmatrix}I_2 & 1 & I_2\\ -m_2 & -p & m'_2\end{pmatrix}.$$

The nuclear spin-rotation term is

$$\begin{aligned}
\langle N, m_N, I_i, m_i|\mathbf{N}\cdot\mathbf{I}_i|N', m'_N, I'_i, m'_i\rangle &= \sum_p (-1)^p \langle N, m_N|T^{(1)}_p(\mathbf{N})|N', m'_N\rangle\langle I_i, m_i|T^{(1)}_{-p}(\mathbf{I}_i)|I'_i, m'_i\rangle \\
&= \sum_p (-1)^p (-1)^{N-m_N} \begin{pmatrix} N & 1 & N' \\ -m_N & p & m'_N \end{pmatrix} \langle N||T^{(1)}(\mathbf{N})||N'\rangle \\
&\times (-1)^{I_i-m_i} \begin{pmatrix} I_i & 1 & I'_i \\ -m_i & -p & m'_i \end{pmatrix} \langle I_i||T^{(1)}(\mathbf{I}_i)||I'_i\rangle \\
&= \delta_{NN'}\delta_{I_iI'_i} \sum_p (-1)^p (-1)^{N+I_i-m_N-m_i} \\
&\times \sqrt{N(N+1)(2N+1)}\sqrt{I_i(I_i+1)(2I_i+1)} \\
&\times \begin{pmatrix} N & 1 & N \\ -m_N & p & m'_N \end{pmatrix} \begin{pmatrix} I_i & 1 & I_i \\ -m_i & -p & m'_i \end{pmatrix}.
\end{aligned}$$

The last term is the nuclear magnetic dipole-dipole tensor term. This term is negligibly small for KRb [109], so we ignore it for simplicity.

The calculations in Chapter 2 that include hyperfine structure were performed with a solver, BialkaliSpectrum.jl[1], written in Julia [257]. We have written a few automated tests for BialkaliSpectrum.jl, some of which are described below, though users should be aware that the code has not yet been thoroughly tested and may contain bugs. The plots in Chapter 2 were created with a Julia plotting library called Makie.jl [258].

A.2 AC Stark shift

Ref. [117] gives the following form for the AC Stark shift:

$$H_{\text{ac}} = -\frac{1}{3}(\alpha_\parallel + 2\alpha_\perp)I_{\text{laser}} - \frac{\sqrt{6}}{3}(\alpha_\parallel - \alpha_\perp)T^{(2)}(\boldsymbol{\epsilon},\boldsymbol{\epsilon})\cdot C_2(\alpha,\beta)I_{\text{laser}}, \tag{A.19}$$

[1] https://github.com/kylematsuda/BialkaliSpectrum.jl. After writing BialkaliSpectrum.jl, we became aware of a similar project Diatomic-py from the Cornish group [259].

where $C_{2p}(\alpha,\beta) = \mathcal{D}^{(2)}_{p0}(\omega)^*$ is the rotation to the molecular frame, with α and β the Euler angles. Expanding, we find matrix elements

$$\begin{aligned}\langle N, m_N|T^{(2)}(\boldsymbol{\epsilon},\boldsymbol{\epsilon})\cdot C_2(\alpha,\beta)|N', m'_N\rangle &= \delta_{N,N'}\sum_p (-1)^p T^{(2)}_p(\boldsymbol{\epsilon},\boldsymbol{\epsilon})\langle N, m_N|C_{2,-p}(\alpha,\beta)|N, m'_N\rangle \\ &= \delta_{N,N'}\sum_p (-1)^p T^{(2)}_p(\boldsymbol{\epsilon},\boldsymbol{\epsilon})\langle N, m_N|\mathcal{D}^{(k)}_{-p,q=0}(\omega)^*|N, m'_N\rangle \\ &= \delta_{N,N'}(-1)^{m_N}(2N+1)\sum_p (-1)^p T^{(2)}_p(\boldsymbol{\epsilon},\boldsymbol{\epsilon}) \\ &\times \begin{pmatrix} N & 2 & N \\ 0 & 0 & 0 \end{pmatrix}\begin{pmatrix} N & 2 & N \\ -m_N & -p & m'_N \end{pmatrix}.\end{aligned}$$

As a check, we will compare this formula against the explicit forms for $N = 1$ given in Ref. [110]. From Ref. [110], the diagonal terms are

$$\langle 1,0|\boldsymbol{\alpha}|1,0\rangle = \frac{\alpha_\parallel + 4\alpha_\perp}{5}\sin^2\theta + \frac{3\alpha_\parallel + 2\alpha_\perp}{5}\cos^2\theta \tag{A.20}$$

$$\langle 1,\pm1|\boldsymbol{\alpha}|1,\pm1\rangle = \frac{2\alpha_\parallel + 3\alpha_\perp}{5}\sin^2\theta + \frac{\alpha_\parallel + 4\alpha_\perp}{5}\cos^2\theta. \tag{A.21}$$

We will assume that $\boldsymbol{\epsilon}$ lies in the **x**-**z** plane, so $\boldsymbol{\epsilon} = (\sin\theta, 0, \cos\theta)$, and then the components of the tensor have simple expressions,

$$T^{(2)}_0(\boldsymbol{\epsilon},\boldsymbol{\epsilon}) = \frac{1}{\sqrt{6}}(2\cos^2\theta - \sin^2\theta) \tag{A.22}$$

$$T^{(2)}_{\pm1}(\boldsymbol{\epsilon},\boldsymbol{\epsilon}) = \mp\sin\theta\cos\theta \tag{A.23}$$

$$T^{(2)}_{\pm2}(\boldsymbol{\epsilon},\boldsymbol{\epsilon}) = \frac{1}{2}\sin^2\theta. \tag{A.24}$$

The diagonal components are

$$\begin{aligned}\langle 1,0|T^{(2)}(\boldsymbol{\epsilon},\boldsymbol{\epsilon})\cdot C_2(\alpha,\beta)|1,0\rangle &= 3\begin{pmatrix} 1 & 2 & 1 \\ 0 & 0 & 0 \end{pmatrix}^2 \frac{1}{\sqrt{6}}(2\cos^2\theta - \sin^2\theta) \\ &= \frac{\sqrt{6}}{15}(2\cos^2\theta - \sin^2\theta) \qquad \text{(A.25)} \\ \langle 1,\pm1|T^{(2)}(\boldsymbol{\epsilon},\boldsymbol{\epsilon})\cdot C_2(\alpha,\beta)|1,\pm1\rangle &= -3\begin{pmatrix} 1 & 2 & 1 \\ 0 & 0 & 0 \end{pmatrix}\begin{pmatrix} 1 & 2 & 1 \\ -1 & 0 & 1 \end{pmatrix}\frac{1}{\sqrt{6}}(2\cos^2\theta - \sin^2\theta) \\ &= -\frac{1}{5\sqrt{6}}(2\cos^2\theta - \sin^2\theta), \qquad \text{(A.26)}\end{aligned}$$

so the full matrix elements are

$$\begin{aligned}
\langle 1,0|\boldsymbol{\alpha}|1,0\rangle &= \frac{1}{3}(\alpha_\parallel + 2\alpha_\perp) + \frac{2}{15}(\alpha_\parallel - \alpha_\perp)(2\cos^2\theta - \sin^2\theta) \\
&= \frac{\alpha_\parallel + 4\alpha_\perp}{5}\sin^2\theta + \frac{3\alpha_\parallel + 2\alpha_\perp}{5}\cos^2\theta \\
\langle 1,\pm1|\boldsymbol{\alpha}|1\pm1\rangle &= \frac{1}{3}(\alpha_\parallel + 2\alpha_\perp) - \frac{1}{15}(\alpha_\parallel - \alpha_\perp)(2\cos^2\theta - \sin^2\theta) \\
&= \frac{2\alpha_\parallel + 3\alpha_\perp}{5}\sin^2\theta + \frac{\alpha_\parallel + 4\alpha_\perp}{5}\cos^2\theta,
\end{aligned}$$

which agree with the expressions from Ref. [110]! Now, let us check the off-diagonal terms,

$$\begin{aligned}
\langle 1,0|T^{(2)}(\boldsymbol{\epsilon},\boldsymbol{\epsilon})\cdot C_2(\alpha,\beta)|1,\pm1\rangle &= \mp 3 \begin{pmatrix} 1 & 2 & 1 \\ & & \\ 0 & 0 & 0 \end{pmatrix} \begin{pmatrix} 1 & 2 & 1 \\ & & \\ 0 & \mp1 & \pm1 \end{pmatrix} \sin\theta\cos\theta \\
&= \pm\frac{\sqrt{3}}{5}\sin\theta\cos\theta \qquad \text{(A.27)} \\
\langle 1,\pm1|T^{(2)}(\boldsymbol{\epsilon},\boldsymbol{\epsilon})\cdot C_2(\alpha,\beta)|1,\mp1\rangle &= -\frac{3}{2} \begin{pmatrix} 1 & 2 & 1 \\ & & \\ 0 & 0 & 0 \end{pmatrix} \begin{pmatrix} 1 & 2 & 1 \\ & & \\ \mp1 & \pm2 & \mp1 \end{pmatrix} \sin^2\theta \\
&= -\sqrt{\frac{3}{2}}\frac{1}{5}\sin^2\theta, \qquad \text{(A.28)}
\end{aligned}$$

so we get

$$\begin{aligned}
\langle 1,0|\boldsymbol{\alpha}|1,\pm1\rangle &= \pm\frac{\sqrt{2}}{5}(\alpha_\parallel - \alpha_\perp)\sin\theta\cos\theta \\
\langle 1,\pm1|\boldsymbol{\alpha}|1,\mp1\rangle &= -\frac{1}{5}(\alpha_\parallel - \alpha_\perp)\sin^2\theta.
\end{aligned}$$

These also match the equations from Ref. [110].

A.3 Comparison to experiment

Here, we briefly describe a few of the checks we have done on the output from BialkaliSpectrum.jl. Basic tests based on symmetry are implemented, for example, requiring that the spectrum is invariant under rotation of all fields (magnetic, electric, and optical) by the same angle.

Another automated test is to compare the calculated KRb spectrum at 545.9 G to the calculated values in Table II of Ref. [111]. Using the molecular parameters given in Ref. [111], we have

good agreement (< 1 kHz, the precision given for the calculations in the paper) with all of the entries in the table, except for the last row, which we believe is a minor typo. (If we use $|1, 0, -3, 1/2\rangle$ as the excited state instead of $|1, 0, -3, 3/2\rangle$, we have agreement with the value reported in the table. This would also make sense given the differential Zeeman shifts at 545.9 G.)

We also checked the calculated AC polarizability against the experimental values in Ref. [110]. We diagonalized the Hamiltonian from the main text of Ref. [110] and compared the polarizabilities of $N = 0$ and 1 with the output of our calculation (with the correct hyperfine states). We get within about 3.5% of the reported values over the full range of polarization angles compared to the of α. The experimental values of α were fitted using a perturbative model: the hyperfine states were only used to calculate the $I = 0$ energies of the states, but the rest of the model included only the $|N, m_N\rangle$ quantum numbers. This makes a small but noticeable difference as shown in the Supplementary Material of Ref. [110], and likely explains why we cannot reproduce the AC Stark shifts exactly with our calculation.

Finally, we also quickly checked the calculation by taking experimental data at $|\mathbf{E}| = 0$ (Figure A.1) and 1 kV/cm (Figure A.2). In both cases, we saw roughly the anticipated spectrum from the calculation. We have also used the calculation to help find the $|0, 0\rangle \rightarrow |1, 0\rangle$ at a variety of other fields, although at high fields the uncertainty of the experiment–calculation agreement is dominated by small uncertainties in the experimental calibration of $|\mathbf{E}|$.

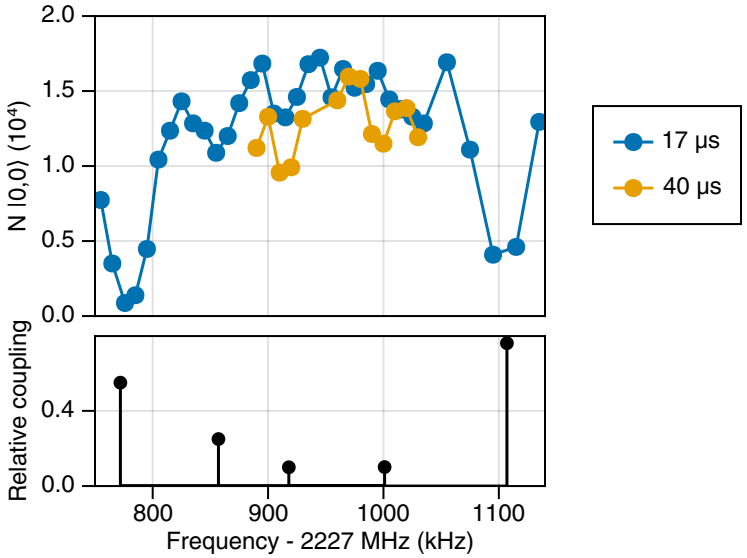

Figure A.1: Microwave spectrum at $|\mathbf{E}| = 0$ and $B = 545.9$ G. The molecules are held in the ODT + VL. Upper panel: Depletion from the ground state $|0, 0, -4, 1/2\rangle$ is measured as a function of the microwave frequency, for two different pulse times 17 μs (blue) and 40 μs (orange). Lower panel: Calculated transition frequencies and coupling strengths considering $|\mathbf{E}|$, B, and the optical traps. The calculated coupling strength depends on the polarization of the microwaves, which is not known (see section 3.4.2). We assumed that the microwave polarization was tilted 30 deg from the quantization axis for this calculation, which roughly reproduces the observed transition strengths.

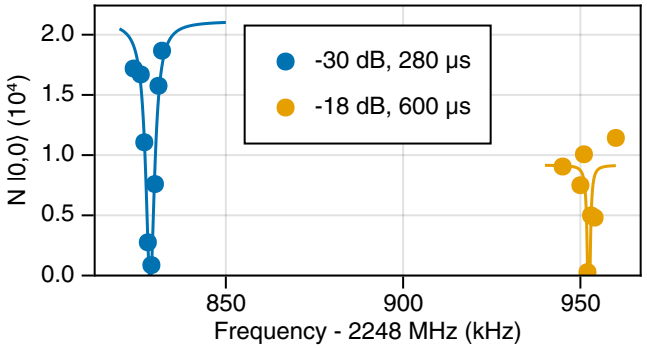

Figure A.2: Microwave spectrum at $|\mathbf{E}| = 1$ kV/cm. Here, $\mathbf{E}$ was oriented with an angle of 36 deg from vertical. The molecules are held in the ODT + VL at $B = 545.9$ G. The blue data points show microwave transfer from the initial state $|0, 0\rangle$ to $|1, 0\rangle$ of the same hyperfine character (m_N is defined relative to $\mathbf{E}$). The calculation predicted another hyperfine state of $|1, 0\rangle$ with a $\sim 10\times$ weaker coupling at about 120 kHz higher transition frequency. We were able to observe this additional state by increasing the power and duration of our pulse (orange points).